

Title	Development, Evaluation and Application of Metal Nanoparticles, Nanophotocatalysts and Nanocomposites
Author(s)	Abdulla-Al-Mamun, Md.
Citation	p.i-xiii,1-184
Issue Date	2010/3/25
URL	http://hdl.handle.net/10232/9157
Rights	

Kagoshima University Repository

**Development, Evaluation and Application of Metal
Nanoparticles, Nanophotocatalysts and
Nanocomposites**

March 2010

Md. Abdulla-Al-Mamun

Development, Evaluation and Application of Metal Nanoparticles, Nanophotocatalysts and Nanocomposites

(金属ナノ粒子, ナノ光触媒およびナノコンポジットの開発, 評価および応用)

In Partial Fulfillment
of the Requirements for the Degree
Doctor of Philosophy in Chemistry

A Dissertation
Presented to
The Academic Faculty

Submitted by-

*Md. Abdulla-Al-Mamun
Graduate School of Science and Engineering
Department of Nature System Science
Kagoshima University
Kagoshima, Japan*

(March 2010)

Development, Evaluation and Application of Metal Nanoparticles, Nanophotocatalysts and Nanocomposites

(金属ナノ粒子, ナノ光触媒およびナノコンポジットの開発, 評価および応用)

Approved by:

Yoshihumi Kusumoto, Prof. & Dr. Sci. (PhD)

Advisor

Department of Chemistry and Bioscience,

Graduate School of Science and Engineering, *Kagoshima University*,

1-21-35 Korimoto, Kagoshima 890-0065, Japan

Junichi Kurawaki Prof. & Dr. Sci. (PhD)

Co-advisor

Department of Chemistry and Bioscience,

Graduate School of Science and Engineering, *Kagoshima University*,

1-21-35 Korimoto, Kagoshima 890-0065, Japan

Yuji Horie, Prof. & Dr. Sci. (PhD)

Co-advisor

Department of Electrical and Electronics Engineering,

Graduate School of Science and Engineering, *Kagoshima University*,

1-21-40 Korimoto, Kagoshima 890-0065, Japan

Date approved: March 05, 2010

This thesis is dedicated to my beloved mother, Begum Rokeya Moqutadar, who always gave the mental support to do the best thing, listened to my aim, gave the encouragement, offered suggestions and advice, and always prayed for me.

ACKNOWLEDGEMENTS

I would like to extend my gratitude to the Ministry of Education, Culture, Sports, Science and Technology (MONBUKAGAKUSHO) of the Japanese Government for the Scholarship grant.

At first, I would like to extend my gratitude and thanks to my supervisor Prof. Yoshihumi Kusumoto for giving me the valuable opportunity to come to Kagoshima University and his lab for my PhD study. I appreciate that he let me work on this project which I like very much and I can do well on it. During those years in my study and research as a graduate student, I learned a lot from him. He taught me how to become a real scientist. His patience and wisdom impressed me very much. Instead of blaming, he always encouraged and helped me when I was not doing well on experiments, papers, and presentation. I really appreciate his support and advices from core of my heart. Without him, I could not achieve so much today. Secondly, I would like to express my sincere gratitude and thanks to Prof. Junichi Kurawaki from whom I received theoretical and practical training in chemistry and also for the useful discussions. Thirdly, I would like to special thanks Prof. Yuji Horie of the department of electronics and electrical engineering for the useful advice and permission to use laser machine in his laboratory.

I am also very thankful to entire staff of the Department of Chemistry and Bioscience, especially Mr. Yoshihisa Ozono and Mr. Terumi Kakoi of Frontier Science Research Center for measurement of XPS, EDAX and FE-SEM, TEM etc., and also thank to Professor Masahiko Hiroi for measurement of XRD. More especially I thank to staff of the Japanese language Center in Kagoshima University. They contributed immensely for my integration in the university as well as in the Japanese community of Kagoshima.

I would like to thank former and present co-workers of our laboratory, especially Dr. Miyuki Ikeda, Dr. Pascaline Ngweniform, Dr. Bashir Ahmmad, Dr. M. Muruganandham and

Mr. Hailong Yang for the useful discussions and friendliness. In addition, I cordially thank to Dr. Shouichi Somekawa who was a former student in our lab. He is so nice guy and so helpful at any time. When I came to the lab, it was him who taught me everything and let me acquaint myself with the lab. Whenever I asked for his help, he was always trying to help me without any consideration. I also thank to my other friends in and out of the Kagoshima University vicinity. I would like to also give the special thanks to my two lab mates, Miss. Chiyo Okamoto and Miss. Aki Mihata for their kind translation of my thesis summary from English to Japanese and their friendly cooperation.

Finally, I would like to thank my dearest wife, Tohfatul Zannat, who always loves and supports me at any time. I also want to thank my father, Md. Abdul Moqutadar, and my mother, Begum Rokeya Moqutadar and my two brothers and three sisters for their support on my study. I would like to also thank my cousin sister, Dr. Shaheda Akther Whab and her husband Dr. Alamgir Hossain for their continued support on my study.

Last but not least, I am very grateful to almighty Allah for his everlasting helps throughout my life.

TABLE OF CONTENTS

ACKNOWLEDGEMENTS	v
-------------------------------	---

CHAPTER 1	1-33
------------------	-------------

INTRODUCTION

1.1 General structural properties of nanoparticles and biological cell.....	3
1.2 Cancer.....	4
1.2.1 Cancer Scenarios in Japan.....	5
1.2.2 Cancer Scenarios in Bangladesh.....	6
1.2.3 Cancer and its Causes	6
1.2.4. Cancer diagnostics.....	7
1.2.5. Cancer therapy.....	9
1.3 Nanotechnology in cancer applications	11
1.3.1 Quantum dots in cancer imaging.....	11
1.3.2 Gold nanoshell in cancer imaging and photothermal therapy.....	11
1.3.3 Polymer nanoparticles in drug delivery.....	12
1.3.4 Gold nanoparticles in cancer imaging.....	12
1.4 Photoelectrochemical cell.....	13
1.4.1 Historical background of Photoelectrochemical cells.....	13
1.4.2 The Energy challenge.....	14
1.5 Photosynthetic and regenerative cells	15
1.5.1 Catalysis with semiconductor / metal nanocomposite	21
1.6 Aim and Objectives.....	24
References.....	25

CHAPTER 2	34-46
------------------	--------------

DETAILS OF THE DIFFERENT EXPERIMENTS CARRIED OUT

2.1 Cell Culture.....	34
2.2 Synthesizes of noble metal Au, Pt, Ag and Cu nanoparticles by laser ablation method	38
2.3 Synthesizes of noble metal Au, Ag and Cu nanoparticles by chemical reduction method.....	39
2.3.1 Preparation of gold colloidal nanoparticles by citrate reduction method.....	39
2.3.2 Preparation of silver colloidal nanoparticles by citrate reduction method.....	40
2.3.3 Preparation of copper colloidal nanoparticles in Water-acetonitrile mixed solvent.....	40
2.4 Preparation of noble metal-semiconductors nanomaterials	41
2.4.1 Preparation of Au capped TiO ₂ (Au@TiO ₂) nanopellet.....	41
2.4.2 Preparation of Ag metal core-TiO ₂ shell (Ag@TiO ₂) composite nanocluster.....	42
2.4.3 Preparation of Cu-TiO ₂ nanocomposite.....	42
2.5 Preparation of solar cell.....	43
2.5.1 Preparation of thin film.....	43
2.5.1. (a) Laser ablation method.....	43
2.5.1. (b) Squeegee method.....	44
2.5.2 Instruments and measurements of solar cell.....	45
References.....	46

CHAPTER 3 **47-58**

**PLASMON-INDUCED PHOTOTHERMAL CELL-KILLING EFFECT
OF GOLD COLLOIDAL NANOPARTICLES ON EPITHELIAL
CARCINOMA CELLS**

Abstract.....	47
3.1 Introduction.....	47
3.2 Experimental.....	50

3.3 Results and discussion.....	52
3.4 Conclusion.....	57
References.....	57

CHAPTER 4 **59-66**

SIMPLE NEW SYNTHESIS OF COPPER NANOPARTICLES IN WATER / ACETONITRILE MIXED SOLVENT AND THEIR CHARECTERIZATION

Abstract.....	59
4.1 Introduction.....	59
4.2 Experimental.....	61
4.3 Results and discussion.....	62
4.4 Conclusion.....	65
References.....	65

CHAPTER 5 **69-87**

ENHANCED PHOTOCATALYTIC CYTOTOXIC ACTIVITY OF Au@TiO₂ NANOPELLETS AGAINST HUMAN EPITHELIAL CARCINOMA (HeLa) CELLS

Abstract.....	67
5.1 Introduction.....	67
5.2 Experimental.....	69
5.2.1 Preparation of TiO ₂ Colloidal Suspension.....	69
5.2.2 Preparation and Characterization of TiO ₂ /Au Nanopellet.....	70
5.2.3 Cell Culture and Cellular Incubation with Colloidal Nanopellet.....	71
5.2.4 Light Irradiation of Colloidal Nanopellets on Cells.....	71
5.2.5 Cells Imaging Method.....	72

5.3 Results and discussion.....	72
5.3.1 Characterization of the Au capped TiO ₂ nanopellet.....	72
5.3.2 Photocatalytic Cancer Cell Killing Enhance Using Gold Capped TiO ₂	77
5.4 Conclusion.....	85
References.....	86

CHAPTER 6

88-108

CYTOTOXIC EVALUTION OF Ag@TiO₂ CORE-SHELL COMPOSITE

NANOCLUSTER AGAINST CANCER CELLS

Abstract.....	88
6.1 Introduction.....	88
6.2 Experimental.....	90
6.2.1 Chemicals and materials.....	90
6.2.2 Synthesis of Ag@TiO ₂ Core-shell Nanocluster Photocatalyst.....	90
6.2.3 Instrumental analysis.....	91
6.2.3 Cell Culture and Cellular Incubation with Colloidal Nanocluster.....	92
6.2.3.1 Cell line and counting method.....	92
6.2.3.2 Light Irradiation of Colloidal Nanocluster on Cells.....	92
6.2.3.3 Cells Imaging Method.....	93
6.3 Results and discussion.....	93
6.3.1 Synthesis and Characterizations of Ag@TiO ₂ Core-shell Nanocluster.....	93
6.3.2 Photocatalytic Cancer Cell Killing Enhance Using Ag@TiO ₂ core-shell nanocluster.....	99
6.4 Conclusion.....	106
References.....	106

NEW SIMPLE SYNTHESIS OF Cu-TiO₂ NANOCOMPOSITE: HIGHLY ENHANCED PHOTOCATALYTIC KILLING OF EPITHELIA CARCINOMA (HeLa) CELLS

Abstract.....	109
7.1 Introduction.....	109
7.2 Experimental.....	111
7.3 Results and discussion.....	112
7.4 Conclusion.....	120
References.....	120

MINERALIZER-ASSISTED SHAPE-CONTROLLED SYNTHESIS, CHARACTERIZATION AND PHOTOCATALYTIC EVALUATION OF CdS MICROCRYSTALS

Abstract.....	122
8.1 Introduction.....	123
8.2 Experimental.....	125
8.3 Results and discussion.....	127
8.3.1. Influence of decomposition temperature and time.....	131
8.3.2. Influence of mineralizer (KNO ₃).....	135
8.3.3. Mechanism.....	144
8.3.4. Photocatalytic hydrogen production.....	147
8.4 Conclusion.....	150
References.....	151

**WET-TYPED Fe₂O₃ SOLAR CELLS BASED ON Fe₂O₃ FILMS
PREPARED BY LASER ABLATION: DRASTIC TEMPERATURE
EFFECT**

Abstract.....	153
9.1 Introduction.....	153
9.2 Experimental.....	154
9.3 Results and discussion.....	155
References.....	160

**A COMPARATIVE STUDY OF PLASMON-INDUCED CHARGE
SEPARATION OF TiO₂, Fe₂O₃, AND ZnO FILMS LOADED WITH
GOLD NANOPARTICLES**

Abstract.....	161
10.1 Introduction.....	161
10.2 Experimental.....	163
10.2.1 Synthesis and characterization of Au nanoparticles	163
10.2.2 Preparation of Au-TiO ₂ , Au-Fe ₂ O ₃ and Au-ZnO film	164
10.2.3 Preparation of Au-semiconductor film (immersed method)	165
10.2.4 Instruments and measurements for characterization of cell	165
10.3 Results and discussion.....	166
10.4 Conclusion.....	172
References.....	173

CHAPTER 11 **174-184**

SUMMARY OF THE DISSERTATION.....174
PUBLICATIONS.....180
CONFERENCE PRESENTATIONS.....183

CHAPTER 1

INTRODUCTION

Noble metal colloidal nanoparticles and noble metal-semiconductor nanomaterials is one of the promising candidates for photothermal and photocatalytic cancer cell killing and photoelectrochemical-cell charge separation. The precise reduction of size and shape of materials to nanometer scale is providing different physical and chemical properties tremendously. As noble metals are reduced in size to ten's place nanometers, a new very strong absorption is observed resulting from the collective oscillation of the electrons in the conduction band from one surface of the particle to the other. This oscillation has a frequency that absorbs the visible light. This is called the surface plasmon absorption.

Noble metals such as copper, silver and gold have a strong visible-light plasmon resonance, whereas most other transition metals show only a broad and poorly resolved absorption band in the ultraviolet region. This difference is attributed to the strong coupling between the plasmon transition and the interband excitation. In addition, the conduction band electrons of the noble metals can move freely, independently from the ionic background, and the ions act only as scattering centers. This gives the electrons in the noble metals a higher polarizability, which shifts the plasmon resonance to lower frequencies with a sharp bandwidth. This strong absorption, giving rise to vivid characteristic color, has been observed and used. In transition metal nanoparticles, decrease in the particle size to the nanometer length scale increases the surface-to-volume ratio. This, together with our ability to make them in different sizes and shapes, makes them potentially useful in the field of catalysis [1-2]. In noble metals the coherent collective oscillation of electrons in the conduction band induces large surface electric fields which greatly enhance the radiative properties of gold, silver and copper nanoparticles when they interact with resonant

electromagnetic radiation [3]. This makes the absorption cross-section of these nanoparticles orders of magnitude stronger than the strongest absorbing molecules [4] and the scattered light becomes orders of magnitude more intense than the fluorescence of organic dyes [5]. These unique properties provide great potential for the nanoparticles to be used in many applications, such as biochemical sensors [6], biological imaging and medical therapeutics [7-12] as well as in catalysis because of their high surface-to-volume ratios [13-14].

In semiconductors reduce size and shape, results from the further confinement of the electronic motion to a length scale that is comparable to or smaller than the length scale characterizing the electronic motion in bulk semiconducting material (called the electron Bohr radius, which is usually a few nanometers) [15]. The emerging field of semiconductor and metal nanoparticles has stimulated much interest in recent years because of their size and shape dependent electronic properties [16-21]. The functional properties of such materials can be greatly improved by capping the semiconductor or metal nanocluster with another layer of compatible material. Such core/shell geometry not only improves the stability of the nanoparticles but also expands the scope of composite nanoclusters in a wide array of applications (e.g., luminescent displays, microelectronics photochemical solar cells, sensors and memory devices) [22-24]. Some examples of core/shell type nanomaterials include semiconductor/semiconductor, [25-28] semiconductor/metal, [29] metal /semiconductor, [30-33] metal/metal, [34-36] and metal/metal oxide [37-40] systems.

Noble metal-semiconductor is one of the most popular heterostructures because of its wide application in photocatalysis [41-46] where the metal in contact with the semiconductor greatly enhances the overall photocatalytic redox process, because the metal acts as a reservoir of photoelectrons, improving the interfacial charge-transfer process and retarding the recombination of photoexcited electron holes of semiconductors [44,46,47-51]. In most cases, the metal nanocrystals were anchored on the surfaces of the semiconductors as isolated “islands” to produce hetero interfaces due to catalytic activity dependent on the

size of the metal nanocrystals [41, 42, 46, 47, 52]. Despite effective catalytic activity, this structural drawback results in exposing metal and oxide surfaces to reactants, products, and surrounding medium. Corrosion or dissolution of the noble metal particles during a photocatalytic reaction becomes problematic in practical applications [52, 53]. It is necessary to design new strategies to either improve the chemical stability or attain higher photoconversion efficiency [52]. Accordingly, heterostructures with metal core and semiconductor shell become increasingly among the strongest candidates as photocatalysts due to their controllable chemical and colloidal stability within the shell and charge transfer between metal cores and semiconductors [52].

1.1 General structural properties of nanoparticles and biological cell

Nanotechnology for cancer research (Also known as cancer nanotechnology) has been attracted as their effective size and shape structure of the nanoparticles. Nanotechnology is a multidisciplinary field, which covers a vast and divers array of devices derived from engineering, biology, physics and chemistry. These nanoscale devices are somewhere from one hundred to ten thousand times smaller than human cells. They are similar in size to large biological molecules (biomolecules) such as enzyme and receptors. As an example, hemoglobin, the molecule that carries oxygen in red blood cells, is approximately 5 nanometers in diameter. Nanoscale devices smaller than 50 nm can easily enter most cells, while those smaller than 20 nm can move out of blood vessels as they circulate through the body [54-56].

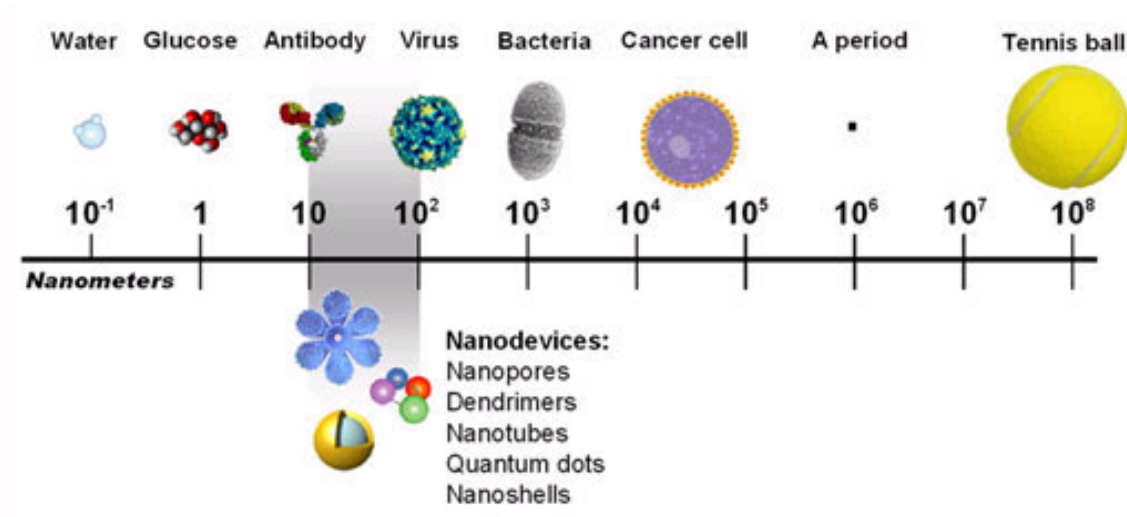


Fig. 1-1: General size and shape feature of nanodevices and biological cell (ref.7)

1.2 Cancer

Cancer is a leading cause of death worldwide: it accounted for 7.9 million deaths (around 13% of all deaths) in 2007 and the total number of cases globally is increasing. Lung, stomach, liver, colon and breast cancer cause the most cancer deaths each year (Fig. 1-2).

The number of global cancer deaths is projected to increase 45% from 2007 to 2030 (from 7.9 million to 11.5 million deaths), influenced in part by an increasing and aging global population. The estimated rise takes into account expected slight declines in death rates for some cancers in high resource countries. New cases of cancer in the same period are estimated to jump from 11.3 million in 2007 to 15.5 million in 2030.

In most developed countries, cancer is the second largest cause of death after cardiovascular disease, and epidemiological evidence points to this trend emerging in the less developed world. This is particularly true in countries in "transition" or middle-income countries, such as in South America and Asia. Already more than half of all cancer cases occur in developing countries.

Lung cancer kills more people than any other cancer - a trend that is expected to continue until 2030, unless efforts for global tobacco control are greatly intensified. Some cancers are more common in developed countries: prostate, breast and colon where as Liver, stomach and cervical cancer is more common in developing countries.

A number of common risk factors have been linked to the development of cancer: an unhealthy lifestyle (including tobacco and alcohol use, inadequate diet, physical inactivity), and exposure to occupational (e.g. asbestos) or environmental carcinogens, (e.g. indoor air pollution), radiation (e.g. ultraviolet and ionizing radiation), and some infections (such as hepatitis B or human papilloma virus infection) [57].

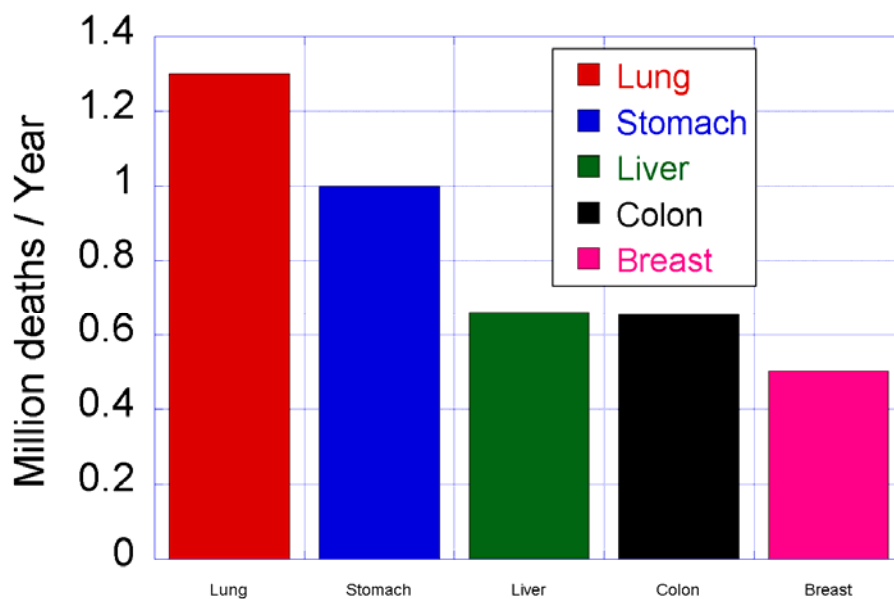


Fig. 1-2: Cancer fact in worldwide.

1.2.1 Cancer Scenarios in Japan

In Japan one in every three people dies of cancer. According to statistics compiled by the Ministry of Health, Labor and Welfare, 336,290 people died of cancer in 2007, accounting for one in every three deaths. Heart diseases, the second biggest killer, accounted for only about half of the number of cancer deaths [58].

Cancer deaths in Japan are surveyed by vital statistics, with 100% coverage. The number of cancer deaths in 2006 in Japan was approximately 329,000. The number of male cancer deaths was 1.5 times greater than that of female cancer deaths. In terms of cancer sites, lung was the leading site (23%) for males, followed by stomach (17%), Liver (11%), colon (7%; same rank when colon and rectum are combined: 11%), and pancreas (6%). The leading site for females was stomach (13%; Note that colon and rectum was the leading cancer death site when combined: 14%), followed by lung (13%), colon (10%), breast (9%), and liver (8%) [59].

1.2.2 Cancer Scenarios in Bangladesh

With the increase of the incidence of Cancer in the country, it has become a matter of serious concern for Bangladesh. Although definite figures about the incidence of cancer is not available in Bangladesh, it is estimated that there are around 800,000 cancer patients in the country of the 130 million people and about 200,000 new cases are being added every year. Around 150,000 cancer patients die annually [60].

1.2.3 Cancer and its Causes

Cancer is a group of diseases characterized by uncontrolled cell division leading to growth of abnormal tissue. It is believed that cancers arise from both genetic and environmental factors and the individual way of life that lead to aberrant growth regulation of a stem cell population, or by the dedifferentiation of more mature cell types.

Many, but not all, cancer-causing agents damage DNA. The agents that can cause cancer are many and varied, but the easier to understand are those that cause damage to DNA, and so generate mutations [61]. These cancer-causing mutagens include chemical carcinogens, viruses, and various forms of radiation-UV light and ionizing radiation such as gamma rays and alpha particles from radioactive decay.

As certain period normal cells are damaged or old they undergo the apoptosis or necrosis death.

Procaspase-3 (Zymogen) →Caspase-3 (Protein)→Suicide by apoptosis

On the other hand cancer cells avoid this apoptosis or necrosis and grow the out of control.

Procaspase-3(Zymogen) →no Caspase-3 (Protein)→Avoid Suicide by apoptosis

The uncontrolled and often rapid proliferation of cells can lead to either a benign tumor or a malignant tumor (cancer). Benign tumors do not spread to other parts of the body or invade other tissues, and they are rarely a threat to life. Malignant tumors can invade other organs, spread to distant locations (metastasize) and become life threatening.

Cancer usually forms as a tumor. Some cancer, like leukemia, does not form tumors. Instead, these cancer cells involve the blood and blood-forming organs and circulate through other tissues where they grow. Often, not all tumors are cancerous. Benign (noncancerous) tumors do not spread (metastasize) to other parts of the body and, with very rare exceptions, are not life threatening [62].

Cancer develops when cells in a part of the body begin to grow out of control. Although there are many kinds of cancer, they all start because of out-of-control growth of abnormal cells. Under normal conditions, the cells in the human body divide and grow in an orderly, controlled manner. Cancer occurs when cells grow in an uncontrolled manner. Instead of dying, they outlive normal cells and continue to form new abnormal cells [63].

The cancer cell is profoundly abnormal cells which can be observed under simple optical microscope. Cancer cell's morphology is different from that of a normal cell. Its nucleus is larger and irregular.

1.2.4. Cancer diagnostics

Conventional cancer diagnostics depends on the cell pathology, such as biopsy, endoscopy, and imaging which all looked at the cell appearance under microscope [64, 65]. Biopsy is the only sure way to test for cancer. In biopsy, the doctor removes a sample of the

tissue on the abnormal area or may removes the whole tumor and then a pathologist examines the tissue under microscope.

Endoscopy is to look into the body by using a thin, lighted tube. Sample tissue or cells can be collected for further examination through the forceps on the tip of the tube. Imaging is to look at the inside of the body using X-ray, or CT (computed tomography), ultrasonography and MRI (magnetic resonance imaging). It usually uses a special dye that is put into the body to stain certain organs and increase the imaging contrast. X-ray imaging is the most common way to make pictures of the inside of the body. CT, sometimes called CAT (computed angled tomography) scan, uses special x-ray equipment to obtain image data from different angles around the body and then uses computer processing of the information to show a cross-section of body tissues and organs. Ultrasonography uses high-frequency sound wave to enter the body and then use the echoes to produce a picture called a sonogram. MRI uses radiofrequency waves and a strong magnetic field to provide remarkably clear and detailed pictures of internal organs and tissues. The technique has proven very valuable for the diagnosis of a broad range of pathologic conditions in all parts of the body including cancer, heart and vascular disease, stroke, spinal and joint problems.

With the advanced development of molecular biology in the last decade, enormous progress has been made to understand the molecular events that accompany malignant transformation and progression by genomics and proteomics [66]. Molecular diagnostics determines how the genes and proteins in cancer cells and or organism are interacting in a cell by expressing these molecular signatures as patterns [67,68]. Compared to the conventional pathology methods, these patterns improve the clinical's ability to diagnostics cancers with more accuracy and they assist early cancer detection. However, these advances have not yet impacted on diagnostics and staging of the majority of cancer cells in real time [69].

1.2.5. Cancer therapy

It is well known that the traditional cancer treatment includes surgery, radiation, hormone therapy and more recently chemotherapy, immunotherapy and combined strategies [70]. Surgery is the oldest form of treatment for cancer. It offers the greatest chance for cure for many types of cancer, especially those that have not yet spread to other parts of the body but not for cancers at late phase. It will continue to be an extremely important weapon against cancer.

Radiation is the second weapon against cancer. Radiation therapy involves treating cancer with beams of high-energy particles, or waves (radiation), such as X-rays, gamma rays, neutrons or pions [71]. Radiotherapists often implant radioactive materials or radioisotopes into tumors. The particles transfer their energy into electrons which ionize the matter they reach such as water and/or the solid constituents of cytoplasm, RNA and DNA. This ionization damages the molecules and leads the free radicals to recombine with oxygen available in the environment. Thus changes the biological properties of the biomolecules such as causing the cell to die or make it impossible to divide. Radiation is much more harmful to cancer cells than it is to normal cells. This is because cancer cells divide more rapidly than do healthy cells. Cells are more vulnerable to damage when they're dividing, making cancer cells to be more susceptible to radiation than normal cells. In addition, normal cells can recover from the effects of radiation more easily than cancer cells. But still it is nonetheless true that it is impossible to kill a tumor without harming the surrounding healthy cells.

Hormone therapy changes the internal environment and prevents the growth of cancers that are hormone-dependent such as breast and prostate cancers. It is usually called androgen deprivation therapy (ADT) or androgen suppression therapy. Controlling cancer of the prostate is the triumph of hormone therapy. Androgens, produced mainly in the testicles, can actually stimulate prostate cancer cells to grow. Hormone therapy is to lower

androgen levels (either by surgery or drugs such as pituitary down-regulators and anti-androgens) can usually make prostate cancers shrink or grow more slowly.

Chemotherapy is most often used to mean taking medicines, or drugs, to treat cancer, especially suitable for those cancers that have been spread out and can not be used by the local methods such as surgery and radiation. Normal cells grow and die in a controlled way. Cancer cells keep dividing and forming more cells without control. Anticancer drugs destroy cancer cells by stopping them from growing or multiplying. They also go after and damage any healthy cells that are quickly dividing, whether it's a cancer cell or not. Lately emerged photothermal therapy have greatly improved the therapy efficiency by injecting contrast agents such as weak emitting dyes [72, 73] into the tumor sites which convert the photoenergy into thermal energy and thus kill the cancer cells. Photosensitizers are also been reported for photodynamic therapy which use photoexcited molecules to transfer their energy to oxygen forming excited singlet oxygen which injures cancer cells [74, 75].

With the development of immunology, immunotherapy (also known as biologic therapy) is emerged as a more specific cancer treatment method. Immunotherapy is a treatment that uses certain parts of the immune system to fight diseases, including cancer. This can be done by stimulating your own immune system to work harder or by using an outside source, such as manmade immune system proteins [76]. Compared to other forms of cancer treatment, such as surgery, radiation therapy, or chemotherapy, immunotherapy is relatively new. One of the immunotherapy is to use monoclonal antibody which specifically target the cancer cells and then block the cancer cell activation or cure the cancer cells by attaching radioactive chemicals on the antibodies [77]. Some monoclonal antibodies that react with specific antigens on certain types of cancer cells have been used in clinical trials [78]. Compared with side effects of standard chemotherapy, the side effects of naked MAbs are usually relatively mild and are often related to an "allergic" reaction.

1.3 Nanotechnology in cancer applications

With the tremendous development of nanotechnology, a variety of nanostructures with different shapes and structures of different composites [79-89] has been provided. These nanostructures demonstrate unique electronic, photonic, catalytic and highly controlled and interesting properties as a consequence of the size reduction from bulk to nanoscale [90-95]. These nanoparticles exhibit similar size dimensions to many common biomolecules such as proteins and DNA, thus offer great possibilities for the integration of nanotechnology to biotechnology. Typical applications include contrast agents for disease diagnostics and therapies [96-99], developing homogenous immuassay [100-102] and assembling new materials [103-104]. The use of nanoparticles in medicine is one of the important directions that nanotechnology is taking at this time. Their applications in drug delivery [105-107], cancer cell diagnostics [108-113] and therapeutics [12,114-115] have been active fields of research.

1.3.1 Quantum dots in cancer imaging

One of the most widely used nanoparticles in the cancer applications are the semiconductor nanocrystals, also referred to as quantum dots, due to their wide absorption ranges and unique size dependent fluorescence properties [110-111]. They are highly fluorescent and photobleach resistant [97-98]. They can be used for imaging cancer cell markers [109]. They can provide single excitation for multicolor images, which is not possible for molecular fluorophors because of their narrow excitation spectra. But the potential human cytotoxicity of the semiconductor material is one major problem for its *in vivo* application.

1.3.2 Gold nanoshell in cancer imaging and photothermal therapy

Another kind of nanoparticles for cancer applications is called gold nanoshell nanoparticles [12, 112, 116-119]. It contains silica core (about 140 nm in diameter) with a thin layer of gold shells (about 10 nm). The absorption band of core-shell particles can be

tuned by adjusting the ratio of the thickness of the gold shell to the diameter of the silica core [116] and thus enables both strong scattering and absorption efficiency. Therefore they can be used as dual imaging/therapy contrast agents [112].

1.3.3 Polymer nanoparticles in drug delivery

Nanoparticles have become a greatly studied for use in drug delivery for therapeutic applications due to their small size which is suited for intravenous delivery. Polymer has several advantages over other nanoparticles such as easy incorporation or incubation of the drug with the nanoparticles, the ability to stabilize the drugs in vivo and no side effects (especially for the biodegradable polymers) [120-124]. Polymer can also be functionalized with cancer marker targeting molecules as other nanoparticles. So the polymer can specifically target the cancer cells and then release the drugs to the cancer [125].

1.3.4 Gold nanoparticles in cancer imaging

Solid gold nanoparticles have been widely interested due to its easy preparation, ready bioconjugation and potential noncytotoxicity [126]. Various methods for the preparation of gold colloids were reported in the 20th century [127]. It only takes several minutes to synthesize the nanoparticles in a boiling auric solution that is reduced by citrate molecules, which is the most popular synthesis method. The sizes of the nanoparticles can be easily changed by changing the citrate concentration [128]. The citrate capped nanoparticles are very stable but the citrate ion can be replaced and functionalized with various ligands for specific applications. The safety of gold nanoparticles is well-known.

Gold nanoparticles have already been used in vivo since the 1950's as a radiotracer [126]. Using the light scattering properties of gold nanoparticles, preliminary studies have reported their use as contrast agents for biomedical imaging using multiphoton plasmon resonance microscopy [9], third-harmonic microscopy [11], optical coherence microscopy [10] and confocal scanning optical microscopy [8].

Gold nanoparticles have several advantages for imaging application compared to other agents. The scattered light is very strong and they are much brighter than chemical fluorophores. They are photobleach resistant and can be easily seen in as low as 10^{-16} M concentration [129]. Sokolov [8] have used confocal microscope to detect the scattering of anti-EGFR/Au nanoparticles for cervical cancer. Irradiation with a laser will only produce single color which is close to the laser wavelength used. When illuminated with a beam of white light, gold nanoparticles will scatter light of many colors. The color of the light is determined by the absorption spectrum of the nanoparticles which depends on the shape and size of the nanoparticles [8]. This color dependent scattering property provides the potential for imaging studies with a simple white light source.

1.4 Photoelectrochemical cell

The increasing energy demand in the near future will force us to seek environmentally clean alternative energy resources. The emergence of nanomaterials as the new building blocks to construct light energy harvesting assemblies has opened up new ways to utilize renewable energy sources.

1.4.1 Historical background of Photoelectrochemical cells

Becquerel's pioneering photoelectric experiments in 1839 were done with liquid not solid-state devices a fact that is often ignored. His research, in which illumination of solutions containing a metal halide salt produced a current between two platinum electrodes immersed in the electrolyte, was motivated by photography. Daguerre had made the first photographic images in 1837, and Fox Talbot followed with the silver halide process in 1839. Although the art of formulating emulsions only became a science with the theoretical analysis of the process by Gurney and Mott [130] in 1938, there was constant empirical progress in the sensitivity of photographic films. Initially, films were particularly insensitive to mid-spectrum and red light. This is now recognized as being due to the semiconductor nature of the silver halide grains: they have a band gap (a gap in the allowed electronic

energy levels) which ranges from 2.7 to 3.2 electron volts (eV) and negligible light absorption at wavelengths longer than 460 nm. Vogel's discovery [131] in 1883 that silver halide emulsions could be sensitized by adding a dye extended the photosensitivity to longer wavelengths. Four years later, the concept of dye enhancement was carried over by Moser [132] from photography to photoelectrochemical cells using the dye erythrosine on silver halide electrodes. This parallel between photography and photoelectrochemistry comes as a surprise to many chemists [133]. That the same dyes were particularly effective for both processes was recognized by Namba and Hishiki at the 1964 International Conference on Photosensitization of Solids in Chicago, which was a seminal event in the history of sensitization [134]. It was also recognized that the dye should be adsorbed on the semiconductor electrodes in a closely packed monolayer for maximum efficiency [135]. At this stage it was still debated whether sensitization occurred by transfer of electrons or of energy from the dye to the semiconductor [136]. Subsequent studies, notably by Hauffe [137], Tributsch and Gerischer [138], showed electron transfer to be the prevalent mechanism both for photographic and for Photoelectrochemical sensitization processes.

Many centuries ago, scientists are success to describe phenomenon of photocatalytic in surface of metal-oxide semiconductor. Firstly, have been issued by Renz in 1921 until 1960, and not responding by scientist. Photocatalytic semiconductor popularity increase since publication Akira Fujishima in Nature magazine was issued in 1972. He was reported decomposition water be oxygen and hydrogen used single crystal TiO_2 with input UV light in low energy.

1.4.2 The Energy challenge

The increasing energy demand in the near future will force us to seek environmentally clean alternative energy resources. The emergence of nanomaterials as the new building blocks to construct light energy harvesting assemblies has opened up new ways to utilize renewable energy sources. Their common dream is to capture the energy that is freely

available from sunlight and turn it into the valuable and strategically important asset that is electric power, or use it to generate fuels such as hydrogen. Photovoltaics takes advantage of the fact that photons falling on a semiconductor can create electron–hole pairs, and at a junction between two different materials, this effect can set up an electric potential difference across the interface. So far, the science of solar cells has been dominated by devices in which the junction is between inorganic solid-state materials, usually doped forms of crystalline or amorphous silicon, and profiting from the experience and material availability resulting from the semiconductor industry.

The development of these new type's metal/semiconductor solar cells is promoted by increasing public awareness that the Earth's oil reserves could run out during this century. As the energy needs of the planet are likely to double within the next 50 years, the stage is set for a major energy shortage, unless renewable energy can cover the substantial deficit left by fossil fuels. Public concern has been heightened by the disastrous environmental pollution arising from all-too-frequent oil spills and the frightening climatic consequences of the greenhouse effect caused by fossil fuel combustion. Fortunately the supply of energy from the Sun to the Earth is gigantic: 321024 joules a year, or about 10,000 times more than the global population currently consumes. In other words, covering 0.1% of the Earth's surface with solar cells with an efficiency of 10% would satisfy our present needs. But to tap into this huge energy reservoir remains an enormous challenge.

1.5 Photosynthetic and regenerative cells

The metal/semiconductor nanoparticles photovoltaic cells are based on photoexcitation of metal nanoparticles and semiconductor like TiO_2 , Fe_2O_3 , ZnO etc molecules. For instance, when the illuminate photon energy is greater then molecular binding energy, the metal nanoparticles become excited due to plasmon resonance and electron flow to the semiconductor conduction band (Fig.1-3) [139]. The electron transfer occurs due to favorable energy difference between the lowest unoccupied molecular orbital (LUMO) of

the metal like gold and the conduction band of Semiconductor. The photogenerated electrons rapidly through the Semiconductor conduction band and are collected by the conducting glass (ITO glass) support.

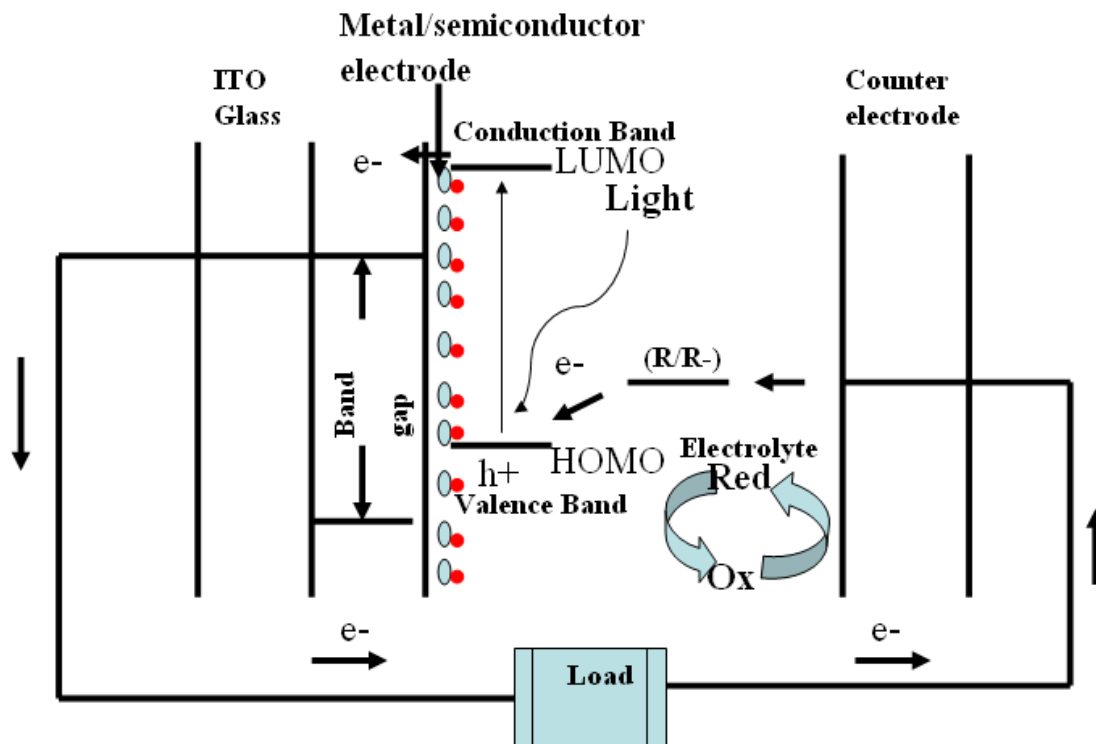


Fig.1-3: Schematic energy diagram of photocurrent and photovoltage generation in solar cell.

The electrons vacancy fills up from the donor solution like electrolyte to the metal nanoparticles. The highest occupied molecular orbital (HOMO) of the metal like Au-molecules lower than redox potential, E_{Redox} of the electrolyte like iodine/triiodide couple. The energy difference provides the driving force for hole injection into the electrolyte. The electrolyte and hole minimized the charge by redox reaction and transport one type of carrier like electron is energetically from the Au-molecule to the semiconductor [140].

Titanium dioxide has been the favoured and representative semiconductor for these studies, following its use by Fujishima and Honda for water photolysis [141]. The band gap energy of a semiconductor is the minimum energy of light required to make the material electrically conductive, or, in other words to get the electrons excited enough to get moving.

Unfortunately TiO_2 have the large band gap (3–3.2 eV, as shown in Fig. 1-4) and absorbs only the ultraviolet part of the solar emission and so has low conversion efficiencies. The energy band diagrams of some representative semiconductors are shown in Fig. 1-4.

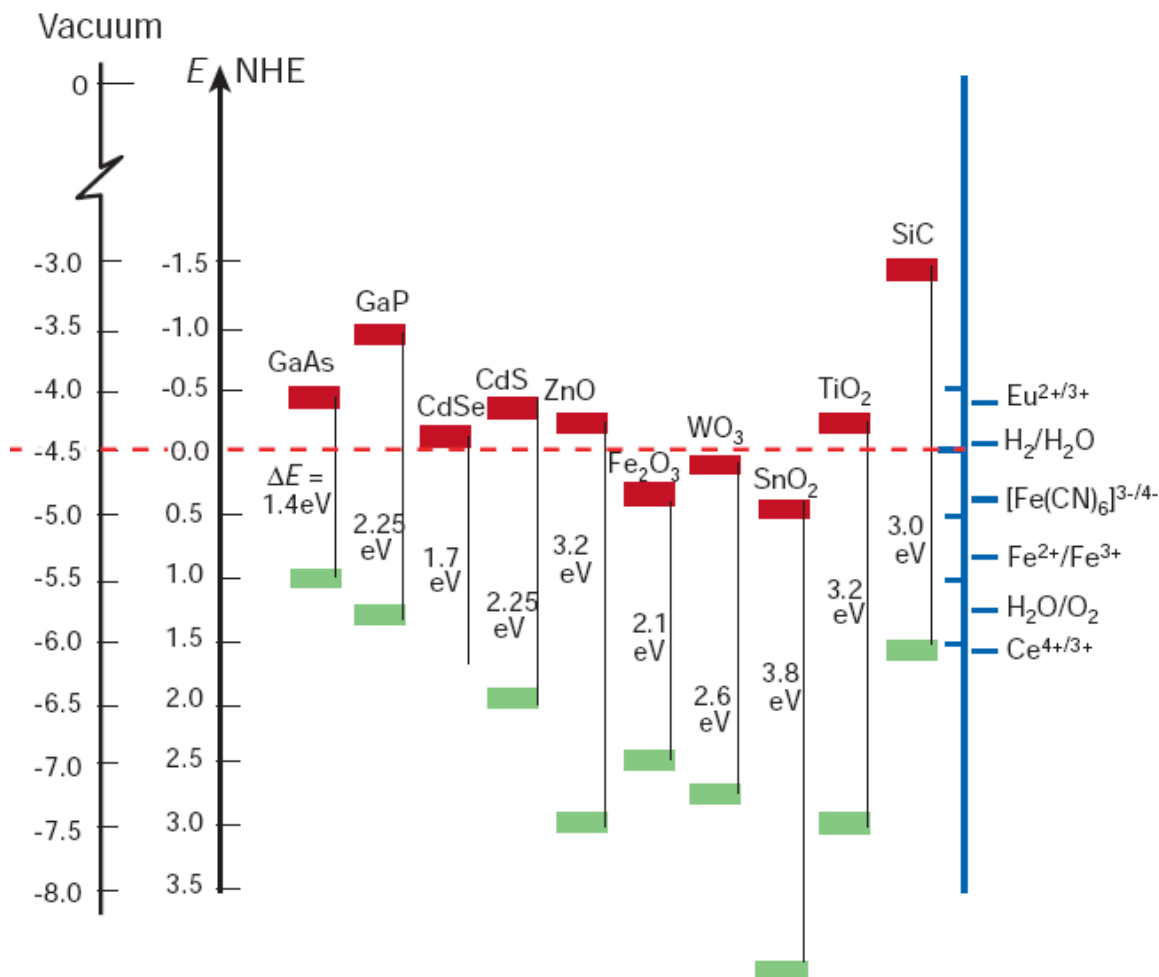


Fig. 1-4: Energy band diagram for typical semiconductor in contact with aqueous electrolyte at pH 1. The lower edge of the conduction band (red colour) and upper edge of the valence band (green colour) are presented along with the band gap in electron volts. The energy scale is indicated in electron volts using either the normal hydrogen electrode (NHE) or the vacuum level as a reference. Note that the ordinate presents internal and not free energy. The free energy of an electron–hole pair is smaller than the band gap energy due to the translational entropy of the electrons and holes in the conduction and valence band, respectively. On the right side the standard potentials of several redox couples are presented against the standard hydrogen electrode potential.

In terms of energy usage, the complete electrolytic decomposition of water is possible if the CB energy is at least as negative (higher in the diagram) as that required to reduce water to hydrogen gas (0.00 V in acids solution), and the VB is at least as positive (lower in diagram) as that required to oxidize water to oxygen gas (+1.23 V). The complete decomposition of water is thus theoretically possible if a semiconductor is illuminated with light that has the minimum band gap energy of 1.23 eV, assuming that the VB and CB energies are placed at exactly the right points.

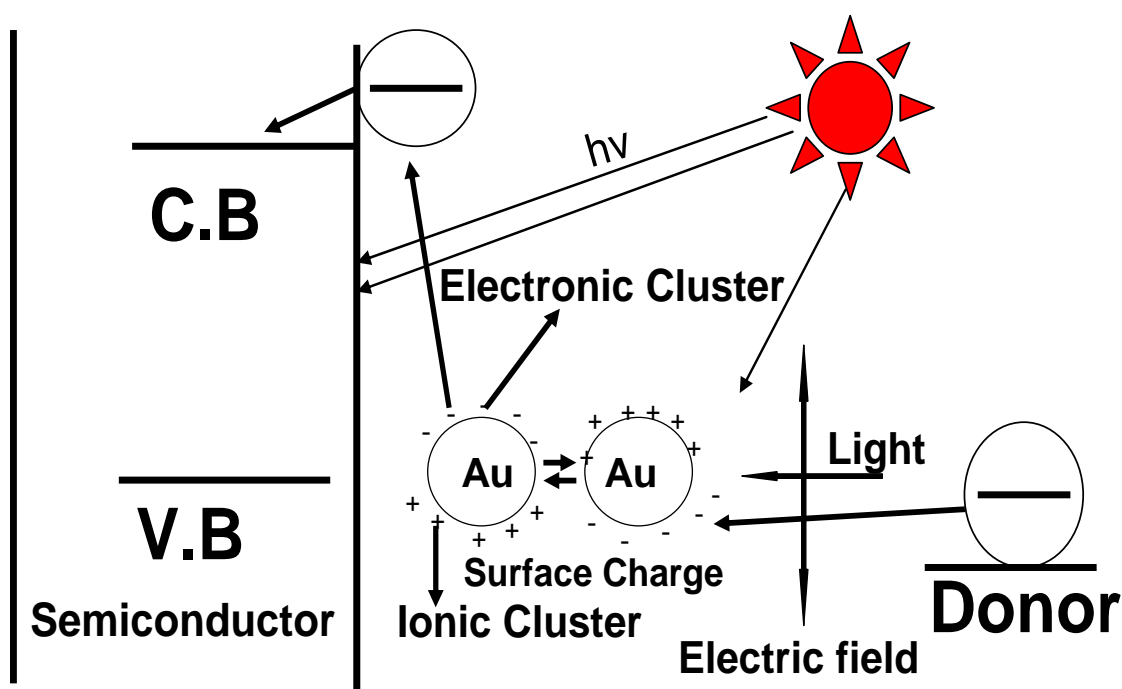


Fig. 1-5: Schematic energy diagram of photocurrent and photovoltage generation in solar cell

The gold nanoparticles photovoltaic cells are based on photoexcitation of Au-nanoparticles and semiconductors like TiO_2 , Fe_2O_3 and ZnO . For instance, when conduction electrons oscillate coherently, they displace an electron cloud from the nuclei giving rise to a surface charge distribution. The Au-nanoparticles become excited due to plasmon resonance and electron cloud flows to the semiconductor conduction band (Fig.1-5). The

photogenerated electrons rapidly passed through the semiconductor conduction band and are collected by the conducting glass (ITO glass) support. The electrons vacancies in the Au-nanoparticles are filled up with the donor in the solution like electrolyte.

When a semiconductor is placed in contact with an electrolyte, electric current initially flows across the junction until electronic equilibrium is reached, where the Fermi energy of the electrons in the solid (E_F) is equal to the redox potential of the electrolyte (E_{redox}), as shown in the Fig 1-3, 1-5, 1-6 and 1-7. The transfer of electric charge produces a region on each side of the junction where the charge distribution differs from the bulk material, and this is known as the space-charge layer. On the electrolyte side, this corresponds to the familiar electrolytic double layer, that is, the compact (Helmholtz) layer followed by the diffuse (Gouy–Chapman) layer. On the semiconductor side of the junction the nature of the band bending depends on the position of the Fermi level in the solid. If the Fermi level of the electrode is equal to the flat band potential, there is no excess charge on either side of the junction and the bands are flat. If electrons accumulate at the semiconductor side one obtains an accumulation layer. If, however, they deplete from the solid into the solution, a depletion layer is formed, leaving behind a positive excess charge formed by immobile ionized donor states. Finally, electron depletion can go so far that their concentration at the interface falls below the intrinsic level. As a consequence, the semiconductor is *p*-type at the surface and *n*-type in the bulk, corresponding to an inversion layer. The illustration in the figure 4 refers to *n*-type materials where electrons are the mobile charge carriers. For *p*-type semiconductors, analogous considerations apply. Positive holes are the mobile charge carriers and the immobile negatively charged states of the acceptor dopant form the excess space charge within the depletion layer.

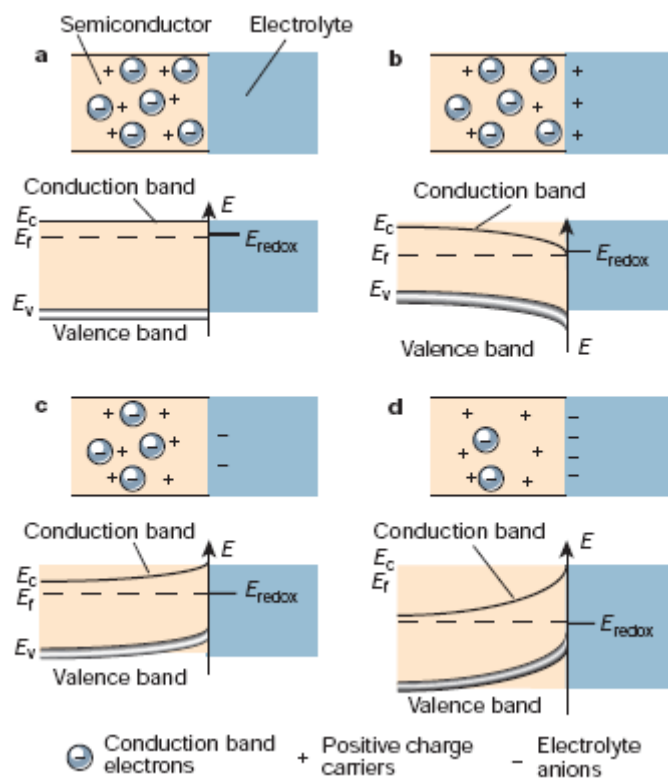


Fig. 1-6: Schematic showing the electronic energy levels at the interface between an n-type semiconductor and an electrolyte containing a redox couple. The four cases indicated are: **a**, flat band potential, where no space-charge layer exists in the semiconductor; **b**, accumulation layer, where excess electrons have been injected into the solid producing a downward bending of the conduction and valence band towards the interface; **c**, depletion layer, where electrons have moved from the semiconductor to the electrolyte, producing an upward bending of the bands; and **d**, inversion layer where the electrons have been depleted below their intrinsic level, enhancing the upward band bending and rendering the semiconductor p-type at the surface.

In view of these prolonged efforts, disillusionment has grown about the prospects of photoelectrochemical cells being able to give rise to competitive photovoltaic devices, as those semiconductors with band gaps narrow enough for efficient absorption of visible light are unstable against photocorrosion. The width of the band gap is a measure of the chemical bond strength. Semiconductors stable under illumination, typically oxides of metals such as

titanium or niobium, therefore have a wide band gap, an absorption edge towards the ultraviolet and consequently insensitivity to the visible spectrum. The resolution of this dilemma came in the separation of the optical absorption and charge-generating functions, using an electron transfer sensitizer absorbing in the visible to inject charge carriers across the semiconductor–electrolyte junction into a substrate with a wide band gap, and therefore stable. Fig. 1-3 shows the operational principle of such a device.

1.5.1 Catalysis with semiconductor / metal nanocomposite

Numerous attempts to shift the spectral response of TiO_2 into the visible, or to develop alternative oxides affording water cleavage by visible light, have so far failed. A number of attempts have been made to add various metals or metal oxides to titanium dioxide as “dopants” so that the material can make use of light in the visible region. The addition of ruthenium or chromium to strontium titanate, for example, can produce a considerable response to visible light. The resulting efficiency, however, is no better because of very low quantum efficiency, i.e. the photogenerated CB electrons and VB holes simply recombine with each other, producing heat, before they can do anything useful.

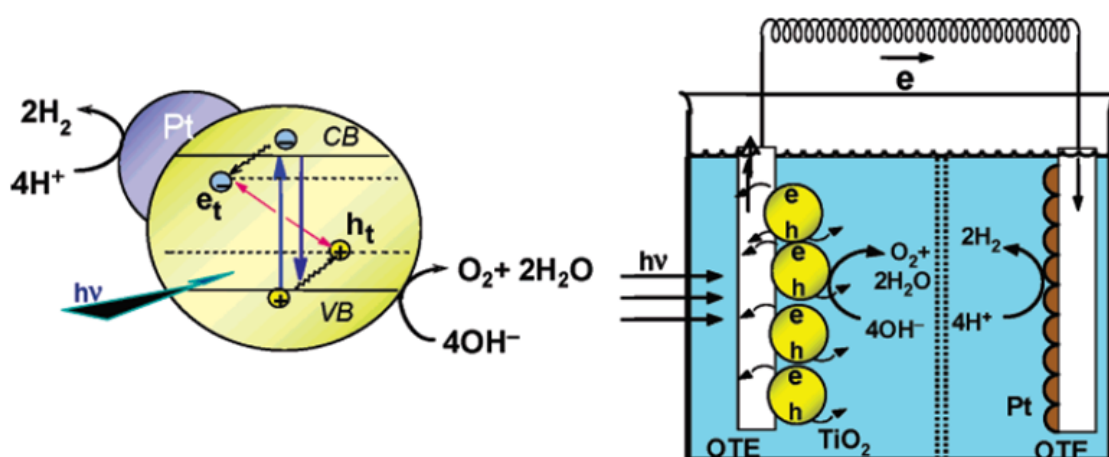


Fig. 1-7: Photocatalytic splitting of water following the band gap excitation of the semiconductor nanoparticle (left) and a photoelectrolysis cell based on a nanostructured semiconductor film electrode (right).

Semiconductor nanoparticles when subjected to band gap excitation undergo charge separation. Because of the small size of particles and high recombination rate, only a fraction (~5%) of these charges can be utilized to induce redox processes at the interface. The photocatalytic processes using TiO₂ and other semiconductors have demonstrated the need to overcome the limitations in achieving higher photoconversion efficiencies. Of particular interest is the use of semiconductor nanostructures for solar hydrogen production by the photocatalytic splitting of water [142-147]. The principle of photocatalysis for producing solar hydrogen is presented in Fig. 1-7.

The noble metal (e.g., Pt), which acts as a reservoir for photogenerated electrons, promotes an interfacial charge-transfer process. A direct correlation between the work function of the metal and the photocatalytic activity for the generation of NH₃ from azide ions has been made for metalized TiO₂ systems. For more than two decades, a number of research groups are involved in modifying the photocatalytic properties of TiO₂ and other semiconductor materials using metal deposits. [142]

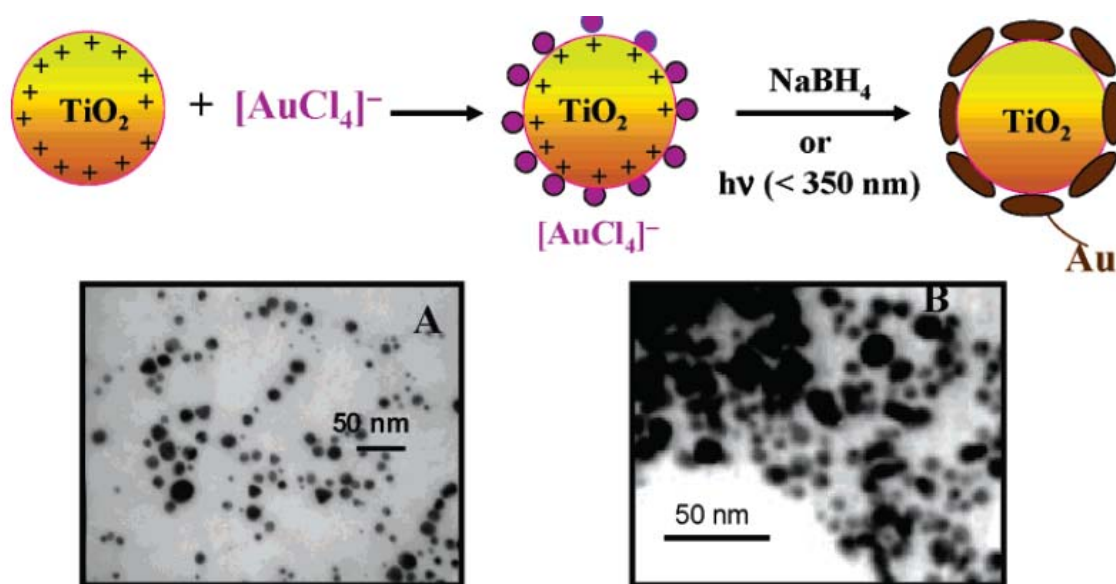


Fig. 1-8: synthetic strategies for preparing semiconductor-gold nanoparticles. TEM images of gold capped TiO₂ particles prepared using (A) Chemical reduction and (B) UV-irradiation are shown.

The principle for preparing such metal-semiconductor nanocomposites is shown in Fig. 1-8. Similar methodology has also been adopted to deposit silver clusters on anatase TiO₂ nanorods. These Ag-TiO₂ nanorods show the possibility of enhancing photocatalytic activities by way of morphology and the size of silver clusters.

Fundamental understanding of the photoinduced interactions between a semiconductor and metal as well as the interfacial charge-transfer process in nanocomposites is important to elucidate the role of noble metals in semiconductor assisted photocatalysis. A better understanding of the energetics of such nanocomposite systems is important for tailoring the properties of next-generation nanodevices. The mediating role of noble metals in storing and shuttling photogenerated electrons from the semiconductor to an acceptor in a photocatalytic process can be understood by designing composite structures with coupled and core-shell geometry (Fig.1-9).

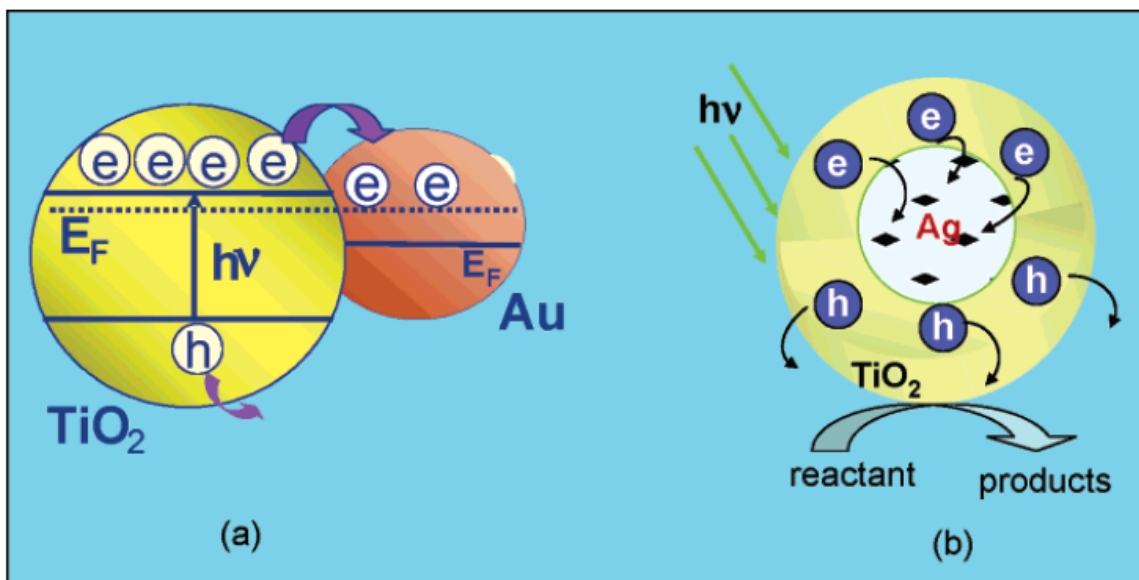


Fig. 1-9: Design of semiconductor-metal nanocomposites using (a) coupled and (b) core-shell geometry.

Metal nanoparticle deposition was found to promote the interfacial charge-transfer process in these composite systems. A ~40% enhancement in the hole transfer efficiency

was confirmed in the laser flash photolysis study of gold capped TiO₂ nanoparticles. The size of nanoparticles as well as the mode of deposition of metal nanoparticles becomes crucial while tailoring the properties of semiconductor films. Similarly, interfacial changes seen when subjected to UV irradiation also influence the overall photocatalytic activity of semiconductor-metal composites. Chemical, electrochemical, and photolytic methods are commonly used for the deposition of noble metals on semiconductor nanoparticles. One simple way to deposit metal on TiO₂ is to choose a metal ion that electrostatically binds to the oxide surface. The gold capped TiO₂ nanoparticles for example can be prepared by first synthesizing a TiO₂ suspension in water (stabilized at pH 1.5) and then capping these particles with [AuCl₄]⁻.

1.6 Aim and Objectives

In this thesis, new simple synthesis noble metal (copper) nanoparticles [148], and the application of gold nanospheres [149] and metal-semiconductors nanomaterials [150-152] in the cancer cell killing therapy are demonstrated in detail. This includes using the surface plasmon absorption band of gold nanoparticles and the strong scattering properties strongly gives the change their size-shape structure under visible light irradiation and give the photothermal cytotoxicity for cancer cell killing, using the particle's strong absorption properties. The efficient energy conversion process from photo energy to local heat energy [149] is used for photothermal cancer therapy. The photocatalytic and photothermal property of metal-semiconductors nanoparticles for the cancer cell killing and solar cell is also described. In addition, the development of novel techniques for preparation and characterizations of noble metal nanoparticles and metal-semiconductors nanophotocatalyst for cancer cell killing and photoelectrochemical cell charge separation is also described and demonstrated. Furthermore, some other related studies such as the surfactant free synthesis of nanoparticles and novel innovative technique for preparation of metal-semiconductor nanophotocatalysts and their inside cells with cell killing mechanism are also discussed.

References

- [1] Clemens Burda, Xiaobo Chen, Radha Narayanan, and Mostafa A. El-Sayed, *Chem. Rev.* **2005**, 105, 1025-1102.
- [2] Kreibig, U.; Vollmer, M. *Optical Properties of Metal Clusters*; New York: Springer, **1995**.
- [3] El-Sayed, M. A. *Acc. Chem. Res.* **2001**, 34(4), 257.
- [4] Link, S.; El-Sayed, M. A. *J. Phys. Chem. B* **1999**, 103, 8410.
- [5] Yguerabide, J.; Yguerabide, E. E. *Anal. Biochem.* **1998**, 262, 137.
- [6] Mirkin, C. A.; Letsinger, R. L.; Mucic, R. C.; Storhoff, J. J. *Nature*, **1996**, 382, 607
- [7] Sokolov, K.; Aaron, J.; Hsu, B.; Nida, D.; Gillanwater, A.; Follen, M.; Macaulay, C.; Adler-Storthz, K.; Korgel, B.; Discour, M.; Pasqualini, R.; Arap, W.; Lam, W.; Richartz Kortum, R. *Technol. Cancer Res. & Treat.* **2003**, 2(6), 491.
- [8] Sokolov, K.; Follen, M.; Aaron, J.; Pavlova, I.; Malpica, A.; Lotan, R.; Richartz-Kortum, R. *Cancer Res.* **2003**, 63, 1999.
- [9] Yelin, D.; Oron, D.; Thiberge, S.; Moses, E.; Silberberg, Y. *Optics Express* **2003**, 11, 1385-1391.
- [10] Raub, C. B.; Orwin, E. J.; Haskell, R. *J. Biomech. Eng.* **2003**, 125, 1-6.
- [11] Yelin, D.; Oron, D.; Korkotian, E.; Segal, M.; Silberberg, Y. *Apply. Phys. B: Lasers and Optics* **2002**, 74 (Suppl.), S97-S101.
- [12] Hirsch, L. R.; Stafford, R. J.; Bankson, J. A.; Sershen, S. R.; Rivera, B.; Rice, R. E.; Hazle, J. D.; Halas, N. J.; West, J. L. *Proc. Natl. Acad. Sci. USA* **2003**, 100, 13549.
- [13] Freund, P. L.; Spiro, M. *J. Phys. Chem.* **1985**, 89, 1074.
- [14] Freund, P. L.; Spiro, M. *J. Chem. Soc., Faraday Trans. 1* **1986**, 82, 2277. 40
- [15] Alivisatos, A. P. *Science*, **1996**, 271, 933-937.
- [16] *Semiconductor Nanoclusters-Physical, Chemical and Catalytic Aspects*; Kamat, P. V., Meisel, D., Eds.; Elsevier Science: Amsterdam, 1997; p 474.

- [17] Alivisatos, P. *J. Phys. Chem.* **1996**, *100*, 13226.
- [18] Henglein, A. *J. Phys. Chem.* **1993**, *97*, 5457.
- [19] Steigerwald, M. L.; Brus, L. E. *Acc. Chem. Res.* **1990**, *23*, 183.
- [20] Link, S.; El-Sayed, M. A. *J. Phys. Chem. B* **1999**, *103*, 8410.
- [21] Bechinger, C.; Ferrere, S.; Zaban, A.; Sprague, J.; Gregg, B. A. *Nature* **1996**, *383*, 608.
- [22] Hagfeldt, A.; Graetzel, M. *Chem. ReV.* **1995**, *95*, 49.
- [23] Klein, D. L.; Roth, R.; Lim, A. K. L.; Alivisatos, P.; McEuen, P. L. *Nature* **1997**, *389*, 699.
- [24] Haesselbarth, A.; Eychmueller, A.; Eichberger, R.; Giersig, M.; Mews, A.; Weller, H. *J. Phys. Chem.* **1993**, *97*, 5333.
- [25] Bedja, I.; Kamat, P. V. *J. Phys. Chem.* **1995**, *99*, 9182.
- [26] Kamalov, V. F.; Little, R.; Logunov, S. L.; El-Sayed, M. A. *J. Phys. Chem.* **1996**, *100*, 6381.
- [27] Mews, A.; Kadavanich, A. V.; Banin, U.; Alivisatos, A. P. *Phys. ReV.* **1996**, *B53*, R13242.
- [28] Kamat, P. V. Composite Semiconductor Nanoclusters. In *Semiconductor Nanoclusters - Physical, Chemical and Catalytic Aspects*; Kamat, P. V., Meisel, D., Eds.; Elsevier Science: Amsterdam, 1997; p 237.
- [29] Kraeutler, B.; Bard, A. J. *J. Am. Chem. Soc.* **1978**, *100*, 4317.
- [30] Shanghavi, B.; Kamat, P. V. *J. Phys. Chem. B* **1997**, *101*, 7675.
- [31] Pastoriza-Santos, I.; Koktysh, D. S.; Mamedov, A. A.; Giersig, M.; Kotov, N. A.; Liz-Marza'n, L. M. *Langmuir* **2000**, *16*, 2731.
- [32] Schreder, B.; Schmidt, T.; Ptatschek, V.; Winkler, U.; Materny, A.; Umbach, E.; Lerch, M.; G. Müller, G.; W. Kiefer, W.; Spanhel, L. *J. Phys. Chem. B* **2000**, *104*, 1677.
- [33] Marignier, J. L.; Belloni, J.; Delcourt, M. O.; Chevalier, J. P. *Nature* **1985**, *317*, 344.

- [34] Freeman, R. G.; Hommer, M. B.; Grabar, K. C.; Jackson, M. A.; Natan, M. J. *J. Phys. Chem.* **1996**, *100*, 718.
- [35] Mulvaney, P.; Giersig, M.; Henglein, A. *J. Phys. Chem.* **1993**, *97*, 7061.
- [36] Henglein, A. *J. Phys. Chem. B* **2000**, *104*, 6683.
- [37] Lawless, D.; Kapoor, S.; Kennepohl, P.; Meisel, D.; Serpone, N. *J. Phys. Chem.* **1994**, *98*, 9619.
- [38] Liz-Marza'n, L. M.; Giersig, M.; Mulvaney, P. *Langmuir* **1996**, *12*, 4329.
- [39] Makarova, O. V.; Ostafin, A. E.; Miyoshi, H.; Norris, J. R.; Meisel, D. *J. Phys. Chem. B* **1999**, *103*, 9080.
- [40] Hardikar, V.; Matijevic, E. *J. Colloid Interface Sci* **2000**, *221*, 133.
- [41] Wu, J. J.; Tseng, C. H. *Appl. Catal. B-Environ.* **2006**, *66*, 51.
- [42] Iliev, V.; Tomova, D.; Todorovska, R.; Oliver, D.; Petrov, L.; Todorovsky, D.; Uzunova-Bujnova, M. *Appl. Catal. A-Gen.* **2006**, *313*, 115.
- [43] Zheng, J. Y.; Yu, H.; Li, X. J.; Zhang, S. Q. *Appl. Surf. Sci.* **2008**, *254*, 1630.
- [44] Subramanian, V.; Wolf, E. E.; Kamat, P. V. *J. Am. Chem. Soc.* **2004**, *126*, 4943.
- [45] Zheng, Y. H.; Chen, C. Q.; Zhan, Y. Y.; Lin, X. Y.; Zheng, Q.; Wei, K.; Zhu, J. F. *J. Phys. Chem. C* **2008**, *112*, 10773.
- [46] Lam, S. W.; Chiang, K.; Lim, T. M.; Amal, R.; Low, G. K. C. *Appl. Catal. B Environ.* **2007**, *72*, 363.
- [47] Lee, M. S.; Hong, S. S.; Mohseni, M. *J. Mol. Catal. A-Chem.* **2005**, *242*, 135.
- [48] Hirakawa, T.; Kamat, P. V. *Langmuir* **2004**, *20*, 5645.
- [49] Hirakawa, T.; Kamat, P. V. *J. Am. Chem. Soc.* **2005**, *127*, 3928.
- [50] Oldfield, G.; Ung, T.; Mulvaney, P. *Adv. Mater.* **2000**, *12*, 1519.
- [51] Berger, T.; Sterrer, M.; Diwald, O.; Kno1zinger, E. *J. Phys. Chem. B* **2005**, *109*, 6061.
- [52] Kamat, P. V. *J. Phys. Chem. C* **2007**, *111*, 2834.
- [53] Subramanian, V.; Wolf, E.; Kamat, P. V. *J. Phys. Chem. B* **2001**, *105*, 11439.

- [54] Johnson, N.P., Butour, j.-L., Villani, G., Wimmer, F.L., Defais, M., Pierson, V., et al., *Prog. Biochem. Med.*, **1989**, *10*, 1-24.
- [55] B. Devika Chithrani, Arezou A. Ghazani, and Warren C. W. Chan, *Nano Lett.*, **2006**, *6*(4), 662.
- [56] Scott E. McNeil, *Journal of Leukocyte Biology*, **2005**, *78*, 10 pages.
- [57] WORLD HEALTH ORGANIZATION (WHO) “The faces of cancer”
- [58] Japan Cancer Society, Cancer in Japan,
- [59] National Cancer Center, Cancer Statistic in Japan 2008.
- [60] Cancer: A Bangladesh Perspective, Mohd. Shamim Iqbal, M2 Graduate Student, Department of Bio-Signal Analysis, Yamaguchi University Graduate School of Medicine, Japan
- [61] Stein, G. S.; Pardee, A. B. *Cell cycle and growth control: biomolecular regulation and cancer*, **2004**, Hoboken, NJ: Wiley-Liss.
- [62] *Oncologie* [electronic resource], **2004**, Paris; New York: Springer.
- [63] *Released news*, **6/6/05**, National Cancer Institute.
- [64] Bair, F. E. *Cancer Sourcebook: Basic Information on Cancer Types, Symptoms, Diagnostic Methods, and Treatments, Including Statistics on Cancer Occurrences World (Health Reference Series)*, Vol. 1, Omnigraphics, **1990**.
- [65] Nakamura, R. M.; Grody, W. W.; Wu, J. T.; Nagle, R. B. *Cancer diagnostics, current and future trend*, Humana Press, **2004**.
- [66] Roulston, J. E.; John, M. S. *Molecular Diagnosis of Cancer Methods and Protocols*, 2nd ed., **2004**.
- [67] Eleftherios, P. D. *Clinical Chemistry* **2003**, *49*, 1272.
- [68] Balmain, A.; Gray J.; Ponder, B. *Nature Genetics* **2003**, *33*, 238.

- [69] Sokolov, K.; Aaron, J.; Hsu, B.; Nida, D.; Gillanwater, A.; Follen, M.; Macaulay, C.; Adler-Storthz, K.; Korgel, B.; Discour, M.; Pasqualini, R.; Arap, W.; Lam, W.; Richartz Kortum, R. *Technology in Cancer Research & Treatment* **2003**, 2(6), 491.
- [70] Miller, A. B.; Hoogstraten, B.; Staquet, M.; Winkler, A. *Cancer* **1981**, 47(1), 207.
- [71] Lucien Israel, *Conquering Cancer*, Random House, New York, **1978**.
- [72] Chen, W. R.; Adams, R. L.; Carubelic, R.; Nordquist, R. E. *Cancer Letters* **1997**, 115, 25.
- [73] Chen, W. R.; Adams, R. L.; Higgins, A. K.; Bartfeld, K. E.; Nordquist, R. E. *Cancer Letters* **1996**, 98, 169.
- [74] D'Cruz, A. K.; Robinson, M. H.; Biel, M. A. *Head & Neck* **2004**, 3, 232.
- [75] McBride, G. *J. Nat. Cancer Inst.* **2002**, 94, 1740.
- [76] Rosenberg, S.A. *Immunity* **1999**, 10(3), 281.
- [77] Weiner, L. M. *Semin Oncol.* **1999**, 26(4 Suppl 12), 41.
- [78] Harari, P. M.; *Endocrine-Related Cancer* **2004**, 11, 689.
- [79] Alivisatos, A. P. *Science*, **1996**, 271, 933-937.
- [80] Link, S.; El-Sayed, M. A. *J. Phys. Chem. B* **1999**, 103, 8410.
- [81] Jana, N. R.; Gearheart, L.; Murphy, C. J. *J. Phys. Chem. B* **2003**, 105, 4065.
- [82] Jin, R.; Cao, Y.; Mirkin, C. A.; Kelly, K. L.; Schatz, G. C.; Zheng, J. *Science* **2001**, 294, 1901.
- [83] Sun, Y.; Xia, Y. *Science* **2002**, 298, 2139.
- [84] Maillard, M.; Giorgio, S.; Pileni, M.-P. *Adv. Mater.* **2002**, 14, 1084.
- [85] Murray, C. B.; Noms, D. J.; Bawendi, M. G. *J. Am. Chem. Soc.* **1993**, 115, 8706.
- [86] Dabbousi, B. O.; Rodriguez-Viejo, J.; Mikulec, F. V.; Heine, J. R.; Mattoussi, H.; Ober, R.; Jensen, K. F.; Bawendi, M. G. *J. Phys. Chem. B* **1997**, 101, 9463.
- [87] Peng, X.; Schlamp, M. C.; Kadavanich, A. V.; Alivisatos, A. P. *J. Am. Chem. Soc.* **1997**, 119, 7019.

- [88] Guzelian, A. A.; Katari, J. E.; Kadavanich, A. V.; Banin, U.; Hamad, K. E.; Juban, A.; Alivisatos, A. P. *J. Phys. Chem.* **1996**, *100*, 7212.
- [89] Hines, M. A.; Guyot-Sionnest, P. *J. Phys. Chem.* **1996**, *100*, 468.
- [90] Link, S.; El-Sayed, M. A. *Annu. Rev. Phys. Chem.* **2003**, *54*, 331.
- [91] Link, S.; El-Sayed, M. A. *Int. Reviews Phys. Chem.* **2000**, *19*(3), 409.
- [92] Schmid, G. *Clusters and Colloids: From Theory to Application*. Weinheim: VCH New York: Academic, **1994**.
- [93] Kamat, P. V.; Meisel, D. *Studies in Surface Science and Catalysis*, Vol. 103, New York: Wiley. *Semiconductor Nanoclusters—Physical, Chemical, and Catalytic Aspects*. Amsterdam: Elsevier. **1997**.
- [94] Edelstein, A. S.; Cammarata, R. C. *Nanoparticles: Synthesis, Properties and Applications*. Bristol: Inst. Phys. **1996**.
- [95] Hagfeldt, A.; Graetzel, M. *Acc. Chem. Res.* **2000**, *33*, 269.
- [96] Niemeyer, C. M. *Angew Chem Int Ed Engl*, **2001**, *40*, 4128.
- [97] Bruchez, M. Jr.; Moronne, M.; Gin, P.; Weiss, S.; Alivisatos, A. P. *Science* **1998**, *281*, 2013.
- [98] Chan, W. C. W.; Nie, S. M. *Science* **1998**, *281*, 2016.
- [99] Pathak, S.; Choi, S.K.; Arnheim, N.; Thompson, M.E. *J. Am. Chem. Soc.* **2001**, *123*, 4103.
- [100] Elghanian, R.; Storhoff, J.J.; Mucic, R.C.; Letsinger, R.L.; Mirkin, C.A. *Science* **1997**, *277*, 1078.
- [101] Dubertret, B.; Calame, M.; Libchaber, A.J. *Nat Biotechnol.* **2001**, *19*, 365.
- [102] Reynolds, R. A.; Mirkin, C. A.; Letsinger, R. L. *J. Am. Chem. Soc.* **2000**, *122*, 3795.
- [103] Mirkin, C. A.; Letsinger, R. L.; Mucic, R. C.; Storhoff, J. J. *Nature* **1996**, *382*, 607.
- [104] Alivisatos, A. P.; Johnsson, K. P.; Peng, X.; Wilson, T. E.; Loweth, C. J.; Bruchez, M. P. Jr.; Schultz, P. G. *Nature* **1996**, *382*, 609.

- [105] Bruchez Jr, M.; Moronne, M.; Gin, P.; Weiss, S.; Alivisatos, A. P. *Nature* **1996**, 382, 609.
- [106] West, J. L.; Halas, N. J. *Annu. Rev. Biomed. Eng.* **2003**, 5, 285.
- [107] Paciotti, G. F.; Myer, L.; Weinreich, D.; Goia, D.; Pavel, N.; McLaughlin, R. E.; Tamarkin, L. *Drug Delivery*, **2004**, 11(3), 169.
- [108] Jain, K. K. *Technol. Cancer Res. & Treat.* **2005**, 4(4), 407.
- [109] Wu, X.; Liu, H.; Liu, J.; Haley, K. N.; Treadway, J. A.; Larson, J. P.; Ge, N.; Peale, F.; Bruchez, M. P. *Nat. Biotechnol.* **2003**, 21, 41.
- [110] Chan, W. C. W.; Maxwell, D. J.; Gao, X.; Bailey, R. E.; Han, M.; Nie, S. *Curr. Opin. Biotechnol.* **2002**, 13, 40.
- [111] Watson, W.; Wu, X.; Bruchez, M. *Bioimaging* **2003**, 34, 296.
- [112] Loo, C.; Lowery, A.; Halas, N.; West, J.; Drezek, R. *Nano letters* **2005**, 5, 709
- [113] El-Sayed, I. H.; Huang, X.; EL-Sayed, M. A. *Nano letters* **2005**, 5, 821.
- [114] El-Sayed, I. H.; Huang, X.; EL-Sayed, M. A. *Cancer letters* **2005**, in press.
- [115] Huang, X.; El-Sayed, I.; Qian, W.; El-Sayed, M. A. *JACS*, **2006**, 128, 2115.
- [116] Oldenburg, S.J. et. al., *Chem. Phys. Letters*, **1998**, 288, 243.
- [117] West, J. L.; Halas, N. J. *Cur. Opin. Biotech.* **2002**, 11, 215.
- [118] Loo, C. H.; Lin, A.; Hirsch, L. R.; Lee, M. H.; Barton, J.; Halas, N. J.; West, J.; Drezek, R. A. *Technology in Cancer Research and Treatment* **2004**, 3, 33.
- [119] O'Neal, D. P.; Hirsch, L. R.; Halas, N. J.; Payne, J. D.; West, J. L. *Cancer Letters* **2004**, 209, 171.
- [120] Kreuter, J.; *Colloidal Drug Delivery Systems*, Marcel Dekker, New York, **1994**, pp 219–342.
- [121] Song, C.; Labhasetwar, V.; Cui, X.; Underwood, T.; Levy, R. J. *J. Control. Release* **1998**, 54, 201.

- [122] Soppimatha, K. S.; Aminabhavia, T. M.; Kulkarnia, A. R.; Rudzinski, W. E. *Journal of Controlled Release* **2001**, *70*, 1.
- [123] Moghimi, S. M.; Hunter, A. C.; Murray, J. C. *Pharmacol. Rev.* **2001**, *53*, 283.
- [124] Vinogradov, S. V.; Bronich, T. K.; Kabanov, A. V.; *Adv. Drug Del. Rev.* **2002**, *54*, 223.
- [125] Kukowska-Latallo, J. F.; Candido, K. A.; Cao, Z.; Nigavekar, S. S.; Majoros, I. J.; Thomas, T. P.; Balogh, L. P.; Khan, M. K.; Jr. Baker, J. R.; *Cancer Res* **2005**, *65*(12), 5317.
- [126] West, J. L.; Halas, N. J. *Cur. Opin. Biotech.* **2002**, *11*, 215- 217.
- [127] Daniel, M. C.; Astruc, D. *Chem. Rev.* **2004**, *104*, 293.
- [128] Thrkevich, J. *Gold Bull.* **1985**, *18*, 86.
- [129] Yguerabide, J.; Yguerabide, E. E. *Analy. Biochem.* **1998**, *262*, 157.
- [130] Gurney, R. W. & Mott, N. F. *Proc. R. Soc. Lond. A*, **1938**, *164*, 151.
- [131] West, W. *Proc. Vogel Cent. Symp. Photogr. Sci. Eng.* **1974**, *18*, 35.
- [132] Moser, J. *Monatsh. Chem.* **1887**, *8*, 373.
- [133] Spitler, M. T. *J. Chem. Educ.* 1983, *60*, 330.
- [134] Namba, S. & Hishiki, Y. *J. Phys. Chem.* **1965**, *69*, 774.
- [135] Nelson, R. C. Minority carrier trapping and dye sensitization. *J. Phys. Chem.* **1965**, *69*, 714.
- [136] Boudon, J. *J. Phys. Chem.* **1965**, *69*, 705.
- [137] Gerischer, H. & Tributsch, H. *Ber. Bunsenges. Phys. Chem.* **1968**, *72*, 437.
- [138] Hauffe, K., Danzmann, H. J., Pusch, H., Range, J. & Volz, H. *J. Electrochem. Soc.* **1970**, *117*, 993.
- [139] Tian, Y. and Tatsuma, T.; *J. Am. Chem. Soc.*, **2005**, *127*, 7632.
- [140] Gratzel, M.; *Nature*, **2001**, *414*, 338.
- [141] Fujishima, A. & Honda, K. *Nature*, **1972**, *238*, 37.
- [142] Bard, A. J.; Fox, M. A. *Acc. Chem. Res.*, **1995**, *28*, 141.

- [143] Amouyal, E., *Sol. Energy Mater. Sol. Cells*, **1995**, 38, 249.
- [144] Parmon, V. N., *Adv. Hydrogen Energy (Hydrogen Energy Prog.)*, **1990**, 8, 801.
- [145] Tanaka, A.; Kondo, J. N.; Domen, K., *Crit. Rev. Surface Chem.*, **1995**, 5, 305.
- [146] Turner, J. A., *Science*, **2004**, 305, 972.
- [147] Prashant V. Kamat, *J. Phys. Chem. C*, **2007**, 111, 2834.
- [148] Abdulla-Al-Mamun, Md.; Kusumoto, Y.; Muruganandham, M.; *Materials Letters*, **2009**, 63(23), 2007.
- [149] Abdulla-Al-Mamun, Md.; Kusumoto, Y.; Mihata, A.; Islam, M. S.; Ahmmad, B.; *Photochem. and Photobiol. Sci.* **2009**, 8, 1125.
- [150] Abdulla-Al-Mamun, Md.; and Kusumoto, Y.; *Chem Lett.* **2009**, 38(8), 826
- [151] Abdulla-Al-Mamun, Md.; Kusumoto, Y.; Islam, M. S.; Yang, H.; *Chem Lett.* **2009**, 38(10), 950.
- [152] Abdulla-Al-Mamun, Md.; Kusumoto, Y.; Islam, M. S.; *Chem Lett.* **2009**, 38(10), 980.

CHAPTER 2

DETAILS OF THE DIFFERENT EXPERIMENTS CARRIED OUT

2.1 Cell culture

Malignant epithelial cell line, HeLa (human cervix epithelial-like cell line) are brought from Cell Bank, RIKEN BioResource Center, 3-1-1 Koyadai, Tsukuba, Ibaraki, 305-0074, Japan. The frozen cells were shipped in dry ice by Yamato Transport Co., LTD, Japan. When the frozen cells arrived in our lab, the cells are stored in a liquid nitrogen bottle. Every week frequently the nitrogen bottle was filled up by nitrogen (about 5 Lt.) take from the engineering faculty nitrogen center.

The chemicals involved in the cell culture are listed below in Table

Minimum Essential Medium (MEM) Eagle: Liquid, Sterile filtered, Endotoxin tested, With Earle`s salts, L-glutamine and NaHCO ₃ , SIGMA-ALDRICH COMPANY LTD. Cat. No: M4655
NBS: Newborn Calf Serum, GIBCO, Invitrogen Corporation, Cat. No: 16010-167
PBS: Phosphate Buffered Saline, pH 7.2, [-] Calcium Chloride, [-] Magnesium Chloride, 1x solution, REF 20012-027 500 mL & 20012-050 10x500 mL, GIBCO, Invitrogen, Cat. No: 20012.
Trypsin-EDTA: 0.25% Trysin-EDTA, 1x solution, GIBCO, Invitrogen, Cat. No: 25200.
Trypan Blue: 0.5%- Trypan Blue Stain Solution, NACALAI TESQUE, INC. Cat. No: 35552-84.

<p>15 ml Centrifuge Tubes:</p> <p>External dimensions 120 x 17 mm, Nunc, Nagle Nunc International, Cat. No: 366060</p>
<p>60 mm Cell Culture Petri Dish:</p> <p>Culture area, 21.5 cm², Max. External dimensions, 60 x 15 mm, Max. External diameter bottom, 53.5 mm, Nunc, Nagle Nunc International, Cat. No: 150288.</p>
<p>Millipore water filter:</p> <p>18.2 MΩ·cm at 25 °C ultrapure water, Reverse osmosis or deionized water, Electrical Ratings: 100 V 50/60 Hz 30 A, MILLIPORE, Cat. No: SIMS70000, Consumables Cat. No: SIMPAKKRJ.</p>
<p>Pipette:</p> <p>1 ml pipette, IWAKI, (IK-PAS-99) soda-lime-glass</p> <p>10 ml pipette, IWAKI, Asahi Glass Co., LTD</p> <p>20 ml pipette , IWAKI, Asahi Glass Co., LTD</p> <p>50 ml pipette, IWAKI, Asahi Glass Co., LTD</p>
<p>Cover slips:</p> <p>Hemocytometer Cover Glass, Size 22x 24 mm, thick 0.4 mm, SLGC, A209</p>
<p>Cell Counter microscale slide:</p> <p>Depth 0.100 mm, 1/400 & 1/25 sqmm, No. B2018, Burker-Turk, SLGC, Japan</p>

Before cell culture, the culture hood (clean bench) bench is clean-up wiping by alcoholic cotton. During the unused time, the culture hood UV lights is continue turn on due to the hood sterilization. In cell culture time, normal light and airflow is continuing. After that, NBS (stored frozen in deep freeze at -20 °C, top layer of the common refrigerator, one day before put in common refrigerator for liquid condition) is taken out and make the separately 20 ml containing NBS of 5 bottles. Also red MEM medium (stored cold at 4 °C, bottom

layer of the common refrigerator) is taken out and make 10% NBS containing 100 ml x 2 bottle MEM medium (later referred as medium) which is always used as the cell culture medium. Remaining 4 bottles NBS is returned to the deep freeze for kept as reserved.

The frozen cell (Hela) are taken out from the nitrogen bottle freezing condition, and warmed up in the hand rubbing until the cells as liquid dissolved condition. The outside of the cell tubes is sterilized by spraying with 85% ETOH and the tubes are immediately placed in the biosafety hood and follow the RIKEN cell bank instruction cell culture. Details, starting cell culture as follows. In biosafety hood, the cell is put on and wiping with 85% ETOH containing cotton (later referred as cotton). Then the tube upper part is wrapping with cotton and breaks the expected marking position. The cells are transferred to the 5 mL containing medium of 15 mL centrifuge tubes by 1 mL sterile pipette and cell mixing with the medium perfectly. The cells are then centrifuge at room temperature, 1000 rpm for 3 mins. The cells are centrifuged down at the tube bottom and the supernatant contained the medium. The supernatant liquid is then disposed by the pipette in the hood and the cells are dissolved with the medium 1.5 ml medium.

The cell suspension is transferred to the 60x15 mm Petri culture dishes (1 or two depending on the cell amount, if the cells amount greater than 50%, used two dish), then the medium solution is added to the dishes to make sure to cover at least the dish bottom. The cells are homogenously dispersed in the whole dish by gently swirling the dishes. The cell amount can be checked under a microscope with 10x or 20 x objectives. The cell dishes are then put in the incubator (5% CO₂, 37 °C) to grow. The live cells fell down and are attached to the dish bottom within 30 mins and grow within 8 hrs. Any dead cells just floated in the medium solution. If too many dead cells are observed after 8 hrs, the dead cells would have to be removed and rinsed out with PBS buffer in the hood and new medium is added. In this way, the live cells can grow healthier and faster.

After 24 hrs, the cells can be cleaved and used for experiments or can be split into required more dishes so the cells keep growing. If no cells are needed, the cells can still keep growing until it reached 80% confluency (80% percentage of the dish bottom is covered by the cells). After 80% confluency, the cells had to be cleaved and separate into more dishes or the cells kept growing and the dish bottom would be fully covered by the cells. When the cells fully covered the plates, the cells might grow layer by layer, or started to change or started to die. It is not recommended to use the cells if the cells grow full of the dish.

The cells are cleaved off the dishes by using Trypsin-EDTA. When the cell dishes are taken out of incubator, the medium is sucked out by the pipette, and few mL PBS buffer is added to rinse out the medium. Trypsin (about 1 ml) is then added to cover the dish bottom and the cell dishes are put in the incubator for about 3 mins. The cell dislodgement is checked under microscope to make sure all the cells come off the dishes (round cells floating and moving in the solution). Few mL medium is then added to the dishes and the cell suspension is collected into 15 mL centrifuge tubes. The cells are then centrifuged at 1200 rpm at 5 mins and cell come down in bottom of centrifuge tube. The cell pellet can be dissolved in medium for experiment requirement or dissolved into medium to start another round cell culture (spit into several tissue culture dishes and let them grow again in the incubator). The cells are allowed to grow, split and grow again so that a lot of cells are prepared for. In our lab we can passage the cell subculture highest 14 times.

In our experiments such as photothermal and photocatalytic experiments, we grow the cells in 60 mm Petri dishes. HeLa cells were cultured in a minimum essential medium (MEM) solution with 10% newborn calf serum (NBS) in a humidified incubator with an atmosphere of 5% CO₂ in air at 37 °C. The HeLa cells were plated at a concentration of about 3×10^5 in 60mm Petri dishes and allowed to grow for 3 days. The HeLa cell viability was examined by treating with nanoparticles or metal-semiconductor nanophotocatalyst

under 24 h incubation in an incubator. To investigate the light irradiation effect, the dish was exposed to light without nanoparticle solution (light control dish) and the other dishes were irradiated with different amount of nanomaterials solution. After light irradiation the colloidal solution was removed and washed with the phosphate buffer saline (PBS, Invitrogen Corporation, Gibco). Then the cells were cleaved by Trypsin-EDTA (Gibco) solution and were stained with trypan blue (Nacalai Tesque, Inc., Kyoto, Japan). Finally, the living cells were counted and calculated as the percentage of the number of the cells against the control dish cells under a 10x in-bright-field microscope. A Xenon lamp with heat cut-off and band-pass filters was used for the light irradiation on HeLa cells. The light power was measured by a spectro-radiometer (Model: LS-100, EKO Instrument Co. Ltd.). A table rotator was used for the Petri dish to confirm the homogeneous light irradiation on the cells. The images were taken using an Olympus inverted CKX41 microscope with a numerical light field condenser, which delivers a very narrow beam of white light from tungsten lamp (6V, 30W halogen illumination) on top of the sample. A 40x objective was used to collect the sample images.

2.2 Synthesizes of noble metal Au, Pt, Ag, and Cu nanoparticles by laser ablation method

Colloidal Au, Pt, Ag and Cu nanoparticles were synthesized by the laser ablation into the metal plate in water solvents. The high purity Gold (99.99%), Platinum (99.99%), Silver (99.99%), and Copper (99.99%) metal plate were purchased from Nilaco Corporation. The Quanta Ray Nd:YAG laser (Spectra-Physics Co., GCR-130-10) operated at pulse width 7 ns and repetition rate 10 Hz. was used for laser ablation on metal plate in Professor Yuji Horie lab, Department of Electrical and Electronics Engineering, Kagoshima University. The metal plate size (Length x Width x Thickness) are Au (10x10x1), Pt (10x10x0.1), Ag (16x16x1) and Cu (16x16x1) mm respectively. The deionized Millipore (18 m Ω .cm) water

was used as a solvent to prepare the all metal colloidal nanoparticles. The experimental setup for laser ablation in water environment is perfectly simple as shown in Fig. 2-1. A solid target (metal plate) is placed under the water in bottle and is exposed to laser through in water as metal target. A rotator was used for rotation with sample bottle.

The fundamental 1064 nm and frequency-doubled 532 nm (Second harmonic generation) wavelengths were selected as light source to irradiate on noble metals. The 532 nm line laser beams was bend at 90° with mirror and focused with a 5-cm lens into a scintillation vial containing the metal solvent. The laser energy output for gold and platinum metal $.88 \pm .05 \text{ J pulse}^{-1}\text{cm}^{-2}$ Copper and Silver metal $1.05 \pm .05 \text{ J pulse}^{-1}\text{cm}^{-2}$. The laser ablation time was carried out for 15 min in 50 ml millipore distilled water.

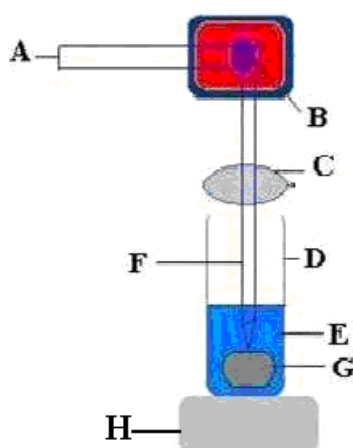


Fig. 2-1: Schematic figure of experimental arrangement for the laser ablation on metal plate in water solvent. **A:** 532 nm laser beam, **B:** Reflection glass, **C:** Lens (5 cm focal length), **D:** Sample vial, **E:** Water, **F:** Focal length, **G:** Metal Target, **H:** Rotator.

2.3 Synthesized of noble metal Au, Ag and Cu colloidal nanoparticles by chemical reduction method

2.3.1 Preparation of gold colloidal nanoparticles by citrate reduction method

The colloidal gold nanoparticles were prepared by citrate reduction from chloroauric acid ($\text{HAuCl}_4 \cdot 4\text{H}_2\text{O}$) following modified method introduce G. Frens [1]. Details 1 gm

chloroauric acid ($\text{HAuCl}_4 \cdot 4\text{H}_2\text{O}$) was dissolved in 100 ml distilled water. Then 0.5 mL (10^{-2} weight %) (500 μl) chloroauric acid solution was added with 50 mL volume distilled water (10^{-2} by weight solution) brought to boiling with magnetic stirrer, and then added freshly prepared 0.5 mL (500 μl) of 1% sodium citrate solution. The reduction of the gold ions by the citrate ions is complete after 5 min while the solution is further boiled for 30 min and then left to cool at room temperature. This method yields spherical particles with an average diameter of about 22 nm.

2.3.2 Preparation of silver colloidal nanoparticles by citrate reduction method

Silver nanoparticles were prepared by reducing AgNO_3 aqueous solution with freshly prepared sodium citrate aqueous solution as following modified method [2]. 1 mM (0.01 weight %) AgNO_3 (18 mg) was dissolved in 100 ml millipore redistilled (Millipore water, 18 m Ω . cm) water and brought to boiling with magnetic stirrer. As the solution is boiling, add 2 ml of a freshly prepared 1% (w/v) sodium citrate aqueous solution to reduce AgNO_3 and generated Ag nanoparticles, leading to a color change of the solution from colorless to greenish-yellow. The solution was kept on boiling for ca. 1 h, and then cooled to room temperature.

2.3.3 Preparation of copper colloidal nanoparticles in water-acetonitrile mixed solvent

Copper nanoparticles were synthesized using copper (II) nitrate and sodium borohydride in a molar ratio of 6:1. Details, 250 mg of $\text{Cu}(\text{NO}_3)_2 \cdot 3\text{H}_2\text{O}$ was dissolved in 70 ml of CH_3CN and 30 ml of purified water. Under vigorous stirring, freshly prepared sodium borohydride solution was injected drop by drop into the argon-bubbled reaction medium via a syringe pump. The injection of the borohydride solution was continued (2 to 8 ml) until color change was observed in wine-reddish color. After the reduction was completed, the

solution was centrifuged and the particles were separated by washing with methanol and dried in a vacuum.

2.4 Preparation of noble metal-semiconductors nanomaterials

2.4.1 Preparation of Au capped TiO₂ (Au@TiO₂) nanopellet

The gold capped nanopellet was synthesized by borohydrate reduction from chloroauric acid (HAuCl₄·4H₂O) using the following method [3] modified by us. The surface of commercially available TiO₂ (P25) (Degussa Corp., diameter ca. 20 nm, surface area 49.9 m²/g) was modified by using hydrochloric acid. The powder of TiO₂ (20mg) was mixed with conc. hydrochloric acid (20 μl) with some water and smashed very hastily. After well smashing the paste was collected and 50 ml colloidal suspension (5 mM (1 M = 1 mol/dm³)) was prepared by vigorous stirring, which was the mother solution to prepare the Au capped TiO₂ of various molar ratio. Prior to addition of the water suspension the pH value was adjusted to ca.1.5 with 0.01 M hydrochloric acid under vigorous stirring. Then the chloroauric acid (0.2 mM) was mixed with TiO₂ suspension under vigorous stirring. The negatively charged [AuCl₄]⁻ ions were adsorbed strongly on the positively charged surface of the TiO₂ nanoparticles and the suspension was allowed to stand for 15 min to ensure the complete adsorption of the [AuCl₄]⁻ ions onto the TiO₂ surface. Reduction of the [AuCl₄]⁻ ions was achieved by the dropwise addition of sodium borohydride (10 mM) until a color became wine red. Next the solution was transferred into a conical flask with a rubber septum and was irradiated with ultraviolet light (15 mW cm⁻²) for at least 5~10 min to reduce the remaining Au^{+3/+2/+1} ions in solution to Au which also capped TiO₂ and N₂ gas was purged into the solution to remove dissolved oxygen for at least 30 min. Then the solution was centrifuged at 1600 x g for 10 min. After the supernatant was removed, the pellet was collected.

2.4.2 Preparation of Ag metal core-TiO₂ shell (Ag@TiO₂) composite nanocluster

Ag@TiO₂ core-shell nanoclusters were prepared by adding 1 mM of AgNO₃ in to the millipore distilled water with vigorous stirring at 60 °C constant temperatures. The Titanium (IV) (triethanolaminate)-isopropoxide (N ((CH₂)₂O) ₃TiOCH (CH₃)₂) TTEAIP of different molar concentration and 2 ml of 1% sodium citrate was added to AgNO₃ solution. The solution was stirred for an additional 15 min to allow complete core-shell formation. The mixer temperature was increase at boiling temperature with vigorous stirring. With continued heating of the solution, the color slowly changed from colorless to light brown. After 90 min, the color of the suspension turned from light to dark brown. After that, the sample suspension was cooled at room temperature. All solutions used were freshly prepared and kept stirring in a closed flask until the next step. After that the solution was transferred in conical flask with rubber spectrum and were N₂-purged in to the solution while irradiated with ultraviolet light (15 mW cm⁻²) for at least 30 min to reduce if have any unreacted Ag⁺ in solution to Ag⁰. Then the solution was centrifuged at 5000 x g for 20 min. The precipitate nanocluster was washed with two times with millipore water and one time with ethanol to remove the citraty of solution and minimize the water content. After the supernatant removed and the cluster was collected.

2.4.3 Preparation of Cu-TiO₂ nanocomposite

The surface of commercially available TiO₂ (P25) (Degussa Corp., diameter ca. 20 nm, surface area 49.9 m²/g) was modified by using hydrochloric acid. The modified TiO₂ colloidal suspension (0.01 M (1 M = 1mol/dm³)) was prepared by dropwise addition of 0.001 M hydrochloric acid until the pH rose to ~3 in 70 vol% acetonitrile-water mixture under vigorous stirring. Then copper (II) nitrate (Cu (NO₃)₂·3H₂O) salt (0.002-0.05 M) was mixed in solution under Ar atmosphere in a rubber septum-capped Pyrex conical flask of ca. 154 cm³, maintaining the reaction mixture in suspension by magnetic stirring. Under

vigorous stirring, freshly prepared sodium borohydride (0.15 M) was injected drop by drop in the reaction medium via a syringe. The injection of the borohydride solution was continued (2 to 8 ml) until the color of the reaction medium turned wine-reddish. After completion of reduction, the suspension was centrifuged and the particles were separated, followed by washing with methanol and drying in a vacuum.

2.5 Preparation of solar cell

2.5.1 Preparation of thin film

The two type's film was prepared by the laser ablation and the squeegee methods.

2.5.1. (a) Laser ablation method

The laser ablation TiO₂ film was prepared as follows: an ITO-coated glass plate (indium-tin oxide coated glass, 8-12 ohm resistance, Aldrich) was deposited with TiO₂ for prepared a high compact thin film by the laser ablation method [4-6]. TiO₂ targets were prepared by mixing 5.5 g of TiO₂ with 0.55 g of paraffin (10%) to prevent cracking. The mixed powder was pressed at 20 MPa for 1 h and calcined at 400 °C for 6 h to form a TiO₂ pellet. The pellet was introduced into a vacuum chamber where the laser pulse enters through a window and impinges on the target materials to be deposited as shown in Fig. 2-2. A laser power of 2.8 J / (pulse cm²) was used throughout the experiment. The wavelength of the laser was 532 nm (Nd-YAG Laser). The distance between the substrate and the target was 3 cm. The substrate was set in room temperature and the laser irradiation time was 5 min. Irradiation of the target with a laser beam melted the target to form a plume. The plume was accumulated on the ITO glass substrate to form the TiO₂ thin film. After ablation TiO₂ coated film was furnace at 500 °C through 1 hour. The Fe₃O₃ and ZnO (Wako, 99.5%) film was also prepared on ITO glass deposited as like same process of TiO₂ film.

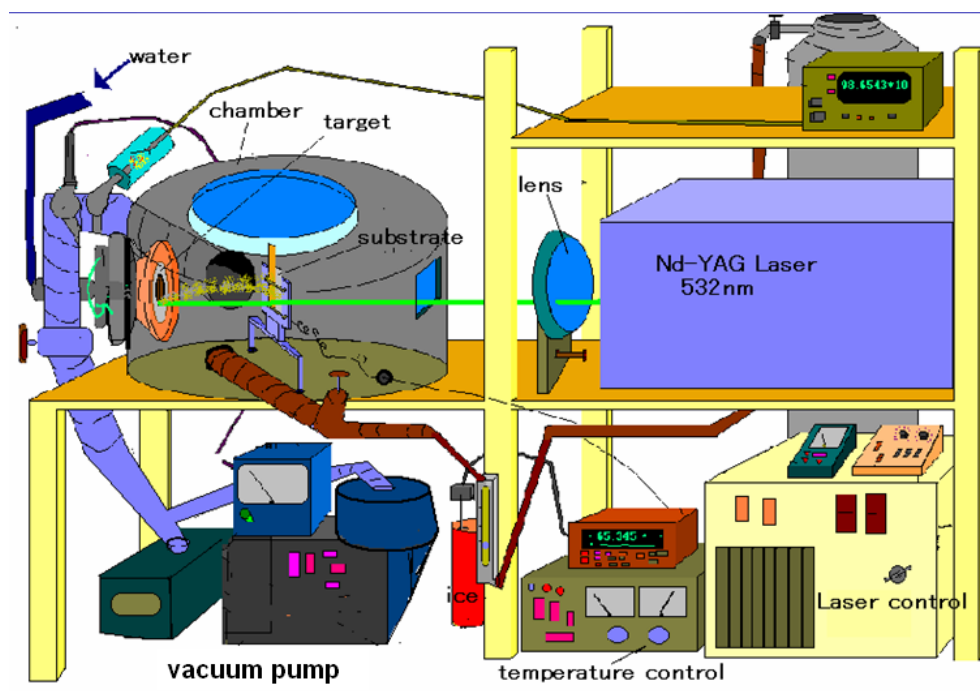


Fig. 2-2: Schematic figure of laser ablated prepared semiconductor thin film.

2.5.1. (b) Squeegee method

The preparation squeegee method is as follows: The powder of molecule (1gm) was mixed with nitric acid (0.1 ml) and water (2 ml). After well mixing, 0.2 ml of Triton X-100 (surfactant) was mixed to get a paste. The paste was then used to prepare the film by squeeze method. Finally the film was heated at 500 °C for 1 h in air environment. The metal/semiconductor nanocluster suspension was mixing with surfactant and directly squeezes on ITO glass. Then the film was also heated at 400 °C for 1 h in an air environment.

The TiO₂ (P25, Degussa Corp. Anatase grade), Fe₂O₃ (Wako, 99.9%) and ZnO (Sigma-Aldrich, 99.9%) high compact thin film was coated on ITO glass (Aldrich, Indium-tin oxide coated glass, 8-12 ohm resistance) by squeegee method. The powder of molecule (1gm) was mixed with conc. nitric acid (0.1 ml) and distilled water (2 ml). Then the high concentric gold nanoparticle was added by drop wise with well mixing. The gold nanoparticles was

adsorb in the surface of semiconductor due to the surface porosity and diffusion. After well mixing, 0.2 ml of Triton X-100 (Wako) was mixed to get a paste. The paste was then used to prepare the film by squeeze method. Finally the film was heated at 400 °C for 1 h in air environment.

2.5.2 Instruments and measurements of solar cell

The Pt counter electrode was prepared by a magnetron sputter method on an ITO glass (Shinku Devices, MSP-10, Japan). The semiconductor film was used as a working electrode in a solar cell where a Pt film was used as a counter electrode. The two electrodes were sandwiched, and then the electrolyte solution was filled between the two electrodes. As the electrolyte 0.8 M of KI and 0.2 M of I₂ (Wako) in water or 0.8M of TBAI (tetra butylammonium iodide (Wako) and 0.2 M of I₂ in acetonitrile were employed. Current-voltage characteristics were measured using Peccell I-V curve analyzer with PECK2400-N program. The Current-voltage (I-V) characteristics under white light irradiation using a xenon lamp (Inotex 300-W LX-300F) with an IR cut-off filter and an L42 cut-off filter (ca. 1/7 sun) was used as a visible light source ($\lambda > \text{ca. } 400 \text{ nm}$). The conditions were recorded with a Keithley2400 multimeter by varying an external load resistance. The IPCE was measured by PRP1-SAO-001, EKO instruments co. Ltd.

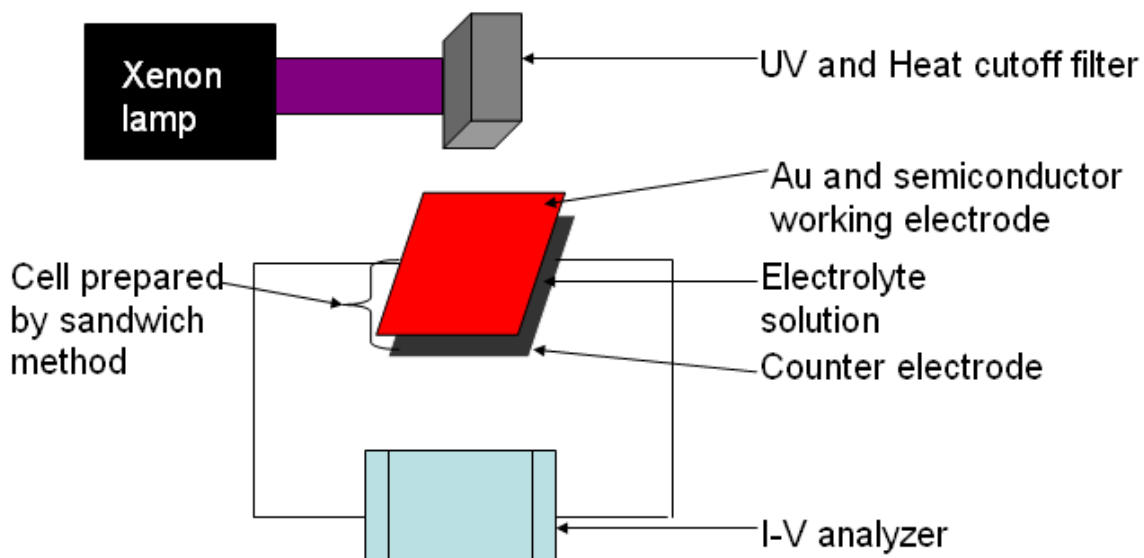


Fig. 2-3: Schematic figures of photoelectrochemical cell measurements

References

- [1] Frens, G.; *Nature Phys. Sci.*, **1973**, 241, 20.
- [2] P. C. Lee, and D. Meisel, *J. Phys. Chem.* **1982**, 86 (17), 3391.
- [3] A. Dawson, P. V. Kamat, *J. Phys. Chem. B* **2001**, 105, 960.
- [4] Bard, A. J.; Fox, M. A. *Acc. Chem. Res.* **1995**, 28, 141.
- [5] Amouyal, E., *Sol. Energy Mater. Sol. Cells*, **1995**, 38, 249.
- [6] Parmon, V. N. *Adv. Hydrogen Energy (Hydrogen Energy Prog.)*, **1990**, 8, 801.

CHAPTER 3

**PLASMON-INDUCED PHOTOTHERMAL CELL-KILLING EFFECT
OF GOLD COLLOIDAL NANOPARTICLES ON EPITHELIAL
CARCINOMA CELLS**

Abstract

Gold colloidal nanoparticles were prepared by the liquid laser ablation of a gold metal plate in water and also by the citrate reduction of $\text{HAuCl}_4 \cdot 4\text{H}_2\text{O}$. The gold colloidal nanoparticles with the plasmonic band strongly absorb light, which is converted to the photothermal energy. This photothermal energy gives a cytotoxic effect on epithelial carcinoma cells. Interestingly, we found that the size and shape of the nanoparticles are changed by light during the photothermal process *in vitro*. The cervical carcinoma cell line (HeLa cell) was incubated with the colloidal gold nanoparticles and then exposed to continuous visible light at 400–600 nm with UV- and heat-cutoff filters. The distinct cell-killing effect was observed by this procedure. In the absence of the gold colloidal nanoparticles, only a small amount of cells were photothermally destroyed. The work has been published in *Photochemical & Photobiological Sciences*, 2009, 8, 1125-1129.

3.1 Introduction

For the past quarter century, cancer nanotechnology has been devoted to the selective destruction of malignant tissue. Noble metal colloidal nanoparticles are known to be potential materials that selectively destroy malignant cells. Nanoparticles smaller than 20 nm can move out of a blood vessel as they circulate through the body [1]. Smaller particles

which are more soluble in hydrophobic or nonpolar oil diffuse more rapidly across the lipid bilayer by passive diffusion [2,3]. The pore size of the blood vessel endothelium wall of a normal cell is *ca.* 10 nm while that of a cancer cell is 10–100 nm [4,5]. The anatomical difference in the structure of blood vessel endothelia near the cancer and the normal cells makes size-tunable nanoparticles feasible to reach selectively on the surface of cancer cells as shown in Fig. 3-1 [6,7]. Moreover, due to the strongly enhanced surface-plasmon resonance at different optical frequencies, noble metal nanoparticles are able to absorb and scatter visible light [8,9].

Gold colloidal nanoparticles have attracted great interest because of their unique optical properties that are not observed in either molecules or bulk materials. A noteworthy characteristic is the size-effective collective oscillation of electrons in the conduction band which enhances the properties of surface plasmon absorption in the visible region [10]. El-Sayed *et al.* have found that the light absorbed by gold nanoparticles is converted into heat on the picosecond time scale [11,12] The ability of gold nanoparticles to efficiently convert the absorbed light to the localized heat can be readily employed for the therapy based on photothermal destruction of various cancerous cells. For example, Huang *et al.* [13]. synthesized and conjugated gold nanorods to anti-epidermal growth factor receptor (anti-EGFR) monoclonal antibodies and incubated in cell cultures with a nonmalignant epithelial cell line (HaCat) and two malignant oral epithelial cell lines (HOC 313 clone 8 and HSC 3). The anti-EGFR antibody-conjugated nanorods bind specifically to the surface of the malignant-type cells and it was found that after exposure to continuous red laser at 800 nm both the malignant cells suffered photothermal injuries at about half of the laser energy that was required for causing death to the nonmalignant cells. Therefore, they concluded that nanorods conjugated to antibody can be used as a selective and efficient photothermal agent for the cancer cell therapy using a harmless and low-energy near infrared laser.

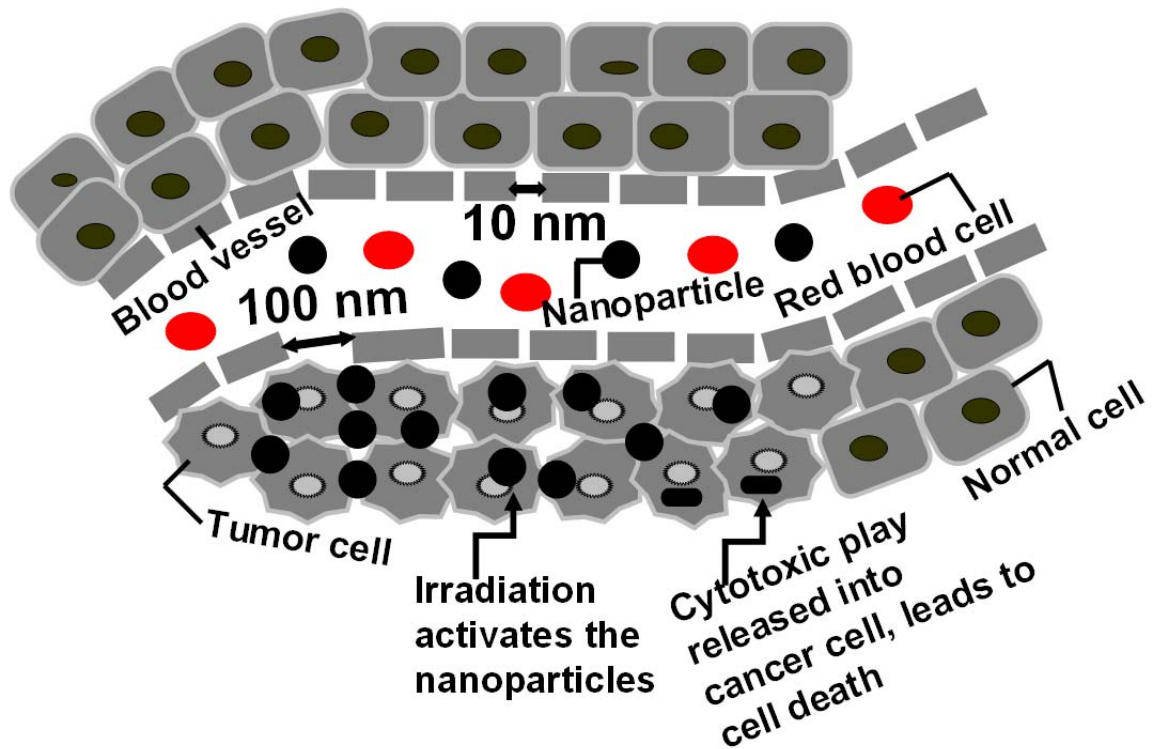


Fig. 3-1: A schematic representation of nanoparticles entering the cancer cell and releasing their cytotoxic action when irradiated.

Lapotko *et al.* [14] reported that light-absorbing clusters of nanoparticles create vapor microbubbles which can damage targeted human leukemia cells. They showed that only targeted cancer cells took up the nanoparticles but normal cells did not. The purpose of the light treatment was to activate nanoparticle clusters and generate bubbles in the target cell using minimal laser light fluence so that the normal cell was not damaged. They also found that the laser fluence threshold of the bubble generation is the lowest for the largest nanoparticle cluster and decrease with an increase of cluster size.

The HeLa cell (also HeLa or hela cell) derived from cervical cancer is a human epithelial cell line used in medical research. So far, no work on photothermal cancer therapy of HeLa cell by gold nanoparticles has been reported except by Takahashi *et al.* [15] who have applied gold nanorods to HeLa cell killing. However, one of the problems they faced was that during the synthesis of gold nanorods a surfactant such as cetyltrimethylammonium bromide (CTAB) was necessary for stabilization of nano colloids. It is known that CTAB

has a toxic effect to the normal cell. In this paper we report the synthesis of surfactant-free gold nanoparticles by the laser ablation of a gold metal plate and the citrate reduction of HAuCl_4 in water, and also their cancer cell killing effect under different light intensities *in vitro*.

3.2 Experimental

The gold colloidal nanoparticles were prepared by the laser ablation of a solid target in water environment and also by the citrate reduction from chloroauric acid ($\text{HAuCl}_4 \cdot 4\text{H}_2\text{O}$). The colloidal nanoparticles were generated by using a Nd: YAG pulsed laser (Spectra-Physics Co., GCR-130-10) operated at 10 Hz with a pulse width of 7 ns and frequency-doubled (second harmonic generation) wavelength 532 nm was selected as a light source to irradiate the gold metal. The laser power-fluence was kept at $0.75 \text{ J pulse}^{-1} \text{ cm}^{-2}$ and the laser ablation time was carried out for 15 min in 50 ml millipore deionized water. Other colloidal gold nanoparticles were prepared by the citrate reduction from chloroauric acid (Wako Pure Chemical Industries, Ltd., Japan) by the method introduced by Frens [16]. Briefly, 1 g chloroauric acid ($\text{HAuCl}_4 \cdot 4\text{H}_2\text{O}$) was dissolved in 100 ml distilled water. Then 0.5 ml chloroauric acid solutions was added in 50 ml of distilled water and after refluxing the solution to the boiling point 0.5 mL of 1% sodium citrate solution were added. The reduction of the gold ions by the citrate ions was completed after 5 min while the solution was further boiled for 30 min and then left to cool at a room temperature. Then the solution was allowed to cool to freezing temperature and condensed by high speed centrifugation. The process was repeated and washed two times with millipore water to minimize the content of citrate. Then the condensed nanoparticles were resuspended in minimum essential medium (MEM).

Absorption spectra were recorded on a UV-visible spectrophotometer (Shimadzu Corporation, MPS-2000, Japan) using a 1 cm path-length quartz cuvette. The size and shape of the nanoparticles were analyzed by transmission electron microscopy (TEM) using a JEOL JEM-3010 VII TEM operating at 300 kV. The nanoparticle surface was characterized by X-ray photoelectron spectroscopy (XPS).

HeLa cells were cultured in a minimum essential medium (MEM) solution with 10% newborn calf serum (NBS) in a humidified incubator with an atmosphere of 5% CO₂ in air at 37 °C. The HeLa cells were plated at a concentration of about 3×10^5 in 60mm Petri dishes and allowed to grow for 3 days. The HeLa cell viability was examined by treating with nanoparticles under 24 h incubation in an incubator. To investigate the light irradiation effect, the dish was exposed to light without nanoparticle solution (light control dish) and the other dishes were irradiated with different amount of Au nanoparticles solution. After light irradiation the colloidal solution was removed and washed with the phosphate buffer saline (PBS, Invitrogen Corporation, Gibco). Then the cells were cleaved by trypsin-EDTA (Gibco) solution and were stained with trypan blue (Nacalai Tesque, Inc., Kyoto, Japan). Finally, the living cells were counted and calculated as the percentage of the number of the cells against the control dish cells under a 10x in-bright-field microscope. A Xenon lamp with heat cut-off and band-pass filters (400–600 nm) was used for the light irradiation on HeLa cells. The light power was measured by a spectro-radiometer (Model: LS-100, EKO Instrument Co. Ltd.). A table rotator was used for the Petri dish to confirm the homogeneous light irradiation on the cells. The images were taken using an Olympus inverted CKX41 microscope with a numerical light field condenser (N.A.0.3), which delivers a very narrow beam of white light from tungsten lamp (6V, 30W halogen illumination) on top of the sample. A 40x objective was used to collect the sample images.

3.3 Results and discussion

Gold nanoparticles show a strong absorption band around 526 nm in the visible region when the frequency of the electromagnetic field is resonant with the coherent electron motion, which is called surface plasmon resonance absorption and is the origin of the observed brilliant color of the nanoparticles in solution [17].

The peak position of surface plasmon resonance shifts to a shorter wavelength with the increase of a diameter when the diameter is less than 20 nm. On the other hand, above 20 nm, the peak position of surface plasmon resonance shifts to a longer wavelength with the increase of the diameter, because light scattering at particle surfaces becomes dominant [18].

However, when the nanoparticles change from nanospheres to nanorods, the surface plasmon absorption spectrum also changes. The surface plasmon absorption of gold nanorods have two bands: a strong longer wavelength band in the near infrared region due to the longitudinal oscillation of electrons and a weak shorter wavelength band in the visible region around 526 nm due to the transverse electronic oscillation. The absorption spectra of the gold nanorods are also sensitive to the aspect ratio (length/width). When the aspect ratio increases, the absorption maximum of the longitudinal band is red shifted [19].

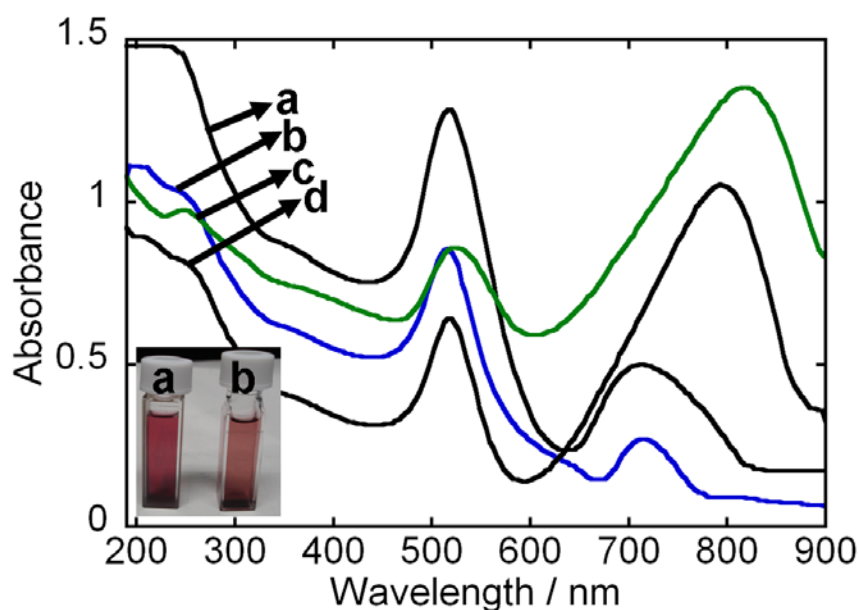


Fig. 3-2: UV-visible absorption spectra of Au colloidal nanoparticles prepared by (a) citrate reduction and (b) laser ablation and those after light irradiation (c and d, respectively).

From the UV-visible spectra of the prepared gold nanoparticles in Fig. 3-2(a) and (b), we can see maximum peak around 526 nm for spherical gold nanoparticles. However, there are also small peaks at around 720 nm, implying that some rod shaped nanoparticles are also present in the both cases. Interestingly, we found that after light irradiation for 5 min the absorbance at 526 nm was decreased and that around 720 nm was increased (Fig. 3-2(c) and (d)). Moreover, it was found that the longitudinal band is red shifted after light irradiation. This implies that by light irradiation gold nanoparticles change their shape from spherical to nanorods. However, the wide longitudinal band indicates that the nanorods after light irradiation are not homogeneous.

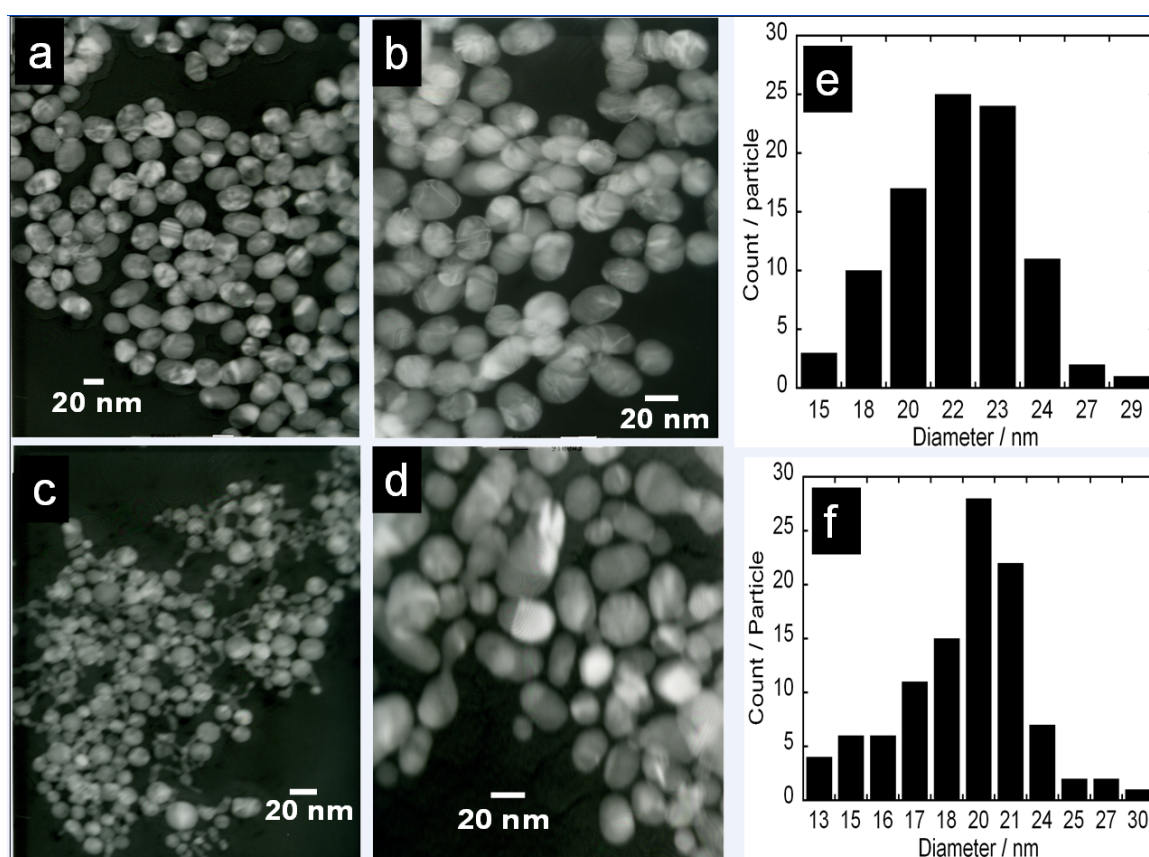


Fig. 3-3: TEM images of gold colloidal nanoparticles obtained by (a) citrate reduction and (c) laser ablation. (b) and (d) show images after 5 min irradiation of (a) and (c), respectively. The histograms (e) and (f) show the particle size distribution of (a) and (c), respectively.

The above facts of the shape and size changes are further confirmed from TEM images of the nanoparticles before and after the light irradiation. The size and shape of the gold nanoparticles prepared by the two methods were found mostly to be spherical and symmetrical, as shown in Fig. 3-3(a) and (c). TEM images show that the average diameters of the gold nanoparticles prepared by the citrate reduction and the laser ablation are around 22 and 20 nm, as shown by histograms in Fig. 3-3(e) and (f), respectively. The shape and size of the gold nanoparticles after 5 min irradiation were also observed by TEM.

The nanoparticles changed their size and shape during light irradiation by increasing their width and length as seen from Fig. 3-3(b) and (d). This evidence shows that the prepared nanoparticles absorb the light and shifts their plasmon band longitudinally to the infra-red (Fig. 3-2(c) and (d)) region due to their size and shape change. We assumed that the thermal energy is released due to the size and shape change of the nanoparticles and this thermal energy results in the cytotoxic effect for the cancer cell destruction. However, further research is needed to proof this fact.

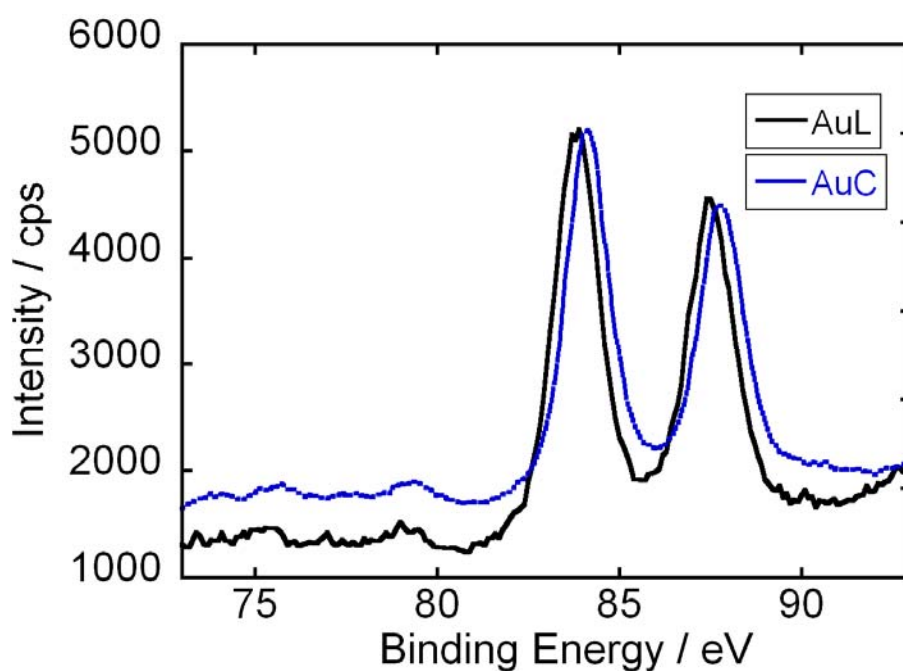


Fig. 3-4: XPS spectra of gold nanoparticles prepared by laser ablation (AuL) and citrate reduction (AuC).

The X-ray photoelectron spectroscopy (XPS) was used to study for the surface composition and electronic states studies of the gold nanoparticles. Fig. 3-4 shows the typical gold XPS spectra of 4f orbital in the as-deposited film. The spectra show the binding energies of Au4f_{7/2} at 83.8 and Au4f_{5/2} at 87.45 eV corresponding to the standard gold, [20] the former of which is also found to be significantly different from Au⁺ 4f_{7/2} (84.6 eV) and Au³⁺ 4f_{7/2} (87.0 eV) but similar to Au⁰ 4f_{7/2} (84.0 eV). The XPS results suggest that the Au species are present in the metallic state and their surface have no charge. This suggests that the nanoparticle surface is hydrophobic and has no reaction with water solvent.

The cells were stained by the trypan blue indicator; the dead cells accumulate the dye resulting in blue color, whereas the live cells have no color. The cell viability was determined as the percentage of the number of the unstained cells against that of the control dish cells. All the data are expressed as the mean of three-time separate culture. In the scale bar of Fig. 3-5, 100 means the number of living cells in control dish in the absence of gold nanoparticles. To test the cell viability, the cell dishes were treated with the different amounts of the Au-colloidal nanoparticles (0.1, 0.5, 1, 2 and 3 ml) and another dish (light controlled dish) was not treated with Au nanoparticles. The concentrations of Au nanoparticles prepared by the citrate reduction in the above volumes were 12, 60, 120, 240 and 360 nM, respectively, and those of Au nanoparticles prepared by laser ablation were 8.4, 42, 84, 168 and 252 nM, respectively.

The cells were found to be mostly viable *ca.* 85–100% under the incubated condition with the nanoparticles without light (Fig. 3-5(a)). Most of the noble inorganic nanoparticles show low toxicity without external energy and promise controlled delivery properties in which the nanoparticles are biodegraded in plasma and cytoplasm of human body [21]. Another experiment was conducted where the cell dishes were treated by the nanoparticles solution and irradiated by the visible light with band pass filter (400–600 nm) for 5 min. Light control experiments without nanoparticles under 5 min light irradiation demonstrated

that about 70–85% equivalent cells were viable as shown in Fig. 5(b) and (c) (light control). The error bars in Fig. 5(b) and (c) represent the maximum and minimum value of each experiment.

Under light irradiation a destructive cell killing effect was found in the presence of nanoparticles with light irradiation; a maximum 98% of cells were killed rapidly. The cell dishes were irradiated with the fluence of 10, 30 and 40 mWcm^{-2} on a turn table rotator. The irradiation covered the whole surface area of the dishes using the turn table rotator. For Au nanoparticles prepared by both the laser ablation and citrate reduction methods the cell killing effect was almost the same. Also changing the light intensity under the same experimental condition gave similar results. Fig. 3-6(a) and (b) show microscopic images of HeLa cells after 24 h incubation only in MEM medium (control dish) and after 5 min irradiation in the same condition (light control dish). From these images it is seen that the cell morphological structure had almost no change after 5 min irradiation.

Fig. 3-6(c) shows the micrographic cell image of nanoparticle-treated HeLa cells after 24 h incubation where some red spots and some aggregated particles are seen. It can be assigned from this image that the nanoparticles are taken up into or in contact with the cells, because these red spots are not observed when the nanoparticles are not present in the medium (Fig. 3-6a and b). Thus, it is obvious that the nanoparticles form aggregates in or on the cells. However, the aggregation of nanoparticles may affect the cancer cells because 10–15% of cancer cells were found to be dead after 24 h incubation with nanoparticles (Fig. 3-5(a)). Fig. 6(d) shows that the HeLa cells suffer photothermal injury at 5 min irradiation with gold nanoparticles. The dim blue-red color shown in the cell images outside the cell surface is due to the cell death. After light irradiation the cells were stained with trypan blue. The blue color (data not shown) showed the cell death.

In photodynamic therapy (PDT), light energy delivered to the tumour site promotes the photosensitiser to an electronically excited state from which a number of reactive oxygen

species, including singlet oxygen, are generated *via* electron or energy transfer processes. As a result, irreversible chemical modifications of a variety of cell constituents are induced. However, such photosensitisers often have the limited selectivity of tumour targeting; moreover, PDT treatment may generate generalized skin photosensitivity which can last for some weeks depending on the PDT agent used [22].

3.4 Conclusion

The prepared Au colloidal nanoparticles are more spherical in shape and give the plasmonic absorption with more intense color. The Au colloidal nanoparticles convert the absorbed light to photothermal energy which causes photothermal cell destruction. During the light irradiation of gold nanoparticles their shape is changed from sphere to nanorod. It was found that the intensity of light gives no significant effect on the photothermal destruction of the cancer cells; therefore low light power and short irradiation time have a distinct potential advantage in a prospective method of cancer therapy.

References

- [1] S. E. McNeil, *J. Leukocyte Biol.*, **2005**, 78, 585.
- [2] B. Alberts, A. Johnson, J. Lewis, M. Raff, K. Roberts and P. Walter, in *Molecular biology of the cell*, ed. S. Gibbs, Garland Science, Taylor & Francis Group, New York, 4th edn, 2002, pp. 616–619.
- [3] I. Brigger, C. Dubernet and P. Couvreur, *Adv. Drug Delivery Rev.*, **2002**, 54, 631.
- [4] Y. Matsumura and H. Maeda, *Cancer Res.*, **1986**, 46, 6387.
- [5] D.R. Siwak, A.M. Tari and G. Lopez-Berestein, *Clin. Cancer Res.*, **2002**, 8, 955.
- [6] N. Kohler, C. Sun, J. Wang and M. Zhan, *Langmuir*, **2005**, 21, 8858.
- [7] B. D. Chithrani, A. A. Ghazani and W. C. W. Chan, *Nano Lett.*, **2006**, 6(4), 662.

- [8] W. P. McConnell, J. P. Novak, L. C. Brousseau, R. R. Fuierer, R. C. Tenent and D. L. J. *Phys. Chem. B*, **2000**, 104, 8925.
- [9] U. Kreibig and M. Vollmer, in *Optical Properties of Metal Clusters*, Springer Series in Materials Science 25, ed. H. K. V. Lotsch, Springer-Verlag, Berlin, 1995, pp. 14–21.
- [10] M. A. El-Sayed, *Acc. Chem. Res.*, **2001**, 34, 257.
- [11] S. Link and M. A. El-Sayed, *Annu. Rev. Phys. Chem.*, **2003**, 54, 331.
- [12] S. Link and M. A. El-Sayed, *Int.Rev. Phys. Chem.*, **2000**, 19, 409.
- [13] X. Huang, I. H. El-Sayed, W. Qian and M. A. El-Sayed, *J. Am. Chem. Soc.*, **2006**, 128, 2115.
- [14] D. O. Lapotko, E. Lukianova and A. A. Oraevsky, *Lasers Surg.Med.*, **2006**, 38, 631.
- [15] H. Takahashi, T. Niidome, A. Nariai, Y. Niidome and S. Yamada, *Chem. Lett.*, **2006**, 35, 500.
- [16] G. Frens, *Nature Phys. Sci.*, **1973**, 241, 20.
- [17] C. F. Bohren and D. R. Huffman, *Absorption and scattering of light by small particles*. John Wiley, New York, 1983.
- [18] M. Kerker, in *The Scattering of light and Other Electromagnetic Radiation*, ed. Ernest M. Loebel, Academic Press, New York, 1969, pp. 27–93.
- [19] S. Link, M. B. Mohamed and M. A. El-Sayed, *J. Phys. Chem. B*, **1999**, 103, 3073.
- [20] C. D. Wagner, W. M. Riggs, L. E. Davis, S. F. Moulder and G. E. Mullenberg, in *Handbook of X-ray photoelectron spectroscopy*, ed. G. E. Mullenberg, Perkin-Elmer Corporation Physical Electronics Division, New York, 1979, p. 154.
- [21] Z. P. Xu, Q. H. Zeng, G. Q. Lu and A. B. Yu, *Chem. Eng. Sci.*, **2006**, 61, 1027.
- [22] I. H. El-Sayed, X. Huang and M. A. El-Sayed, *Cancer Lett.*, **2006**, 239, 129.

CHAPTER 4

SIMPLE NEW SYNTHESIS OF COPPER NANOPARTICLES IN WATER / ACETONITRILE MIXED SOLVENT AND THEIR CHARECTERIZATION

Abstract

Copper nanoparticles were successfully synthesized by the borohydride reduction of copper nitrate salt in water/CH₃CN mixed solvent under inert argon-purged conditions. Cu nanoparticles were synthesized in large-scale production for the first time by introducing CH₃CN into water and preventing oxidation during the preparation of nanoparticles. Nanoparticles were characterized by using UV-visible absorption spectroscopy, transmission electron microscopy (TEM), X-ray photoelectron spectroscopy (XPS) and X-ray diffraction (XRD) techniques. High resolution TEM pictures showed the formation of homogeneous cubic-structured copper nanoparticles with sizes less than 100 nm. This new kind of synthesis method shows the excellent stability compared with that of citrate-protected copper nanoparticles, which may provide an efficient way to improve the fine tuning of the structure and size of copper nanoparticles. The work has been published in *Materials Letters*, 2009, 63, 2007-2009.

4.1. Introduction

Nanometer-sized particles have attracted extensive research interest, mainly due to the quantum effect by which the material properties are tunable in the particle size as well as the surface morphology [1]. Noble metal nanoparticles have attracted much attention due to their special optical, electronic and catalytic properties [2]. Among various metal particles,

copper nanoparticles have attracted considerable attention because of their catalytic, optical and electrical conducting properties [3-6]. Copper nanoparticles are particularly attractive for application in cancer cell killing and germicides.

Among the variety of nanometer-sized metal particles, the coinage metal group, i.e., Cu, Ag and Au, have been studied most extensively. In general, stabilizing reagents are introduced during the preparation for acquiring colloidal dispersions. In comparison with Ag and Au, copper particles are highly unstable under ordinary conditions. Cu colloids turn yellow or are precipitated immediately after exposure to air in solution. Therefore, an inert gas environment is required to stabilize copper solution.

Nanoparticles are small and not thermodynamically stable for crystal growth. Therefore the nanoparticles must be protected during the reaction either by adding surface protecting agents such as organic ligands and inorganic capping materials or by placing in inert environment such as inorganic matrix and polymers.

A number of preparation techniques have been reported for metallic copper colloids with metal salts as starting materials, such as the thermal reduction and sonochemical reduction [3], the surface-protecting chemical reduction [7-8], the radiation method [9] and the laser ablation method [10]. The citrate-protected copper colloidal nanoparticles turned olive-green and were precipitated immediately, indicating oxidation [11-12] in an aerobic condition.

We have studied to grow nano-sized single crystals of copper in a mixed solvent of acetonitrile and water. A thorough literature scan reveals that no single crystals of copper were grown in large scale production so far. In order to grow bulk-scale single crystals, the growth conditions have to be optimized accordingly. Hence, in the present work attempts have been made to investigate the nucleation parameters of copper, which are the prerequisite for investigating the growth mechanism of bulk-scale single crystals. The stable copper colloidal nanoparticles in a mixture solvent of acetonitrile and water with

argon-gas purging were prepared for the first time and thereby the possibility of growing bulk-scale single crystals of copper was also examined.

4.2. Experimental

Copper (II) nitrate ($\text{Cu}(\text{NO}_3)_2 \cdot 3\text{H}_2\text{O}$), acetonitrile, methanol, and sodium borohydride (NaBH_4) were purchased from Wako Pure Chemical Industries Ltd. All chemicals are used as received without further purification. The water used was purified through a Millipore system. The copper colloidal nanoparticles were synthesized using borohydride-reduction method under inert gas conditions.

Copper nanoparticles were synthesized using copper (II) nitrate and sodium borohydride in a molar ratio of 6:1. 250 mg of $\text{Cu}(\text{NO}_3)_2 \cdot 3\text{H}_2\text{O}$ was dissolved in 70 ml of CH_3CN and 30 ml of purified water. Under vigorous stirring, freshly prepared sodium borohydride solution was injected drop by drop into the argon-bubbled reaction medium via a syringe pump. The injection of the borohydride solution was continued (2 to 8 ml) until color change was observed in wine-reddish color. After the reduction was completed, the solution was centrifuged and the particles were separated by washing with methanol and dried in a vacuum.

The UV-vis absorption spectra of the colloids were recorded with a UV-vis spectrophotometer (Shimadzu Corporation, UV-1800). The average diameters and size distributions of the copper particles were obtained from the enlarged photographs of a transmission electron micrograph (JEOL JEM-3010 VII, operated at 300 kV). The crystal structure identification was made by X-ray diffraction (XRD) using a PANalytical Advance X-ray diffractometer with $\text{CuK}\alpha$ radiation. Further evidence for the purity of samples was obtained by X-ray photoelectron spectroscopy (XPS) analysis. The XPS patterns were recorded on an X-ray photoelectron spectrometer (Shimadzu, ESCA-1000) using $\text{MgK}\alpha$ X-ray as the excitation source and C1s (284.6 eV) as the reference line.

4.3. Results and discussion

UV-visible absorption spectra of copper nanoparticles in aqueous acetonitrile solution are shown in Fig. 4-1. The characteristic absorption peak at around 575 nm is due to the surface plasmon band of Cu colloids. Copper nanoparticles synthesized by other methods were reported to display the surface plasmon band also at ~ 575 nm [7, 13]. The strong surface plasmon band may depend on the individual particle property including sizes, shapes, solvents and reducing agents employed. The strong surface-plasmon absorption band observed at 575 nm may be due to the formation of non-oxidized copper nanoparticles. The broadness of the absorption band (Fig. 4-1) probably arises from the wide size distribution of copper nanoparticles.

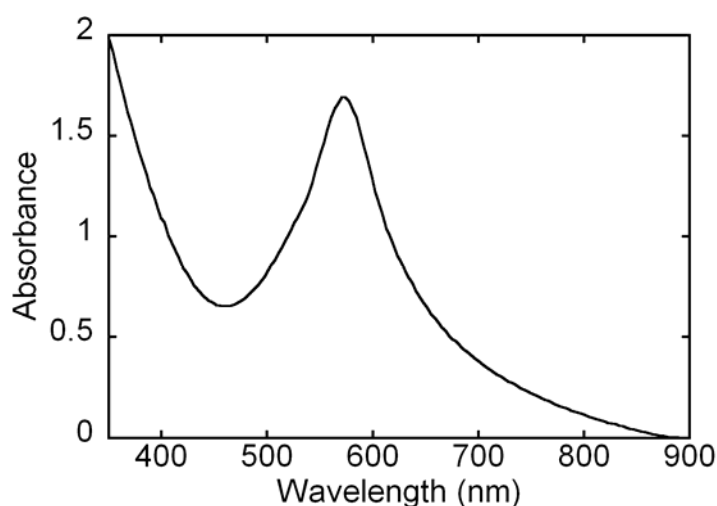


Fig. 4-1: UV-vis absorption spectra of copper colloids prepared in aqueous acetonitrile solution by borohydride reduction under the argon purge.

The TEM images for the copper nanoparticles are shown in Fig. 4-2. Most of the particle average sizes are less than 100 nm and the nanocrystals have the cubic structure. Very small amounts of spherical nanocrystals and triangles were also observed. The electron diffraction patterns of the nanocrystals are shown in the inset of Fig. 4-2. The diffraction patterns show

the concentric rings corresponding to the (111), (200), (220) and (311) reflection. These distances are characteristic of the face-centered cubic (fcc) structure of copper (metal). It should be noted that the rings are constituted of a collection of spots typical of the different nanocrystal orientations. Hence, it can be concluded that (metal) copper nanocrystals are formed.

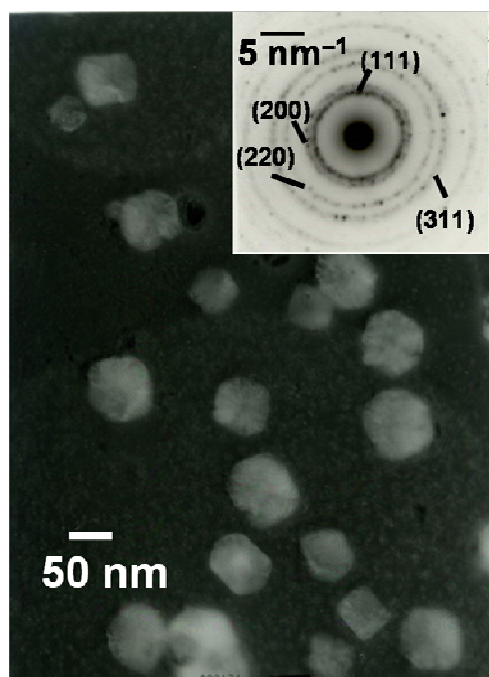


Fig. 4-2: TEM micrographs of cubic copper nanocrystals few minutes after the preparation. A inset shows the electron diffraction pattern of a selected area of copper nanoparticles.

The presence of metallic copper was confirmed by the XPS analysis. The peaks $2p_{3/2}$ and $2p_{1/2}$ observed at 932.4 and 952.2 eV were ascribed to the metallic copper [Fig. 4-3 (left)].

The X-ray diffraction pattern of copper nanoparticles is shown in Fig. 4-3 (right). The peaks at (111) (43.473 eV), (200) (50.375 eV), (220) (73.997 eV) and (311) (89.934 eV) planes belong to the fcc metallic Cu (JCPDS, PDF, File No. 00-001-1241). The other peaks belong to Cu_2O (JCPDS, PDF, File No. 01-071-3645), indicating that Cu_2O also coexists partly together with copper particles. The coexisting Cu_2O is considered to be due to some oxidation in air environment.

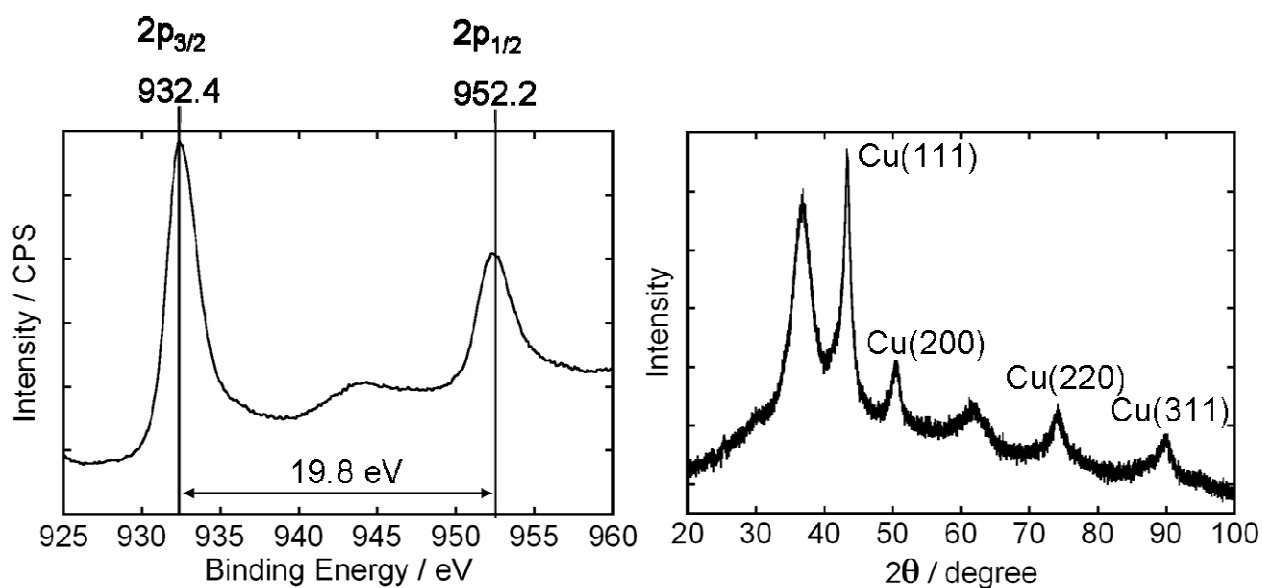


Fig. 4-3: The X-ray photoelectron spectroscopic (XPS) scan survey in the region of Cu 2p [Left]. The XRD pattern of Cu nanoparticles [Right].

We could prepare the copper nanoparticles by the reduction of copper nitrate salt in the acetonitrile-water mixed solvent. We propose the following mechanism. Acetonitrile, aprotic solvent, protected the oxidation by OH^- ions at the Cu-nanoparticle interface and produces the stable copper nanoparticles during the reduction at room temperature under argon gas atmosphere. Acetonitrile immediately captures the reduced copper nanoparticles with prevention of an oxidation and also prevents the oxidation of nanoparticles by oxygen. For comparison, we prepared the copper nanoparticles by borohydride reduction in citrate (protic solvent)-water mixed solvent under purged argon gas. The copper nanoparticles thus obtained showed the immediate precipitation and the color was changed to the greenish blue, indicating the formation of oxidized nanoparticles (Fig.4-4A). This means that the protic solvent (citrate) used can not protect the oxidation by OH^- ions and the aprotic solvent (acetonitrile) is useful as protecting solvent for the Cu nanoparticles.

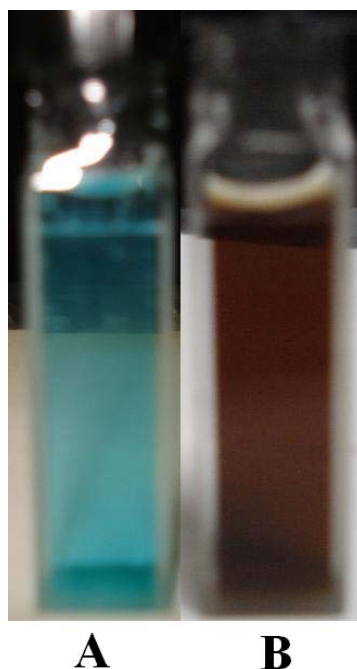


Fig. 4-4: Photographs of solutions of Cu nanoparticles synthesized using (A) citrate-protected and (B) acetonitrile-protected methods. The bluish green color shows the oxidized nanoparticles and the wine-reddish color shows the stable nanoparticles.

4. 4. Conclusions

Acetonitrile was used for the first time as a protective agent for the preparation of copper nanoparticles and was responsible for the formation of well-stabilized nanoparticles. The copper nanoparticles were mostly cubic in shape with diameter less than 100 nm. This synthesis method affords a simple and efficient way to prepare the metallic Cu nanoparticles in large-scale production in acetonitrile-water mixed solvent.

References

- [1] Hayat MA. Colloidal gold: principles, methods and applications Vol. I. New York: Academic Press; 1989.
- [2]. Daniel MC, Astruc D. *Chem Rev* **2004**, *104*,293.

- [3] Arul Dhas N, Paul Raj C, Gedanken A. *Chem Mater* **1998**, *10*, 1446.
- [4] Vitulli G, Bernini M, Bertozzi S, Pitzalis E, Salvadori P, Coluccia S et al. *Chem Mater* **2002**, *14*, 1183.
- [5] Huang HH, Yan FQ, Kek YM, Chew CH, Xu GQ, Ji W et al. *Langmuir* **1997**, *13*, 172.
- [6] Liu Z, Bando Y. *Adv Mater* **2003**, *15*, 303.
- [7] Wu Szu-H, Chen Dong-H. *J Colloid Interface Sci* **2004**, *273*, 165.
- [8] Hirai H, Wakabayashi H, Komiyama M. *Chem Lett* **1983**, *12*, 1047.
- [9] Joshi SS, Patil SF, Iyer V, Mahumuni S. *Nanostruct Mater* **1998**, *10*, 1135.
- [10] Yeh MS, Yang YS, Lee YP, Lee HF, Yeh YH, Yeh CS. *J Phys Chem* **1999**, *103*, 6851.
- [11] Neddersen J, Chumanov G, Cotton TM. *Appl Spectrosc* **1993**, *47*, 1959.
- [12] Samim M, Kaushik N K, Maitra A. *Bull Mater Sci* **2007**, *30*, 535.
- [13] Creighton JA, Eadon DG. *J Chem Soc, Faraday Trans* **1991**, *87*, 3881.

CHAPTER 5

ENHANCED PHOTOCATALYTIC CYTOTOXIC ACTIVITY OF

Au@TiO₂ NANOPELLETS AGAINST HUMAN EPITHELIAL

CARCINOMA (HeLa) CELLS

Abstract

The photocatalytic cancer cell-killing activity of the metallic Au-capped TiO₂ (Au@TiO₂) composite colloidal nanopellet has been investigated on HeLa cells under the UV-visible light irradiation. The Au@TiO₂ composite nanopellet photocatalyst with the uniform Au capped TiO₂ structure was successfully synthesized by a simple reducing HAuCl₄ on the surface of TiO₂ nanoparticles. The morphological structure and surface specifics of Au@TiO₂ were characterized by using UV-visible absorption spectroscopy, TEM, SEM, XPS, EDX and XRD analysis. The photocatalytic cell-killing activity of the Au@TiO₂ nanopellet was found to vary with the molar ratio of Au to TiO₂. The direct involvement of the metal particles in mediating the electron transfer from the photoexcited TiO₂ under the band gap excitation is considered to carry out the efficient photocatalytic reaction on the cells. The charge separation and the interfacial charge-transfer promote the photocatalytic cancer-cell killing more than the TiO₂ semiconductor alone. It was found that the TiO₂ nanoparticles capped with low concentration of gold (TiO₂: Au molar ratio is > 1:1) killed more malignant (HeLa) cells by 50% than the same concentration of TiO₂ semiconductor nanoparticles. The work has been published in Chemistry Letters, 2009, 38(10), 950-951 and communicated paper in Applied Catalysis A: General.

5. 1. Introduction

The rising of cancer in the world demands an increase in efforts towards the development of novel and effective photocatalysts for killing cancer cell. A variety of nanocomposite semiconductor materials have been synthesized in recent years to improve the efficiency of photocatalytic processes. The functional properties of such materials can be greatly improved by capping the semiconductor or metal nanocluster with another layer of compatible material.

When a semiconductor absorbs the photons with energy greater than its band gap, the photons excite electrons of a semiconductor catalyst, moving them from the valance to the conductance band. Removal of an electron from the valance band creates a positively charged vacancy called a hole. These electrons and holes in single component semiconductor nanoparticles exhibit relatively poor photocatalytic efficiency (<5%) and the majority of the photogenerated charge carriers undergo recombination [1-2]. The conduction band electrons must be removed rapidly from TiO₂ to prevent the recombination with the holes and allow the successfully charge separation for enhancing the photocatalytic activity.

Heterogeneous photocatalysis based on TiO₂ has been the focal point of numerous investigations in recent years because of the chemical stability of this material, its nontoxicity, and its potential utility for total destruction of organic compounds in polluted air and wastewater. The band gap (E_g) of TiO₂ anatase is ~ 3.2 eV, which corresponds to only a limited portion (3-4%) of the solar spectrum. This relatively large band gap has significantly limited more widespread application, particularly to indoor situations [3-4]. Various methods have been suggested to enhance the efficiency of photocatalytic processes involving TiO₂ under visible light irradiation, including doping, functionalization of the surface with metal particles, and reduction of particle size to the nanoscale. The deposition of a noble metal on semiconductor nanoparticles is an essential factor for maximizing the efficiency of photocatalytic reactions. The noble metal (e.g., Pt), which acts as a sink for

photoinduced charge carriers, promotes interfacial charge-transfer processes [1, 5]. The TiO₂ lattice with metal ions introduces new energy levels in the band gap which can be tailored to extend the photoresponsiveness into the visible light region. Recent many studies have shown that metal or metal ion doped semiconductor composites exhibit shift in the Fermi level to more negative potentials [6-9]. Such a shift in the Fermi level improves the energetics of the composite system and enhances the efficiency of interfacial charge-transfer process.

The photocatalysis reactions of gold capped TiO₂ have been studied as several phototechnologies, such as water-splitting reaction, microelectronics photochemical solar cell, sensor and memory devices [10-14]. Very few studies have investigated the application of gold capped TiO₂ to biology and medicine, as for example an anticancer modality. In this paper we have reported the effect of photocatalytic gold capped TiO₂ on cancer cells in several concentration and molar ratio of TiO₂ and gold nanoparticles. In experiment we used HeLa cells, a human cancer cell line, we observed a distinct cell killing in vitro with the combination of gold capped TiO₂ and UV-Visible (350-600 nm) light irradiation. We also compare the cell killing effect of only TiO₂ and gold capped TiO₂. We observed the gold capped TiO₂ need half of irradiation time and about >50% cells have been killed than same concentration of TiO₂ treatments.

5. 2. Experimental

5.2.1 Preparation of TiO₂ Colloidal Suspension

The photocatalyst TiO₂ (Degusa, P25) was used with a mainly anatase structure (ca. 80%) under the shape of non-porous polyhedral particles of ca. 20 nm mean size with surface area of 49.9 m²/g. The powder of TiO₂ (20mg) was mixed with concentrated hydrochloric acid (20 μL) with some water and smashed very hastily. After thorough crashing the paste was collected and prepared of 50 mL colloidal suspension with vigorous

stirring. The 50 mL (5mM (1 M = 1 mol dm⁻³)) solution was the mother solution to prepare the various concentration ratio of Au capped TiO₂. Prior to addition of the water suspension the pH value was adjusted to ca. 1.5 with 0.01 M hydrochloric acid under vigorous stirring.

5.2.2 Preparation and Characterization of TiO₂/Au Nanopellet

The gold-capped nanopellets were prepared by borohydrate reduction from hydrogen tetrachloroaurate (III) tetrahydrate (HAuCl₄·4H₂O) as following method [4] modified by us. Four different suspensions of gold-capped TiO₂ nanopellet were prepared by keeping the gold concentration constant at 0.2 mM while varying the TiO₂ concentration from 4 to 0.05 mM. These four TiO₂/Au suspensions contained [TiO₂]: [Au] ratios of 20:1, 10: 1, 1:1, and 0.25:1 respectively. All the concentrations are based on molecular concentrations.

TiO₂/Au nanopellet were prepared by adding the HAuCl₄ (Aldrich) solution to the colloidal TiO₂ suspension in water while stirring vigorously. The negatively charged [AuCl₄]⁻ strongly adsorbs on the positively charged surface of the TiO₂ nanoparticles. The solution was stirred for an additional 15 min to allow complete adsorption of [AuCl₄]⁻ ions onto the TiO₂ surface. Reduction of the [AuCl₄]⁻ was achieved by the dropwise addition of sodium borohydride (8-10 mM) until a color change was observed. The reduced gold solutions made with TiO₂: Au ratios of 20:1, 10:1, and 1:1 were wine red in color, while the solution with a TiO₂: Au ratio of 0.25:1 solution was dark purple in color. All solutions used were freshly prepared and kept stirring in a closed flask until the next step.

After that the solution was transferred in conical flask with rubber septum and were irradiated with ultraviolet light (15 mW cm⁻²) for at least 5~10 min to reduce absorbed any remaining Au^{+3/+2/+1} in solution to Au by TiO₂ photocatalysis and also N₂ purged the solution to remove dissolve oxygen at least 30 min. Then the solution was centrifuged at 1600 x g for 10 min. After the supernatant removed and the pellet was collect and sterilized by auto-clave. Next the pellet was dispersed in 10 ml MEM (Minimum Essential Medium) solution and store at 4°C.

Absorption spectra were recorded on a UV-visible spectrophotometer (Shimadzu Corporation, MPS-2000, Kyoto, Japan) in a 1 cm pathlength quartz cuvette solution. The size and shape of the nanopellet is analyzed by transmission electron microscopy (TEM) using a JEOL, JEM-3010 VII, TEM operating a 300 kV. The nanopellet surface condition was also analyzed by FE-SEM (Hitachi, S-4100H), XPS (Quantum-2000, Scanning ESCA-1000 microprobe with Magnesium α radiation, Shimadzu) and XRD (PANalytical). The quantitative chemical composition of the Au / TiO₂ composite nanocluster surface was also measured using an energy dispersive X-ray spectrometer EDX (Energy Dispersive using X-ray, Philips, XL 30CP) attached to the cold field SEM.

5.2.3 Cell Culture and Cellular Incubation with Colloidal Nanopellet

Cell line and counting method

A typical cancer cell line, Human Cervix Epitheloid Carcinoma (HeLa), was used in this study. The cells were cultured in minimum essential medium eagle (MEM, Sigma) plus 10% new born calf serum (NBS, Invitrogen Corporation, Gibco) at 37 °C under 5% CO₂. The cells were plated at a concentration about 3×10^5 in 60-mm Petri dishes and were allowed to grow for 3 days. The old culture medium was replaced with nanopellet colloidal solution and recultured 24 hours in incubator. The colloidal solution was removed, and washed with phosphate buffer saline (PBS, Invitrogen Corporation, Gibco). After the cells were cleaved by Trypsin-EDTA (Gibco) and cells were staining with trypan blue (Nacalai Tesque, INC, Kyoto, Japan). Then, the cells were counted under 10x in bright field microscope. The cell survival was determined as the percentage of the number of unstained (live) cells against the control dish cells.

5.2.4 Light Irradiation of Colloidal Nanopellets on Cells

For the light irradiation experiment, a continuous wavelength Xenon CX-04E lamp, Inotech, Japan was used. The light wavelength was the 350-600 nm (V-B46, Asahi Techno

glass, Using band pass filter) and passed through a heat cutoff filter. The light power was measured by spectroradiometer, Model: LS-100, EKO Instruments Co. Ltd. The power of light maximum was 35 mW/cm^2 and irradiation time was 5 min for each dish. The cells cultured in, for 3 days and replaced the medium with colloidal nanopellet solution, and then incubated for 24 hours. After that exposed the light, one dish only light irradiation without nanopellet solution (Light control Dish) and others dish used with different quantity of colloidal nanopellet solution. Next the colloidal solution was removed, and washed with phosphate buffer saline (PBS) and then stained with trypan blue to test cell viability and counting. Dead cell accumulated the dye and stained blue color while living cells have no color. The living cells were counting and resolute as the percentage of the number cells against the control dish cells.

5.2.5 Cells Imaging Method

The images were taken using an inverted Olympus CKX41 microscope with a numerical light field condenser, which delivers a very narrow beam of white light from tungsten lamp (Transmitted light 6V30W halogen illumination) on top of the sample. A 40x objective was used to collect only the scattered light from the samples. The light field pictures were taken using an Olympus digital camera (Model No. C-5060, wide Zoom).

5.3 Results and Discussion

5.3.1 Characterization of the Au capped TiO₂ nanopellet

Gold capped TiO₂ nanopellet have visible absorption band at around 550 nm. The TiO₂ lattice with metal ions introduces new energy levels in the band gap. The band gap of TiO₂ can be tailored to extend the photoresponsiveness into the visible light region. TiO₂ is quite stable photocatalyst, but since the band gap is large ($E_g = 3.2 \text{ eV}$) and only active in the

ultraviolet region which is <10% of the overall solar intensity. When the heterogeneous photocatalysis like TiO₂ is capped by the noble metals like gold its increases the wavelength response in visible region as well as their excitation of wide band gap [4, 15].

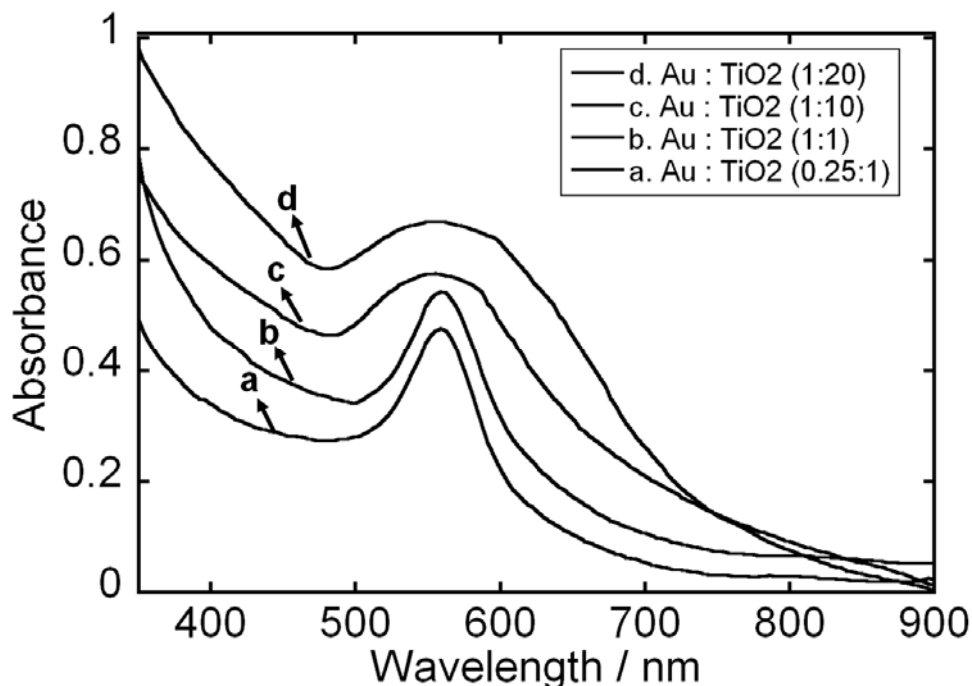


Fig. 5-1: Absorption spectrum of Au@TiO₂ various colloidal nanopellet suspensions in water. The gold concentration was fixed in 0.2 mM and the TiO₂ concentration was varied. The Au: TiO₂ molar ratios were maintained at (a) 0.25:1, (b) 1:1, (c) 1:10, and (d) 1:20.

The visible absorbance spectra of the four different TiO₂/Au colloidal solutions were clearly characterized by the visible region peak of gold capped TiO₂ nanopellet (Fig. 5-1). All the four solutions contained the constant amount of gold (0.2 mM), but different TiO₂ core concentrations. These experimental conditions allowed us to achieve different gold distribution on the TiO₂ core and compare the spectral properties. In the solutions containing lower TiO₂ molar ratio concentrations (i.e., when the ratio of TiO₂: Au is maintained at a ratio less than 1:1), a sharp and prominent absorption corresponding to the surface plasmon band of gold is observed. Apparent absorption of TiO₂ particles in the visible region (Fig.5-1, (a) 0.05 and (b) 0.2 mM) should contain light scattering, because the

solution's gold molar concentration higher than TiO_2 . On the other hand at higher TiO_2 molar concentrations (i.e., when the ratio of TiO_2 : Au is maintained at 20:1 and 1:1), we observed the peak of photocatalytically deposited one was red-shifted and broadened due to the light refraction of anatase TiO_2 [16] and band in the -IR region (Fig. 1, spectrum c and d) of Au/ TiO_2 nanopellet. Possible mechanism may be the extra charged of TiO_2 surface at high TiO_2 molar concentrations, which oxidize the gold and weak interaction between the TiO_2 core and the capping gold layer, thus inducing some aggregation (Aggregation at TEM image Fig.5-2 (a) and (b)).

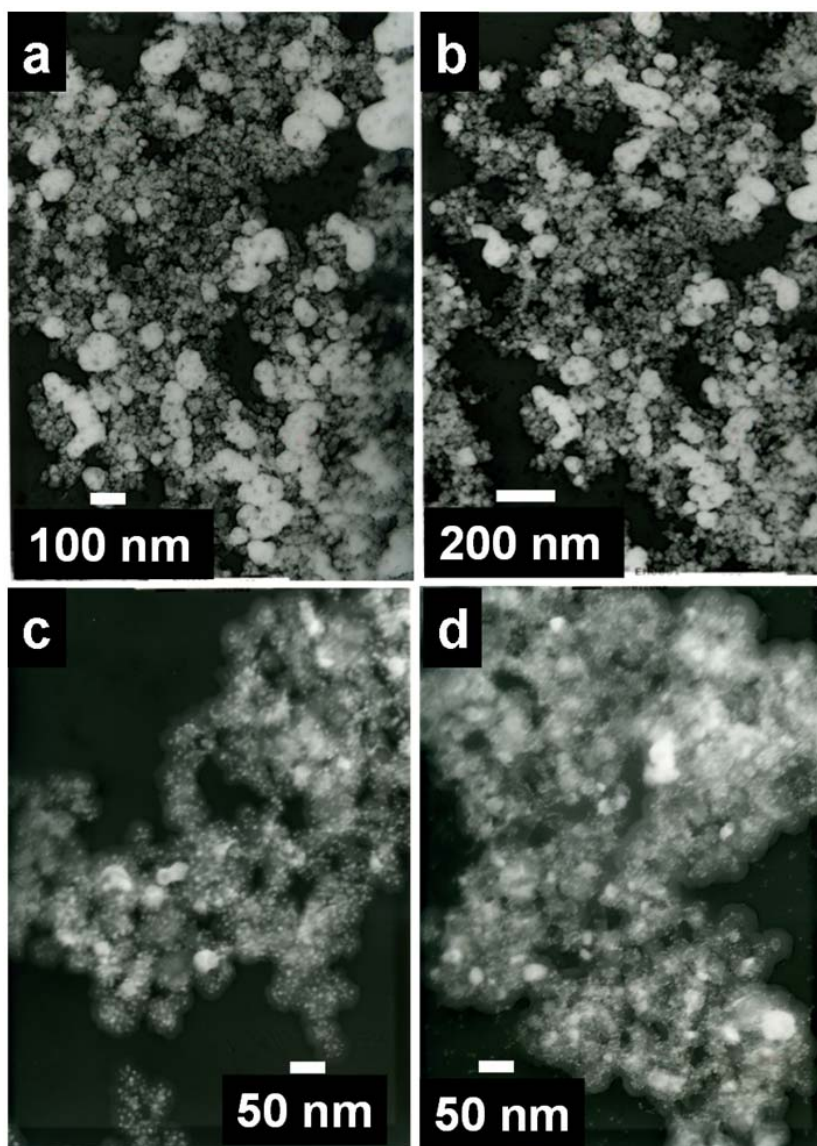


Fig. 5-2: TEM images of TiO₂/Au nanopellets recorded after 10 min UV light irradiation. The ratios of TiO₂: Au was (a) 20:1, (b) 10:1, (c) 1:1 and (d) 0.25:1.

The transmission electron images of four different gold capped TiO₂ nanopellets are shown in Fig. 5-2. The nanopellet as deposited on the copper grid exhibit a wide disparity in particle size. These composite nanopellets are mostly spherical in shape. The pellet overall diameter range is 10-40 nm. For the high core: shell (TiO₂: Au) ratio of 20:1 (as well as for 10:1) we observe fairly well dispersed particles with a particle diameter of ~40 nm. These particles have a relatively thin gold shell with no significant change in particle size compared to the TiO₂ core. For a TiO₂: Au ratio of 1:1, we observe an increase in the size of TiO₂/Au particles (particle diameter ~50 nm). These particles also tend to be in close proximity to each other. As observed from the absorption spectrum in Fig. 1, these particles maintain individual identity and exhibit noticeable aggregation effects. However the TiO₂/Au particles containing a low concentration of TiO₂ (TiO₂: Au ratio of 0.25:1) showed significant growth in the particle size with a particle diameter ranging from 20 to 50 nm. Moreover, particles remain closely packed, thus inducing aggregation effects. The TEM images of 4 mM and 2 mM as clearly seen from spectra d and c respectively in Fig. 5-1, close-packed clusters exhibit absorption in the red and infrared region. These observations support the hypothesis that the gold capping continues to occur on TiO₂ particles even at very high ratio of TiO₂: Au. On the other hand lower concentration of TiO₂ was increased the Au concentration in solution and gives the plasmon absorption peak at ~550 nm (Fig. 5-1, spectra b (0.2 mM) and a (0.05 mM)). This relevant TEM image is clearly shows the lot of dotted Au nanoparticles on TiO₂ surface in Fig.5-2 (c) and (d). The decreased TiO₂ core concentration leads to the formation of larger size particles with decreased stability of the sol.

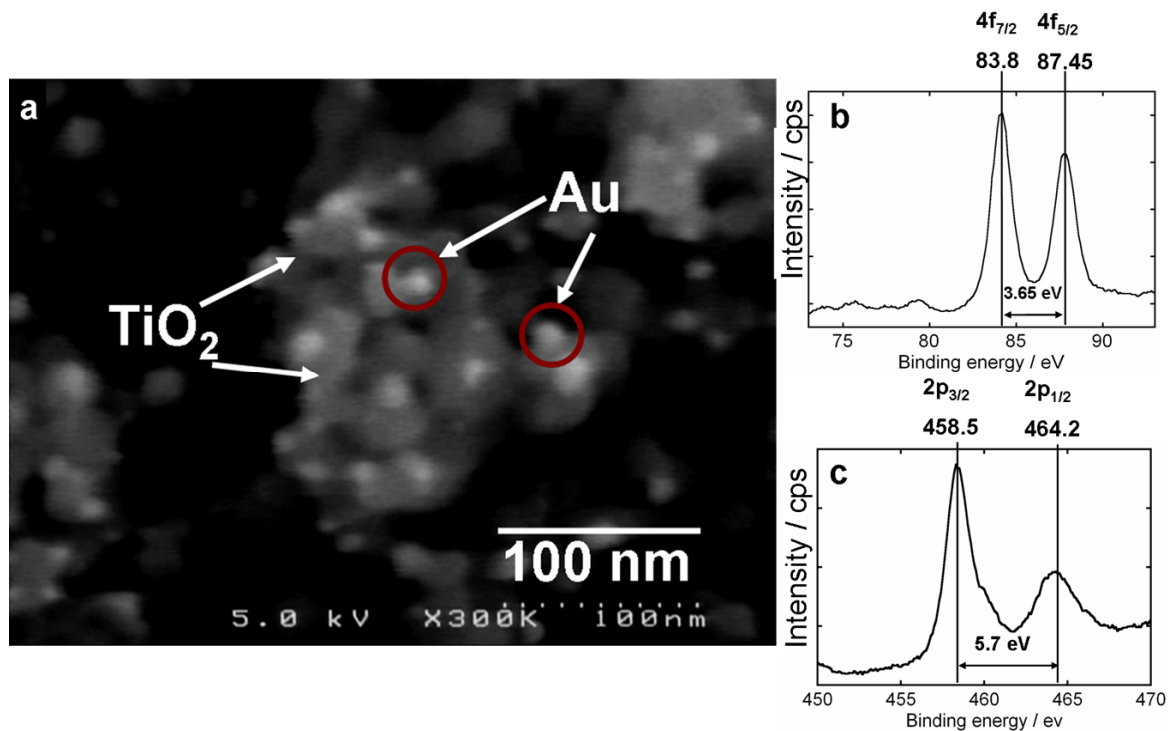


Fig. 5-3: (a) FE-SEM image of TiO₂/Au nanopellets. The XPS scan survey in the region of (b) Au 4f and (c) Ti 2p of the as-prepared Au@TiO₂ nanopellets. The ratio of this two image TiO₂/Au was 20:1.

The FE-SEM micrograph measurements have found that the gold metal nanoparticles are forming a cluster on TiO₂ surface. The TiO₂: Au molar ratio 20:1, only about 5% of the semiconductor TiO₂ surface area was covered. A large surface area of the semiconductor TiO₂ is still exposed (Fig. 5-3a). The electron captures properties at the Schottky barrier of the metal in the contact with semiconductor surface. The FE-SEM images shows the small area of the semiconductor TiO₂ surface that the actually covers. We verified that the capped gold was metallic by X-Ray photoelectron spectroscopy (XPS) (Fig. 5-3 b). The peaks observed at 83.8 and 87.45 eV were ascribed to metallic gold. The peaks located at 464.2 eV corresponding to the Ti 2p_{1/2} and another one located at 458.5 eV is assigned to Ti 2p_{3/2}. The splitting between Ti 2p_{1/2} and Ti 2p_{3/2} is 5.7 eV, indicating a normal state of Ti⁴⁺ in as-prepared mesoporous TiO₂ shows in Fig. 3 (c).

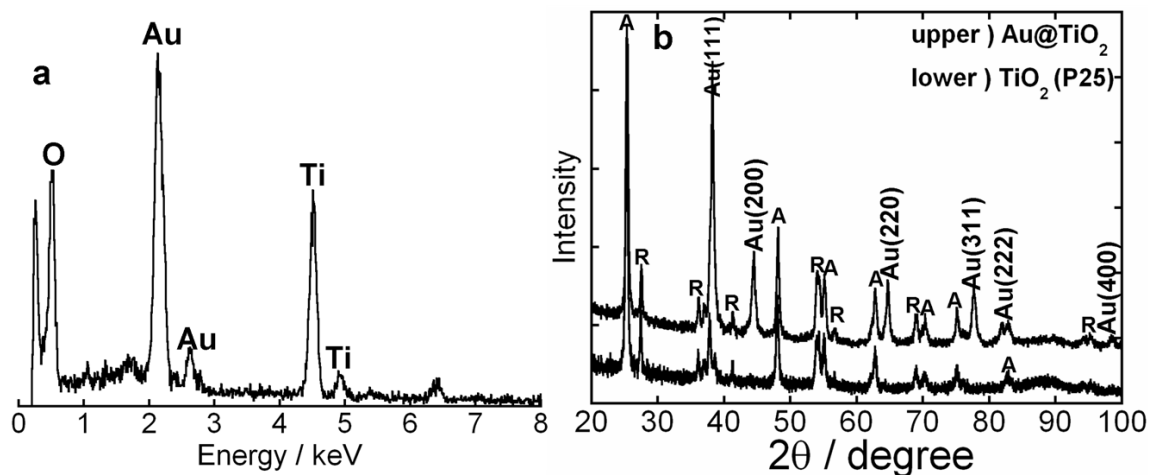


Fig. 5-4: (a) EDX spectra of Au / TiO₂, the strong Au and Ti signals in the EDX spectrum indicate that the Au is metallic and Ti consist of mixed oxides. (b) XRD pattern of Au@TiO₂ and TiO₂ (P25), Confirming the formation of pure metallic gold.

EDX was employed to obtain the quantitative information on the amount and the distribution of gold and TiO₂ species in the sample. The EDX analyses show the presence of gold, titanium and oxygen as part of the composition of the material (Fig. 5-4(a)). The wide-angle x-ray diffraction (XRD) patterns of Au / TiO₂ and pure TiO₂ (P25) nanocluster are shown in Fig. 5-4.(b) Compared with the pure TiO₂, Au / TiO₂ exhibits new peaks emerged at $2\theta = 38.185^\circ$, 44.393° , 64.578° , 77.549° , 81.724° and 98.137° which can be attributed to the diffraction peaks of (1 1 1), (2 0 0), (2 2 0), (3 1 1), (222) and (400) planes of Au, (JCPDS, PDF, File No. 00-004-0784) respectively, demonstrating the formation of metallic Au. The Au diffraction peaks are broad and low, suggesting that Au particles formed on the surface of TiO₂ show small crystalline size.

5.3.2 Photocatalytic Cancer Cell Killing Enhance Using Gold Capped TiO₂

In the vitro experiments transmission electron microscopy (TEM) observation was showed that the TiO₂ particles were absorbed on the cell membrane and phagocytized into the cytoplasm during 24-h incubation with the cells reported in reference [17]. There are

many report demonstrated that nanoscale size smaller than 50 nm can easily enter most cells, while those smaller than 20 nanometers can move out of blood vessels as they circulate through the body. The size of the blood vessel endothelium wall porosity of normal cell is 10 nm while that of cancer cell is 10-100nm. The anatomical difference of blood vessel and the nanoparticles in size and property are selective targeting of nanosize device for cancer cells [18-21].

The metal semiconductor composite system was applied in the cancer cell as a photocatalysis. Single component semiconductor nanoparticles exhibit relatively poor photocatalytic efficiency (<5%) since the majority of the photogenerated charge carriers undergo recombination [1]. It has been shown that the photocatalytic electron transfer processes at the semiconductor interface can be greatly enhanced by depositing a noble metal on the semiconductor particle [22-26]. It is well known that TiO₂ nanoparticles undergo charge separation under band gap excitation (anatase, e.g = 3.2 eV). The UV light irradiation (e.g ~ 400 nm) is therefore capable of exciting TiO₂ nanoparticles and initiating the redox reactions at the interface.

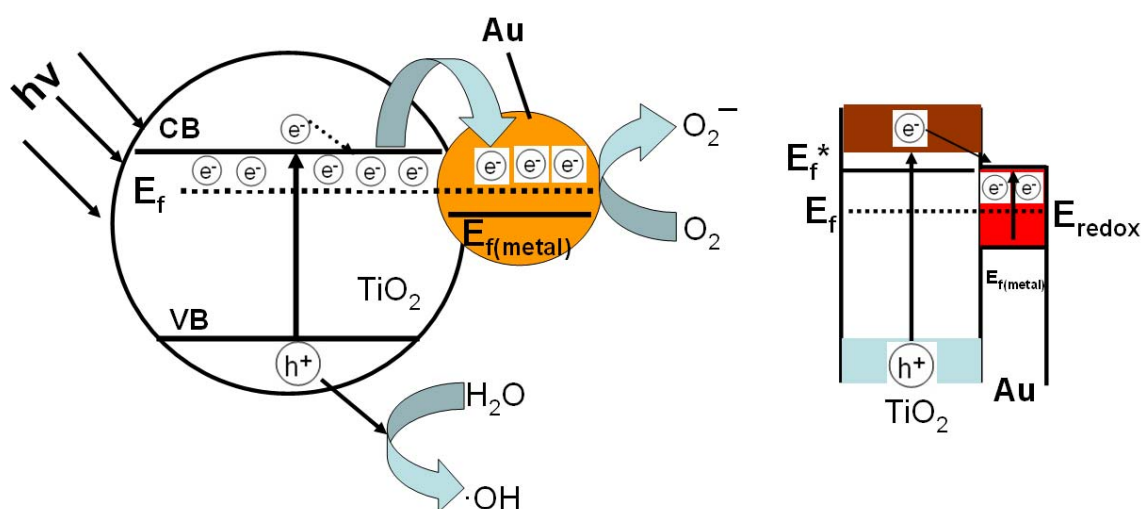
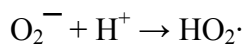
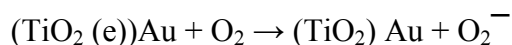
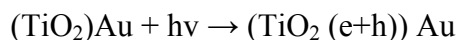


Fig. 5-5: Proposed mechanism for the interfacial charge separation of gold capped TiO₂ nanopellet (Au@TiO₂) under the irradiation of UV-visible (350-600 nm) light irradiation

(left). Fermi level equilibration of metal-semiconductor nanocomposite with the redox reaction after light irradiation (right). (E_f^* = Apparent Fermi level)



It is well known that reactive oxygen species (ROS) such as hydroxyl radicals and hydrogen peroxide formed on photoexcited gold capped TiO_2 nanopellet in water solution. The highly oxidizing hydroxyl and hydrogen peroxide species are expected cytotoxic to the cells [27].

It was reported that a photogenerated hole will react with a water molecule to form an $\cdot\text{OH}$, H_2O_2 and $\text{O}_2\cdot$ which are also reported to be formed on the photoexcited TiO_2 particles can be expected to be toxic to cells [28, 29]. The photo-induced electrons can transfer to the surface of gold nanoparticles and reduced the dissolve O_2 easily and the photo-generated holes on the TiO_2 surface can react with water to produce powerful oxidative radicals $\cdot\text{OH}$ and $\text{HO}_2\cdot$. The reaction mechanism is shown in Fig. 5-5.

The oxidation of the photogenerated holes and oxidizing radicals directly at the semiconductor/metal interface is an important process. It can be a major factor in determining the overall photocatalytic efficiency of metal semiconductor nanocomposites. After excitation the electron migrates to the metal where it becomes trapped and electron-recombination is suppressed. The hole is then free to diffuse to the semiconductor surface where oxidation of organic species can occur [30]. The metal is also important for the photocatalytic properties of the semiconductor by changing the distribution of electrons. For example, the metal and the n-type semiconductor have different Fermi level positions. The metal has a higher work function (Φ_m) than the semiconductor (Φ_s). When the two species come in contact the Fermi levels of the metal and semiconductor align causing electrons to flow to the metal from the semiconductor. The decrease in electron density within the semiconductor leads to an increase in the hydroxyl group acidity. This in turn affects the photocatalytic process on the semiconductor surface [31, 32]. Amy dawson et al shows in the absence of gold capping TiO_2 nanoparticles generate $(\text{SCN}_2)^{\cdot-}$ radicals with a quantum yield of 0.09. Changes in $\Phi(\text{SCN}_2)^{\cdot-}$ were seen as they vary the gold shell concentration. At low concentrations of gold they saw an increase in the efficiency of oxidation process. For a $[\text{Au}]: [\text{TiO}_2]$ ratio of 0.17 they saw more than 40% enhancement in the oxidation efficiency ($\Phi(\text{SCN}_2)^{\cdot-} = 0.13$) [4].

To compare the cell killing enhancing viability, the cell dishes incubated with different amount of MEM content colloidal nanopellet solution (0.2 ml, 0.5 ml, 1 ml, 2 ml and 3 ml) and another dish without nanopellet solution (controlled dish) were incubated.

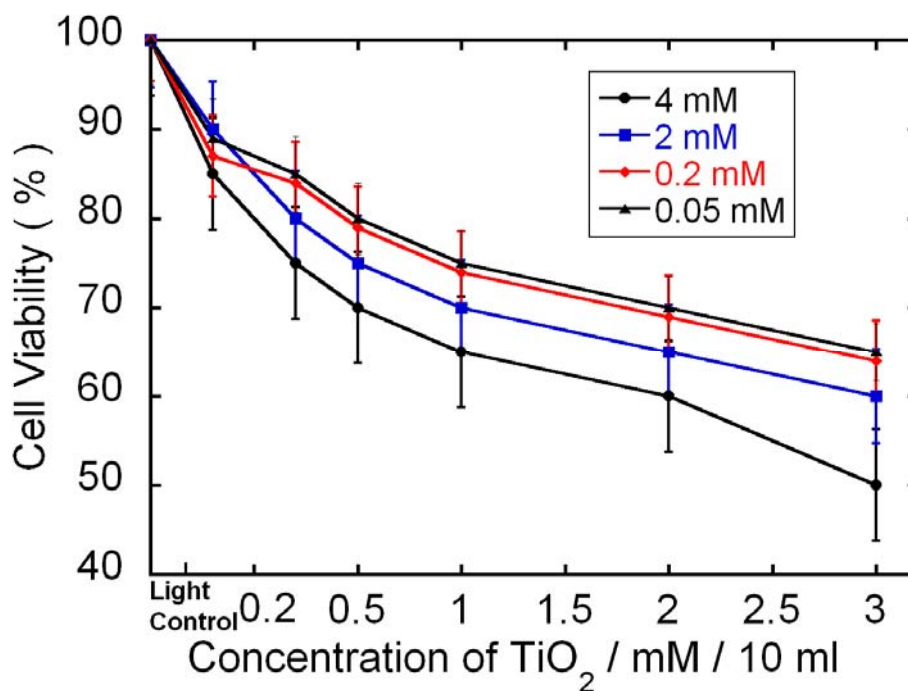


Fig. 5-6: Surviving fraction of HeLa cells incubated in MEM medium containing different concentration of TiO₂ nanoparticles 4mM, 2mM, 0.2 mM and 0.05mM. The 100% show the control dish and viability was calculated by the number of live cell percentage against the control dish cell. Bars represent the region of measured 3 times data average and the points represent the mean value from three measurements.

The cells were stained by trypan blue indicator, the dead cell accumulates dye resulting in colored, whereas live cell have no color. The cell survival was determined as the percentage of the number of the unstained cells against that of the control dish cells. All data are expressed as the mean of three time separate culture. The 100% means the control dish cell as in the absence of Au capped TiO₂. Fig. 5-6 shows that TiO₂ content MEM solution treated HeLa cell at 24 h incubated condition. The surviving viability under 5 min light irradiation without TiO₂ more or less 85-90 % cells are viable. When the TiO₂ was added, the HeLa cells were killed at a TiO₂ concentration much higher rate as shown in Fig. 5-6. When the concentration of TiO₂ was 4 mM/10ml MEM in 3 ml treatment maximum

50 % of the cells were killed after 5 min irradiation, and also that when concentration of TiO_2 was 2 mM, 0.2 mM and 0.05 mM , highest 40%, 36% and 35% of the cells were killed respectively. Surviving fraction of HeLa cells depend on amount of TiO_2 and irradiation time by about 50 $\mu\text{g}/\text{ml}$ with 10 min light irradiation most of the cells were killed [27]. But it was reported that UV light penetration depth into the tissue is limited to a few fraction of a millimeter [33]. Although longer time light irradiation is very painful and burn over the entire body. The gold capped TiO_2 nanopellet irradiation time is very short with low light power intensity. Low light power of intensity is very good for body. Although gold capped TiO_2 nanopellet induced the cell death by photochemical conversion of the gold-capped TiO_2 nanopellet provided heat is insufficient to damage the neighboring normal cells.

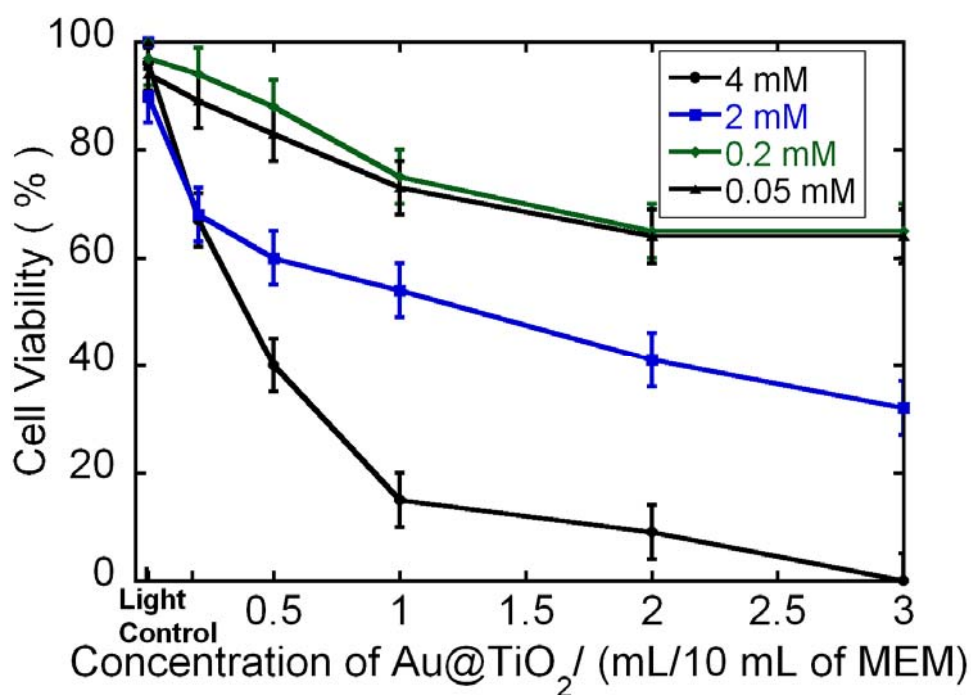


Fig. 5-7: Surviving fraction of HeLa cells incubated in MEM medium containing Au/ TiO_2 nanopellet with different TiO_2 :Au ratios : (4mM) 20:1, (2mM) 10:1, (0.2 mM) 1:1 and (0.05) 0.25:1 with 5 min after irradiation by Xenon lamp. The 100% show the control dish and viability was calculated by the number of live cell percentage against the control dish

cell. Bars represent the region of measured 3 times data average and the points represent the mean value from three measurements.

Fig.5-7 shows the viability of HeLa cell treated by the gold capped TiO_2 at 24 h incubated condition. The 4 mM with 5 min light irradiation 100% cell was killed in the presence of 3 ml Au capped TiO_2 nanopellet treatment, whereas in same concentration of TiO_2 treatment, 50 % cells have been killed as shown in Fig. 5-6. It can be said, TiO_2 with Au capped enhanced the cell killing by about 50% and also irradiation time is need half (5 min) than only TiO_2 treatment. The cell killing effect of gold capped TiO_2 depend on the TiO_2 : Au ratio. When the TiO_2 : Au is 20:1, 100% of the cell was killed under 5 min irradiation and also when the ratio of TiO_2 : Au was 10:1, 1:1 and 0.25: 1 cell killing 32%, 64%, 65% of the cells were killed respectively.

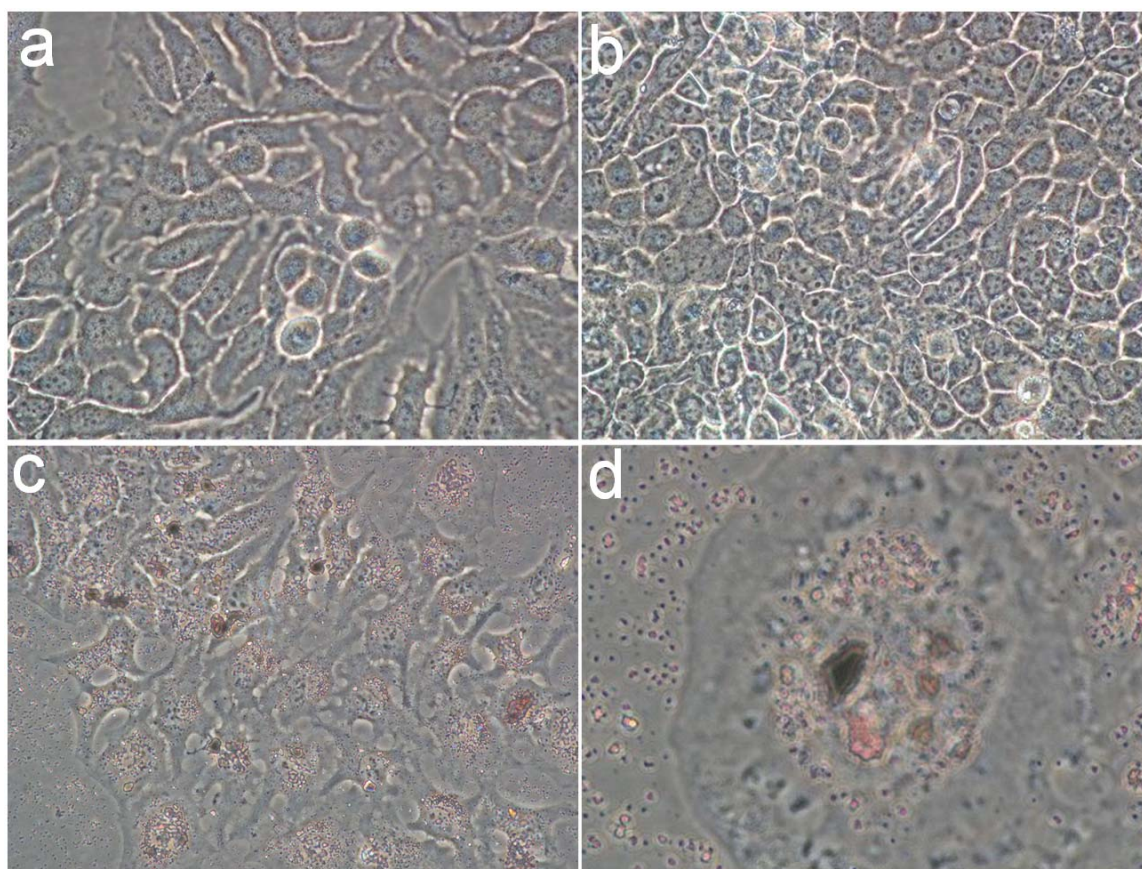


Fig. 5-8: Microscopic image of HeLa cell (a) After incubation control dish cell (b) After incubation with 5 min light irradiation cells (c) After incubation Au@TiO₂ nanopellet 5 min light irradiation with cells. (d) Photocatalytic injured single cell. (Magnification x 400)

Fig. 5-8(a) and (b) show microscopic images of HeLa cells after 24 h incubation only in MEM medium containing (control dish) and after 5 min irradiation in the same condition (light control dish). From these images it is seen that the cell morphological structure had almost no change after 5 min irradiation. Fig. 5-8 (c) shows the micrographic cell image of nanopellet-treated HeLa cells after 24 h incubation with 5 min light irradiation where some red spots and some aggregated particles are seen. It can be assigned from this image that the nanopellet are taken up into or in contact with the cells, because these red spots are not observed when the nanopellet are not present in the medium (Fig. 5-8a and b). Thus, it is obvious that the nanopellet form aggregates in or on the cells. Fig. 5-8 (d) shows that the HeLa cells (single cell) suffer photocatalytic injury at 5 min irradiation with Au@TiO₂ nanopellet. The dim blue-red color shown in the cell images outside the cell surface is due to the cell death. After light irradiation the cells were stained with trypan blue. The blue color (data not shown) showed the cell death.

The time threshold for cell death of the HeLa cells is about half that needed than only TiO₂ treated HeLa cells (Fig. 5-6 and 7). The dim white-red color shown in the cell images outside the cell surface is due to the cell died from prolonged exposure of the cells in MEM solution outside the cell incubator. The white-red spot was shown the gold capped TiO₂ nanopellet in the cytoplasm was gathered forming larger aggregates. It can be concluded to particles are taken up or in contact with the cells, because these white-red spots are not observed when nanopellet are not present in the medium. However, under dark conditions without light illumination, the cell killing effect does not change (Figure is not shown) for every measurement using TiO₂ or Au capped TiO₂ nanopellet. Illumination in the absence

of TiO₂ and Au capped TiO₂ nanopellet does not result in the photocatalytic cell killing of HeLa cell. Therefore, the presence of both UV-visible light irradiation and TiO₂ or Au capped TiO₂ nanopellet is necessary for the efficient cell killing.

Obviously here the one question is common, how about the scavenger reactive oxygen species (ROS) like ·OH, H₂O₂, and O₂^{·-} on HeLa cell? There are many reports for the scavenger experiment. In the presence of L-tryptophan, ·OH is quenched, the cell survival rate was increased [27, 34]. In the presence of catalase, the cell surviving was increase due to the catalase decomposition of the reactive H₂O₂ via following reaction $H_2O_2 \rightarrow H_2O + O_2$ [27]. In the presence of superoxide dismutase (SOD), the surviving was also increased due to the antioxidant action like superoxide conversion into the hydrogen peroxide then aid to the catalase H₂O₂ converted to the water and oxygen [29].

5. 4. Conclusion

The gold capped TiO₂ nanopellet photo catalyst were successfully prepared by a simple reduction method. The investigation of catalytic activity of four different suspensions of gold-capped TiO₂ nanopellet showed that the [TiO₂]: [Au] ratio of 20:1 was better photocatalytic optimum cell killing than the others ratio concentration. Lower concentration of TiO₂ was increased the Au concentration in solution and gives the plasmon absorption peak at ~550 nm. The decreased TiO₂ core concentration leads to the formation of larger size particles with decreased stability of the sol. Higher concentration of TiO₂ close-packed clusters was exhibit absorption in the red and infrared region and the gold capping continues to occur on TiO₂ particles. The maximum [TiO₂]: [Au] concentration photocatalytic activity is very high than the only TiO₂ treated HeLa cell. When the concentration of TiO₂ was 4 mM maximum 50 % of the cells were killed after 5 min irradiation. The same concentration of TiO₂ with gold loading treatment 100% cells was killed rapidly after 5 min irradiation. The gold loading of the TiO₂ semiconductor catalyst was greatly enhance the photocatalytic

activity than the only TiO₂ semiconductor. However Au capped TiO₂ semiconductor catalytic activity in visible light region and the time threshold for cell killing of the HeLa cells is about half that needed than only TiO₂ treated HeLa cells. Gold loading TiO₂ is greatly enhance the photocatalytic cancer cell killing activity than the only TiO₂ treated. Lower irradiation time, low light power intensity is very good for body. Although gold capped TiO₂ nanopellet induced the cell death by photochemical conversion of the gold-capped TiO₂ nanopellet provided heat is insufficient to damage the neighboring normal cells.

References

- [1] P. V. Kamat, *Chem. Rev.* **1993**, *93*, 267.
- [2] A. L. Linsebigler, G. Lu, J. T. Jr. Yates, *Chem. Rev.* **1995**, *95*, 735.
- [3] M. Anpo, M. Takeuchi, *J. Catal.* **2003**, *216*, 505.
- [4] A. Dawson, P. V. Kamat, *J. Phys. Chem. B* **2001**, *105*, 960.
- [5] J. A. Bard, *J. Phys. Chem.* **1982**, *86*, 172.
- [6] G. Burgeth, H. Kisch, *Coord. Chem. Rev.* **2002**, *230*, 41.
- [7] A. Wood, M. Giersig, P. Mulvaney, *J. Phys. Chem. B* **105** (2001) 8810-8815.
- [8] M. Jakob, H. Levanon, P. V. Kamat, *Nano Lett.* **2003**, *3*, 353.
- [9] V. Subramanian, E. E. Wolf, P. V. Kamat, *J. Phys. Chem. B* **2003**, *107*, 7479.
- [10] A. J. Bard, M. A. Fox, *Acc. Chem. Res.* **1995**, *28*, 141.
- [11] Y. Tian, T. Tatsuma, *J. Am. Chem. Soc.* **2005**, *127*, 7632.
- [12] C. Bechinger, S. Ferrere, A. Zaban, J. Sprague, B. A. Gregg, *Nature*, **1996**, *383*, 608.
- [13] A. Hagfeldt, M. Graetzel, *Chem. Rev.* **1995**, *95*, 49.
- [14] D. L. Klein, R. Roth, A. K. L. Lim, P. Alivisatos, P. L. McEuen, *Nature* **1997**, *389*, 699.
- [15] J. D. Jackson, *Classical Electrodynamics*, third ed., Wiley & Sons, New York, 1975, pp. 424-425.

- [16] A. Fujishima, K. Hashimoto, T. Watanabe, TiO₂ photocatalysis: fundamentals and applications, BKC, Inc., Tokyo, 1999, pp. 124-125.
- [17] R. Cai, K. Hashimoto, K. Itoh, Y. Kubota, A. Fujishima, *Bull. Chem. Soc. Jpn.* **1991**, *64*, 1268.
- [18] Scott E. McNeil, *Journal of Leukocyte Biology*, 2005, *78*, 585.
- [19] N. Kohler, C. Sun, J. Wang, M. Zhang, *Langmuir*, **2005**, *21*, 88584.
- [20] B. Devika Chithrani, A. Arezou Ghazani, Warren C. W. Chan, *Nano Letters*, **2006**, *6*, 662.
- [21] Y. Matsumura, H. Maeda, *Cancer Research*, **1986**, *46*, 6387.
- [22] N. R. de Tacconi, J. Carmona, K. Rajeshwar, *J. Phys. Chem. B* **1997**, *101*, 10151.
- [23] A. Heller, *Pure Appl. Chem.* **1986**, *58*, 1189.
- [24] Y. Nosaka, Y. Ishizuka, H. Miyama, *Ber. Bunsen-Ges. Phys. Chem.* **1986**, *90*, 1199.
- [25] Y. Chen, Z. Wei, Y. Chen, H. Lin, Z. Hong, H. Liu, Y. Dong, C. Yu, W. Li, *J. Mol. Catal.* **1983**, *21*, 275.
- [26] Y. Nakato, H. Tsubomura, *Isr. J. Chem.* **1982**, *22*, 180.
- [27] R. Cai, Y. Kubota, T. Shuin, H. Sakai, K. Hashimoto, A. Fujishima. *Cancer Research* **1992**, *52*, 2346.
- [28] C. D. Jaeger, A. J. Bard, *J. Phys. Chem.* **1979**, *83*, 3146.
- [29] R. Cai, Y. Kubota, T. Shuin, H. Sakai, K. Hashimoto and A. Fujishima, *Chem. Lett.* **1992**, *3*, 427.
- [30] Amy L. Linsebigler, G Lu, Jr. John T. Yates, *Chem. Rev.* **1995**, *95*, 735.
- [31] E. H. Rhoderick, R. H. Williams, *Metal-Semiconductor Contacts*, (2nd ed.), Oxford University Press, New York, 1988, pp. 11.
- [32] N. Jafiezic-Renault, P. Pichat, A. Foissy, R. Mercier, *J. Phys. Chem.* 1986, *90*, 2733.
- [33] L. J. Steven, R. W. David, M. R. Steven, *Photochem. Photobiol.* **1987**, *45*, 637.
- [34] R. C. Armstrong, A. J. Wallow, *Radiat. Res.* **1969**, *40*, 563.

CHAPTER 6

CYTOTOXIC EVALUTION OF Ag@TiO₂ CORE-SHELL COMPOSITE NANOCLUSTER AGAINST CANCER CELLS

Abstract

The Ag metal core on TiO₂ shell (Ag@TiO₂) composite nanocluster photocatalyst with uniform size, shape and core-shell structures were successfully synthesized by a simple citrate reduction method. The core-shell structure of Ag@TiO₂ nanocluster was characterized by using TEM, SEM, XPS, EDX and XRD analysis. It was found that the Ag core is in metallic form which covered by TiO₂ shell with 3-5 nm thickness and the core-shell particles size was about of 30 nm. The photocatalytic cell killing performance of Ag@TiO₂ core-shell photocatalyst has been investigating under the UV-visible light (350-600 nm) irradiation. The photocatalytic cell killing efficiency of the Ag@TiO₂ core-shell composite nanoclusters depends on the molar concentration of TiO₂. Ag: TiO₂ with molar concentration from 1:1 to 1:9 was studied and 1:7 mM was found to be optimum. The direct involvement of the Ag metal particles in mediating electron transfer between photoexcited TiO₂ under the band gap excitation is explained to carry out the photocatalytic reaction on cells. The charge separation and interfacial charge-transfer is well tailored and the photocatalytic cancer cell killing efficiencies of Ag@TiO₂ is better than the TiO₂ semiconductor. It was found that the Ag@TiO₂ with low concentration was killed more malignant (HeLa) cells by 80% when the compare to TiO₂ semiconductor nanoparticles. The work has been published in Chemistry letters, 2009, 38(10), 980-981, NSTI-Nanotech, 2009, 2, 11-14, and communicated paper in Journal of Physical Chemistry C.

6.1. Introduction

Metal nanoparticles such as Au and Ag play an important role on semiconductor to enhance the photocatalytic activity. They have also exhibited the electric, magnetic and optical properties [1-3] and also widely exploited for use photocatalytic degradation of organic contaminants in polluted air and waste water [4-6]. The metal ion doping such as PtIV, IrIV, RhIII, AuIII, PdII, CoII and NiII into TiO₂ are directly influence the intrinsic properties of the TiO₂ and extends its catalytic photoresponse into the visible region.⁷ Metal nanoparticles deposited in to TiO₂ nanostructure undergo Fermi level equilibration following the UV-excitation and enhance the efficiency of charge-transfer process [8,9]. Charge recombination or the grain boundary of heterogeneous semiconductor is often limits the efficiency of light energy conversion. The semiconductor-metal composites system is can suppress the charge recombination and extent the energy conversion efficiency [10]. The semiconductor-metal nanoclusters system metal nanoparticles are dispersed on oxide surface. The photogenerated electrons of TiO₂ are capable to oxidize the metal nanoparticles, that's depend on reactants and surrounding medium. Corrosion or dissolution of the noble metal particles during the photocatalytic reaction is likely to limit the use of noble metal such as Ag and Au [11-13]. A better synthetic design can significantly improve the catalytic performance of metal-oxide composite. Tsutomu Hirakawa et al. [3] found that the metal core outer shell semiconductor TiO₂ photocatalytic properties such as photoinduced charge separation, band gap excitation charge equilibrium in Fermi level as well as core-shell structures a superior catalyst.

Generally Ag nanoparticles are chemically very reactive, it can be oxidized at direct contact with TiO₂ and can produce silver oxide (Ag₂O). For this problem to prevent the oxidation we introduce the very simple new method to prepare the Ag@TiO₂ by citrate reduction which can capping the Ag nanoparticles and reduce rapidly in boiling temperature of isopropanol and also provided the N₂ purged and UV irradiation on solution. Our point of view, if the solutions have no Ag⁺ ion, it can not be reacting with dissolve O₂.

Ag/TiO₂ had been successfully used to enhance the photocatalytic decomposing organic compounds and photokilling bacteria [14-16]. To increase the photocatalysis cancer cell (HeLa) killing efficiency due to the plasmon excited metal nanoparticles with excitation of electron-hole pairs in TiO₂ have never been reported to the best of our knowledge. In this paper we have reported the effect of photocatalytic performance of core-shell Ag@TiO₂ on cancer cells in several concentrations and molar ratio of TiO₂ and silver nanocluster. We also compare the cell killing efficiency of TiO₂ with Ag@TiO₂ nanoclusters. We found that the Ag@TiO₂ photocatalytic cell killing needs one fourth of irradiation time and about >80% cells have been killed than the same concentration of TiO₂ treatments.

6.2. Experimental Section

6.2.1 Chemicals and materials

Titanium (IV) (triethanolaminate)-isopropoxide (N((CH₂)₂O)₃TiOCH(CH₃)₂) (TTEAIP) (80 wt % solution in 2-propanol) was purchased from ALDRICH, AgNO₃ (99.8%) and sodium citrate (99.0%) were purchased from Wako Pure Chemical Industries, Ltd. TiO₂ (Degusa, P25) was used with a mainly anatase structure (ca. 80%) under the shape of non-porous polyhedral particles of ca. 20 nm mean size with surface area of 49.9 m²/g.

6.2.2 Synthesis of Ag@TiO₂ Core-shell Nanocluster Photocatalyst

The Ag@TiO₂ core-shell nanocluster was prepared from AgNO₃ salt and Titanium (IV) (triethanolaminate)-isopropoxide (TTEAIP). AgNO₃ and TTEAIP were used as a source of Ag and TiO₂. Five different suspensions of Ag@TiO₂ nanocluster were prepared by keeping the AgNO₃ concentration constant at 1mM while varying the TTEAIP concentration from 1,3,5,7 and 9 mM. These five Ag/TiO₂ suspensions contained [Ag]:[TiO₂] ratios were 1:1, 1:3, 1:5, 1:7 and 1:9 respectively. All concentrations are based on molar concentrations.

Ag@TiO₂ core-shell nanoclusters were prepared by adding 1 mM (1 mM = 1 mol/dm³) of AgNO₃ to the millipore distilled water with vigorous stirring at 60 °C constant temperature.

The TTEAIP of different molar concentrations and 2 ml of 1% sodium citrate were added to AgNO₃ solution. The solution was stirred for an additional 15 min to allow complete core-shell formation. The mixer temperature was increase at boiling temperature with vigorous stirring. With continued heating of the solution, the color slowly changed from colorless to light brown. After 90 min, the color of the suspension turned from light to dark brown. After that, the sample suspension was cooled at room temperature. All solutions used were freshly prepared and kept stirring in a closed flask until the next step.

Next the solution was transferred in conical flask with a rubber septum and the solution was purged with N₂ gas. Then the solution was irradiated with ultraviolet light (15 mW cm⁻²) for at least 30 min to reduce if have any unreacted Ag⁺ in solution to Ag⁰. Then the solution was centrifuged at 5000 rpm for 20 min. The precipitate nanocluster was washed with two times with millipore water and one time with ethanol to remove the remaining citrate solution and minimize the water content. After the supernatant was removed, clusters were collected and sterilized in an autoclave. Then the composite nanoclusters were dispersed in 5 mL MEM (minimum essential medium) solution and stored at 4 °C.

6.2.3 Instrumental analysis

Absorption spectra were recorded on a UV-visible spectrophotometer (Shimadzu Corporation, MPS-2000, Japan) using a 1 cm path-length quartz cuvette. The size and shape of the nanocluster is analyzed by transmission electron microscopy (TEM) using a JEOL, JEM-3010 VII, TEM operating at 300 kV. Samples for TEM were prepared by ultrasonically dispersing in absolute ethanol, then placing a drop of this suspension onto a carbon coated copper grid and then dried in air. The nanocluster surface condition was also analyzed by a field-emission scanning electron microscope (FE-SEM, Hitachi, S-4100H), X-ray photoelectron spectroscopy (XPS, Quantum-2000, Scanning ESCA-1000 microprobe with Magnesium α radiation, Shimadzu) and X-ray diffraction (XRD, PANalytical) analyzer. Prior to FE-SEM measurements, the samples solution were dropped on glass plate and then

dried in air approximately one week. Then glass containing sample was coated with platinum by using a magnetron sputter and then placed in the SEM for the analysis with desired magnifications. The XRD patterns were recorded using a X'Pert PRO PANalytical diffractometer over the scanned angle from 10 ° to 100 ° at a scanning rate of 3 ° per minute. The X-ray photoelectron spectra were collected on an ESCA-1000 X-ray photoelectron spectrometer (XPS), using Mg K α X-ray as the excitation source. The quantitative chemical composition of the Ag@TiO₂ composite nanocluster surface was also measured using an energy dispersive X-ray spectrometer EDX (Energy Dispersive using X-ray, Philips, XL 30CP) attached to the cold field SEM.

6.2.3 Cell Culture and Cellular Incubation with Colloidal Nanocluster

6.2.3.1 Cell line and counting method

A typical cancer cell line, Human Cervix Epitheloid Carcinoma (HeLa), was used in this study. The cells were cultured in minimum essential medium eagle (MEM, Sigma) plus 10% new born calf serum (NBS, Invitrogen Corporation, Gibco) at 37 °C under 5% CO₂. The cells were plated at a concentration about 3x10⁵ in 60-mm Petri dishes and were allowed to grow for 3 days. The old culture medium was replaced with nanocluster colloidal solution and recultured 24 hours in incubator. The colloidal solution was removed, and washed with phosphate buffer saline (PBS, Invitrogen Corporation, Gibco). After the cells were cleaved by Trypsin-EDTA (Gibco) and cells were staining with trypan blue (Nacalai Tesque, INC, Kyoto, Japan). Then, the cells were counted under 10x in bright field microscope. The cell survival was determined as the percentage of the number of unstained (Live) cells against the control dish cells.

6.2.3.2 Light Irradiation of Colloidal Nanocluster on Cells

In photocatalytic experiment, a continuous wavelength xenon CX-04E lamp, Inotech, Japan was used. The light wavelength was 350-600 nm (V-B46, Asahi Techno glass, Using as a

band pass filter) and passed through a heat cutoff filter. The light power was measured by using a spectroradiometer, Model: LS-100, EKO Instruments Co. Ltd. The power of light maximum was 35mW/cm^2 and irradiation time was 5 min for each dish. A table rotator was used for the Petri dish to confirm the homogeneous light irradiation on the cells. The cells cultured in, for 3 days and replaced the medium with colloidal nanocluster solution, and then incubated for 24 hours. After that exposed the light, one dish only light irradiation without nanocluster solution (Light control Dish) and others dish used with different quantity of colloidal nanocluster solution. The colloidal solution was removed, and washed with phosphate buffer saline (PBS) and then stained with trypan blue to test cell viability and counting. Dead cell accumulated the dye and stained blue color while living cells have no color. The living cells were counting and resolute as the percentage of the number cells against the control dish cells.

6.2.3.3 Cells Imaging Method

The images were taken using an inverted Olympus CKX41 microscope with a numerical light field condenser (N.A.0.3), which delivers a very narrow beam of white light from tungsten lamp on top of the sample. A 40x objective was used to collect only the scattered light from the samples. The light field pictures were taken using an Olympus digital camera (Model No. C-5060, wide Zoom).

6.3. Results and Discussion

6.3.1 Synthesis and Characterizations of Ag@TiO₂ Core-shell Nanocluster

The citrate reduction method was used to obtain the silver nanoparticles from silver nitrate which yields uniform particles size with of Titanium (IV) (triethanolaminate)-isopropoxide (TTEAIP) in boiling temperature. It has been demonstrated that the colloidal Ag@TiO₂ suspensions are very stable than the one post synthesis by dimethylformaamide (DMF) reduction prepared Ag@TiO₂ suspension. It is important that the reduction rate of

Ag^+ ion is greater than the rate of formation of TiO_2 shell [3]. We optimized the several batch preparations and found that at $60\text{ }^\circ\text{C}$ temperature is suitable for Ag@TiO_2 core-shell nanocluster formation. The Ag^+ ions were reduced by sodium citrate to form Ag nanoparticles and may quickly interact with the amine group of TTEAIP. The reduction rate of Ag^+ to Ag^0 and hydrolysis of TTEAIP rapidly improve to make TiO_2 shell formation on Ag particles to yield of core-shell cluster is increase the temperature to boiling temperature. It is very important to care the Ag particles, because it can oxidize when contact the surface oxygen of TiO_2 . But, in the presence of sodium citrate silver colloidal nanoparticles were coated thickly and homogeneously and it is protecting the oxidation [17, 18]. The suspension is than heated another hour leading to color change to dark brown. We purged the N_2 in suspension and UV irradiation to remove the any Ag^+ in solution or any layer of oxide on silver surface. With UV irradiation and N_2 purged to make the TiO_2 -saturated Ag@TiO_2 nanocluster suspensions. Finally, the suspension was centrifuged and removed the water content of Ag@TiO_2 core-shell nanocluster.

The stability of Ag@TiO_2 core-shell structure was tested by suspending the nitric acid at pH 2. The Ag cluster, stabilized by nitric acid, is readily dissolve in acidic solution (pH=2). The prepared Ag@TiO_2 colloidal nanoclusters remain stable in acid solution. If the TiO_2 shell cluster was thin or cluster formed separately or independently is quite stable in nitric acid. The stability test in acidic solution asserts the argument that the TiO_2 shell on the Ag core is uniform and provides the protection against acid induced corrosion.

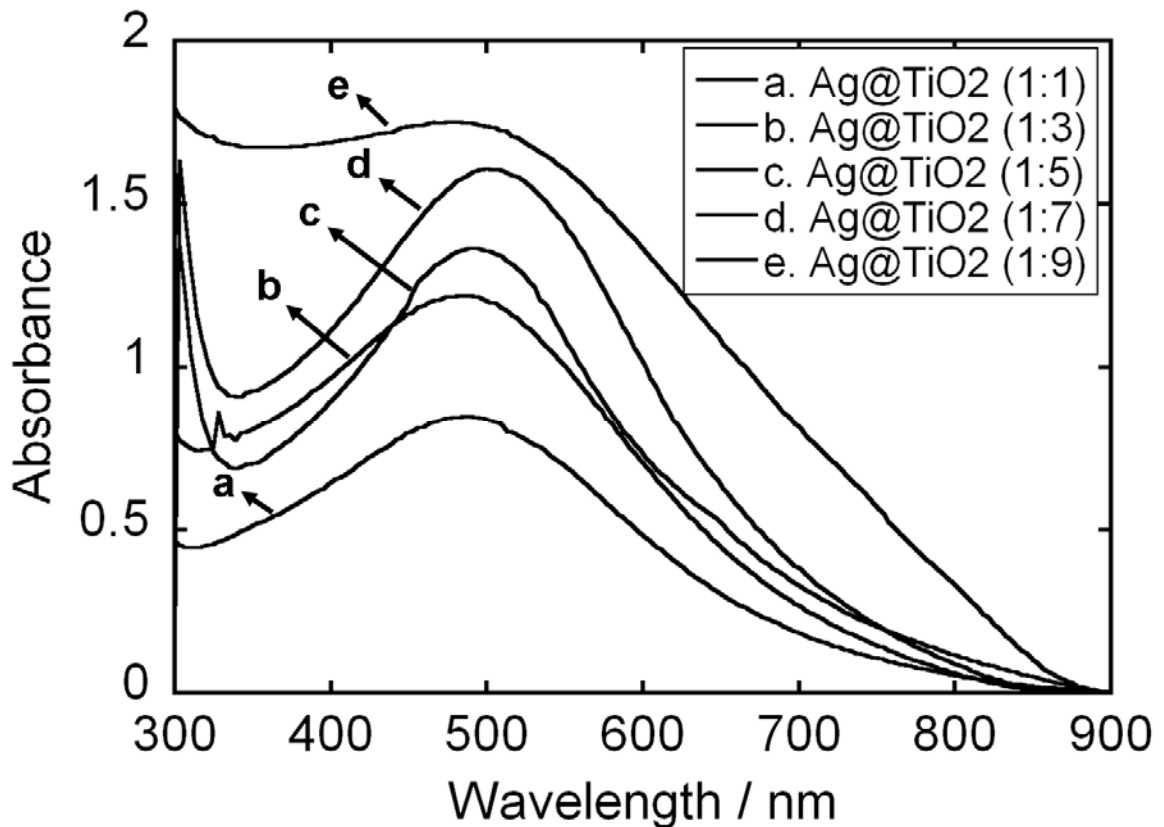


Fig. 6-1: Absorption spectra of Ag@TiO₂ various colloidal composite nanocluster suspensions in water. The Ag: TiO₂ molar ratios were maintained at (a) 1:1, (b) 1:3, (c) 1:5, (d) 1:7 and (e) 1:9.

UV-visible absorption spectra of Ag@TiO₂ colloidal nanocluster suspension with different TiO₂ as well as TTEAIP contents are shown in Fig.6-1. Ag@TiO₂ is shows the strong absorption in the visible region with plasmonic peak. The evidence of plasmonic peak in curve showed that the Ag core is not oxidized. The absence of plasmonic peak in curve is associated with the oxidation of Ag nanoparticles [19]. This visible absorption arises from the surface plasmon band of Ag core and is strongly influenced by the oxide shell. The lower concentration of TiO₂ shell was observed a dampening and broadening surface plasmon band (Fig.6-1, spectrum a and b) and higher concentration of TiO₂ shell can not seen the plasmon band of Ag core (Fig.6-1, spectrum e).

It is interesting to note that, increase the shell thickness is to increase the concentration of the precursor of TiO₂. The result (Fig.6-1) indicates that increasing the TiO₂ shell thickness

the absorption bands of Ag@TiO₂ gradually increase than decrease. We found the optimizing shell thickness with uniform covering of Ag@TiO₂ at 1:5 and 1:7 molar ratio concentrations.

Ag@TiO₂ catalyst exhibit strong absorption band in the visible region and the maximum was found at about 500 nm. The TiO₂ lattice with metal ions introduces new energy levels in the band gap. UV-visible diffuse reflectance spectroscopy (Fig. is not shown) was employed to estimate the band-gap energies of the prepared Ag@TiO₂ nanocomposites. Firstly, to establish the type of band-to-band transition in these synthesized particles, the absorption data were fitted to equations for direct band-gap transitions. The minimum wavelength required to promote an electron depends upon the band-gap energy E_{bg} of the photocatalyst and is given by: $E_{bg} = 1240 / \lambda$ eV; where λ is the wavelength in nanometers.²⁰ The band gap excitation of Ag@TiO₂ is 2.50 eV and undergoes charge separation participate in the redox processes at the TiO₂ shell interface at about 500 nm.

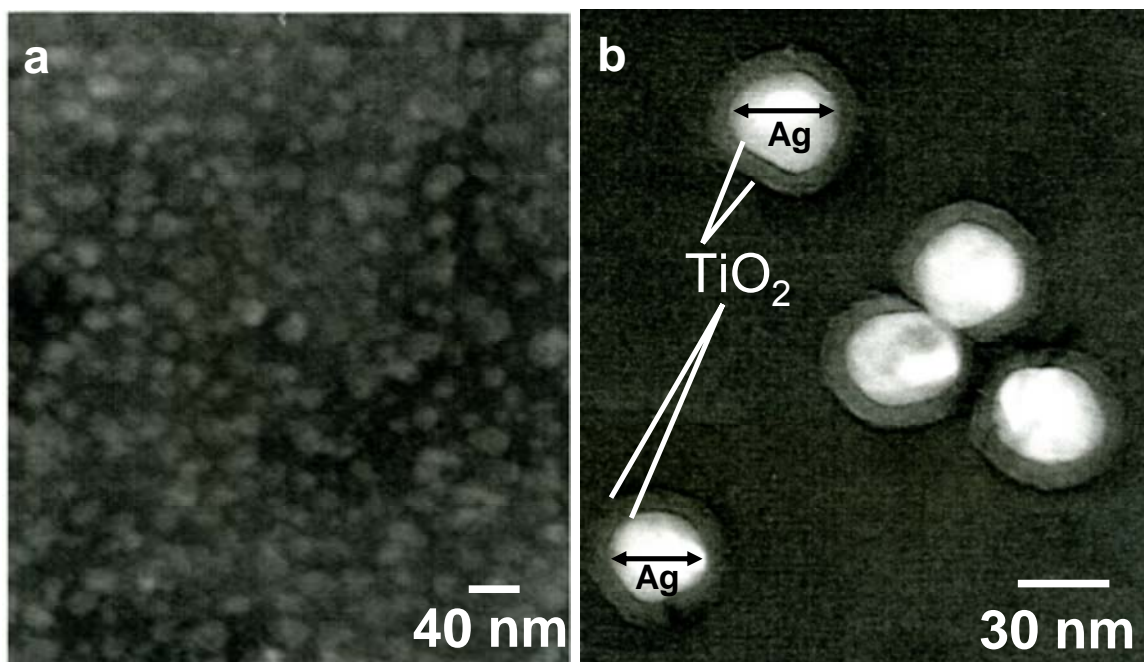


Fig. 6-2: Transmission electron micrograph of Ag@TiO₂ composite nanocluster. (a) Ag is uniformly covered by TiO₂ layer (milk spot). (b) Ag@TiO₂ showing the well crystalline nature of Ag metallic core and the uniform shell thickness of TiO₂. The Ag: TiO₂ molar ratio is 1:7 in (a) and (b).

The Ag@TiO₂ core-shell structures were confirmed by Transmission electron micrographs (TEM) image and are shown in Fig.6-2. The milky colored spots represent Ag nanoparticles covered with a TiO₂ layer are shown Fig.6-2 (a). The TEM image shows that the Ag@TiO₂ forms a well-dispersed core shell structure. These core-shell composite nanoclusters are mostly spherical and overall diameters ranges were 20-40 nm. The round dark structures of TiO₂ shell on Ag core were clearly evident and shell is uniformly covered on the core (Fig.6-2 b). All Ag core particles have an uniform thin capping of TiO₂ and the shell thickness in the range of about 3-5 nm.

The FE-SEM image of Ag@TiO₂ core-shell composite nanocluster shows that the Ag was covered with TiO₂ nanocluster and the particles diameter is about 30 nm.

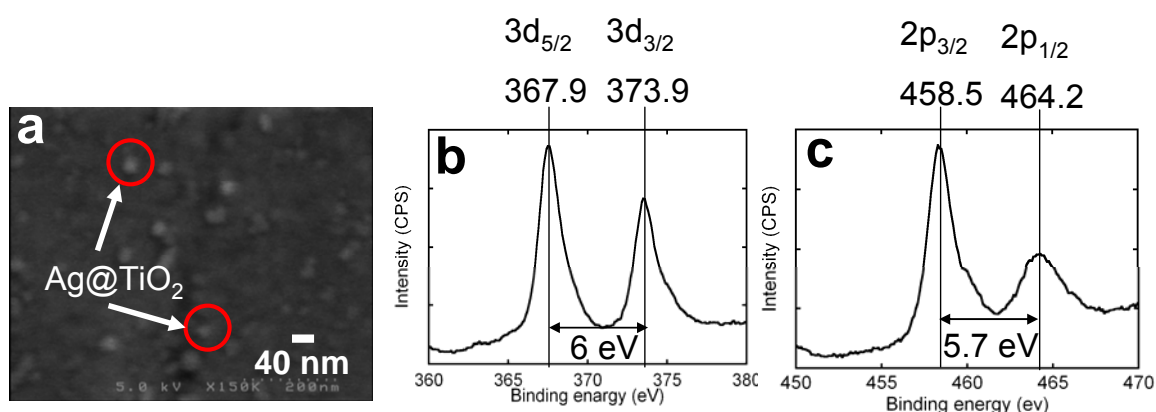


Fig. 6-3: (a) FE-SEM image of the Ag@TiO₂ nanocluster morphology. The X-ray photoelectron spectroscopic scan survey in the region of (b) Ag 3d (c) Ti 2p of the as-prepared Ag@TiO₂ nanoclusters. The Ag: TiO₂ molar ratio is 1:7.

The presence of metallic Ag core was confirmed by X-ray photoelectron spectroscopy (XPS) analysis. The peaks observed 3d_{3/2} and 3d_{5/2} at 373.9 and 367.9 eV were ascribed to metallic silver (Fig.6-3 (b)). XPS analysis results of TiO₂ are shown in Fig.6-3 (c). The

peaks located at 464.2 eV corresponding to the Ti 2p_{1/2} and another one located at 458.5 eV is assigned to Ti 2p_{3/2}. The splitting between Ti 2p_{1/2} and Ti 2p_{3/2} is 5.7 eV, indicating a normal state of Ti⁴⁺ in as-prepared mesoporous TiO₂ [21].

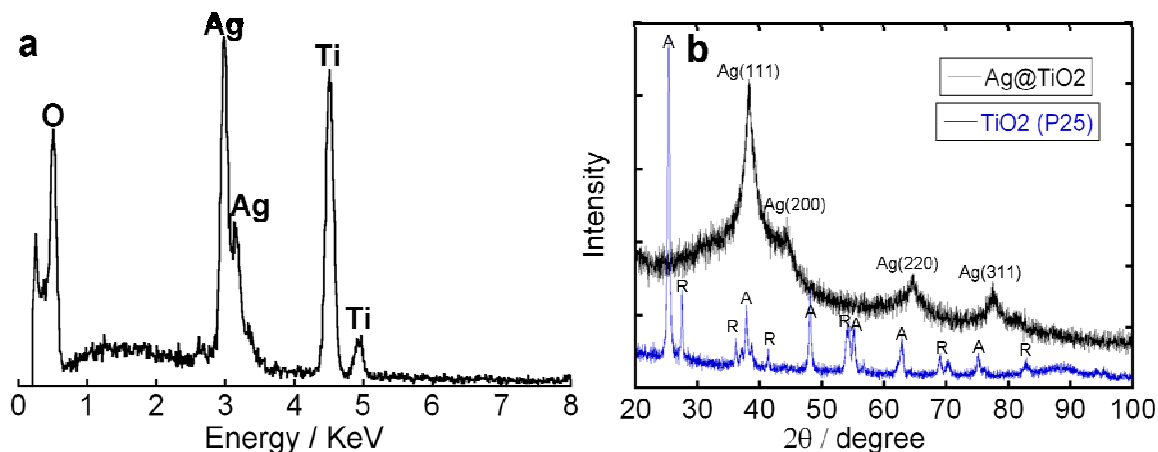


Fig. 6-4: (a) EDX spectra of Ag@TiO₂, the strong Ag and Ti signals in the EDX spectrum indicate that the Ag is metallic and Ti consist of mixed oxides. (b) XRD pattern of Ag@TiO₂ and TiO₂ (P25), Confirming the formation of pure metallic silver. The Ag: TiO₂ molar ratio is 1:7 in (a) and (b).

EDX was employed to obtain the quantitative information on the amount and the distribution of silver and TiO₂ species in the sample. The EDX analyses show the presence of silver, titanium and oxygen as part of the composition of the material (Figure 4(a)). The wide-angle x-ray diffraction (XRD) patterns of Ag@TiO₂ and TiO₂ (P25) nanocluster are shown in Fig.6-4. The presence of peaks at 38.09 (111), 44.28 (200), 64.42 (220) and 77.36 (311) planes are belongs to metallic silver, which clearly confirm Ag is in metallic form. No appearance of silver oxide characteristic peak indicates that Ag^o exists in the crystal lattices of TiO₂. It is very difficult to identify the TiO₂ in XRD analysis and peaks were not clearly observed. This may be due to the low amount of TiO₂ in Ag@TiO₂ nanocluster which densely covered Ag nanoparticles. However, a little typical anatase phase of TiO₂ peak at 38.59° was observed.

6.3.2 Photocatalytic Cancer Cell Killing Enhance Using Ag@TiO₂ core-shell nanocluster

In the vitro experiments transmission electron microscopy (TEM) observation was showed that the TiO₂ particles were absorbed on the cell membrane and phagocytosis into the cytoplasm during 24-h incubation with the cells reported in reference [22]. There are many report demonstrated that nanoscale size smaller than 50 nanometers can easily enter most cells, while those smaller than 20 nanometers can move out of blood vessels as they circulate through the body. The size of the blood vessel endothelium wall porosity of normal cell is 10 nm while that of cancer cell is 10-100nm. The anatomical difference of blood vessel and the nanoparticles in size and property are selective targeting of nanosize device for cancer cells [23-26].

UV light can excite an electron from valance band to conductance band in TiO₂ semiconductor, leaving to hole in the valance band [27]. This electron-hole in direct competition with trapping process. The rate of trapping and the photocatalytic activity of TiO₂ will be enhanced by retarding the electron-hole recombination. The Ag core in Ag@TiO₂ can be slowing the electron-hole recombination on the surface of TiO₂ particles. As a result trapped electron in conduction band and trapped hole in valance band are free charge carriers in the conduction and valance bands.

But, interestingly in Ag@TiO₂ core-shell nanoclusters, Ag core are able to photoinduced charging electrons under UV irradiation and dark discharge them on demand. The electron charging and discharging depend on the two major factor (i) dielectric of the medium (ii) the density of electrons of the metal cluster. If the photoinduced excitation of Ag@TiO₂ is carried out in the presence of an electron acceptor such as thionine dye or oxygen, the photogenerated electrons are scavenged by the acceptor molecules [3].

A new mechanism has been proposed for the Ag@TiO₂ photocatalytic activity on cancer cell. The photoexcited electrons are penetrated or transferred quickly through TiO₂ shell

into the Ag nanocore as the two systems until the charge Fermi level equilibrium condition (shows in reactions first and second). After a favorable Fermi level ($E_f = 0.4 \text{ V Vs NHE}$) electrons are facilitate quick transfer from excited TiO_2 and initiating the redox reactions at the interface of TiO_2 shell (Fig.6-5).

The reactive oxygen species (ROS) such as hydroxyl radicals and hydrogen peroxide formed on photoexcited Ag@TiO_2 nanocluster in MEM content water solution. The highly oxidizing hydroxyl and hydrogen peroxide species are expected toxic to the cells [28].

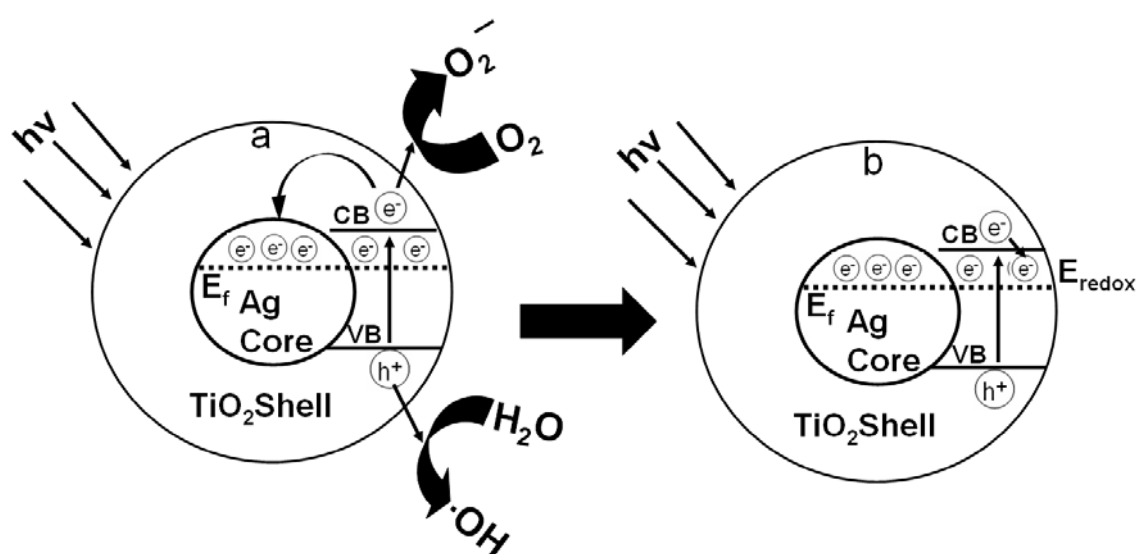
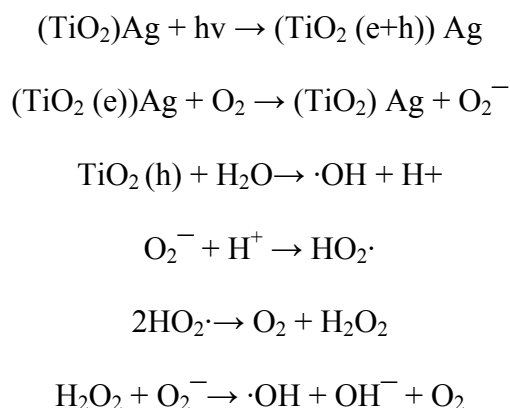


Fig. 6-5: Proposed mechanism for the interfacial charge separation of Ag@TiO_2 nanocluster under the UV-visible (350-600 nm) light irradiation.



It was reported that a photogenerated hole will react with a water molecule to form $\cdot\text{OH}$, H_2O_2 and $\text{O}_2\cdot$ which can be expected toxic to cells [29, 30]. The photo-induced electrons transfer to the interfacial surface of excited TiO_2 and then electrons transferring to Ag core

until the Fermi level equilibrium [3]. Some of electron can be transfer the TiO_2 surface and reduced the dissolve O_2 easily, because dissolve oxygen also one of the good acceptor of electron is shown in Figure 5 a. Both of the case photo-generated holes on the TiO_2 surface can react with water to produce powerful oxidative radicals $\cdot\text{OH}$ and $\text{HO}_2\cdot$ is shown reaction mechanism and Fig.6-5. The Ag core act as a schottky barrier of TiO_2 excited electron and protect the electron-hole recombination. As a result promotes the photo induce interfacial charge-transfer process as well as enhance the photocatalytic cell killing than only TiO_2 .

The oxidation of the photogenerated holes and oxidizing radicals directly at the semiconductor/metal interface is an important process. It can be a major factor in determining the overall photocatalytic efficiency of metal semiconductor nanocomposites. After excitation the electron migrates to the metal where it becomes trapped and electron-recombination is suppressed. The hole is then free to diffuse to the semiconductor surface where oxidation of organic species can occur [31]. The metal is also important for the photocatalytic properties of the semiconductor by changing the distribution of electrons. For example, the metal and the n-type semiconductor have different Fermi level positions. The metal has a higher work function (Φ_m) then the semiconductor (Φ_s). When the two species come in contact the Fermi levels of the metal and semiconductor align causing electrons to flow to the metal from the semiconductor. The decrease in electron density within the semiconductor leads to an increase in the hydroxyl group acidity. This in turn affects the photocatalytic process on the semiconductor surface [32, 33].

To test the cell killing enhancing viability, the cell dishes were treated and incubated with different amount of MEM content Ag@TiO_2 colloidal nanocluster solution (4 μl , 8 μl , 12 μl , 16 μl and 20 μl) and another dish (light controlled and control dish) was not treated with nanocluster solution.

The cells were stained by the trypan blue indicator; the dead cells accumulate the dye resulting in blue color, whereas the live cells have no color. The cell viability was

determined as the percentage of the number of the unstained cells against that of the control dish cells. All the data are expressed as the mean of three-time separate culture. In the scale bar of Fig.6-6 and 7, 100 means the number of living cells in control dish in the absence of Ag@TiO₂ nanocluster.

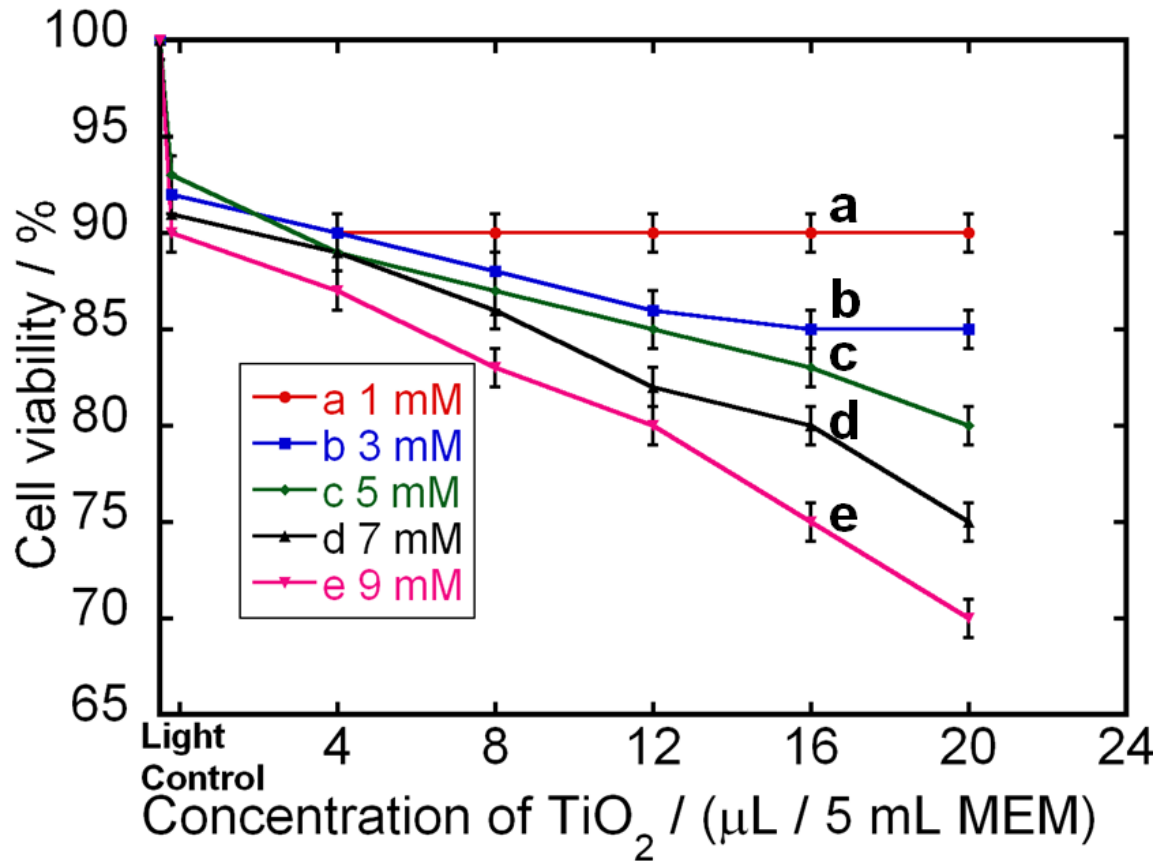


Fig. 6-6: Surviving fraction of HeLa cells incubated in MEM medium containing 1 mM, 3 mM, 5 mM, 7 mM and 9 mM concentration of TiO₂ nanoparticles. The 100% show the control dish and viability was calculated by the number of live cell percentage against the control dish cell. Bars represent the region of measured 3 times data average and the points represent the mean value from three measurements.

Fig.6-6 shows that TiO₂ content MEM solution treated HeLa cell at 24 h incubated condition. The surviving viability under 5 min light irradiation without TiO₂ more or less 90-95 % cells are viable. When the TiO₂ was added, the HeLa cells were killed at a TiO₂ concentration much higher rate as shown in Figure 6. When the concentration of TiO₂ was 9

mM/5ml MEM in 20 μ l treatment maximum 30 % of the cells were killed after 5 min irradiation, and also that when concentration of TiO_2 was 7 mM, 5 mM, 3 mM and 1 mM , highest 25%, 20%, 15% and 10% of the cells were killed respectively. Surviving fraction of HeLa cells depend on amount of TiO_2 and irradiation time by about 50 μ g/ml with 10 min light irradiation most of the cells were killed. 34

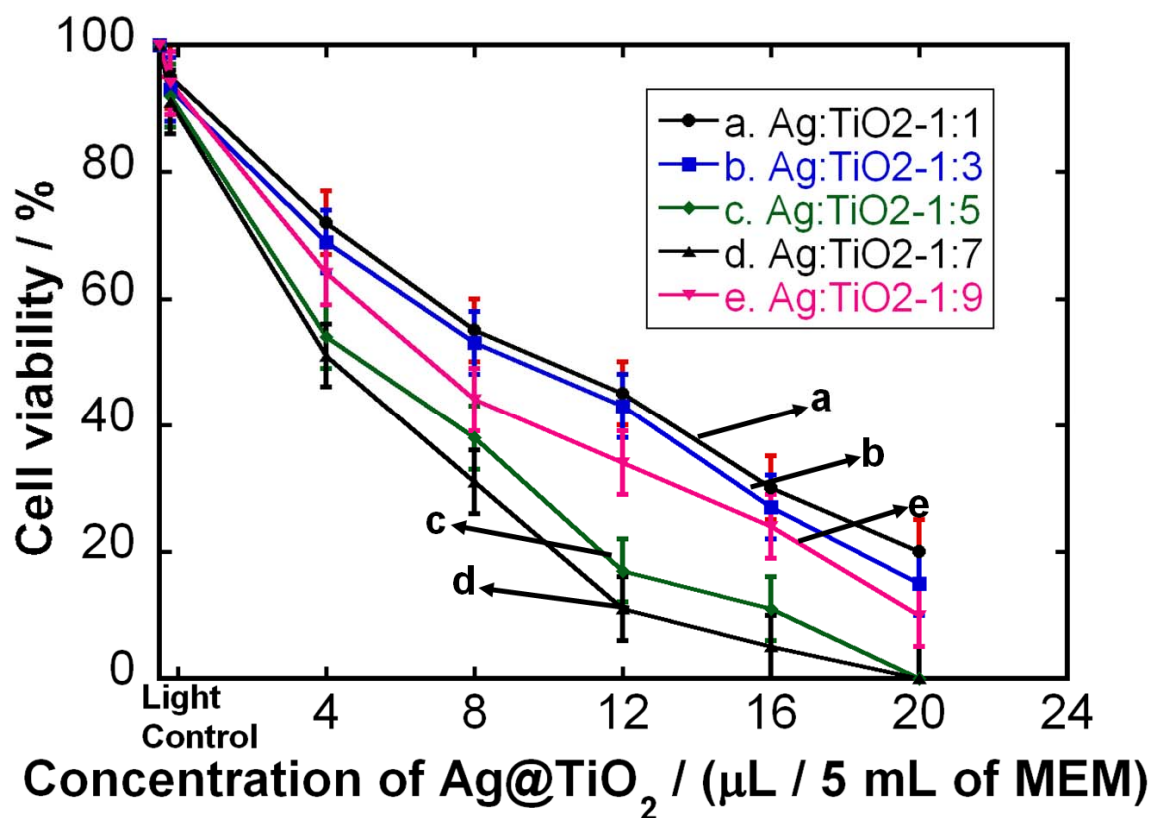


Fig. 6-7: Surviving fraction of HeLa cells incubated in MEM medium containing Ag@TiO₂ core-shell nanocluster with different Ag:TiO₂ ratios; (1mM) 1:1, (3mM) 1:3, (5 mM) 1:5, (7 mM) 1:7 and (9 mM) 1:9 with 5 min irradiation by Xenon lamp. The 100% show the control dish and viability was calculated by the number of live cell percentage against the control dish cell. Bars represent the region of measured 3 times data average and the points represent the mean value from three measurements.

Fig.6-7 shows the viability of HeLa cell treated by the Ag@TiO₂ at 24 h incubated condition. About 20 μ l of Ag@TiO₂ with molar ratio of 1:5 and 1:7 in 5 min light irradiation 100% cell was killed rapidly, whereas in same concentration of TiO₂ treatment

(5 and 7 mM), maximum 25 % and 20% cells have been killed as shown in Figure 6. It can be said, TiO₂ shell with Ag core enhanced the cell killing efficiency by about 80% and also irradiation time is need one third (5 min) than only TiO₂ treatment.

The cell killing effects of Ag@TiO₂ nanocluster depend on the Ag: TiO₂ molar ratio. When the Ag:TiO₂ is 1:5 and 1:7 maximum 100% of the cell were killed under 5 min irradiation and also when the ratio of Ag:TiO₂ was 1:1, 1:3 and 1: 9 cell killing maximum 80%, 85%, 90% were killed respectively. The photocatalytic activity is depending on the TiO₂ shell thickness as well as higher molar concentration. The shell thickness increase the concentration of the precursor TiO₂ (TTAEIP) was recognized from the TEM images (Fig. is not shown). Photocatalytic activity of Ag@TiO₂ catalyst increase when the molar ratio increase from 1:1-1:7 and 1:5, 1:7 was found to be optimum. How ever, further increase the molar ratio of TiO₂ decrease the photocatalytic activity. The lack of available charged of TiO₂ shell surface at low TiO₂ concentration (1:1 and 1:3 molar ratio) and the thick shell thickness of TiO₂ significant dampening of the surface plasmon band (1:9 molar ratio) was implied the decrease of photocatalytic activity on cancer (HeLa) cell.

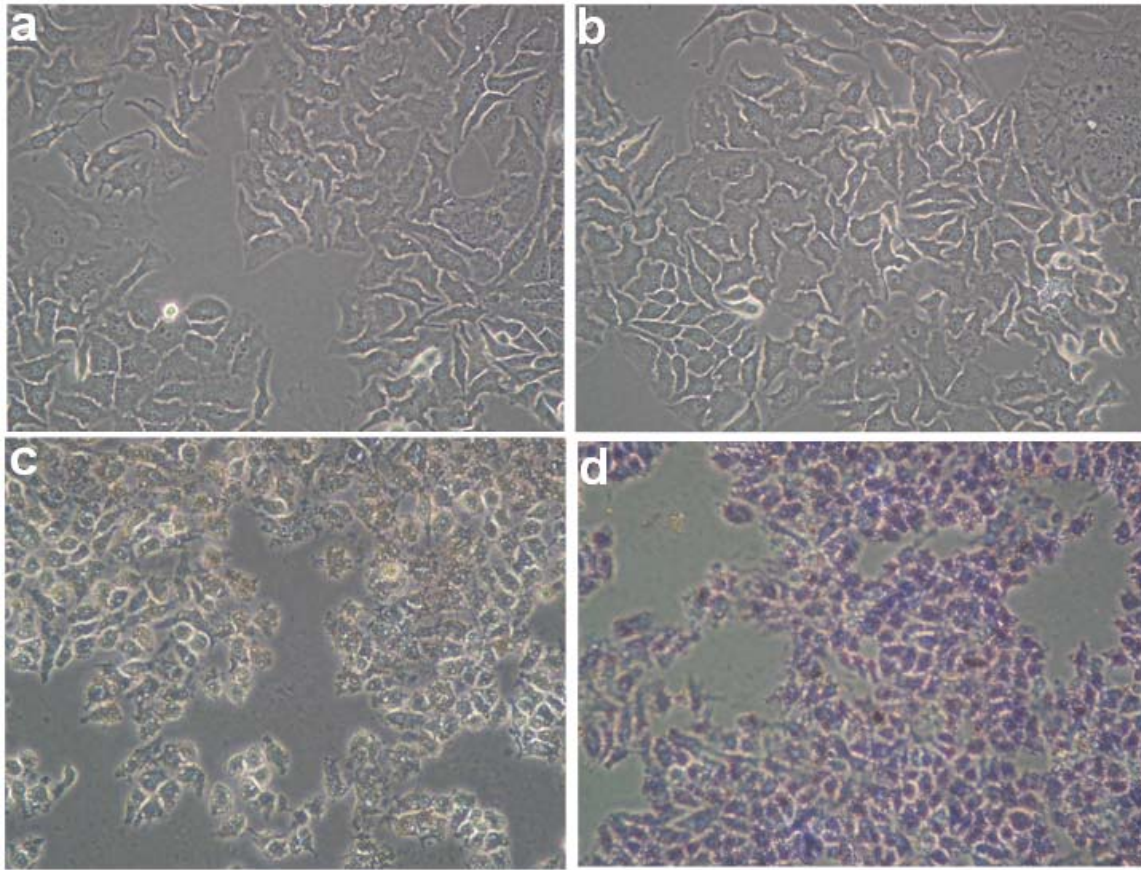


Fig. 6-8: Microscopic image of HeLa cell (a) After incubation control dish cell (b) After incubation with 5 min light irradiation cells (c) After incubation Ag@TiO₂ nanopellet 5 min light irradiation with cells (d) Dead cells confirmed by trypan blue. (Magnification 10x 20)

Fig.6-8 a and b shows a microscopic image of HeLa cells after 24h of incubation only medium containing control dish cell and 5 min irradiation light control dish cell. These two figures showed that the cell morphological structure was mostly no change after 5 min irradiation. Fig.6-8 c shows that the HeLa cells suffer photochemical injury at a 5 min irradiation with Ag@TiO₂ at 24 h incubated. The time threshold for cell death of the HeLa cells is about one third that needed than only TiO₂ treated HeLa cells. The dim white-red color shown in the cell images outside the cell surface is due to the cell died from prolonged exposure of the cells in MEM solution outside the cell incubator. The white-red spot was shown (Fig.6-8 c) the Ag@TiO₂ nanocluster in the cytoplasm was gathered forming larger

aggregates. It can be concluded to particles are taken up or in contact with the cells, because these white-red spots are not observed (Fig.6-8 (a and b)) when nanocluster are not present in the medium. Dead cell was also confirmed by trypan blue indicator (Fig.6-8 d).

It was reported that UV light penetration depth into the tissue is limited to a few fraction of a millimeter [35]. Moreover longer time light irradiation is very painful and burn over the entire body. The Ag@TiO₂ nanocluster treated cancer cells irradiation time is very short with low light power intensity. Low light power of intensity is very good for body. Although Ag@TiO₂ core-shell nanocluster induced the cell death by photochemical conversion and provided heat is insufficient to damage the neighboring normal cells.

However, under dark conditions without light illumination, the cell killing effect does not change (Fig. is not shown) for every measurement using TiO₂ or Ag@TiO₂ core-shell nanocluster. Illumination in the absence of TiO₂ and Ag@TiO₂ nanocluster does not result in the photocatalytic cell killing of HeLa cell. Therefore, the presence of both UV-visible light irradiation and TiO₂ or Ag@TiO₂ nanocluster is necessary for the efficient cell killing.

6.4. Conclusion

We introduce the new simple method to prepare the Ag@TiO₂ core-shell composite nanoclusters. We probed the Ag is metallic condition and TiO₂ shells is uniformly covered on core, determined by XPS, TEM and XRD analysis. We compare the photocatalytic enhancing activity of Ag@TiO₂ and TiO₂ (P25) on cancer (HeLa) cell not been reported in our best of knowledge. The Ag@TiO₂ core-shell nanoclusters have been found to increase the efficiency of interfacial charge-transfer as well as also increase the photocatalytic activity on cancer (HeLa) cell killing.

References

[1] Naoi K.; Ohko Y.; Tatsuma, T. *J. Am. Chem. Soc.* **2004**, *126*, 3664.

- [2] Aliev, F.; Correa-Duarte, M.; Mamedov, A.; Ostrander, J. W.; Giersig, M.; Liz-Marza'n, L. M.; Kotov, N. *Adv. Mater.* **1999**, *11*, 1006.
- [3] Hirakawa T.; Kamat, P. V. *J. Am. Chem. Soc.* **2005**, *127*, 3928.
- [4] Kamat, P. V. *Chem. Rev.* **1993**, *93*, 267.
- [5] Hoffmann, M. R.; Martin, S. T.; Choi, W.; Bahnemann, D. W. *Chem. Rev.* **1995**, *95*, 69.
- [6] Linsebigler, A. L.; Lu, G.; Yates, J. T. Jr. *Chem. Rev.* **1995**, *95*, 735.
- [7] Zang, L.; Macyk, W.; Lange, C.; Maier, W. F.; Antonius, C.; Meissner, D.; Kisch, H. *Chem. Eur. J.* **2000**, *6*, 379.
- [8] Jakob, M.; Levanon, H.; Kamat, P. V. *Nano Lett.* **2003**, *3*, 353.
- [9] Subramanian, V.; Wolf, E. E.; Kamat, P. V. *J. Am. Chem. Soc.* **2004**, *126*, 4943.
- [10] Kamat, P. V. *J. Phys. Chem. B* **2002**, *106*, 7729.
- [11] Subramanian, V.; Wolf, E.; Kamat, P. V. *J. Phys. Chem. B* **2001**, *105*, 11439.
- [12] Subramanian, V.; Wolf, E. E.; Kamat, P. V. *Langmuir* **2003**, *19*, 469.
- [13] Lahiri, D.; Subramanian, V.; T.Shibata; Wolf, E. E.; Bunker, B. A.; Kamat, P. V. *J. Appl. Phys.* **2003**, *93*, 2575.
- [14] Elahifard, Mohammad R.; Rahimnejad S.; Haghighi S.; Gholami, Mohammad R. *J. Am. Chem. Soc.* **2007**, *129*, 9552.
- [15] Liu, Y.; Wang, X.; Yang, F.; Yang, X. *Microporous and Mesoporous Materials* **2008**, *114*, 431.
- [16] Hu, C.; Lan, Y.; Qu, J.; Hu, X.; Wang, A. *J. Phys. Chem. B* **2006**, *110*, 4066.
- [17] Murphy, C. J.; Jana, N. R. *Adv. Mater.* **2002**, *14*, 80.
- [18] Ung, T.; Liz-Marza'n, L. M.; Mulvaney, P. *Langmuir* **1998**, *14*, 3740.
- [19] Awazu, K.; Fujimaki, M.; Rockstuhl, C.; Tominaga, J.; Murakami, H.; Ohki, Y.; Yoshida, N.; Watanabe, T. *J. Am. Chem. Soc.* **2008**, *130*, 1676.
- [20] Bhatkhande, D.S.; Pangarkar, V.G.; Beenackers, A.A. *Journal of Chemical Technology and Biotechnology* **2001**, *77*, 102.

- [22] Wagner, C.D.; Riggs, W.M.; Davis, L.E.; Moulder, J.F. Hand Book of X-ray Photoelectron Spectroscopy, Mullenberg, G.E.; Eds.; Perkin–Elmer Corporation Physical Electronics Division, 1979, pp 112 and 68.
- [22] Cai, R.-X.; Hashimoto, K.; Itoh, K.; Kubota, Y.; Fujishima, A. *Bull. Chem. Soc. Jpn.* **1991**, *64*, 1268.
- [23] McNeil, Scott E. *Journal of Leukocyte Biology*, **2005**, *78*, 585.
- [24] Kohler, N.; Sun, C.; Wang, J.; Zhang, M. *Langmuir* **2005**, *21*, 8858.
- [25] Devika Chithrani, B.; Ghazani, Arezou A.; Warren Chan, C. W. *Nano Letters* **2006**, *6*, 662.
- [26] Matsumura Y.; Maeda, H. *Cancer Research*, **1986**, *46*, 6387.
- [27] Fujishima, A.; Honda, K. *Nature* **1972**, *238*, 37.
- [28] Cai, R.; Kubota, Y.; Shuin, T.; Sakai, H.; Hashimoto, K.; Fujishima, A. *Cancer Research* **1992**, *52*, 2346.
- [29] Jaeger, C. D.; Bard, A. J. *J. Phys. Chem.* **1979**, *93*, 3146.
- [30] Cai, R.; Kubota, Y.; Shuin, T.; Sakai, H.; Hashimoto, K.; Fujishima, A. *Chem. Lett.* **1992**, *3*, 427.
- [31] Linsebigler, Amy L.; Lu, G.; Yates Jr., J. T. *Chem. Rev.* **1995**, *95*, 735.
- [32] Rhoderick, E. H.; Williams, R. H. *Metal-Semiconductor Contacts*, 2nd ed.; Oxford University Press: New York, 1988; p 11.
- [33] Jafiezic-Renault, N.; Pichat, P.; Foissy, A.; Mercier, R. *J. Phys. Chem.* **1986**, *90*, 2733.
- [34] Chen, Y.; Wei, Z.; Chen, Y.; Lin, H.; Hong, Z.; Liu, H.; Dong, Y.; Yu, C.; Li, W. *J. Mol. Catal.* **1983**, *21*, 275.
- [35] Steven L. J.; David R. W.; Steven. M. R., *Photochem. Photobiol.* **1987**, *45*, 637.

CHAPTER 7

NEW SIMPLE SYNTHESIS OF Cu-TiO₂ NANOCOMPOSITE: HIGHLY ENHANCED PHOTOCATALYTIC KILLING OF EPITHELIA CARCINOMA (HeLa) CELLS

Abstract

The metallic Cu nanoparticles on heterogeneous TiO₂ surface have been successfully deposited by the new simple borohydride reduction of copper nitrate salt in water / CH₃CN aqueous mixture under Ar atmosphere. The synthesized Cu-TiO₂ nanocomposite show light absorption in the wide visible region and XPS studies show that the Cu exists in metallic form. The catalytic activity of the Cu-TiO₂ nanocomposite were evaluated by application in the photocatalytic cancer cell-killing (HeLa) under the UV-visible light irradiation. The Cu-TiO₂ nanocomposite showed higher photocatalytic activity than commercial TiO₂ (P25) under the similar experimental conditions. Based on the observed results, a plausible mechanism was proposed. The morphological structure and the surface species of Cu-TiO₂ nanocomposites were determined by using UV-vis absorption spectroscopy, TEM, XPS, XRD, and EDX techniques. The work has been published in Chemistry Letters, 2009, 38(8), 826-827 and communicated paper in Topics in catalysis.

7.1 Introduction

Titanium dioxide is broadly used as a photocatalyst because it is photochemically stable, non-toxic and economical. But, unfortunately the band gap (E_g) of TiO₂ anatase is ~3.2 eV, which corresponds to only a limited portion (3-4%) of the solar spectrum. This relatively large band gap has significantly limited its more widespread application, particularly to indoor situations [1, 2]. Moreover, the efficiency of photocatalytic reaction is limited by the

high recombination rate of electrons and holes in the single component of TiO₂ semiconductor leading to relatively poor photocatalytic efficiency (<5%). Many studies have been devoted to the improvement of photocatalytic efficiency of TiO₂, such as deposition of noble metals [3–8], doping of metal or nonmetal ions [9–13] etc.

The deposition of a noble metal on semiconductor nanoparticles is an essential factor for maximizing the efficiency of photocatalytic reactions. The noble metal (e.g., Pt), which acts as a sink for photoinduced charge carriers, promotes interfacial charge-transfer processes [14-15]. The TiO₂ lattice with metal ions introduces new energy levels in the band gap which can be tailored to extend the photosensitivity in the visible light region. Recent many studies have shown that metal or metal ion doped semiconductor composites exhibit shift in the Fermi level to more negative potentials [16-19]. Such a shift in the Fermi level improves the activity of the composite system and enhances the efficiency of interfacial charge-transfer process.

Metal oxide supported copper nanoparticles are employed as highly active heterogeneous catalyst for the photodegradation of organic pollutants [20, 21]. But a direct relationship between absorption and photodegradation of organic compound could not be found. In some cases, copper oxide or copper ions play a photocatalytic role on photodegradation of organic compounds and the absorption of compounds or intermediate compounds on the catalyst surface may act as poison [22]. Some studies have suggested that observed enhancement of the photocatalytic degradation rates was due to electron trapping by the copper ions leading to the prevention of electron hole-recombination [20, 21]. Despite a large number of studies have been carried out on these Cu / TiO₂ systems, many aspects with regard to the roles of copper species with multivalent states in the photocatalytic reaction remain unclear.

In this communication we report the preparation of highly active photocatalyst of TiO₂ supported copper nanoparticles by a simple chemical method in a mixture of water / CH₃CN.

Moreover, to our best knowledge, we report here for the first time the photocatalytic cancer cell killing using Cu deposited TiO₂ nanocomposite except our one report [23].

7.2 Experimental

The Cu-TiO₂ nanocomposites were prepared by a very simple chemical method. Commercially available TiO₂ (P25) surface (Degussa Corp., diameter ca. 20 nm, surface area 49.9 m²/g) were modified by using hydrochloric acid. The modified TiO₂ colloidal suspension (0.01 M) was prepared by dropwise addition of 0.001 M hydrochloric acid until the pH rose to ca. 3 in 70 vol% acetonitrile-water mixture under vigorous stirring. Then the copper (II) nitrate (Cu (NO₃)₂·3H₂O) salt (0.002-0.05M) were mixed in various molar ratio under Ar atmosphere in a rubber septum capped pyrex conical flask of ca. 154 cm³, maintaining the reaction mixture in suspension by a magnetic stirrer. Under vigorous stirring, freshly prepared sodium borohydride (0.15 M) was drop by drop injected in the reaction medium via syringe. The injection of the borohydride solution was continued (2 to 8 ml) until the color of reaction medium turns to wine-reddish. After completion of reduction, the suspension was centrifuged and the particles were separated followed by washing by methanol and drying in a vacuum.

The UV-visible extinction spectra of the colloid were recorded with a UV-vis spectrophotometer (Shimadzu Corporation, MPS-2000). The average diameters and size distributions of the Cu-TiO₂ nanocomposite particles were obtain from the enlarged photographs of transmission electron micrograph (TEM, JEOL, JEM-3010 VII, operating at 300 kV). The nanocomposite surface condition was also analyzed by Field-emission scanning electron microscope (FE-SEM, Hitachi, S-4100H), crystal structure identification was made by X-ray diffraction (XRD) using a PAN alytical Advance X-ray diffractometer with CuK α (λ =1.5405 nm) radiation. The quantitative chemical composition of the Cu-TiO₂ composite nanocluster surface was also measured using an energy dispersive X-ray spectrometer EDX (Energy Dispersive using X-ray, Philips, XL 30CP) attached to the cold

field SEM. Further evidence for the purity of samples was obtained by X-ray photoelectron spectroscopy (XPS) analysis. The XPS patterns were recorded on an X-ray photoelectron spectrometer (Shimadzu, ESCA-1000) using MgK α X-ray as the excitation source and choose C1s (284.6 eV) as the reference line.

HeLa cells were cultured in a minimum essential medium (MEM) solution with 10% newborn calf serum (NBS) in a humidified incubator with an atmosphere of 5% CO₂ in air at 37 °C. The HeLa cells were plated at a concentration of about 3x10⁵ in 60-mm Petri dishes and allowed to grow for 3 days. The HeLa cell viability was examined by treating with nanocomposite under 24 h incubation in an incubator. A Xenon lamp with heat cut-off and band-pass filters (350-600 nm) with an average intensity 30 mW cm⁻² was used for the light irradiation on HeLa cells. The light power was measured by a spectro radiometer (Model: LS-100, EKO Instrument Co. Ltd.). The images were taken using an Olympus inverted CKX41 microscope with a numerical light field condenser, which delivers a very narrow beam of white light from tungsten lamp on top of the sample. A 40x objective was used to collect the sample images.

7.3 Results and discussion

Cu deposited on TiO₂ surface composite nanocluster in acetonitrile-water mixed solvent were prepared by electrostatic adsorption of [CuNO₃]⁻ ion on TiO₂ surface followed by reduction with NaBH₄. The reaction time acetonitrile was inert to OH scavenger oxidation at the Cu-nanoparticles and TiO₂ interface and unlike water to produce the stable copper nanoparticles at normal temperature under argon gas atmosphere. The aprotic solvent (acetonitrile) with protic solvent (water) is useful for protect the oxidation by OH⁻ ions as protecting solvent for the Cu nanoparticles [23, 24].

Fig. 7-1A shows the absorption spectra of Cu-TiO₂ nanocomposite suspensions show a strong light absorption in wide visible region with clear plasmonic peak. The plasmonic peaks indicate that the Cu is not oxidized, because the absence of plasmonic peak in the

absorption spectra is associated with oxidation of Cu nanoparticles. These result implied that the Cu-TiO₂ nanocomposite may possess excellent photocatalytic performance in the visible-light region. The lower ratios of Cu:TiO₂ resulted in the obscurity of the surface plasmon band due to increase in excessive oxygen on the Cu nanoparticles surface (Fig. 7-1A, spectrum a). At higher ratios of Cu:TiO₂ the plasmon bands of Cu nanoparticles result in increase in the absorbance and broadening due to increase in the particle size (Fig. 7-1A (d and e)). The results (Fig. 7-1A) indicate that by increasing the Cu content, the plasmon absorption of the Cu-TiO₂ nanocomposite increases with increasing Cu molar ratios.

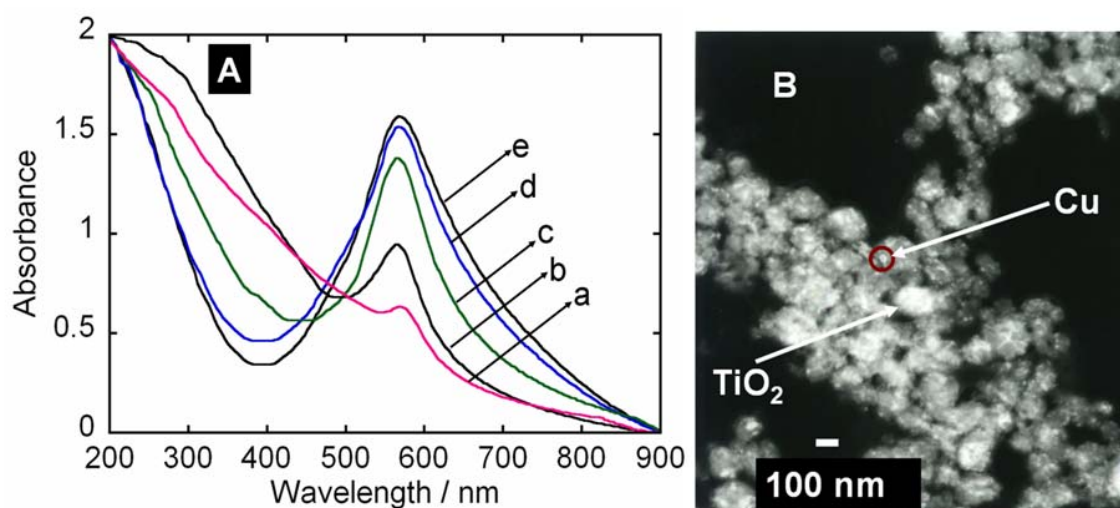


Fig. 7-1: (A) Absorption spectra of Cu-TiO₂ various colloid suspension nanocomposite in water-acetonitrile solution. The Cu:TiO₂ molar ratios were maintained at (a) 0.2:1, (b) 0.5:1, (c) 1:1, (d) 2:1, and (e) 5:1. (B) The Transmission electron microscope picture of Cu-TiO₂ nanocomposites. Cu nanoparticles (white spot) composited with TiO₂ particles are shown in the TEM image (Cu-TiO₂ = 1:1).

The TEM image shows the Cu nanoparticles (white spot) fairly well dispersed on TiO₂ surface with particles overall diameter of 10-100 nm (see also the inset in Fig. 3A).

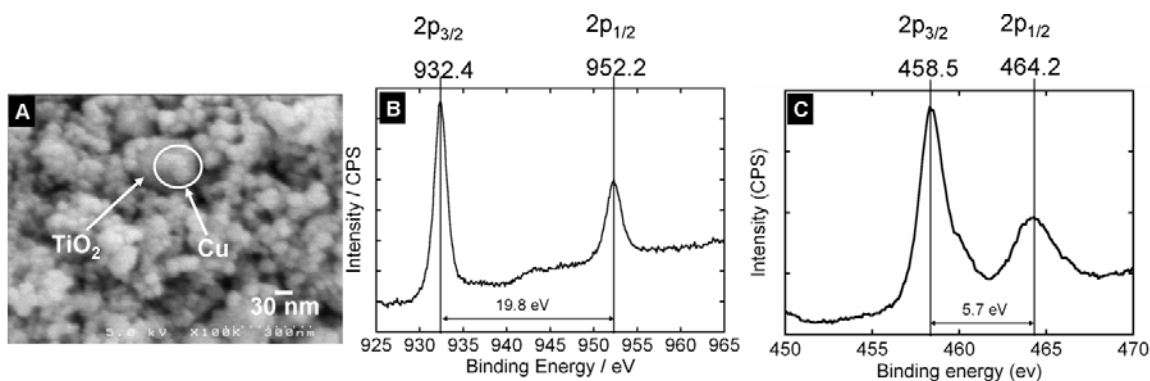


Fig. 7-2: (A) FE-SEM image of the Cu-TiO₂ nanocomposite morphology. The X-ray photoelectron spectroscopic scan survey in the region of (B) Cu 2p (C) Ti 2p of the as prepared Cu / TiO₂ nanocluster (Cu-TiO₂ = 1:1).

As seen from Fig. 7-2, (A) the FE-SEM image of Cu-TiO₂ composite nanocluster shows that the TiO₂ was uniformly covered by Cu nanoparticles. The presence of metallic copper was confirmed by XPS analysis. The peaks observed 2p_{3/2} and 2p_{1/2} at 932.4 and 952.2 eV were ascribed to metallic copper (Fig. 7-2. B). TiO₂ was also determined by XPS as shown in Fig. 7-2 (C). The peaks located at 464.2 eV corresponding to the Ti 2p_{1/2} and another one located at 458.5 eV is assigned to Ti 2p_{3/2}. The splitting between Ti 2p_{1/2} and Ti 2p_{3/2} is 5.7 eV, indicating a normal state of Ti⁴⁺ in as-prepared mesoporous TiO₂ [25].

EDX was employed to obtain the quantitative information on the amount and the distribution of copper and TiO₂ species in the sample. Fig. 7-3 (A) shows the EDX spectra of Cu capped TiO₂ nanoclusters and it was found that the content of Cu: Ti: O (16: 18: 66) (in %) and (35: 30: 35) (wt%) calculated the average by three different selected areas. This result indicates that the molar ratio of Cu and TiO₂ is 1:1.

The wide-angle x-ray diffraction (XRD) patterns of Cu / TiO₂ and pure TiO₂ (P25) nanocluster are shown in Fig. 7-3 (B). Compared with the pure TiO₂, Cu / TiO₂ exhibits new peaks emerged at $2\theta = 43.473^\circ$, 50.375° , 73.997° , 89.934° and 95.578° which can be attributed to the diffraction peaks of (1 1 1), (2 0 0), (2 2 0), (3 1 1) and (222) planes of polycrystalline Cu, (JCPDS, PDF, File No. 00-001-1241) respectively, demonstrating the

formation of metallic Cu. The Cu diffraction peaks are broad and low, suggesting that Cu particles formed on the surface of TiO₂ show small crystalline size. Another faint peak are belonged to the Cu₂O (JCPDS, PDF, File No. 01-071-3645), which means a small part of Cu₂O coexists with copper particles in some samples. May be the coexisting Cu₂O is formed due to the oxidation of some Cu in air.

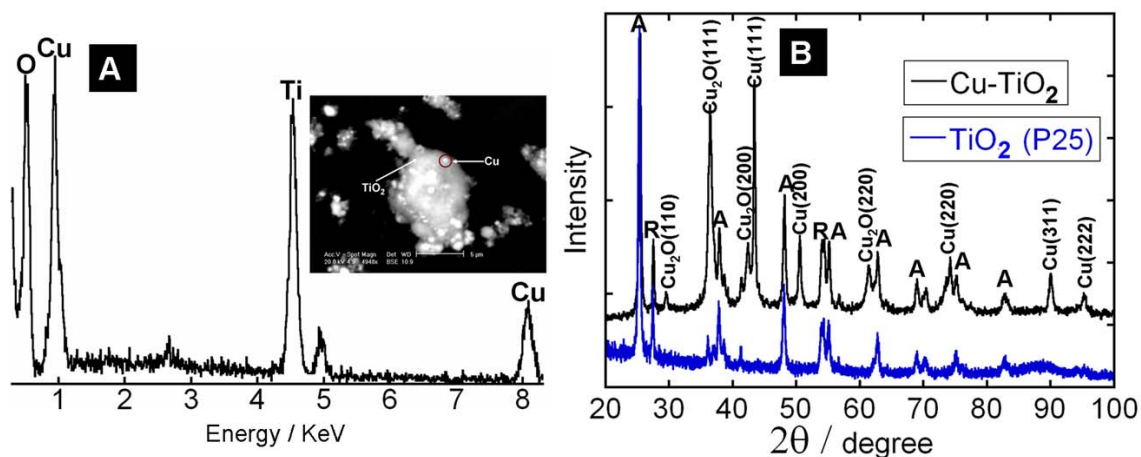


Fig. 7-3: (A) EDX spectra of Cu / TiO₂, the strong Cu and Ti signals in the EDX spectrum indicate that the Cu is metallic and Ti consist of mixed oxides. Insets, cold-field SEM image shows the Cu on the TiO₂ surface (B) XRD pattern of Cu-TiO₂ composite nanocluster, confirming the formation of pure metallic copper and TiO₂ (P25) semiconductor composite nanocluster within some partial Cu₂O.

Controlled experiments using in the absence of Cu-TiO₂ and TiO₂ were done for cancer cell killing under UV-visible light irradiation. In the scale bar of Fig. 4A and 4B, 100 means the number of living cells in control dish. To compare the cell killing enhancing viability TiO₂ (P25) to Cu-TiO₂ nanoparticles, the cell dishes incubated with different amount of MEM content colloidal composite nanoparticles solution (4, 8, 12, 16, and 20 μL). The cells were stained by the trypan blue indicator; the dead cell accumulates the dye resulting in blue color, whereas the live cells have no color. The cell viability was determined as the percentage of the number of the unstained cells against that of the control dish cells.

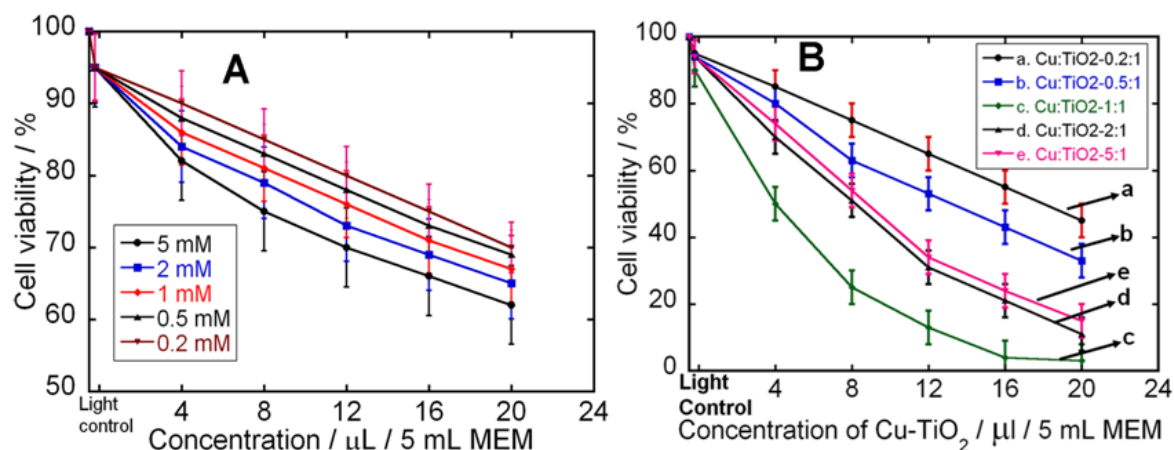


Fig. 7-4: Surviving fraction of HeLa cells incubated in MEM medium containing (A) TiO_2 and (B) Cu-TiO_2 nanocomposite. The 100% show the control dish and viability was calculated by the number of live cell percentage against the control dish cell. Bars represent the region of measured 3 times data average and the points represent the mean value from three measurements.

In absence of light, the cells were found to be mostly viable ca. 90-100% under the incubated condition with the nanocluster (Fig. 7-4A and 4B) colloidal solutions. However, after 5 min of light irradiation, the amount of cell killing was maximum 40% in 20 μL MEM content TiO_2 treatments (Fig. 7-4A). The destructive cell killing effect was found in the presence of Cu-TiO_2 nanocomposite with light irradiation; maximum cells were killed rapidly. The 20 μL MEM content of Cu-TiO_2 (1:1 molar ratio) with 5 min light irradiation 100% cell were killed, whereas in same concentration of TiO_2 treatment, 40 % cells were killed as shown in Fig. 7-4A and 4B. The error bars in Fig. 4 represent the maximum and minimum value of each experiment.

In the lower molar ratio region (ratio < 1:1), some Cu_2O particles may be formed and may cover the surface of TiO_2 , which may lead to decrease in the photocatalytic cytotoxicity (Fig. 7-4B). At the optimum ratio (1:1), the photothermal killing due to the plasmonic absorption (Fig. 7-1A) of Cu nanoparticles may also contribute to the cytotoxicity. However, in the higher molar ratio region (ratio > 1:1), excessive Cu

nanoparticles obstruct the light absorption by TiO_2 , which may also lead to decrease in the photocatalytic cell killing (Fig. 7-4B).

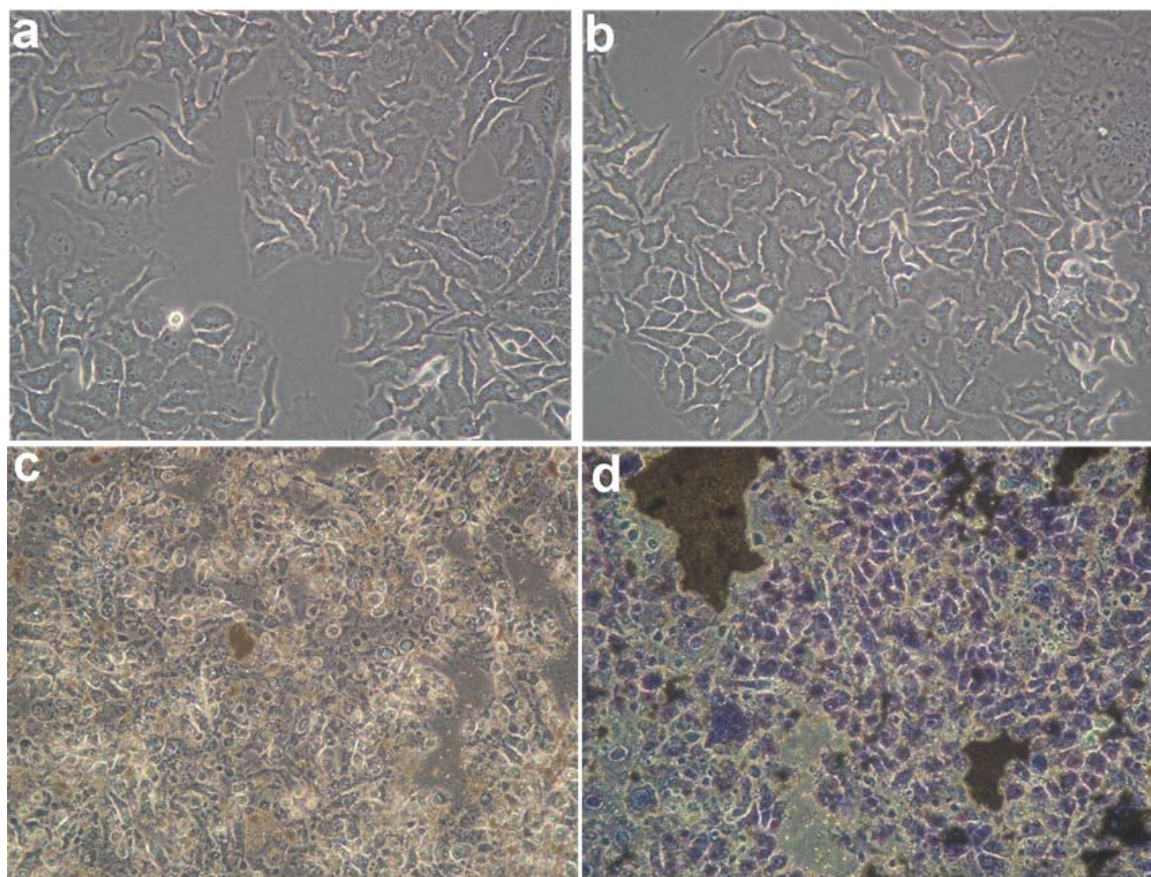
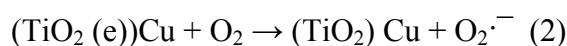
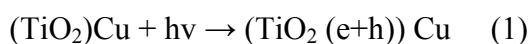


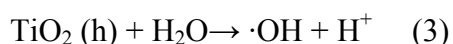
Fig. 7-5: Microscopic images of HeLa cells (Magnification 200). (a) With neither Cu–TiO₂ nanocomposites nor light. (b) After 5-min light irradiation without the nanocomposites. (c) After 5-min light irradiation with the nanocomposite. (d) Dead cells stained with trypan blue.

Fig. 7-5 shows microscopic images of HeLa cells before (a) and after (b)–(d) light irradiation. Figures 4a and 4b show that the cell morphology is largely unchanged after 5-min irradiation. Fig.7-4c shows that the HeLa cells suffer severe photochemical injury under 5-min irradiation with the Cu–TiO₂ nanocomposite. After light irradiation, cells were stained with trypan blue; cells stained blue (Fig. 7-5d) indicated cell death.

In the case of noble metal such as Cu, an electron from photoexcited TiO₂ is transferred to Cu and then initiating the redox reactions at the interface. The transfer of electrons from the excited TiO₂ into Cu continues until the systems attain equilibration. Since the electron accumulation increase the Fermi level of the composite shifts closer to the conduction band of the semiconductor [17-19, 26]. After the Fermi level equilibration, the photoinduced electrons can transfer to the surface of Cu nanoparticles and can easily reduce the dissolved O₂ as shown in Fig. 7-6. It is well known that molecular oxygen accepts the photogenerated electrons to form the superoxide anion (O₂^{•-}) as shown in reaction (2). Generally, O₂^{•-} is less reactive and has a short lifetime and therefore the role of O₂^{•-} in succeeding reactions is not understood well [27].



The photogenerated holes on the TiO₂ surface can react with water to produce powerful oxidative radicals such as ·OH and HO₂· via reactions (3) and (4). While O₂^{•-} is not considered so reactive and further reduced slowly to H₂O₂ as shown in reaction (5) [28]. H₂O₂ is more reactive than O₂^{•-} and is easily decomposed to ·OH as shown in reaction (6) [29].



The highly oxidizable hydroxyl radicals (·OH), hydrogen peroxide (H₂O₂) and superoxide radicals (O₂^{•-}) which are reported to be formed on the surface of photoexcited TiO₂ particles can be expected to be toxic to cells [27].

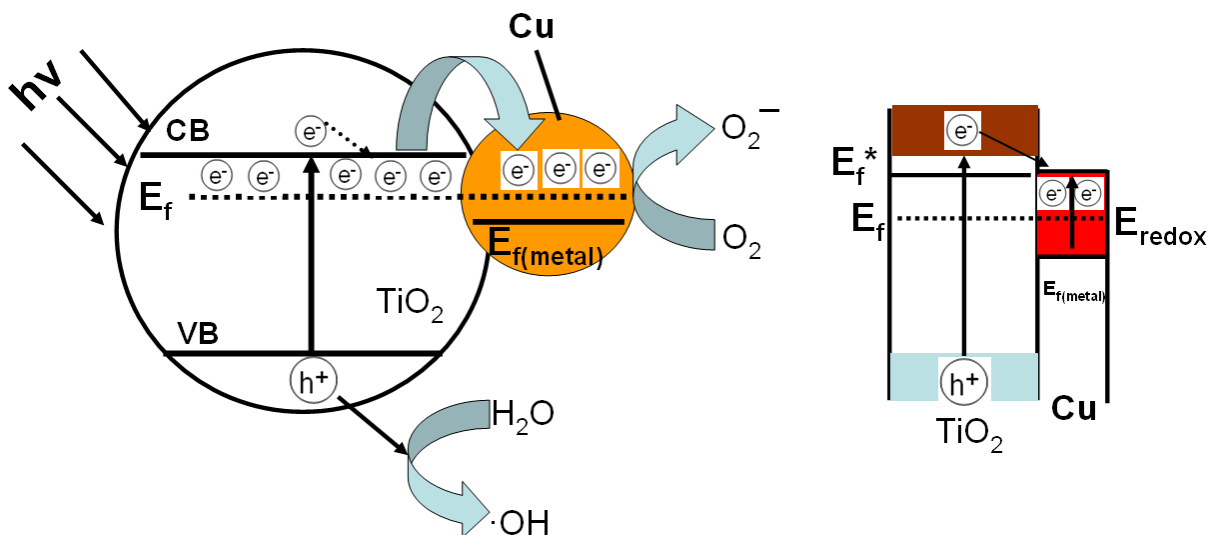


Fig. 7-6: Interfacial charge separation process of Cu / TiO₂ nanoclusters under the irradiation of UV-visible (350-600 nm) light. Fermi level equilibration of Metal-semiconductor nanocomposite with the redox reaction after light irradiation. E_f* (Apparent Fermi level)

The oxidation of the photogenerated holes and oxidizing radicals directly at the semiconductor / metal interface is an important process. It can be a major factor in determining the overall photocatalytic efficiency of metal semiconductor nanocomposites. After excitation the electron migrates to the metal where it becomes trapped and electron-recombination is suppressed. The hole is then free to diffuse to the semiconductor surface where oxidation of organic species can occur [30].

In order to confirm the reaction mechanism, under dark conditions without light illumination, the cell killing effect does not change (data not shown) for every measurement using TiO₂ or Cu / TiO₂ nanocluster. Illumination in the absence of TiO₂ and Cu / TiO₂ nanocluster does not result in the photocatalytic cell killing of HeLa cell. Therefore, the presence of both UV-visible light irradiation and TiO₂ or Cu / TiO₂ nanocluster is necessary for the efficient cell killing.

7.4 Conclusions

We have shown that under UV-visible light irradiation, the deposition of Cu nanoparticles on TiO₂ induces a significant photocatalytic effect. Deposition of Cu on TiO₂ surface may give better results for photocatalytic cell killing. Comprehensive studies are underway in our laboratory to further reveal the mechanism for the synergy effect of Cu nanoparticles enhancing the photocatalytic activity of TiO₂.

References

- [1] M. Anpo, M. Takeuchi, *J. Catal.* **2003**, *216*, 505.
- [2] A. Dawson, P. V. Kamat, *J. Phys. Chem. B* **2001**, *105*, 960.
- [3] M. Bowker, D. James, P. Stone, R. Bennett, N. Perkins, L. Millard, J. Greaves, A. Dickinson, *J. Catal.* **2003**, *217*, 427.
- [4] J.M. Herrmann, J. Disdier, P. Pichat, *J. Catal.* **1988**, *113*, 72.
- [5] E. Stathatos, P. Lianos, P. Falaras, A. Siokou, *Langmuir* **16** (2000) 2398.
- [6] T.G. Schaaff, D.A. Blom, *Nano. Lett.* **2** (2002) 507.
- [7] B. Sun, A.V. Vorontsov, P.G. Smirniotis, *Langmuir* **2003**, *19*, 3151.
- [8] S. Kim, W. Choi, *J. Phys. Chem. B* **2002**, *106*, 13311.
- [9] S. Jeon, P.V. Braun, *Chem. Mater.* **2003**, *15*, 1256.
- [10] S. Klosek, D. Raftery, *J. Phys. Chem. B* **2001**, *105*, 2815.
- [11] A. Patra, C.S. Friend, R. Kapoor, P.N. Prasad, *Chem. Mater.* **2003**, *15*, 3650.
- [12] J. Premkumar, *Chem. Mater.* **2004**, *16*, 3980.
- [13] J.D. Bryan, S.M. Heald, S.A. Chambers, D.R. Gamelin, *J. Am. Chem. Soc.* **2004**, *126*, 11640.
- [14] P. V. Kamat, *Chem. Rev.* **1993**, *93*, 267.
- [15] J. A. Bard, *J. Phys. Chem.* **1982**, *86*, 172.
- [16] G. Burgeth, H. Kisch, *Coord. Chem. Rev.* **2002**, *230*, 40.
- [17] A. Wood, M. Giersig, P. Mulvaney, *J. Phys. Chem. B* **2001**, *105*, 8810.

- [18] M. Jakob, H. Levanon, P. V. Kamat, *Nano Lett.* **2003**, 3, 353.
- [19] V. Subramanian, E. E. Wolf, P. V. Kamat, *J. Phys. Chem. B* **2003**, 107, 7479.
- [20] M. Bideau, B. Claudel, L. Faure, M. Rachimoellah, *Chem. Eng. Commun.* **1990**, 93, 167.
- [21] K.I. Okamoto, Y. Yamamoto, H. Tanaka, M. Tanaka, A. Itaya, *Bull. Chem. Soc. Jpn.* **1985**, 58, 2015.
- [22] D. Hufschmidt, D. Bahnemann, J.J. Testa, C.A. Emilio, M.I. Litter, *J. Photochem. Photobiol. A: Chem.* **2002**, 148, 223.
- [23] M. Abdulla-Al-Mamun and Y. Kusumoto, *Chem. Lett.* **2009**, 38, 826.
- [24] M. Abdulla-Al-Mamun, Y. Kusumoto, M. Muruganandham, *Mater. Lett.* **2009**, 63, 2007.
- [25] C. D. Wagner, W. M Riggs, L.E Davis, S.F Moulder, G.E. Mullenberg, Handbook of x-ray photoelectron spectroscopy (Perkin-Elmer corporation, Physical Electronics Division, New York, 1979).
- [26] V. Subramanian, E. E. Wolf, P. V. Kamat, *J. Am. Chem. Soc.* **2004**, 126, 4943.
- [27] R. Cai, Y. Kubota, T. shuin, H. Sakai, K. Hashimoto, A. Fujishima, *Cancer Research* **1992**, 52, 2346.
- [28] J.R. Harbour, J. Tromp, M. L. Hair, *Can. J. Chem.* **1985**, 63, 204.
- [29] M. Fujihira, Y. Satoh, T. Osa, *Nature*, **1981**, 293, 206.
- [30] Amy L. Linsebigler, G Lu, Jr. John T. Yates, *Chem. Rev.* **1995**, 95, 735.

CHAPTER 8

MINERALIZER-ASSISTED SHAPE-CONTROLLED SYNTHESIS, CHARACTERIZATION AND PHOTOCATALYTIC EVALUATION OF CdS MICROCRYSTALS

Abstract

High quality, well crystallized, single crystal, wurtzite CdS hexagonal microtowers (with and without tubular structure) and CdS with octahedral geometry were successfully synthesized by tuning the solvent ratio of water and ethanol for the first time on a large scale without using any catalysts or templates. The products were characterized by X-ray diffraction (XRD), energy-dispersive X-ray spectrometry (EDX), transmission electron microscopy (TEM) and field emission scanning electron microscopy (FE-SEM). CdS with microtowers, octahedral geometry and hexagonal plates was formed by thermal decomposition of cadmium thiocyanate at 400 °C under open atmospheric conditions. The influence of solvent, initial precursor concentration, decomposition temperature and time on the morphology of CdS was investigated and the results were discussed. The XRD results showed that the cadmium thiocyanate complex is completely decomposed into CdS at 300 °C for 2 h and the wurtzite phase was formed under all experimental conditions, which open a door for well crystallized, single phase CdS synthesis on a large scale. The diffuse reflectance spectra showed that CdS microtowers have strong visible light absorption compared with the octahedral geometry, revealing the existence of a profound shape-property relationship of CdS. The CdS microtowers with a Pt co-catalyst showed a high rate of photocatalytic hydrogen production from water containing 0.1 M Na₂S and 0.1M Na₂SO₃ as sacrificial reagents under visible light irradiation ($\lambda \geq 400$ nm). The possible growing

mechanism of various types of the CdS morphology was also discussed. The work has been published in *Journal of Physical Chemistry C*, 2009, 113(45), 19506-19517.

8.1. Introduction

Semiconductor nanostructures have been attracting attention because of their unique optical, mechanical, electronic and catalytic properties, which are highly dependent on size and shape which differ from those of their bulk counterparts. CdS has attracted considerable interest in optoelectronic applications because of its band gap energy (2.5 eV) in the visible region and due to its nonlinear properties; it is now widely used for photoelectric conversion in solar cells, light emitting diodes for flatpanel displays, lasers and thin film transistors [1–5]. A number of methods have been explored to fabricate CdS crystals, such as thermal evaporation, hydrothermal method, chemical vapor deposition process, template method, thermal decomposition method and solvothermal process [6-11]. Most of the synthetic schemes described above required the use of rather complicated procedures or the pre-synthesis of cluster precursors. Therefore it is necessary to develop a very simple procedure in large scale synthesis and it remains as a challenge for chemists and material scientists. It was suggested that the size, morphology and structure of nano/micro crystallites are very important factors for determining the optical and electronic properties of CdS nanocrystals. CdS usually exists in the cubic sphalerite and the hexagonal wurtzite phase. At room temperature and atmospheric pressure the bulk wurtzite structure is in the thermodynamically stable phase under normal conditions. The intrinsic energy difference between these two phases of CdS is very small, so the controlled growth of CdS nanocrystals in only one phase at a time is difficult to achieve [12-14]. Cadmium ions may coordinate with many organic and inorganic ligands which are used to prepare CdS nanomaterials. For example, cadmium sulfide and zinc sulfide nanowires were prepared using cadmiumdiethyldithiocarbamate, $\text{Cd}(\text{S}_2\text{CNEt}_2)_2$, and zincdiethyldithiocarbamate, $\text{Zn}(\text{S}_2\text{CNEt}_2)_2$, respectively, as precursors in a gold nanocluster-catalyzed vapor-liquid-solid

growth process.⁸ Water soluble CdS quantum dots were prepared from a [(2,2-bipyridine)Cd(SC{O}Ph)₂] complex by simply refluxing in an aqueous solution [15]. The thiocyanate ion, (SCN⁻), is an interesting and widely studied ligand, which coordinates with a variety of metal ions. It may form either thiocyanato (M-SCN) or isothiocyanato (M-NCS) complexes which are further decomposed into metal sulfides with high purity [16]. Cadmium thiocyanate complex formation and its thermal decomposition in the presence of air are shown in the following chemical reaction.



One of the most favored photocatalysts is CdS by itself or as a mixture with other semiconductors such as TiO₂ and these semiconductor photocatalysts perform better when loaded with Pt cocatalysts [17, 18]. The CdS-based photocatalysts are known to be the most active in the hydrogen production from water. Unfortunately, they undergo severe photocorrosion under irradiation unless there exist hole scavengers in the solution (as sacrificial reagents) such as sulfides (S²⁻) and sulfites (SO₃³⁻) [19]. In this work, we have synthesized CdS microtowers with and without tubular structure, octahedral geometry and hexagonal plates by using thermal decomposition of cadmium thiocyanate under open atmospheric conditions. Cadmium thiocyanate complexes had been prepared in water and in other organic solvents by using various cadmium and thiocyanate salts as starting precursors. Moreover, many studies were done on various aspects of cadmium thiocyanate complex formation [20-22]. Earlier studies confirmed that the cadmium thiocyanate complex could be decomposed at 300 °C resulting in CdS with other byproducts which are mentioned in equation 1 and 2. However, we for the first time fabricated various morphological CdS microcrystals under various experimental conditions by using the thermal decomposition of cadmium thiocyanate coordination complexes. The decomposition temperature and solvents were crucial factors in defining the shapes of the CdS microstructures. To the best of our

knowledge, no reports were available for the preparation of CdS microtowers and octahedral geometric CdS and their application to hydrogen production.

8.2. Experimental Section

Cadmium nitrate tetrahydrate, anhydrous cadmium chloride, cadmium acetate dehydrate, potassium thiocyanate, ethanol, methanol and 1-propanol were purchased from Wako Chemical Co. Ltd. All chemicals were of analytical grade and used as received without further purification. For all experimental works, deionized and doubly distilled water was used. Cadmium nitrate tetrahydrate and potassium thiocyanate were used as cadmium and thiocyanate sources, respectively. In a typical experiment, 13.72 g of $\text{Cd}(\text{NO}_3)_2 \cdot 4\text{H}_2\text{O}$ were dissolved in 25 mL water and then 50 mL of ethanol (99.99%) were added under constant stirring (solution 1); 16.71 g of potassium thiocyanate were separately dissolved into another 25 mL of water (solution 2). Under magnetic stirring, solution 2 was then added drop by drop (30-45 min) into solution 1. The solution is stirred for another 30 minutes. The solid (KNO_3) formed during the reaction was removed by filtration and then clear solution was evaporated in a hotplate until it becomes a semi-solid which is transferred into a porcelain dish for the decomposition process. Similar experiments were also performed by changing the solvents or solvents ratios under identical conditions. The thermal decomposition of the final residue was carried out under open atmospheric conditions at 300 °C and 400 °C for 2 h. After decomposition at desired time, the oven was allowed to cool down to room temperature naturally and then the samples were washed with plenty of water and methanol and dried in an oven at 110 °C for 30 min. Various amounts of Pt-loaded CdS were prepared by a photodeposition method. The required weight of prepared CdS powder was added into a Pyrex flask of 50 mL containing a mixed solvent of $\text{H}_2\text{O}/2$ -propanol (70:30 v/v) including a required amount of H_2PtCl_6 and the sample solution was irradiated by a Hg lamp under the N_2 gas flow. Before irradiation, the mixture was

ultrasonically dispersed for 5 min and the catalyst was maintained in suspension by means of magnetic stirring. Photoreduction of H_2PtCl_6 to Pt particles took place and Pt was deposited on the CdS surface. After irradiation, the filtered Pt loaded samples were washed with distilled water and ethanol and dried in a desiccator. The sample is denoted as Pt/CdS. For hydrogen production measurements, about 30 mg of CdS photocatalyst were dispersed by a magnetic stirrer in 40 mL of aqueous solution containing 0.1 M Na_2SO_3 and 0.1 M Na_2S as sacrificial reagents in a cylindrical flask. The top of the flask was sealed with a silicone rubber septum. To remove oxygen gas, the suspended solution was bubbled with Ar gas (about 5 ml/min) for 1h with stirring. The light irradiation was carried out under an Ar atmosphere with stirring. The evolved gas was sampled through the silicone rubber septum by using a locking-type syringe at a constant time interval and the sampled gas was quantitatively analyzed by a gas chromatograph (detector; thermal conductivity detector (TCD), column packing; molecular sieve 5 Å, carrier gas; Ar). A xenon lamp (Ushio, 500 W) was also used as a visible light source with an L42 cut-off filter. The XRD patterns were recorded using a X'Pert PRO PAN analytical diffractometer over the scanned angle from 10 ° to 100 ° at a scanning rate of 5 ° per minute. High resolution transmission electron microscope (HR-TEM) images were recorded using JEOL JEM-2100 HR-TEM which also attached EDX analysis. Samples for HR-TEM were prepared by ultrasonically dispersing the catalyst into absolute ethanol, then placing a drop of this suspension onto a copper grid and dried in air. The working voltage of TEM was 200 kV. Elemental analysis was carried out using Vario EL III CHNOS elemental analyzer (Germany). The X-ray photoelectron spectra were collected on an ESCA-1000 X-ray photoelectron spectrometer (XPS), using Mg $K\alpha$ X-ray as the excitation source. The morphology of the catalyst was examined using a Hitachi S-4800 FE-SEM. Prior to FE-SEM measurements, the samples were mounted on the carbon platform. The plate containing the sample was coated with platinum by using a magnetron sputter and then placed in the SEM for the analysis with

desired magnifications. UV-visible diffuse reflectance spectra were recorded using a Shimadzu MPS-2000 spectrophotometer and barium sulfate as a standard.

8.3. Results and discussion

Initially, the thermal decomposition of the cadmium thiocyanate complex was carried out at 300 °C and 400 °C under the open air and nitrogen atmospheric conditions. The decomposition under both conditions results in CdS and its XRD patterns are quit similar as shown in Fig. 8-1. The XRD results clearly confirm the suitability of open air atmospheric conditions for the CdS preparation. However, the FE-SEM analysis showed that the morphology of CdS formed under nitrogen atmospheric conditions at 300 °C for 2 h was different from one observed under the open atmospheric conditions (see Fig. 8-4a and 8-4b) and no morphological changes were noted at 400 °C. Thus, for the large scale preparation the open atmospheric condition would be desirable and therefore all decomposition was carried under open air atmospheric conditions. The synthesized CdS microcrystals were analyzed by using XRD, FE-SEM, TEM and other required analytical techniques. The EDX microanalysis demonstrates that the crystal consists of Cd and S elements. Moreover, according to the quantitative analysis of EDX, the Cd: S molar ratio is about 1:1.02, which is consistent with stoichiometric ratio of CdS.

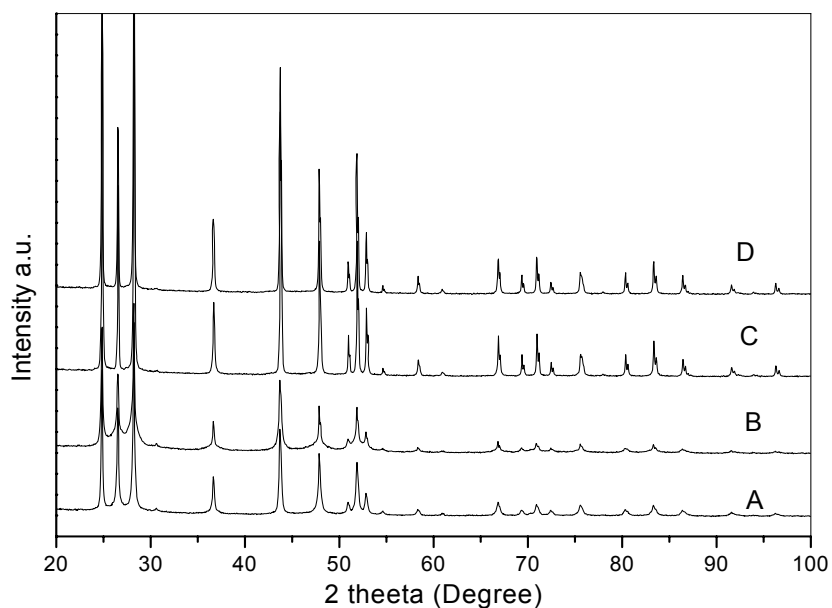


Fig. 8-1a: XRD of CdS synthesized under (A) nitrogen atmospheric condition at 300 °C for 2 h, (B) open air atmospheric condition at 300 °C for 2 h, (C) nitrogen atmospheric condition at 400 °C for 2 h and (D) open air atmospheric condition at 300 °C for 2 h.

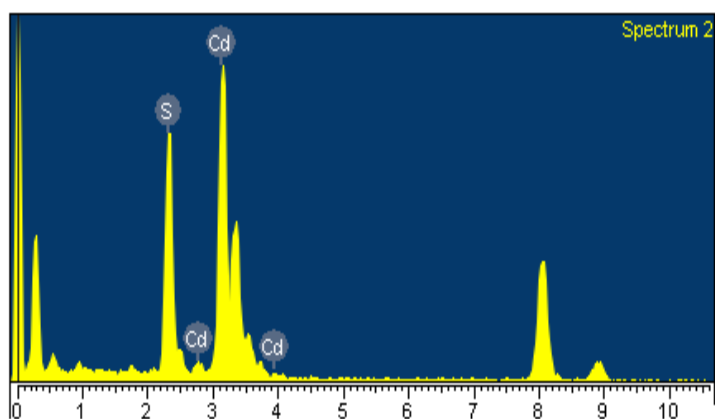
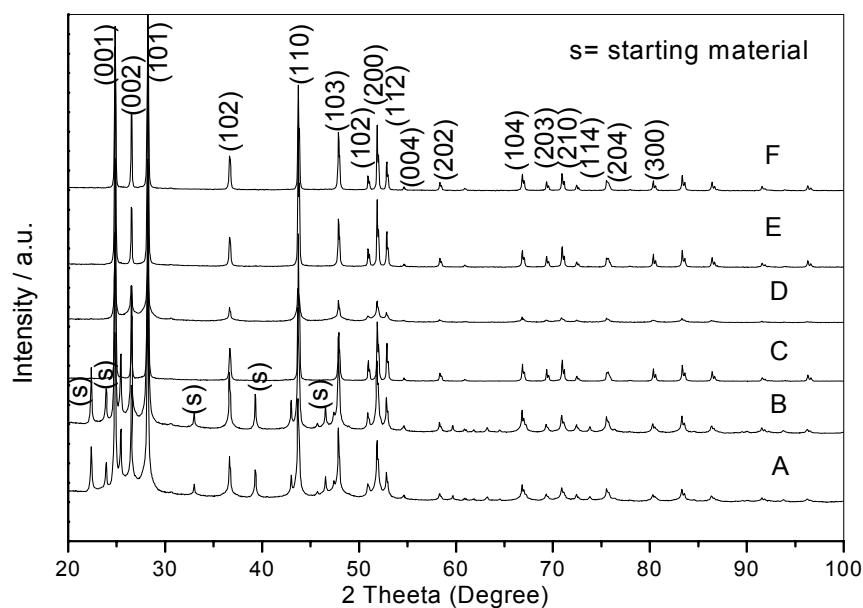


Fig. 8-1b. EDX analysis of CdS at 400 °C for 2 h.

The XRD patterns of synthesized CdS microcrystals in different time at 300 °C and at 400 °C are shown in Figure 2.

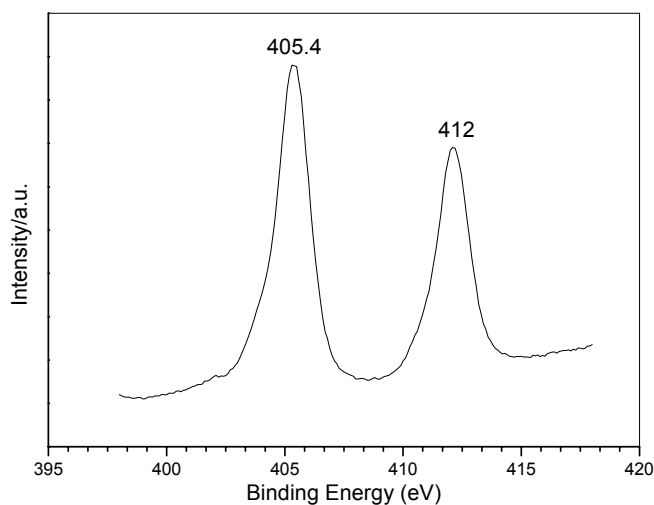


(a)

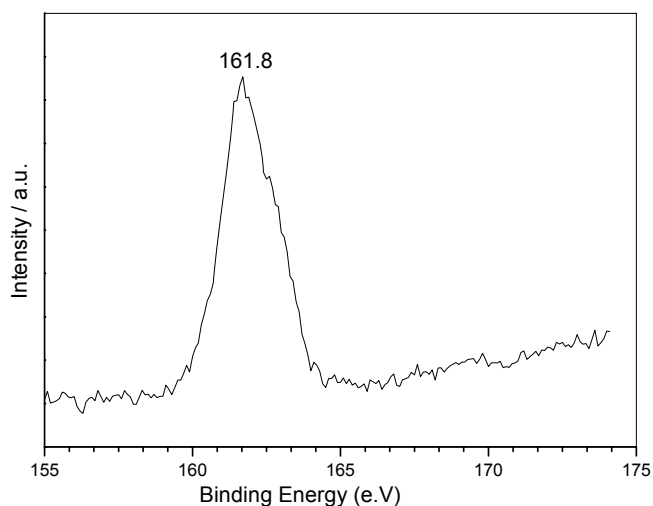
Fig. 8-2. (a) XRD of CdS synthesized at various decomposition time and temperature. Decomposition at 300 °C for (A) 30 min, (B) 1 h and (C) 2 h and the decomposition at 400 °C for (D) 30 min, (E) 1 h and (F) 2 h.

The XRD results confirm that the cadmium thiocyanate complex is completely decomposed into pure CdS after 2 h at 300 °C. At the early stage of decomposition periods (30 min, 1 h), in addition to CdS peaks, some additional peaks were noted at 22.4 °, 23.9 °, 25.4 °, 33°, 39.3 °, 43.6 °, 46.5 °, 59.7 °, 63.2 ° and 73.8 ° which are suspected to arise from the starting materials. Thus, all these peaks are less intense and completely disappeared after 2 h. Moreover, due to colloidal nature of the cadmium thiocyanate complex we were not able to analyze XRD and therefore we could not compare with the synthesized CdS. Nevertheless, pure CdS were formed even at the early stages of decomposition time (30 min, 1 h) at 400 °C. No other impurity peaks appeared in XRD, which indicates the formation of pure CdS, being in good agreement with XPS results. All XRD peaks in Fig. 8-2 can be assigned to the hexagonal wurtzite with the lattice parameters of $a = 4.14 \text{ \AA}$ and $c = 6.72 \text{ \AA}$ [S. G.P63mc (186)] (JCPDS 02-0549). The characteristic peaks at 28.3 °, 43.9 ° and 51.9 ° corresponds to (101), (110) and (112) planes of wurtzite CdS. The d spacing values of peaks at 26.5 °, 43.9

$^{\circ}$ and 52.18° imply the absence of cubic phase CdS. Generally, the CdS fabrication at high temperatures results in wurtzite-phase crystals. The XPS analysis has been performed in order to understand the chemical nature of synthesized CdS. The XPS results of CdS microtowers synthesized at 400°C for 2 h are presented in Fig. 8-3. The XPS results confirmed the absence of possible impurities like potassium. However, a very small amount of nitrogen (0.4%) and carbon (0.2%) impurities were noted in the elemental analysis. The Cd 3d XPS peaks found at 405.4 eV and 412 eV indicated cadmium presented as cadmium sulfide. Similarly, the S 2p peak found at 161.8 eV implies that sulfur exists as sulfides. No additional peaks were observed at 165 eV to 170 eV, which clearly demonstrated absence of an oxidized form of sulfur. The observed XPS values are in good agreement with earlier reports [23,24]. Therefore, this synthetic methodology is the suitable for single phase, well crystallized CdS preparation.



(a)



(b)

Fig. 8-3: XPS spectra of CdS microtower synthesized under open atmospheric conditions at 400 °C for 2 h (A) Cd 3d spectra and (b) S 2p spectra.

8.3.1. Influence of decomposition temperature and time

In the studies on decomposition temperature (300 °C and 400 °C) and reaction time dependence of the growth of CdS microcrystals, the growing time was kept at 2 h, 5 h and 10 h. The complete decomposition of cadmium thiocyanate complex at 300 °C for 2 h yields porous aggregates as shown in Fig. 8-4b. The resulting porous aggregates morphology was not affected by further prolonged decomposition time (10 h) which suggested the stability of porous aggregates. However, some interesting morphology was noted when the decomposition was carried out at 400 °C. The thermal decomposition at 400 °C for 2 h results in a mixture of two types of microtowers (see Fig. 8-4c), i.e., one is with tubular structure and another one is without tubular structure as shown in Fig. 8-4c1

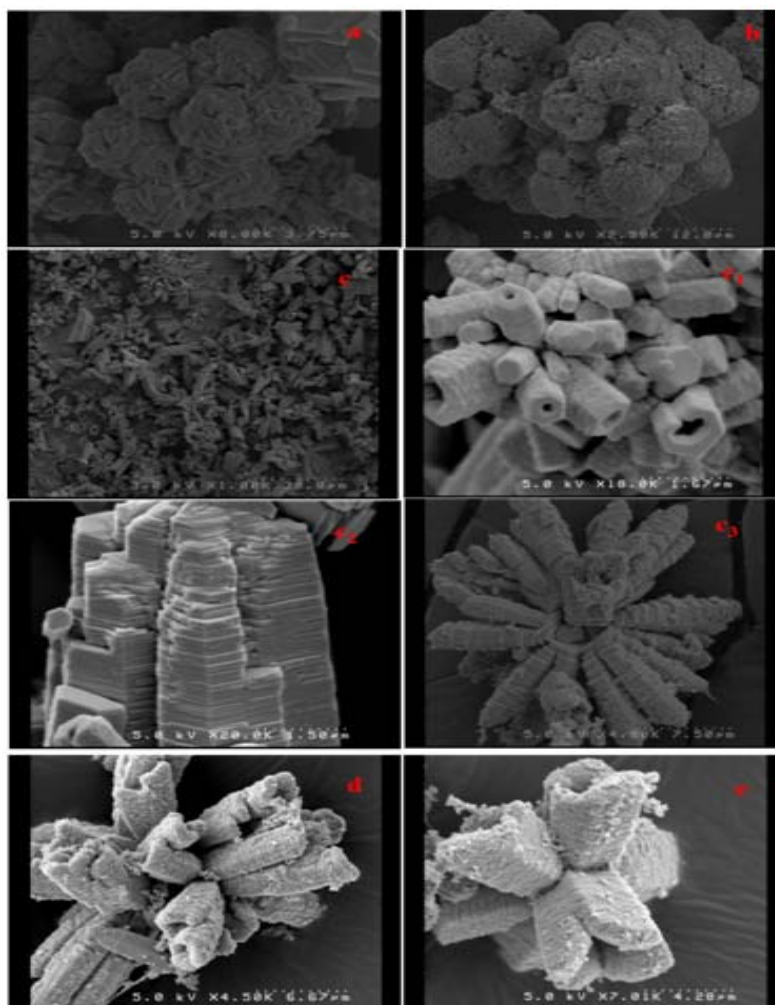


Fig. 8-4: FE-SEM pictures of CdS synthesized (a) under nitrogen atmospheric conditions at 300 °C for 2 h and under open air atmospheric conditions (b) at 300 °C for 2 h, (c) at 400 °C for 2 h; (c₁) tubular micro tower formed at 400 °C for 2 h, (c₂) hexagonal plate stacked microtower formed 400 °C 2 h, (c₃) 3D pyramid like shaped CdS formed at 400 °C for 2 h and (d) at 400 °C for 5 h (e) at 400 °C for 10 h.

and 4c₂, respectively. The pores of the tubular microtower are wide, not uniform and micrometer in size. The tubular microtower was covered by smooth and rough surfaces at early stage of decomposition. However, when the decomposition time was further increased to 2h, the entire tubular tower surface became smooth and the pore width became contractive compared with ones formed at the early stages. The percentage of tubular

morphology is higher than that of hexagonal plate-stacked morphology. It is interesting to note that the microtowers without tubular morphology were assembled with ordered thick hexagonal plates stacked together. The resulting towers were further connected to each other yielding 3D pyramid like morphology as shown in Fig. 8-4c3. The CdS hexagonal microtower morphology is noted for the first time though reported in other inorganic materials [25,26]. When the decomposition time was further increased to 5h and 10h, the morphology of the noted microtowers was distorted and the degree of distortion increased with increasing decomposition time as shown in Fig. 8-4d. The morphology of the microtowers noted after 10 h was porous and the pore width was very wide and the length of the towers was short as compared to one noted after 2 h as seen in Fig. 8-4e. The XRD results shown in Fig. 8-5 confirmed the good stability of CdS even with prolonged thermal treatment and does not show possible new impurities like CdO or CdSO₄. Thus, prolonged calcination in fact will anneal the microcrystals, in which there occur atom exchange, migration and reconstruction, causing increase of the size of the nanoparticles and the fast growth rate at high temperature results in the deterioration of the microtower morphology [27]. The above results confirmed that 2 h decomposition time is suitable for the hexagonal tubular tower fabrication.

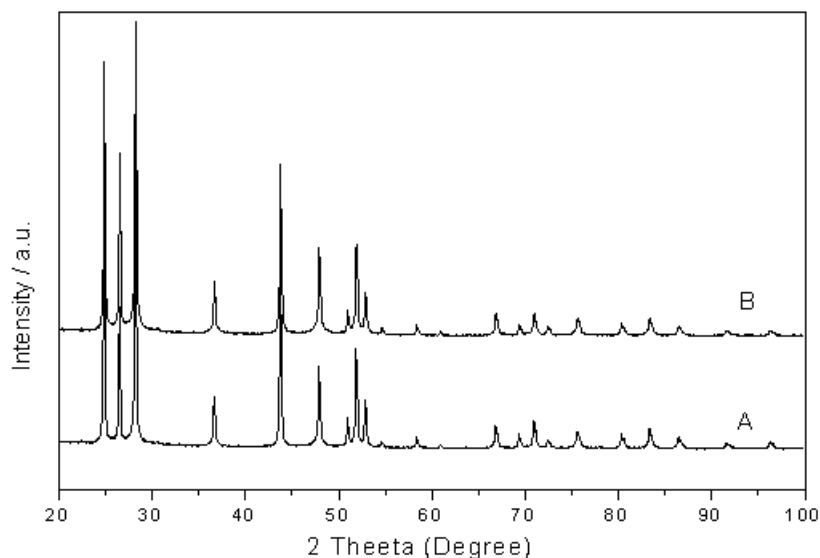


Fig. 8.5: (a) XRD of CdS synthesized in 400 °C at (A) 5 h and (B) 10 h.

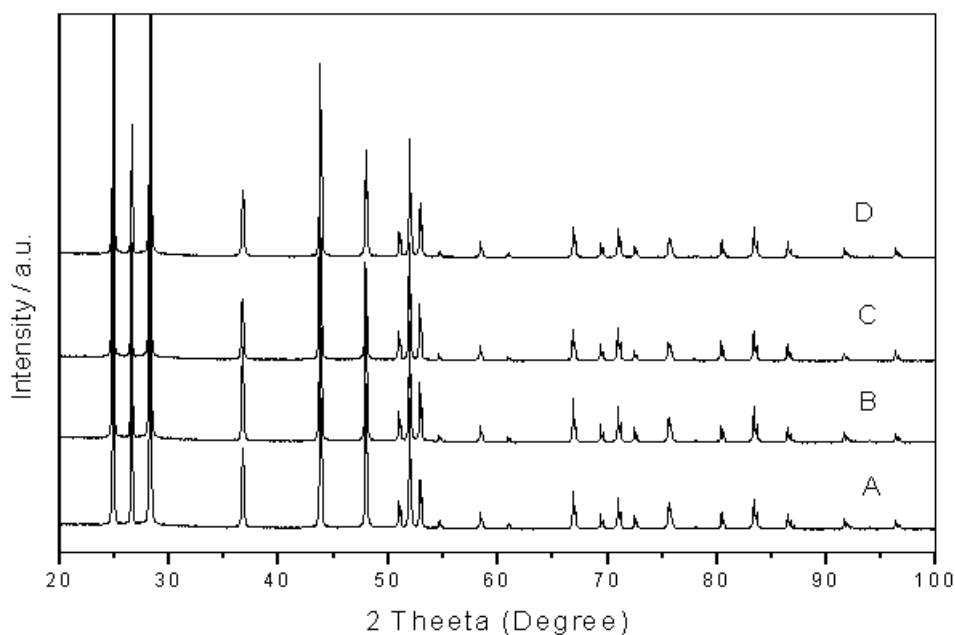


Fig. 8-6: XRD of CdS synthesized by using (A) pure aqueous solvent at 300 °C for 2 h, (B) pure aqueous solvent at 400 °C for 2 h, (C) water: methanol mixed solvent (1:1) at 400 °C for 2 h and water: n-propanol mixed solvent (1:1) at 400 °C for 2 h.

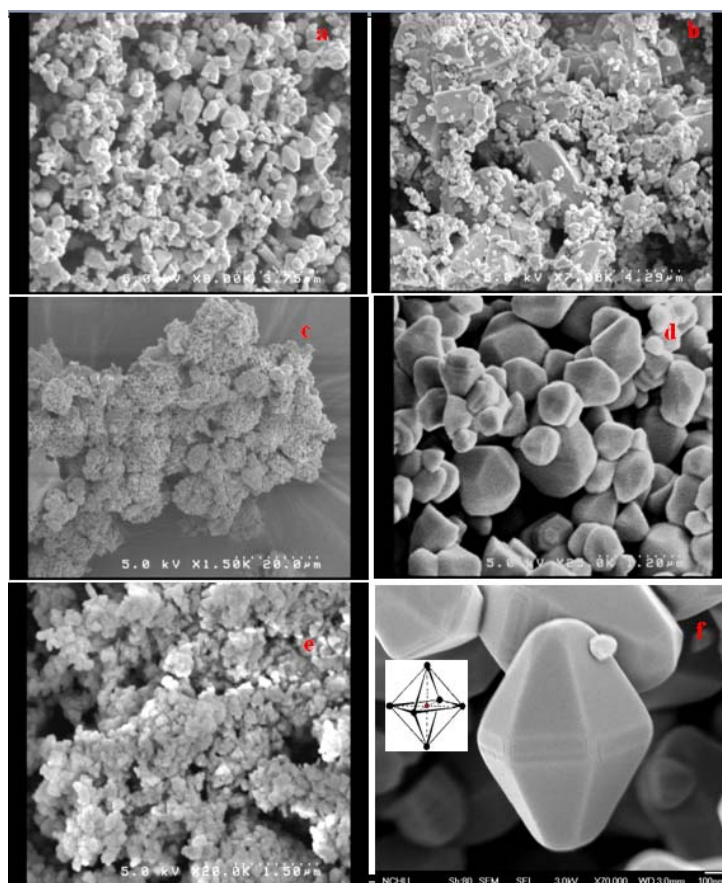


Fig. 8-7: FE-SEM pictures of CdS synthesized for 2 h (a) in aqueous solvent at 300 °C, (b) in water : ethanol (3:1 v/v) mixed solvents at 300 °C, (c) in water : ethanol (1:3 v/v) mixed solvents at 300 °C, (d) in aqueous solvent at 400 °C, (e) in water : ethanol (3:1 v/v) mixed solvents at 400 °C and (f) in water : ethanol (1:3 v/v) mixed solvents at 400 °C, (insert showing model of octahedral geometry).

8.3.2. Influence of mineralizer (KNO₃)

The influence of solvents on the morphology of the synthesized CdS has been investigated and it was found that the solvents play a very important role to control the morphology. The roles of various solvents on the CdS synthesis processes have been reported [28,29]. However, in our study solvents played an indirect role on the CdS fabrication which is quite different from the literature reports. It is interesting to note that

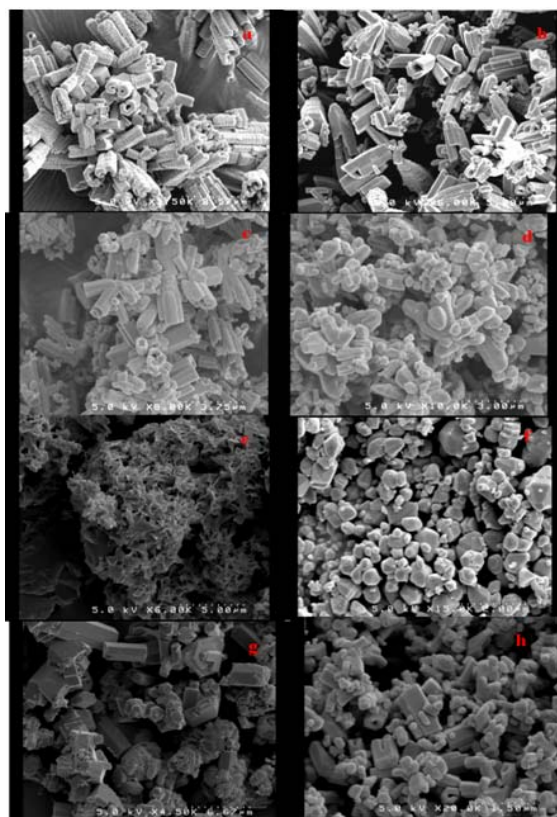


Fig. 8-8: FE-SEM pictures of CdS synthesized for 2 h (a) in water : methanol (1:1 v/v) mixed solvents at 300 °C, (b) in water : methanol (1:1 v/v) mixed solvents at 400 °C, (c) in

water : 1-propanol (1:1 v/v) mixed solvents at 300 °C, (d) in water : 1-propanol (1:1 v/v) mixed solvents at 400 °C and CdS synthesized by using various initial concentration of cadmium ion in water:ethanol (1:1) mixed solvent (e) 2.5g of initial Cd²⁺ concentration at 300 °C, (f) 2.5g of initial Cd²⁺ concentration at 400 °C, (g) 0.5 g of initial Cd²⁺ concentration at 300 °C and (h) 0.5 g of initial Cd²⁺ concentration at 400 °C.

the solvents were used to prepare only cadmium thiocyanate complex and not used during the thermal decomposition process. While keeping other experimental conditions constant, the solvent influence was investigated by varying the volume ratio of water: ethanol at 1:0, 1:1, 1:3 and 3:1. Due to the solubility limitations and higher concentration of the starting precursors, water is essential to prepare the cadmium thiocyanate complex. The XRD results of CdS prepared in pure aqueous solvent and in mixed solvent (alcohol-aqueous) are shown in Fig. 8-6. The XRD results clearly suggested that the nature of solvent and solvents ratio did not influence the crystal structure of wurtzite phase CdS and it is not a surprised result. Hence higher temperature CdS preparation favors wurtzite crystal phase growth. The FE-SEM picture clearly shows that the solvent volume ratio influences the morphology of CdS. By simply adjusting the volume ratio of the water and

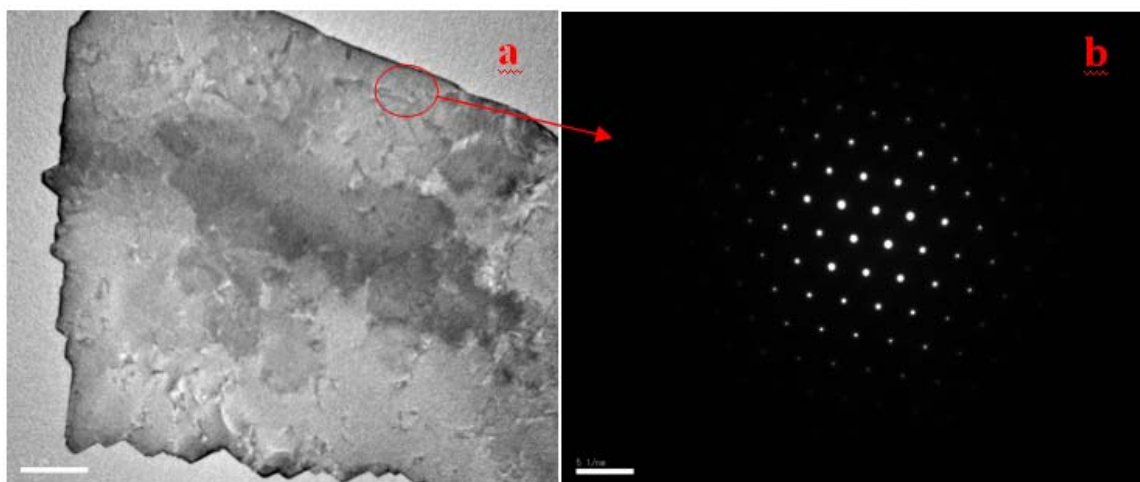


Fig. 8-9: HR-TEM pictures of CdS (a) microtowers surfaces and (b) SAED patterns microtowers.

ethanol solvents, the CdS morphology can be easily varied. Initially, the cadmium thiocyanate complex was prepared in aqueous solution (without a cosolvent) and its thermal decomposition at 300 °C resulted in mixtures of various sized nano/microtubes, nanoparticles, octahedron and distorted octahedron geometry as shown in Fig. 8-7a. Similarly, a water: ethanol (3:1) solvent yields small amount microtubes with nanoparticles mixtures as shown in Fig. 8-7b. However, further increase in the volume of ethanol as a co-solvent to water resulted in porous aggregates (Fig. 8-4b and 8-7c) which suggested that the addition of ethanol favors porous aggregates formation at 300 °C. Moreover, decomposition at 400 °C yields different results and no linearity was noted and we could not make a general conclusion. Both octahedral and disordered octahedral geometry were observed in water solvent at 400 °C as shown in Fig. 8-7d. Moreover, in the water-ethanol (3:1) mixed solvent at 400 °C nanoparticles and small amount of microtube aggregates were obtained as shown in Fig. 8-7e. The noted morphological size is very small and therefore the highly magnified FESEM pictures were not shown clearly. However, further increase in the ethanol volume ratio to 1:1 and 1:3 results in hexagonal microtowers (discussed earlier) and octahedral geometry with small amount of hexagonal plate, respectively, as shown in Fig. 8-4c and 8-7f. The details of microtower morphology were discussed earlier. The degree of disorder of octahedral geometry is less compared with one which is formed from aqueous solution and these experimental conditions are suitable for the CdS preparation with octahedral geometry. The influence of ethanol as a co-solvent on the morphological changes can be explained by considering two important factors. When we used ethanol for the preparation of cadmium thiocyanate, KNO_3 was generated as a byproduct and the amount of KNO_3 formed increased with increasing amount of ethanol in the reaction mixture. About

4.3 and 7.7 g of KNO_3 were generated from water: ethanol solvent mixtures of 1:1 and 1:3, respectively. However, no KNO_3 was generated in pure aqueous solvent and in water-ethanol (3:1 volume ratio) solvent, which suggests that the addition of ethanol facilitates the KNO_3 generation in the solvent mixture. In all our experiments, the formed solid byproduct was removed before the evaporation of solvent mixture on the hotplate. However, we believe that some KNO_3 could dissolve in the reaction solution since its solubility in water is relatively higher (36 g/100ml at 25 °C).

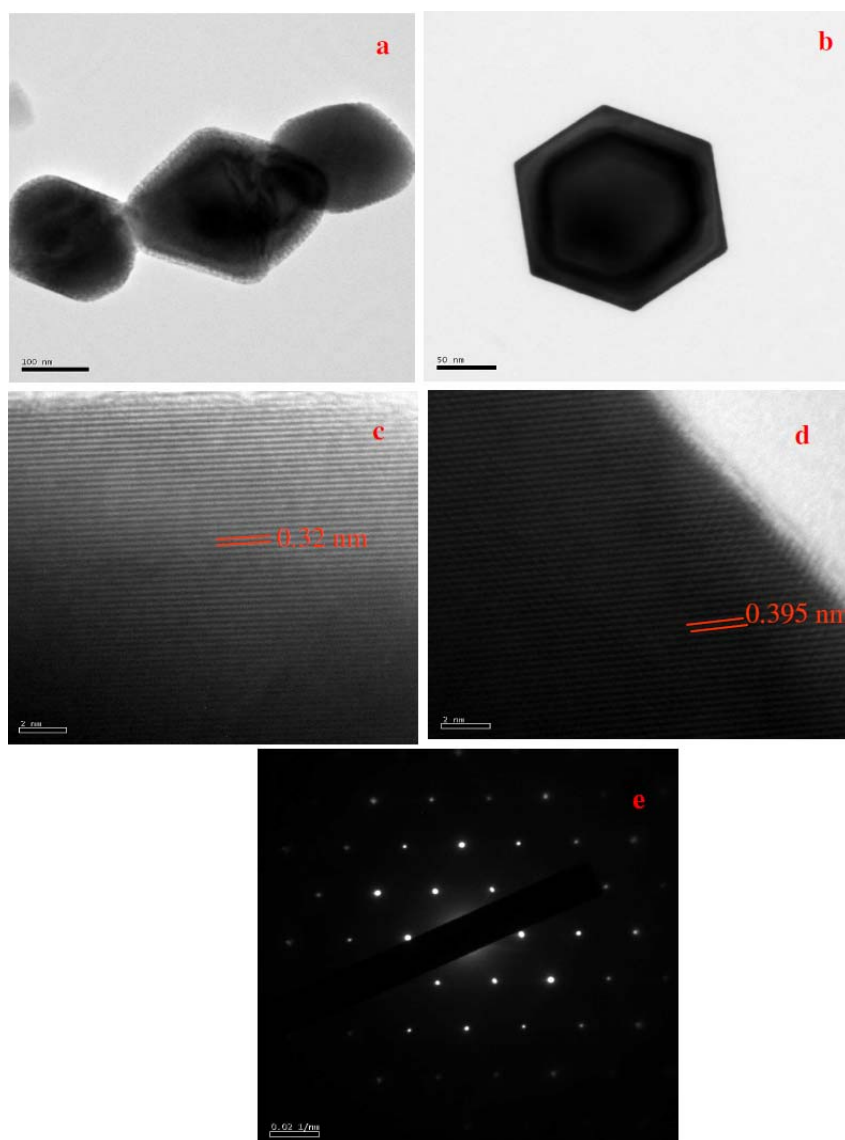


Fig. 8-10: HR-TEM pictures of (a) CdS octahedral geometry, (b) hexagonal plate, (c) lattice fringes of octahedral geometry, (d) lattice fringes of hexagonal plate and (e) SAED patterns of octahedral geometry.

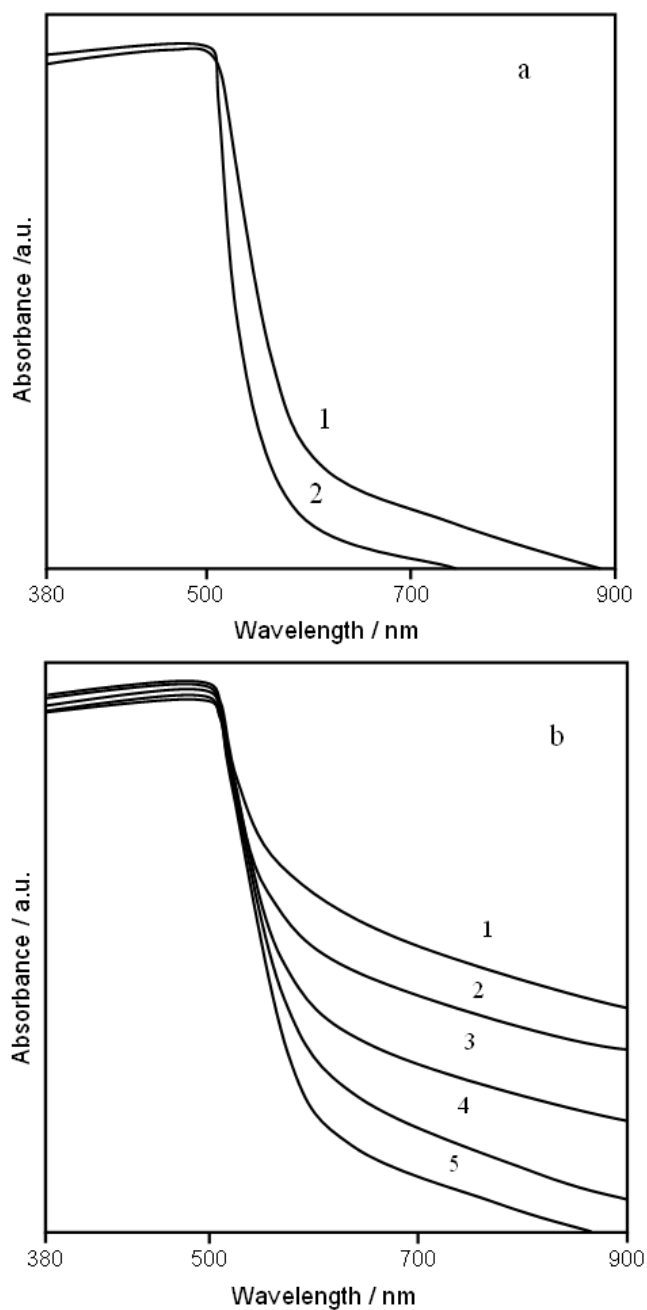


Fig. 8-11: Diffuse reflectance spectra of (a): microtower (1) and octahedral geometry (2) and (b): Pt deposited CdS microtower, (1) 10% (2) 1% (3) 0.5% (4) 0.25% Pt and (5) without platinum deposited CdS.

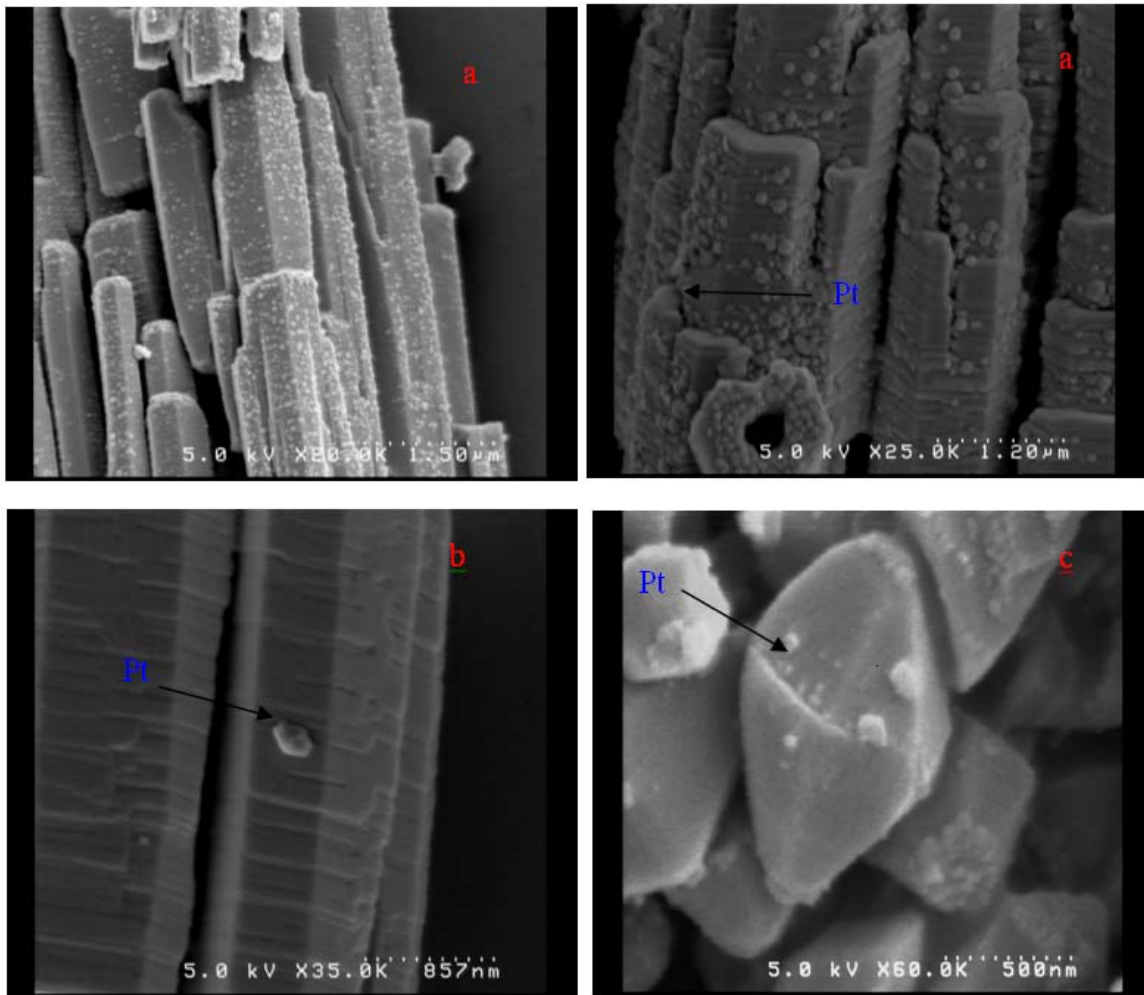


Fig. 8-12: FE-SEM pictures of Pt-deposited CdS microtowers, (a) 10% Pt (b) 1% Pt and (c) 10% Pt deposited octahedral geometry.

The water soluble KNO_3 may be present with cadmium thiocyanate complex after evaporation of the solvent and may influence the CdS crystal growth. The second important variable that we speculate is the solvation effect during the cadmium thiocyanate formation in the presence of alcohol. The complex formation between thiocyanate ions and different metal ions has been investigated from interesting ambient nature of SCN^- ion, which can bind to metal ions through either the hard nitrogen or soft sulfur end depending on the hardness and softness of the central cation involved. For example, Zn^{2+} and Hg^{2+} ions behave as hard and soft acids, respectively, and a Cd^{2+} ion has an intermediate character.³⁰ Earlier studies confirmed that thiocyanate ions bind to Zn^{2+} ions through the nitrogen atom,

but to Hg^{2+} ions through the sulfur atom. Furthermore, thiocyanate ions bind to cadmium ions through nitrogen and sulfur atoms in aqueous solution. Thus, the cadmium bidentate complex is expected to be $[\text{Cd}(\text{NCS})(\text{SCN})]$ in aqueous solution [31]. It is thus expected that the binding energy to cadmium (II) ions of the hard N and soft S ends of the SCN^- ions is very close to each other in water. In such a case, solvation of thiocyanate ions might also play an essential role for determining the N^+ or S-bonding to Cd^{2+} ions [32]. From the above discussion and literature reports, we strongly believe that the coordination structure of the complex is

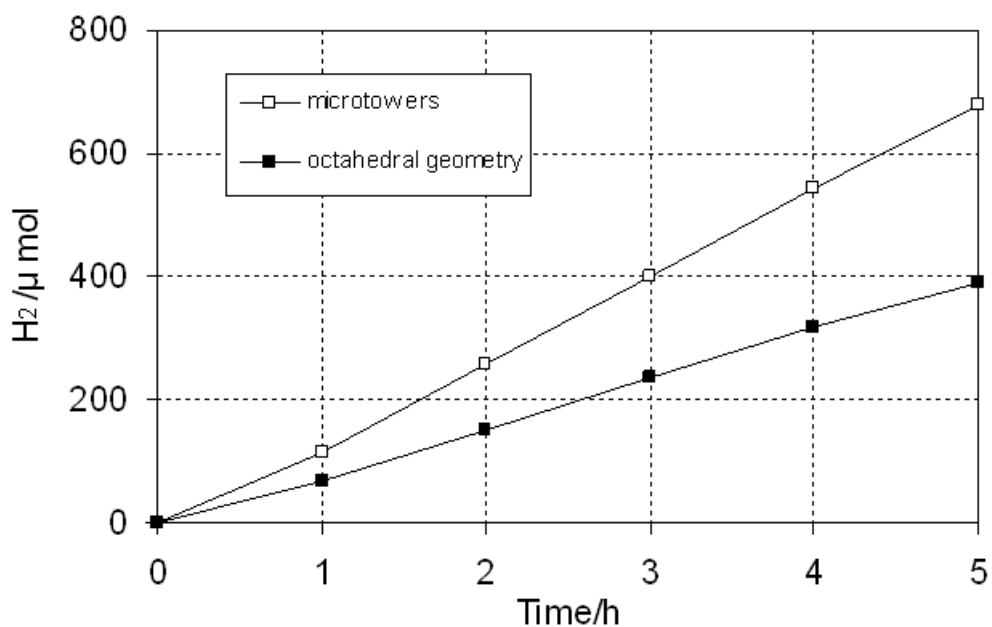


Fig. 8-13: Photocatalytic hydrogen production over 10% Pt-loaded CdS microcrystals.



Fig. 8-14: Catalytic recyclability of CdS microtowers. (A) CdS microtowers and (B) commercially available CdS nanoparticles.

affected by the solvent which eventually yields different morphology after decomposition. In order to support the above discussion, separate experiments were done by replacing ethanol solvent with methanol and 1-propanol as a co-solvent. All experiments were done with alcohol: water mixed solvent at a 1:1 volume ratio and keeping other experimental conditions constant. The decomposition results are presented in Fig. 8-8. Obviously, if methanol was used as a co-solvent, microtowers were formed at 300 ° C and 400 ° C as shown in Fig. 8-8a and 8-8b, respectively. The formed microtowers are not uniform in size and length and small amount hexagonal plates were also noted. However, 1-propanol as a co-solvent yields microtowers and octahedral geometry with small amount of nanoparticles at 300 °C and 400 °C as shown in Fig. 8-8c and 8-8d, respectively. About 4 g and 1g of KNO_3 solid were separated from water-methanol and water-1-propanol solvent mixtures, respectively. Though the KNO_3 generation in water-methanol solvent is almost similar to water-ethanol solvent (4.3g), but the CdS morphology at 300 ° C was different. These results are quit different from those obtained in ethanol solvent as discussed earlier. From these results we can conclude that the salvation effect may also influence the morphology of the synthesized CdS microcrystal by coordination structural changes of cadmium thiocyanate complex [21]. More detailed investigation of coordination structural changes of metal complexes in different solvents and its effect on the morphology of nanomaterials should be performed separately which will open a door to a clear conception and the detailed studies are currently underway in our laboratory. Another important variable that influences the microcrystal is precursor concentrations. Earlier studies confirmed that the initial concentration of the precursor could influence the morphology of CdS [33, 34]. However, we used various initial precursor concentrations to prepare the cadmium thiocyanate complex which was further used for the CdS preparation. Therefore, the study of influence of initial precursor's concentration on the morphology of nanomaterials is quit different from the earlier literature reports. While keeping water: ethanol solvent mixtures

constant at a 1:1 volume ratio and Cd^{2+} to SCN^- mole ratio fixed at 2:1, changing the initial precursor concentration results in changing the morphology of CdS substantially. The initial concentration of Cd^{2+} was taken at 5 g, 2.5 g and 0.5 g and the decomposition were investigated. The XRD results confirmed that all the synthesized CdS at various initial concentrations possesses the wurtzite crystal structure. As we discussed earlier, the higher initial concentration of cadmium ion (5 g) results in porous aggregates and microtowers. When the precursor concentration was reduced by one-half (2.5 g), porous aggregates and ordered/disordered hexagonal geometry were obtained at 300 °C and 400 °C as shown in Fig. 8-8e and 8-8f, respectively. If the precursor concentration further reduced by ten times (0.5 g), nanodisk, nanoplates and microtubes at 300 °C and also microtubes mixed with nanoparticles at 400 °C were noted as shown in Fig. 8-8g and 8-8h, respectively. The aforementioned results clearly indicate that the initial precursor concentration is also important parameters for the microcrystal fabrication. As we mentioned earlier, about 4.3 g of KNO_3 solid were separated at 5g of Cd^{2+} initial concentration and no KNO_3 was separated at low initial concentrations (2.5 g and 0.5g). Therefore, the starting precursor concentration has indirect effect on the final CdS morphology. The reason for these morphological changes of CdS might be due to different amount of dissolved KNO_3 which could influence the crystal growth during the cadmium thiocyanate thermal decomposition. Under different initial precursor concentrations, we strongly believe that no other variables can influence the crystal growth except KNO_3 .

8.3.3. Mechanism

To the best of our knowledge, the influence of KNO_3 on the CdS crystal growth has not been reported though used in other nanomaterial synthetic processes. However, the influence of KNO_3 on the crystal growth has been confirmed earlier. For example, Wang et al. synthesized BiFeO_3 nanoflakes by using a KNO_3 -assisted hydrothermal method and

found that KNO_3 played a key role in the formation of nanoflakes [35]. Similarly, BiFeO_3 powders were also synthesized by using molten KNO_3 – NaNO_3 mixture at $500\text{ }^\circ\text{C}$ [36]. Thus, our experimental results have given clear evidence to claim that KNO_3 determine the morphology of CdS. As we discussed earlier that KNO_3 could influence the CdS crystal growth and to support the mechanism, some controlled experiments were also done. The formation of various morphological CdS has been examined by using different cadmium salts as cadmium precursors and keeping potassium thiocyanate as a thiocyanate source. The CdS microtowers and octahedral geometry formation were not facilitated when we use cadmium chloride or cadmium acetate as a source for a cadmium ion which yields potassium chloride and potassium acetate as byproduct, respectively. The results clearly explain the importance of mineralizer (KNO_3) on the formation of aforementioned morphological CdS. The second direct evidence obtained in a separate experiment by decomposing cadmium thiocyanate along with KNO_3 . The cadmium thiocyanate complex was prepared in water: ethanol (1:1) solvent mixture and without filtering the formed KNO_3 , solvents were evaporated on the hot plate followed by decomposing at two different temperatures. Obviously, CdS does not possess any definite morphology (not shown in Figure) at both decomposition temperatures whereas porous aggregates and microtowers were formed when KNO_3 was removed before the solvent evaporation which suggests the influence of KNO_3 during the CdS crystal growth. The aforementioned two evidences clearly confirm the role of KNO_3 on the CdS microcrystal fabrication. In the absence of templates or other structure-directing agent, it is generally believed that the self-assembled mechanism (directed aggregation) can play a very important role on the formation of nano/micro structured materials. The thermal decomposition of the cadmium thiocyanate complex at desired temperature results in weakening the chelation of Cd^{2+} -SCN complex and Cd^{2+} will be released gradually. At the same time, due to the thermal effect C=S double bonds of thiocyanate will be broken to release S^{2-} anions. Then the active S^{2-} reacts with

Cd^{2+} to generate the CdS nuclei and nanoparticles are further obtained with the continuous supply of these building blocks. Due to high surface energy of the CdS particles they can aggregate (self-assembled) each other into porous aggregates at 300 °C. It is interesting to note that porous aggregates are formed upto 380 °C and it is stable even at prolonged decomposition time (10 h) as discussed earlier. A similar mechanism is also proposed in CdS towershaped rod fabrication [37]. These results suggested that KNO_3 had similar effect on the CdS growth if the decomposition was carried out between 300 and 380 °C. However, the decomposition at 400 °C results in the microtowers morphology. The melting and decomposition points of KNO_3 are 334 °C and 400 °C, respectively and therefore it is reasonable to expect two different types of environment during the crystal growth of CdS. The aforementioned discussion clearly indicated two different types of KNO_3 influence (before mineralization and during mineralization) on the CdS crystal growth. However, it is hard to know exactly how KNO_3 influences the CdS growth during a mineralization process and further multifold analyses are necessary to understand such a detailed mechanism. Moreover, we believed that during the decomposition process at 400 °C, KNO_3 could inhibit the crystal growth and crystal nucleation and the degree of influence depends on the amount of KNO_3 present in the system. High temperatures generally result in the formation of wurtzite-phase seeds, followed by fast unidirectional growth because the (001) face of crystalline wurtzite is more reactive than the other faces.³⁸ Therefore, KNO_3 may assist fast anisotropic growth at the (001) face, suggesting that CdS microtowers grow along the c direction. Due to the bigger size of the microtower we could not get the full images in the HRTEM analysis which limits the information about the microtowers formation mechanism. However, a part of the microtowers surface image is shown in a HR-TEM picture (Fig. 8-9a). From the image we can understand that the microtower was assembled by various nanosize plates and followed by the Ostwald ripening process. The SAED pattern of microtowers (Fig. 8-9b) suggested that the microtower is single crystal. We noted two

different types of microtowers; one is hexagonal thick nanoplates/nanoparticles which stacked together and another one is tubular structures which coexisted. Such distinct morphology may be derived from the heterogeneous nucleation under two different environments during the crystal growth. Another interesting, noted morphology is octahedral geometry and we believe that it may be also formed in a way similar to the microtower fabrication. However, the degree of KNO_3 influence on the crystal growth may be the main reason for the selective growth of the octahedral geometry. The HR-TEM images of octahedral geometry and hexagonal plate are shown in Fig. 8-10a and 8-10b, respectively. The picture clearly showed porous structure on octahedral geometry and well crystallized, defect free lattice fringes as shown in Fig. 8-10c. Similarly, the hexagonal plate formed along with octahedral geometry has also well crystallized, defect free lattice fringes as shown in Fig. 8-10d. The selected-area electron diffraction (SAED) analysis confirmed that the octahedral geometry is a single crystal as shown in Fig. 8-10e.

8.3.4. Photocatalytic hydrogen production

Due to very suitable band structure, the CdS photocatalyst has been successfully used for the photocatalytic hydrogen production under visible light irradiation. It is well known that many properties of CdS such as crystalline phase, size, morphology, specific surface area and defect, etc. can affect its photocatalytic activity [39]. The HR-TEM results confirmed that all synthesized CdS are well crystallized, high quality and defect-free single crystals which are basic requirements of a catalyst for high photocatalytic activity. Therefore, it is very interesting to study the photocatalytic activity of CdS with different morphology and physical properties. It was suggested that specific surface structure (morphology) of photocatalysts is effective for the suppression of recombination between photogenerated electrons and holes and for the separation of H_2 evolution sites from oxidation reaction sites [40]. In our studies, CdS microcrystals have been prepared at higher temperatures, resulting

in well crystallized, single phase microcrystals. Generally, the wurtzite phase CdS is preferred over the cubic phase for better photocatalytic activity, which was confirmed in many earlier studies. For example Matsumura et al. found that 2% Pt-doped CdS hexagonal crystal structure is much more efficient than that of cubic crystal structure [41]. The surface area of the microtowers and octahedral geometry were found to be $1.2 \text{ m}^2\text{g}^{-1}$ and $5.3 \text{ m}^2\text{g}^{-1}$, respectively. The HR-TEM showed the porous structure in the octahedral geometry and hexagonal plate. The nitrogen adsorption analysis curve indicated type II adsorption which is characteristics of macroporous materials. However, due to low pore volume we could not find a pore size curve during the nitrogen adsorption analysis. Therefore we could not present pore size and pore volume of the catalyst. The UV-visible diffuse reflectance spectra (DRS) of CdS microtowers and octahedral geometry are shown in Fig. 8-11a. The results clearly reveal that the visible light absorption of the microtower morphology is higher than that of the octahedral geometry with the onset absorption wavelength (band gap) i.e., 600 nm (2.06 eV) and 560 nm (2.21 eV), respectively. Moreover, these absorption differences might be due to the differences in their morphology. The FESEM picture of Pt-deposited CdS shows that the Pt particles are distributed on the surfaces of the microtowers and the octahedral geometry and the particles sizes of Pt are in the nanometer range as shown in Fig. 8-12. No morphologic and structural differences have been observed between the assynthesized CdS microstructures and the Pt-loaded CdS microstructures. The EDS spectra of the Ptloaded CdS micro structures show strong Cd and S signals with a Cd: S ratio of 1:1.02, which indicates the stability of CdS after photodeposition. The DRS spectra of Pt deposited CdS microtowers are presented in Fig. 8-11b. Obviously, increase in the amount of platinum increases the visible light absorption of the catalysts. Therefore it is reasonable to expect higher photocatalytic activity when the amount of deposited platinum increases on the CdS surface. The concentration of the sacrificial reagents was optimized and found that 0.1 M Na_2SO_3 and 0.1 M Na_2S were suitable for the efficient hydrogen

production. The photocatalytic activity of CdS microtowers and octahedral geometry with and without deposited platinum for H₂ evolution using 0.1 M Na₂SO₃ and 0.1M Na₂S as sacrificial reagents under visible light irradiation has been investigated. Under the same experimental condition, hydrogen evolution from photocatalytic decomposition with and without Pt-deposited CdS under dark was negligible. The rates of hydrogen production of microtowers and octahedral geometry without Pt deposition are 5.5 μ mol h⁻¹ and 1.9 μ mol h⁻¹, respectively, which implies that the platinum is essential as a co-catalyst for the efficient hydrogen production. The results clearly indicate that the hydrogen production rate of the microtowers is 2.9 times higher than that of the octahedral geometry. The reasons for the low activity are due to the weaker interaction of SO₃²⁻ ions with the CdS surface and the less efficient hole transfer, and thus the probability of e⁻/h⁺ recombination is higher [42]. However, the rate of hydrogen evolution rapidly increases from 23 μ mol h⁻¹ in the presence of 0.01 % of Pt-loaded CdS to the maximum rate of 138 μ mol h⁻¹ in the presence of 10% Pt-loaded CdS. We could not find the optimum platinum loading in the investigated range from 0.1 to 10 wt%, suggesting that higher amounts of platinum are necessary for more efficient hydrogen production. Similarly, the hydrogen evolution rate of 10% Pt-loaded octahedral geometry was 79 μ mol h⁻¹ which is 1.74 times less than the microtower catalyzed hydrogen production rate as shown in Fig. 8-13. The above results suggest the good photocatalytic activity of microtowers despite its low surface area. It is known that sulfides with small surface areas of <10 m² g⁻¹ still show good photocatalytic activity because of their good crystallinity and less crystal defects that can largely reduce the bulk electron–hole recombination during the migration of electrons and holes to the surface of CdS. Nevertheless, the rate of hydrogen production was low compared to some results reported in the literature [42]. This difference in the efficiency is due to the difference in the irradiation lamp power, amounts of catalyst and concentration of sacrificial reagents which can influence the hydrogen production in a great extent. Therefore, optimization of

experimental parameters is necessary for comparison. The catalytic recyclability of the microtowers has been studied and compared with commercially available CdS photocatalysts. About 0.025 g of the microtower catalysts were suspended in 7 mL of water and ultrasonicated for 5 min and the separation was noted after 5 min as shown in Fig. 8-14. Obviously, CdS microtowers (A) are quite easily separated in a short time as compared to commercial CdS colloids (B), which indicates that the CdS microtowers are easily recyclable photocatalysts. Similar observation was also reported in the literature [43,44]. In conclusion, CdS microtowers are a highly efficient and easily recyclable photocatalyst.

8.4. Conclusion

The CdS microtower, hexagonal plate and octahedral geometry were successfully fabricated on a large scale by using a simple methodology. The XRD analysis confirmed that the synthesized CdS microcrystals are in pure wurzite phase and well crystalline nature. The thermal decomposition time and temperature appreciably influence the morphology of the CdS microtowers. The influence of ethanol cosolvent on the morphology of CdS microcrystals was investigated and found that the solvent ratio is an important parameter to control the morphology. The initial precursor concentration and solvent ratios also play an important role to decide the morphology of microcrystals. The nitrogen adsorption analysis results showed the low surface area of the microcrystals and the presence of macroporous structure in the octahedral geometry. The DRS spectra showed that the microtowers have more visible light absorption over the octahedral geometry. A plausible mechanism of CdS microcrystal fabrication has been discussed. About 10 % Pt-deposited CdS microcrystals showed higher hydrogen production rate over non-Pt-deposited catalyst confirming that co-catalysts are necessary for efficient hydrogen production. The CdS microcrystals can be easily recyclable after usage in the photocatalytic processes.

References

- [1] Morkel, M.; Weinhardt, L.; Lohmüller, B.; Heske, C.; Umbach, E.; Riedl, W.; Zweigart, S.; Karg, F. *Appl. Phys. Lett.* **2001**, *79*, 4482.
- [2] Schlamp, M. C.; Peng, X. G.; Alivisatos, A. P. *J. Appl. Phys.* **1997**, *82*, 5837.
- [3] Peng, X. G.; Schlamp, M. C.; Kadavanich, A. V.; Alivisatos, A. P. *J. Am. Chem. Soc.* **1997**, *119*, 7019.
- [4] Wang, Z. L. *Adv. Mater.* **2000**, *12*, 1295.
- [5] Zhang, J.; Jiang, F. H.; Zhang, L. D. *J. Phys. Chem. B* **2004**, *108*, 7002.
- [6] Kar, S.; Satpati, B.; Satyam, P. V.; Chaudhuri, S. *J. Phys. Chem. B* **2005**, *109*, 19134.
- [7] Wang, Q. Q.; Xu, G.; Han, G. R. *Crys. Grow. Des.* **2006**, *6*, 1176.
- [8] Barrelet, C. J.; Wu, Y.; Bell, D. C.; Lieber, C. M. *J. Am. Chem. Soc.* **2003**, *125*, 11498.
- [9] Thiruvengadathan, R.; Regev, O. *Chem. Mater.* **2005**, *17*, 3281.
- [10] Jun, Y-W.; Lee, S-M.; Kang, N-J.; Cheon, J. *J. Am. Chem. Soc.* **2001**, *123*, 5150.
- [11] Yang, J.; Zeng, J. H.; Yu, S. H.; Yang, L.; Zhou, G. E.; Qian, Y. Y. *Chem. Mater.* **2000**, *12*, 3259.
- [12] Yeh, C. Y.; Lu, Z. W.; Froyen, S.; Zunger, A. *Phys. Rev. B.* **1992**, *46*, 10086.
- [13] Manna, L.; Milliron, D. J.; Meisel, A.; Scher, E. C.; Alivisatos, A. P. *Nat. Mater.* **2003**, *2*, 382.
- [14] Chu, H.; Li, X.; Chen, G.; Zhou, W.; Zhang, Y.; Jin, Z.; Xu, J.; Li, Y. *Crys. Grow. Des.* **2005**, *5*, 1081.
- [15] Zhang, Z. H.; Chin, W. S.; Vittal, J. J. *J. Phys. Chem. B.* **2004**, *108*, 18569.
- [16] Bahta, A.; Parker, G-A.; Tuck D-G. *Pure & Appl. Chem.* **1997**, *69*, 1489.
- [17] Zeleya-Angel, O.; Castillo-Alvarado, F.L.; Avendano-Lopez, J.; Escamilla-Esquivel, A.; Contreras-Puente, G.; Lozada-Morales, R.; Torres-Delgado, R. *Solid State Commun.* **1997**, *104*, 161.

- [18] Zelaya-Angel, O.; Alvarado-Gil, J.J.; Lozada-Morales, R.; Vargas, H.; Ferreira da Silva, A. *Appl. Phys. Lett.* **1994**, *64*, 291.
- [19] Lee, O. D. H.; Noble, R.; Finnigan, D.; Orloff, S.; Tenpas, E.; Park, C.; Fagan, J.; Wang X. W. *Thin Solid Films.* **1996**, *290*, 13.
- [20] Ptaszyński, B.; Skiba E.; Krystek, J. *J. Therm. Ana. Calorim.* **2001**, *65*, 231.
- [21] Ohtaki, H. *Pure. Appl. Chem.* **1987**, *59*, 1143.
- [22] Ishiguro, S.; Yamamoto, K.; Ohtaki, H. *Bull. Chem. Soc. Jpn*, **1986**, *59*, 1009.
- [23] Hota, G.; Idage, S.B.; Khilar, K.C. *Colloids and Surfaces A: Phys and Eng.* **2007**, *293*, 5.
- [24] Duran, J. D.G.; Guindo, M.C.; Delgado, A.V.; Caballero, F.G. *J. Colloid and Interface. Sci.* **1997**, *193*, 223.
- [25] Yan, Y-G.; Zhang, Y.; Zeng, H-B.; Zhang, L.D. *Crys. Grow. Des.* **2007**, *7*, 940.
- [26] Tong, Y. H.; Liua, Y. C.; Shao, C. L.; Mu, R. X. *Appl. Phys. Lett.* **2006**, *88*, 123111.
- [27] Li, Y.; Li, X.; Yang, C.; Li, Y. *J. Mater. Chem.* **2003**, *13*, 2641.
- [28] Chu, H.; Li, X.; Chen, G.; Zhou, W.; Zhang, Y.; Jin, Z.; Xu, J.; Li, Y. *Crys. Grow. Des.* **2005**, *5*, 1801.
- [29] Yang, C-S.; Awschalom, D. D.; Stucky, G. D. *Chem. Mater.* **2001**, *13*, 594.
- [30] Yamaguchi, T.; Yamamoto, K.; Ohtaki, H. *Bull. Chem. Soc. Jpn.* **1985**, *58*, 3235.
- [31] Ishiguro, S.; Yamamoto, K.; Ohtaki, H. *Bull. Chem. Soc. Jpn*, **1986**, *59*, 531.
- [32] Ishiguro, S-I.; Takamuku, T.; Ohtaki, H. *Bull. Chem. Soc. Jpn.* **1988**, *61*, 3901.
- [33] Li, Y.; Li, X.; Yang, C.; Li, Y. *J. Mater. Chem.*, **2003**, *13*, 2641.
- [34] Xi, L.; Xiu, W.; Tan, W.; Boothroyd, C.; Lam, Y. M. *Chem. Mater.* **2008**, *20*, 5444.
- [35] Wang, Y.; Xu, G.; Yang, L.; Ren, Z.; Wei, X.; Weng, W.; Du, P.; Shen, G.; Han, G. *Ceramics International.* **2009**, *35*, 1285.
- [36] He, X.; Gao, L. *Ceramics International.* **2009**, *35*, 975.
- [37] Zhang, P.; Gao, L. *Langmuir*, **2003**, *19*, 208.
- [38] Li, Y.; Li, X.; Yang, C.; Li, Y. *J. Mater. Chem.* **2003**, *13*, 2641.

- [39] Ashokkumar, M. *Int. J. Hydro. Ener.* **1998**, *23*, 427.
- [40] Tsuji, I.; Kato, H.; Kobayashi, H.; Kudo, A. *J. Am. Chem. Soc.* **2004**, *126*, 13406.
- [41] Matsumura, M.; Furukawa, S.; Saho, Y.; Omura, H. T. *J. Phys. Chem.* **1985**, *89*, 1327.
- [42] Bao, N.; Shen, L.; Takata, T.; Domen, K. *Chem. Mater.* **2008**, *20*, 110.
- [43] Muruganandham, M.; Wu, J.J. *Appl. Catal. B: Environ.* **2008**, *80*, 32.
- [44] Zhang, Q.; Fan, W.; Gao, L. *Appl. Catal. B: Environ.* **2007**, *76*, 168.

CHAPTER 9

WET-TYPED Fe_2O_3 SOLAR CELLS BASED ON Fe_2O_3 FILMS PREAPRED BY LASER ABLATION: DRASTIC TEMPERATURE EFFECT

Abstract

A wet type solar cell based on Fe_2O_3 films prepared by the laser ablation method was investigated. The performance was increased drastically by the thermal treatment of the Fe_2O_3 /FTO films. This enhancement effect is caused by the improvement of the binding interface between FTO and Fe_2O_3 . The work has been published in *Electrochemistry Communications*, 2009, 11(11), 2150-2151.

9.1. Introduction

Photovoltaic devices are based on the concept of charge separation at an interface of two materials of different conduction mechanism. To date, this field has been dominated by solid-state junction devices, usually made of silicon, profiting from the experience and material availability resulting from semiconductor industry. The dominance of the photovoltaic field by inorganic solid-state junction devices is now being challenged by developments in nanocrystalline and conducting polymer films [1,2]. A dye-sensitized solar cell (DSC) has been also recognized as a reasonable solar energy conversion device [3] since Grätzel et al. had improved the efficiency drastically [4,5].

$\alpha\text{-Fe}_2\text{O}_3$ is an attractive semiconductor material due to its good stability, low cost, and narrow bandgap (2.2 eV) giving an absorption spectrum in the visible light region [6,7]. Previously, we reported the wet-type solar cell based on the Fe_2O_3 film [8].

In this study, we focused on the effect of the calcination temperature on the interaction of Fe_2O_3 and FTO for the improvement of the Fe_2O_3 -film solar cells. The laser ablation

method was used for the preparation of Fe₂O₃ films on the FTO or ITO glass because a strong thin uniform film can be prepared by this method.

9.2. Experimental

The wet-type Fe₂O₃ solar cells were prepared as follows. First, the Fe₂O₃ thin film was deposited on an ITO glass (indium-tin-oxide coated glass, 8-12 ohm, Aldrich) by a conventional laser ablation method. FTO (F doped indium tin oxide) glasses (1-2 ohm, Fujikura) were also used as a substrate at higher temperatures. As for the preparation of the Fe₂O₃ target, 0.55 g of paraffin were mixed with 5.5 g of α -Fe₂O₃ (99.9%, Wako) to prevent cracking. The mixed powder was pressed at 20 MPa for 1 h and calcined at 500 °C for 6 h to form an Fe₂O₃ disk pellet.

The pellet disk thus prepared was introduced into the chamber and then the experimental conditions were adjusted. The wavelength of the laser pulse (Nd-YAG Laser, Spectra-Physics Co., GCR-130-10) was 532 nm. The laser power was 2.8 J / (pulse cm²) and the repetition rate of the laser pulse was 10 Hz. The distance between the substrate (ITO or FTO glass) and the target (α -Fe₂O₃) was 3 cm. The substrate was set at room temperature and the laser irradiation time was 5 min. Irradiation of the target with a laser beam melted the target to form a plume. The plume was accumulated on the substrate to form the Fe₂O₃ thin film. The films prepared by the laser ablation method were calcined at different temperatures under air. The Pt counter electrode was prepared by sputtering Pt onto an ITO or FTO glass. The two electrodes were sandwiched and then the electrolyte solution was filled between the two (Fe₂O₃ and Pt) electrodes. A solution containing 0.8 M KI and 0.2 M I₂ was used as the electrolyte.

Current-voltage characteristics were measured using a Peccell I-V curve analyzer (PECK2400-N). A xenon lamp (Inotex 300-W LX-300F) with an IR cut-off filter was used as a light source (1 sun).

The thin films prepared were characterized by XRD (X-ray diffraction, Rigaku Rint-2000) and FE-SEM (field emission scanning electron microscope, Hitachi S-4100).

IPCE (incident photon to current conversion efficiency) values of the Fe₂O₃ solar cells were measured using an IPCE analyzer (EKO, PRP1-SAO-001) to estimate the quantum yield of the solar cells.

9.3. Results and discussion

Fig. 9-1 shows the calcination-temperature dependence of the I-V curves of the solar cells under light irradiation (1 sun). The FTO glasses were used at higher temperatures of calcinations due to a markedly decrease in the conductivity of ITO [9]. The open circuit voltage (V_{oc}), the short circuit current (I_{sc}), the fill factor (FF) and the overall energy conversion efficiency (η) are shown in Table 1. The thickness of the Fe₂O₃ films prepared by the squeegee method (ca. 100 μm) is 100 times larger than that of the laser ablation method (ca. 1 μm). In the squeegee method, V_{oc} , I_{sc} , FF and η were 0.23 V, 0.28 mA cm^{-2} , 0.35 and 0.023 %, respectively [8]. This performance (V_{oc} , I_{sc} , FF and η) is almost the same as the results of the laser ablation (see Table 1). Therefore, we can say that the quality of Fe₂O₃ films prepared by the laser ablation method is high in spite of the thin film thickness; the thickness is ca. 1 μm in the laser ablation and ca. 100 μm in the squeegee. The performance of the Fe₂O₃ solar cell increases sharply with the calcination temperature up to 700 °C after the laser ablation at room temperature. The efficiency of the solar cell based on the Fe₂O₃ film calcined at 700 °C was about 1000 times higher than that based on the non-calcined film. The IPCE values of the Fe₂O₃ solar cell using the Fe₂O₃/FTO film calcined at 700 °C were measured as shown in Fig. 9-2. The absorption spectrum of the Fe₂O₃ film is

also shown in the inset of Fig. 9-2. The IPCE and absorption curves of the Fe₂O₃ film overlap with each other, suggesting that the Fe₂O₃ solar cell operates on the light absorption of Fe₂O₃. Maximum IPCE values of the solar cell under UV (360 nm) and visible light (420 nm) was 6% and 4%, respectively.

Table 9-1: Calcination-temperature dependence of V_{oc}, I_{sc}, FF and η.

Calcination temperature/ °C	V _{oc} / V	I _{sc} / mA	FF	η/%
a (non-calcined (ITO))	0.01	0.01	0.25	0.000034
b (300 (ITO))	0.11	0.12	0.28	0.0036
c (500 (ITO))	0.18	0.31	0.25	0.014
d (500 (FTO))	0.22	0.24	0.35	0.018
e (600 (FTO))	0.27	0.35	0.34	0.032
f (700 (FTO))	0.29	0.37	0.33	0.035
g (800 (FTO))	0.22	0.21	0.28	0.013

To examine the cause for the improvement of the Fe₂O₃ solar-cell performance by the calcination after the laser ablation at room temperature, the Fe₂O₃ films were analyzed by SEM and XRD as shown in Fig. 9-3 and Fig. 4, respectively.

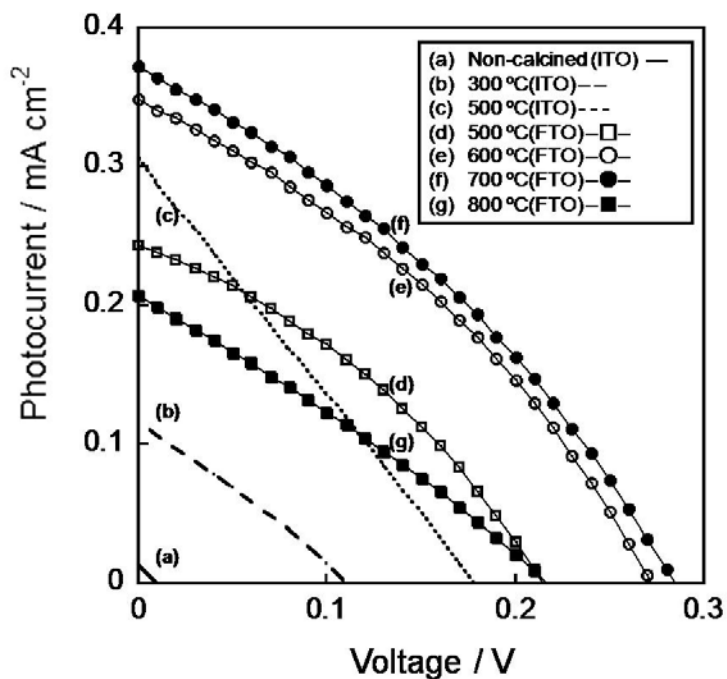


Fig. 9-1: Calcination-temperature dependence of I-V curves (under 1 sun) of the solar cells based on the Fe_2O_3 films prepared by the laser ablation ((laser power: $2.8 \text{ J / (pulse cm}^2\text{)}$, distance between substrate and target: 3 cm, irradiation time: 5 min, atmosphere: O_2 13 Pa, room temperature). The electrolyte is 0.8 M of KI and 0.2 M of I_2 in water.

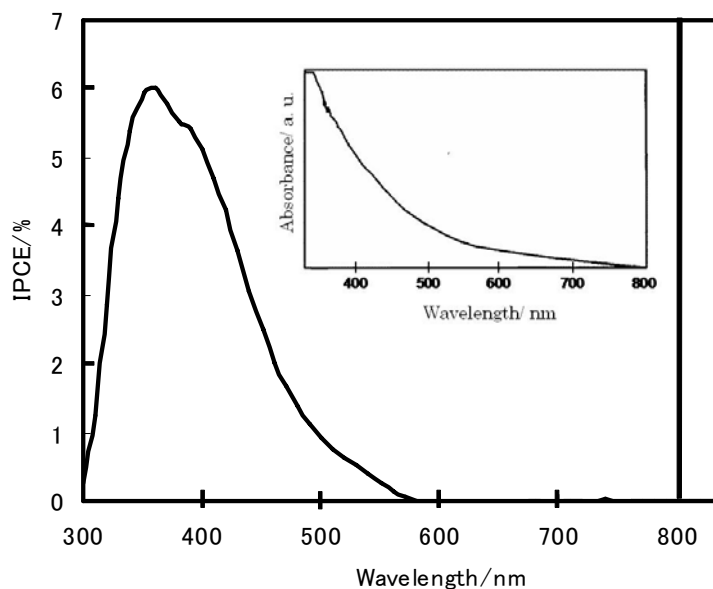


Fig. 9-2: An IPCE curve of the Fe_2O_3 solar cell using the Fe_2O_3 film prepared by the laser ablation on the FTO glass (for the conditions, see the figure caption to Fig. 9-1) and the

absorption spectrum of the Fe_2O_3 film (inset). The electrolyte is 0.8 M of KI and 0.2 M of I_2 in water. The calcination temperature is 700 °C.

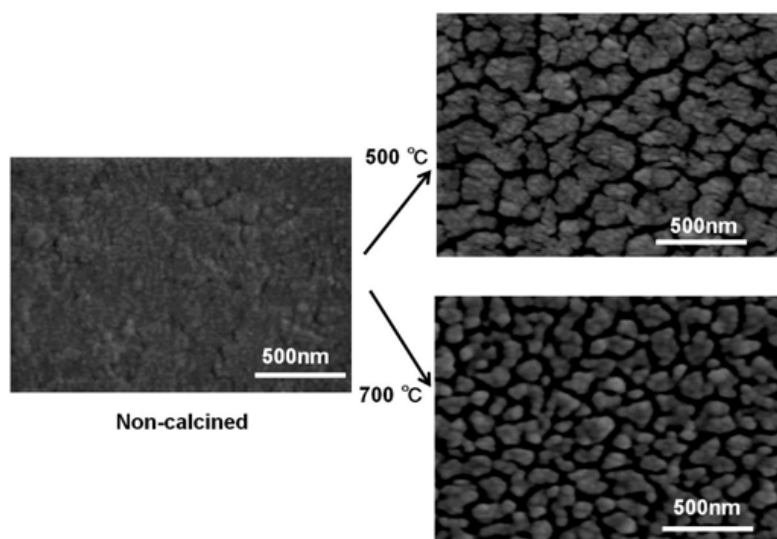


Fig. 9-3: SEM images of the Fe_2O_3 thin films calcined at different temperatures after the laser ablation (for the conditions, see the figure caption to Fig. 9-1).

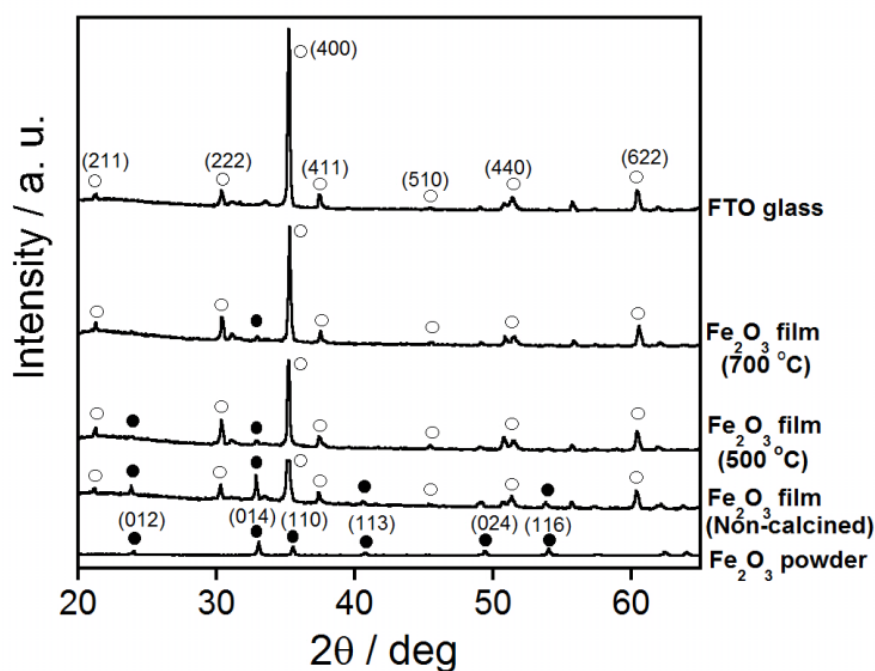


Fig. 9-4: Calcination-temperature dependence of XRD patterns of the Fe_2O_3 film prepared by the laser ablation (for the conditions, see the figure caption to Fig. 1). The peaks of Fe_2O_3 are marked by the solid circle and those of FTO are marked by the open circle.

SEM images show that particles of Fe_2O_3 grow with calcinations. One of the reasons for improvement of the solar-cell performance by calcinations is the suggestion that bonds between Fe_2O_3 and FTO are intensified due to growth of particles, resulting in the improvement of electron conductivity between Fe_2O_3 and FTO. However, the performance of the solar cell decreased at 800 °C due to damage of FTO. The XRD patterns in Fig. 9-4 show that the intensity of the peaks of Fe_2O_3 (012), (014), (113) and (116) was decreased by the calcination while the intensity of the peaks of FTO is almost the same after calcination. It is suggested that the periodicity of the Fe_2O_3 crystal lattice was disturbed by the interactional diffusion of Fe_2O_3 and FTO at high temperatures, resulting in decreased XRD peak intensity. The performance of the solar cell is considered to be improved because the smoothness of the interface decreases the resistance of the Fe_2O_3 /FTO interface. A part of Fe_2O_3 lattices is probably fused into FTO lattices, resulting in the improvement of the electron conductivity between Fe_2O_3 and FTO. We can say from Table 9-1 that a rapid increase in the efficiency by calcination is achieved by each improvement of I_{sc} , V_{oc} and FF, especially a remarkable increase of I_{sc} . It is suggested that this rapid increase of I_{sc} is caused by a decrease of the resistance at the interface between FTO and Fe_2O_3 . Moreover, it is also suggested that the increase of V_{oc} and FF is caused by a decrease of the defects of the Fe_2O_3 films. The details are now under investigation.

In an attempt to prepare the high performance solar cell without the thermal treatment, we prepared Fe_2O_3 films by laser ablation at high substrate temperatures; however the efficiency was almost zero. We consider the reason of low efficiency as follows. When the substrate temperature is high, the migration of the Fe_2O_3 particles is promoted by the thermal energy of the heated substrate. The surface of the film probably becomes smoother by the migration, and therefore the surface area was decreased drastically resulting in the low performance of the solar cells.

It is concluded that the thermal treatment after the laser ablation at room temperature is important to improve the performance of the thin film-type solar cells.

References

- [1] H. N. Cong, M. Dieng, C. Sene, P. Chartier, *Sol. Energy Mater. Sol. Cells* **2000**, *63*, 23.
- [2] N. Kudo, Y. Shimazaki, H. Ohkita, M. Ohoka, S. Ito, *Sol. Energy Mater. Sol. Cells* **2007**, *91*, 1243.
- [3] H. Tsubomura, M. Matsumura, Y. Nomura, T. Amamiya, *Nature* **1976**, *261*, 402.
- [4] B. O'Regan, M. Grätzel, *Nature* **1991**, *353*, 737.
- [5] M. Grätzel, *Nature* **2001**, *414*, 338.
- [6] S. U. M. Khan, J. Akikusa, *J. Phys. Chem. B* **1999**, *103*, 7184.
- [7] U. Bjorksten, J. Moster, M. Grätzel, *Chem. Mater.* **1994**, *6*, 858.
- [8] S. Somekawa, Y. Kusumoto, K. Miyamae, T. Kamiwaki, Y. Horie, in: D. Yogi Goswami, Y. Zhao (Eds.), *Proc. ISES Solar World Congress 2007*, Tsinghua University Press, Beijing, 18-21 Sep., 2007, p. 1329.
- [9] T. Kawashima, H. Matsui, N. Tanabe, *Thin solid films* **2003**, *445*, 241.

CHAPTER 10

**A COMPARATIVE STUDY OF PLASMON-INDUCED CHARGE
SEPARATION OF TiO₂, Fe₂O₃, AND ZnO FILMS LOADED WITH
GOLD NANOPARTICLES**

Abstract

The gold colloidal nanoparticle was prepared by citrate reduction from chloroauric acid (HAuCl₄). An ITO glass was coated by laser ablation and squeegee method with nanoporous TiO₂, Fe₂O₃ and ZnO film and films were loaded with Au-nanoparticles. The film was characterized by UV-visible absorption transmittance spectroscopy, SEM, XPS, EDX and XRD techniques. The gold nanoparticles are absorbed visible light by plasmonic and photoexcited electrons was flow to the TiO₂, Fe₂O₃ and ZnO conduction band. The cells were evaluated by short circuit current and open circuit voltage. In this study we compare the difference semiconductor with Au-nanoparticles and found Au-TiO₂, Au-Fe₂O₃, Au-ZnO film is one of the challenging photo-current producers than the dye synthesized solar cell (DSSC) with good efficiency and durability.

10.1 Introduction

Au-nanoparticles are interested for solar cell because of their collective oscillation of electrons in the conduction band induces large surface electric fields which greatly enhance the properties of surface plasmonic absorption in visible range [1]. The conduction band electrons of noble metals can move freely, independently from the ionic background and the ions act only as scattering centers [2]. This gives the electrons in the noble metals a higher polarizability, which shifts the Plasmon resonance to lower frequencies with a sharp

bandwidth. The gold nanoparticles colloidal solutions have also the stronger magnitude than that most strongly absorbing light, light scattering, stability and intense more than the organic dyes [3-4].

The nanoparticles quantum confinement is widely used terminology for the study of nanocrystals. As the size of a crystal decreases to the nanometer regime, the size of the particle begins to modify the properties of the crystal. The electronic structure is altered from the continuous electronic bands to discrete or quantized electronic levels. As a result, the continuous optical transitions between the electronic bands become discrete and the properties of the nanomaterial become size-dependent [5-8]. In a spherical nanocrystal surrounded by an infinite potential barrier, the energy of the electron and hole quantum-size levels depend on quantum number, electron and hole effective mass, crystal radius, and root of spherical Bessel function. Thus, with decreasing nanocrystal size, the energy of the lowest electron and hole quantum-size levels increase as well as the total energy of optical transitions between these levels [9]. When the size of the nanocrystal is smaller than the Bohr radius of the exciton of the corresponding bulk material, the band energy evolves into discrete energy levels, and the optical transitions near the band edge involve only the s conduction band level for electrons and the top three p levels in the valence band levels for holes [10].

The gold nanoparticles photovoltaic cells are based on photoexcitation of Au-nanoparticles and semiconductor like TiO_2 , Fe_2O_3 , ZnO etc molecules. For instance, when the illuminate photon energy is greater than molecular binding energy, the Au-nanoparticles become excited due to Plasmon resonance and electron flow to the semiconductor conduction band [4]. This mechanism already been discusses in chapter one, 1.5 Photosynthetic and regenerative cells.

The electron transfer occurs due to favorable energy difference between the lowest unoccupied molecular orbital (LUMO) of the gold and the conduction band of

semiconductor. The photogenerated electrons rapidly through the semiconductor conduction band and are collected by the conducting glass (ITO glass) support.

The electrons vacancy fills up from the donor solution like electrolyte to the Au-nanoparticles. The highest occupied molecular orbital (HOMO) of the Au-molecules lower than redox potential, E_{Redox} of the iodine/triiodide couple. The energy difference provides the driving force for hole injection into the electrolyte. The electrolyte and hole minimized the charge by redox reaction and transport one type of carrier like electron is energetically from the Au-molecule to the semiconductor [11].

In this paper we introduced the two kinds of Au nanoparticles such as laser ablated prepared and citrate reduction prepared nanoparticles and established the new kinds of mechanism with exchange the difference semiconductor.

10.2 Experimental Section

10.2.1 Synthesis and characterization of Au nanoparticles

Gold colloidal nanoparticles were prepared by citrate reduction from chloroauric acid ($\text{HAuCl}_4 \cdot 4\text{H}_2\text{O}$, Wako pure chemical, Japan) as following method introduced by G. Frens [12]. In details, 1 gm chloroauric acid ($\text{HAuCl}_4 \cdot 4\text{H}_2\text{O}$) was dissolved in 100 ml distilled water. Then 0.5 mL chloroauric acid solution was added in 50 mL volume (10^{-2} by weight solution) distilled water and refluxed to boiling, and then added to 0.5 mL of 1% sodium citrate solution. The reduction of the gold ions by the citrate ions is complete after 5 minutes while the solution is further boiled for 30 min and then left cool to room temperature. Then the solution was condensed by high speed centrifugation. The Au nanoparticles characterization was already discusses in chapter 3. Please refer to see for characterization in chapter 3.

10.2.2 Preparation of Au-TiO₂, Au-Fe₂O₃ and Au-ZnO film

The two type's film was prepared by the laser ablation and the squeegee methods. A nanoporous TiO₂ (P25, Degussa Corp. Anatase grade) was used for the two method. The laser ablation TiO₂ film was prepared as follows: an ITO-coated glass plate (indium-tin oxide coated glass, 8-12 ohm resistance, Aldrich) was deposited with TiO₂ for prepared a high compact thin film by the laser ablation method [13-15]. TiO₂ targets were prepared by mixing 5.5 g of TiO₂ with 0.55 g of paraffin (10%) to prevent cracking. The mixed powder was pressed at 20 MPa for 1 h and calcined at 400 °C for 6 h to form a TiO₂ pellet. The pellet was introduced into a vacuum chamber where the laser pulse enters through a window and impinges on the target materials to be deposited. A laser power of 2.8 J / (pulse cm²) was used throughout the experiment. The wavelength of the laser was 532 nm (Nd-YAG Laser). The distance between the substrate and the target was 3 cm. The substrate was set in room temperature and the laser irradiation time was 5 min. Irradiation of the target with a laser beam melted the target to form a plume. The plume was accumulated on the ITO glass substrate to form the TiO₂ thin film. After ablation TiO₂ coated film was furnace at 500 °C through 1 hour. The Fe₃O₃ (Wako, 99.5%) and ZnO (Sigma-Aldrich, 99.9%) film was prepared on ITO glass deposited as like same process of TiO₂ film.

The TiO₂ (P25, Degussa Corp. Anatase grade), Fe₂O₃ (Wako, 99.9%) and ZnO (Sigma-Aldrich, 99.9%) high compact thin film was coated on ITO glass (Aldrich, Indium-tin oxide coated glass, 8-12 ohm resistance) by squeegee method. The preparation of squeegee method is as follows. The powder of molecule (1gm) was mixed with conc. nitric acid (0.1 ml) and distilled water (2 ml). Then the high concentrated gold nanoparticle was added by drop wise with well mixing. The gold nanoparticles was adsorb in the surface of semiconductor due to the surface porosity and diffusion. After well mixing, 0.2 ml of Triton

X-100 (Wako) was mixed to get a paste. The paste was then used to prepare the film by squeeze method. Finally the film was heated at 400 °C for 1 h in air environment.

10.2.3 Preparation of Au-semiconductor film (immersed method)

The laser ablated and squeegee method prepared semiconductor was immersed in citrate reduction prepared gold aqueous colloidal nanoparticles suspension for 10 hours and rinsed thoroughly with Millipore water, then natural dried in air. The absorption time was carried out repeated the sample immersed in solution many times.

10.2.4 Instruments and measurements for characterization of cell

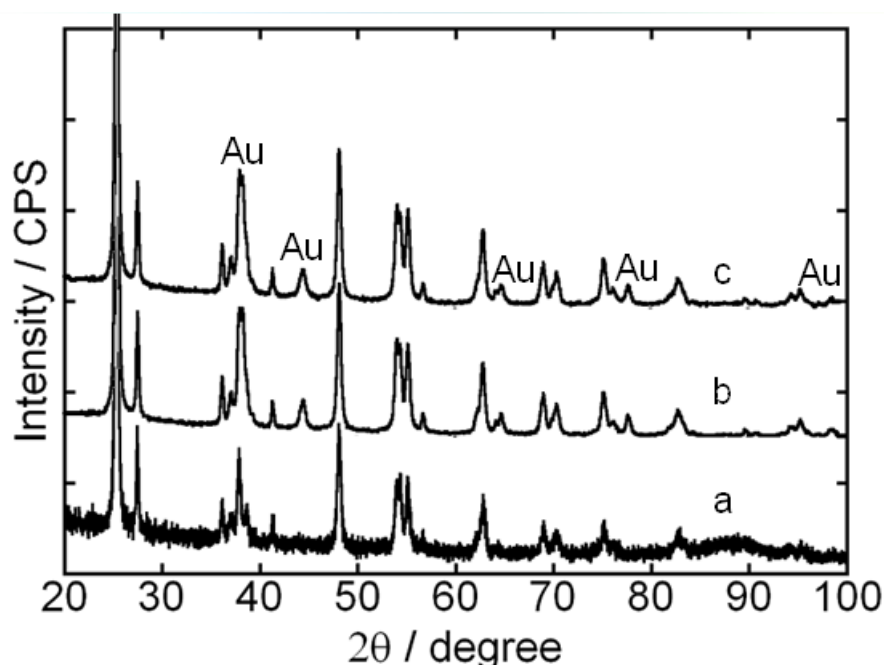
The Pt counter electrode was prepared by a magnetron sputter method on an ITO glass (Shinku Devices, MSP-10, Japan). The semiconductor film was used as a working electrode in a solar cell where a Pt film was used as a counter electrode. The two electrodes were sandwiched, and then the electrolyte solution was filled between the two electrodes. As the electrolyte 0.8 M of KI and 0.2 M of I₂ (Wako) in water or 0.8M of TBAI (tetra butylammonium iodide (Wako) and 0.2 M of I₂ in acetonitrile were employed. Current-voltage characteristics were measured using Peccell I-V curve analyzer with PECK2400-N program. The Current-voltage (I-V) characteristics under white light irradiation using a xenon lamp (Inotex 300-W LX-300F) with an IR cut-off filter and an L42 cut-off filter (one sun) was used as a visible light source ($\lambda > ca. 400 \text{ nm}$). The conditions were recorded with a Keithley2400 multimeter by varying an external load resistance. The IPCE was measured by PRP1-SAO-001, EKO instruments co.Ltd.

The UV-visible transmission spectra of films were measured using a UV-visible spectrophotometer (Shimadzu Corporation, MPS-2000). The thin films were characterized by X-ray diffraction (XRD) using an X-ray diffractometer (PANalytical) with Cu K α

radiation. The field emission Scanning Electron Microscope (FE-SEM, HITACHI, S-4100H) was used for the characterizations of films. The films surface was also measured using an energy dispersive X-ray spectrometer EDX (Energy Dispersive using X-ray, Philips, XL 30CP) attached to the cold field SEM. The structure of films were analyzed by X-ray photoelectron spectroscopy (XPS) using a Quantum-2000 Scanning ESCA-1000 microprobe (Shimadzu) with Mg α radiation.

10.3 Results and Discussion

Fig.12-1 shows the XRD spectrum of Au-TiO₂, Au-ZnO and Au-Fe₂O₃ films, prepared by squeegee method respectively. The spectrum was analyzed to the standard data sheet JCPDS and also standardization comparison with own XRD data. The Fig. 10-1 clearly shows that TiO₂, Fe₂O₃ and ZnO was not changed or not destroyed after squeegee method. The results also show that particles have crystal structure and arrays properties. The gold nanoparticles were not detected or very little detected, because of their small size and low thickness of film.



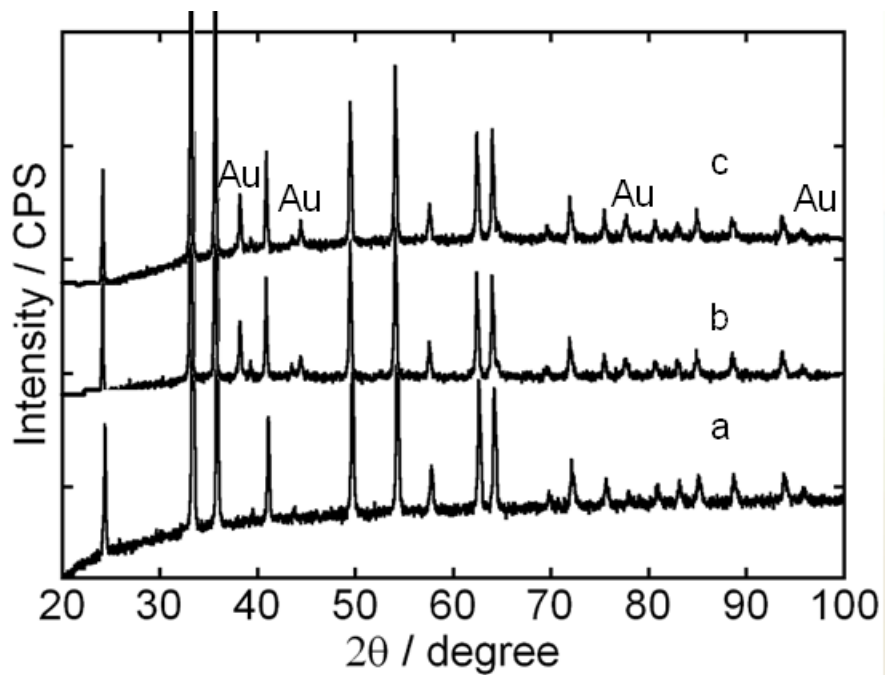
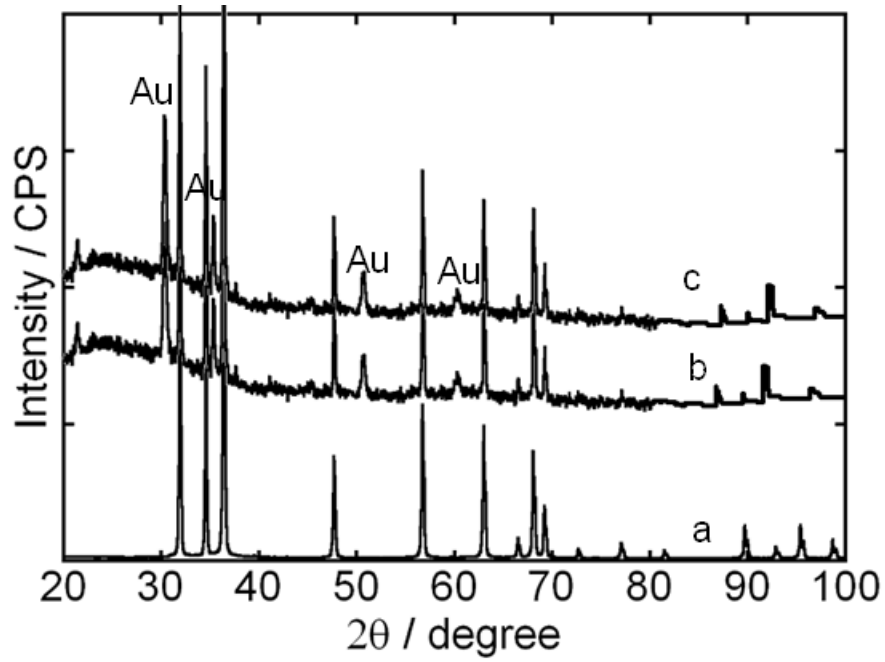


Fig. 10-1: XRD analysis of the ITO-films arrays squeegee method prepared films. Upper: (a) Only TiO_2 , (b) Au-TiO_2 film at 0°C , (c) Au-TiO_2 films at 400°C , Middle: (a) Only ZnO (b) Au-ZnO film at 0°C (c) Au-ZnO films at 400°C and Lower: (a) Only Fe_2O_3 (b) $\text{Au-Fe}_2\text{O}_3$ films at 0°C , and (c) $\text{Au-Fe}_2\text{O}_3$ films at 400°C .

The Au-nanoparticles absorption of films peak were determined by using UV-visible transmission spectra. The transmission peaks was clearly observed due to the Plasmon resonance peaks (Fig. 10-2) of gold nanoparticles around 550 nm. For all the films, Au-metals nanoparticles peaks was approved the films contained the gold nanoparticles and Au-nanoparticles direct electron transfer in to the semiconductor conduction band.

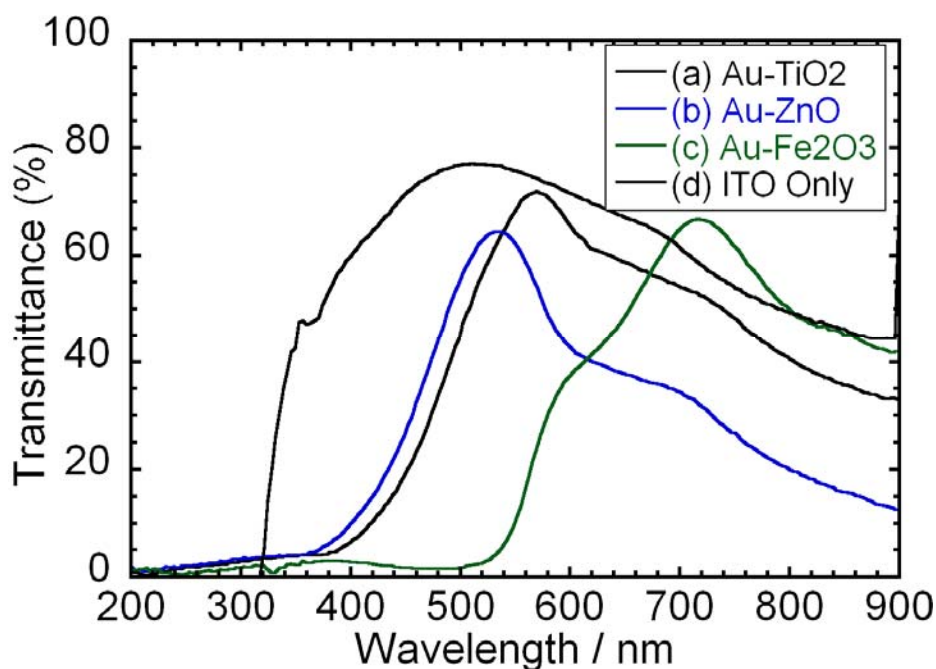
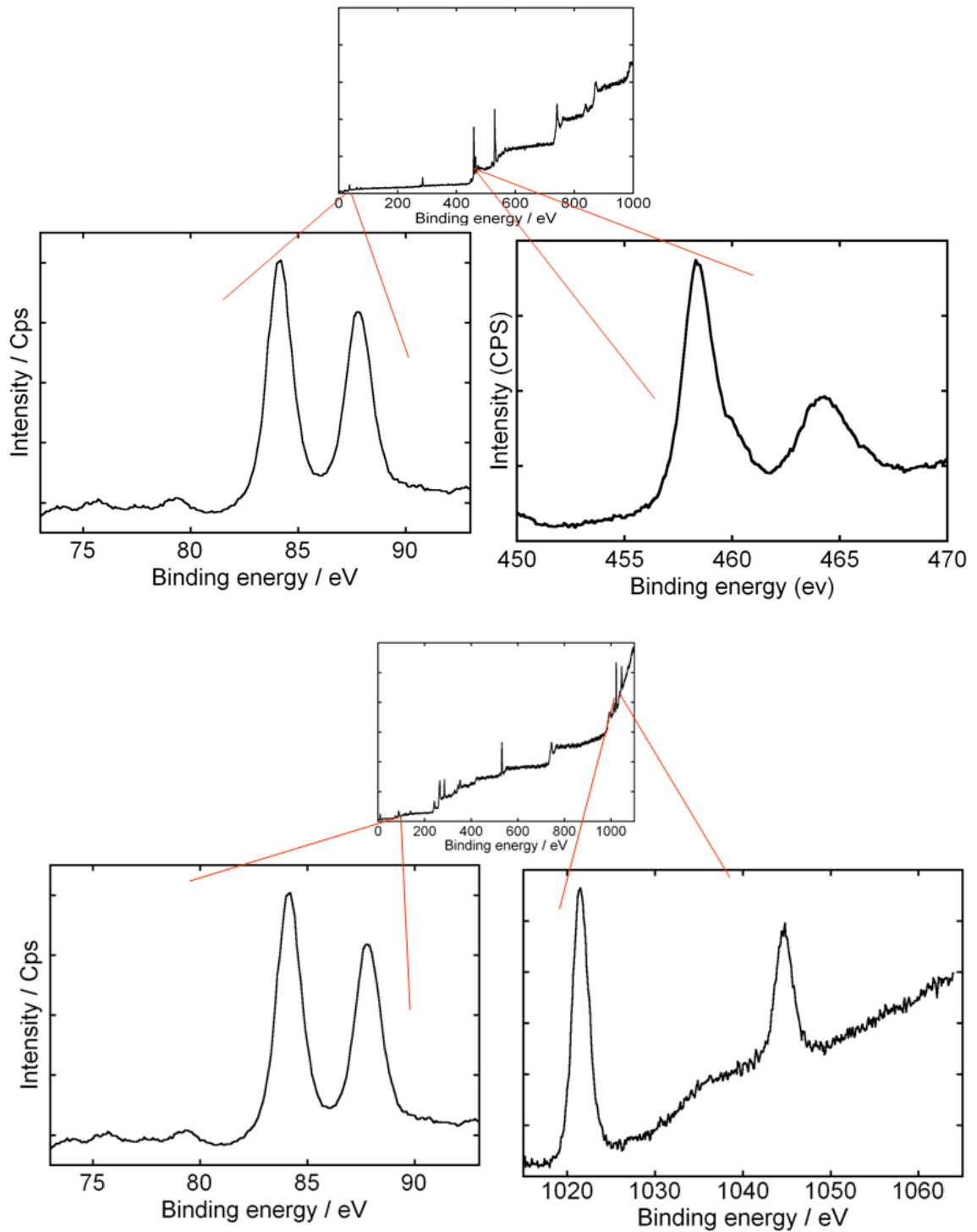


Fig. 10-2: The UV-Visible reflection spectra of Au-TiO₂, Au-ZnO and Au-Fe₂O₃ films.

We characterized of film to determine the Au-nanoparticles by the x-ray photoelectron spectroscopy (XPS) analysis (Fig. 10-3). All of prepared film was showed the gold metallic peaks 87.7 and 84 eV. The film surface have no charge either it didn't reaction in film condition.



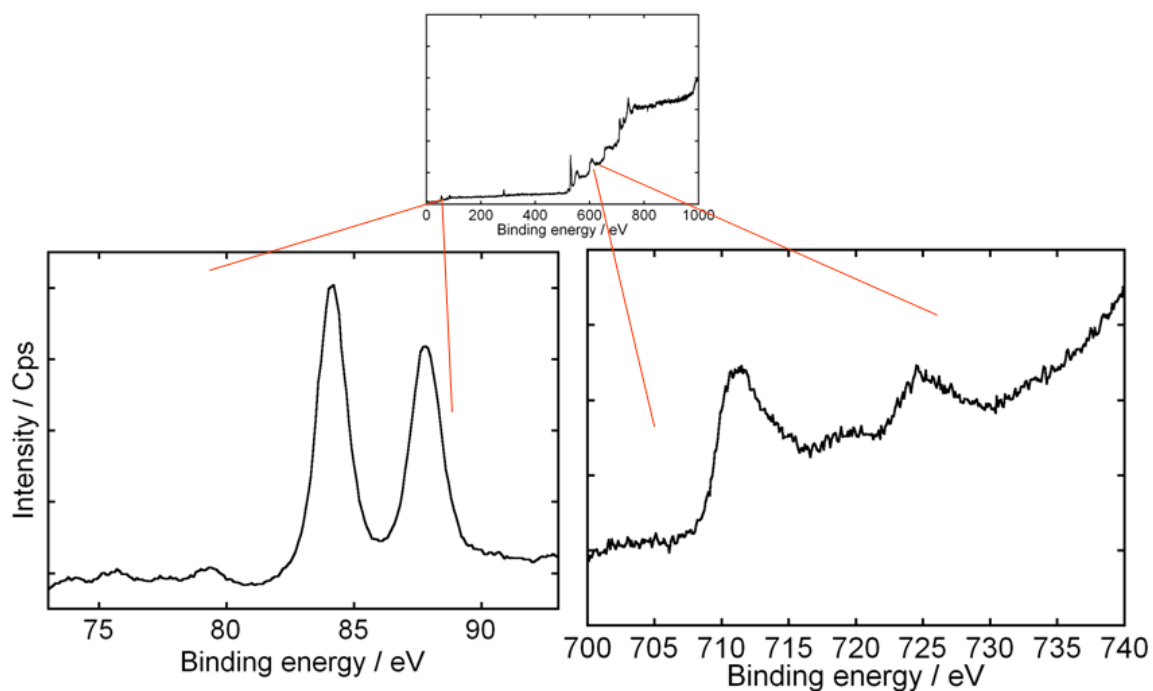


Fig. 10-3: XPS spectra of Au-TiO₂, Au-ZnO and Au-Fe₂O₃ films in photovoltaic cell.

We also recorded The SEM images of the film and nanoparticles arrays. The nanoparticles were observed in films (Fig. 10-4) and the diameter of particles size about 20nm respectively. The image showed that Au-nanoparticles have the wide surface area and distributed in surface homogeneously.

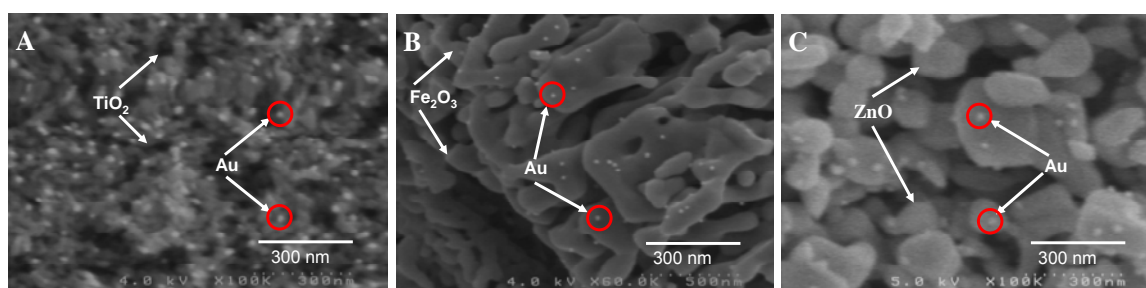


Fig. 10-4: FE-SEM images of [A] Au nanoparticles on TiO₂; [B] Au nanoparticles on Fe₂O₃; [C] Au nanoparticles on ZnO. The scale bar shown 300 nm

It has been well known that photoelectrochemical cells consists of a semiconducting materials coated photoanode and metal coated cathode electrode exhibit electrical energy from light [16]. The ITO glass coated TiO_2 film with Au-nanoparticles was used as a photoanode combined with I_2 solution (water solvent) electrolyte as an electron donor. The open circuit voltage, the short circuit current and the fill factor were found 0.30 V, 0.89 mA cm^{-2} and 0.59 and also the maximum efficiency of cell is 4.1 respectively (Fig. 10-5, a).

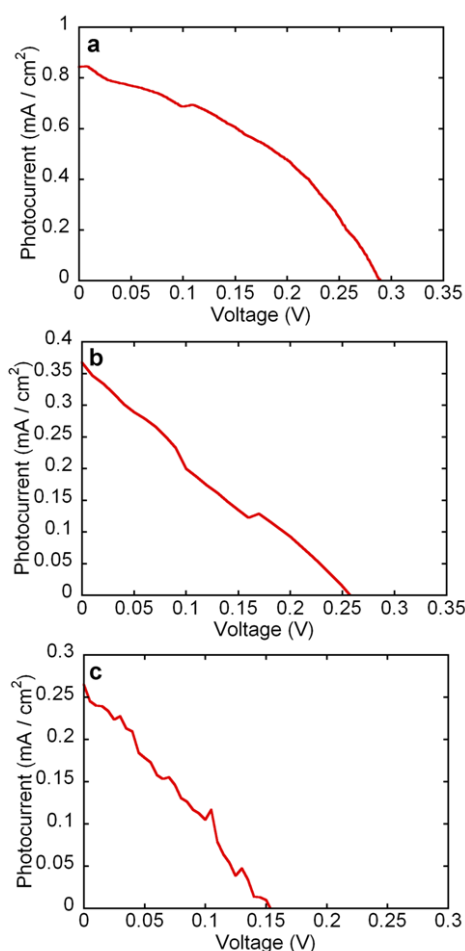


Fig. 10-5: Photocurrent-voltage characteristics of the cell with the (a) Au- TiO_2 (b) Au- Fe_2O_3 and (c) Au-ZnO film.

The Fe_2O_3 film was characterized by three types of Voltage-current method. The Au-colloidal nanoparticles solution with deposited Fe_2O_3 semiconductor film and immersed Fe_2O_3 film was produced very little amount of current (Fig. is nor shown). But the voltage resistance is good than TiO_2 and ZnO. The laser ablated Fe_2O_3 porosity is less than

squeegee prepared Fe_2O_3 film for that result Au-excited electron can not pass the easily. When the light photon illuminate the cell Au-nanoparticles and Fe_2O_3 are excited and gives the electron, that's electron cannot pass thoroughly into the ITO glass. For that result, it can be said Fe_2O_3 is not good semiconductor to passing the electron into the ITO glass. Maximum current and voltage was found of Au- Fe_2O_3 (squeegee method prepared) 0.37 mA cm^{-2} and 0.26 respectively are shown in Fig. 10-5 b. The fill factor and efficiency were mostly same 0.39 and 0.38 respectively.

The most widely used oxide as semiconductor is TiO_2 , although other wide band semiconductor oxides such as ZnO have also been employed. ZnO are interested, because their unique properties such as, higher binding energy (60 meV), wide band gap (3.37 eV), high break down strength, cohesion and excitation stability. Moreover, ZnO is one of the hardest materials in the family of II-VI semiconductors. When the light was illuminated on cell a short-circuit current density (I_{sc}) 0.25 mA/cm^2 and open-circuit voltage (V_{oc}) 0.15 V , the fill factor is 0.46 respectively (Fig 5c). After 5 min ZnO is decompose and produce current, voltage and fill factor 0.26 mA/cm^2 , 0.15V and fill factor 0.27 respectively. These have the wide opportunity to research on the solar cell. We would try to prepare stable ZnO semiconductor solar cell in our lab.

10.4 Conclusion

In conclusion we have fabricated and squeegee photovoltaic cells by using TiO_2 , Fe_2O_3 and ZnO. It was found that squeegee Au- TiO_2 film was produced more current (0.89 mA/Cm^2) than the Au-ZnO and Au- Fe_2O_3 films prepared cell. We have introduced new semiconducting materials Fe_2O_3 and ZnO with Au nanoparticles were found very impulsive photocurrent. We found the highest photocurrent with good efficiency and fill factor was Au- TiO_2 film (0.8 mA/Cm^2) prepared photovoltaic cell. We also proved that excited gold particles inject the electron cloud to semiconducting materials was accomplished the charge separation and electron gap fill-up from the donor electrolyte.

References

- [1] EI-Sayed, M. A.; *Acc.Chem.Res.* **2001**, *34*, 257-264.
- [2] Ashcroft, N. W.; Mermin, N.D.; *Solid State Physics*; Saunders College: Philadelphia, PA, 1976.
- [3] Link, S.; EI-Sayed, M. A.; *J. Phys. Chem. B* **1999**, *103*, 8410-8426.
- [4] Tian, Y. and Tatsuma, T.; *J. Am. Chem. Soc.*, **2005**, *127*, 7632-7637.
- [5] Alivisatos, A. P.; *J. Phys. Chem.* **1996**, *100*, 13226
- [6] Brus, L. E.; *Appl. Phys. A* **1991**, *53*, 465.
- [7] Alivisatos, A. P.; *Science* **1996**, *271*, 933.
- [8]Gaponenko. *Optical Properties of Semiconductor Nanocrystals*; Cambridge University Press: Cambridge, U.K., 1998.
- [9] Murray, C. B.; Norris, D. J.; Bawendi, M. G. *J. Am. Chem. Soc.* **1993**, *115*, 8706.
- [10] Yoffe, A. D. *Adv. Phys.* **2001**, *50*, 1.
- [11] Gratzel, M.; *Nature*, **2001**, *414*, , 338-344.
- [12] Frens. G., *Nature Physical Science*, **1973**, *241*, 20-22.
- [13] X. Zou, N. Maesako, T. Nomiyama, Y. Horie, T. Miyazaki,; *Solar Energy Materials and Solar Cells*, **2000**, *62*,133-142.
- [14] H. Usui, O. Miyamoto, T. Nomiyama, Y. Horie, T. Miyazaki,; *Solar Energy Materials and Solar Cells*, **2005**, *86*,123-134.
- [15] S. Somekawa, Y. Kusumoto, M. Ikeda, M. Takenouchi, P. Ngweniform, Y. Horie,; *Proceedings of Renewable Energy* **2006**, 1368-1371.
- [16] M. Gratzel; *Photoelectrochemical Cells*, **2001**, *414*, 338-344.

CHAPTER 11

SUMMARY OF THE DISSERTATION

This thesis is aimed to newly synthesize the noble metal nanoparticles and metal-semiconductor nanophotocatalysts at exploring the application of both nanomaterials in cancer cell killing therapy and photoelectrochemical cell charge separation and hydrogen production. Cancer is one of the leading causes of death in the world and preparation to the light energy harvesting assemblies for efficient light energy conversion to electric energy due to the worldwide increasing energy demand and crisis with remedy of the environment pollution. Searching for efficient method of selective cancer cell killing therapy and efficient light energy conversion to electric energy are extremely active field today. With the great development of nanotechnology, various nanoparticles in different structure, shapes and composites provides good potential for their application in cancer cell killing therapy and photoelectrochemical cell charge separation. The noble metal nanoparticles has drawn much attention on cancer cells because noble metal nanoparticles have size encourage electronic and optical properties, surface plasmon absorption, tunable and enhanced scattering and absorption properties as well as photostability and potential noncytotoxicity. Their strong absorption provides a possibility for them to be a used in photothermal cancer cell killing therapy. The metal nanoparticles on semiconductors and metal ions in semiconductor lattice structure have promoted the interfacial charge separation and tailored the photoresponse in visible light region. This two properties of metal-semiconductors nanophotocatalysts have provide the possibility of photocatalytic cancer cell killing and photoelectrochemical cell charge separation and hydrogen production. In this thesis, we showed with experimental results and discussion that both noble metal (Au)

nanoparticles and metal-semiconductor nanophotocatalysts has efficient for cancer cell killing and photoelectrochemical charge separation and also hydrogen production.

Chapter 1 shows a general feature introduction of the entire studies. First, the opportunities and advantage of noble metal nanoparticles and metal–semiconductors nanophotocatalysts was discussed for cancer cell killing and photoelectrochemical charge separation. General background scenarios of cancer and energy crisis in the world wide were also described in this chapter. The photothermal and photocatalytic cancer cell killing mechanism and photoelectrochemical cell charge separation mechanism were also described in this chapter. Finally, the aim and objectives of this study are discussed.

Chapter 2 gives details of the different experiments carried out.

Chapter 3 shows the plasmon-induced photothermal cell-killings effect of gold colloidal nanoparticles on epithelial carcinoma cells. Gold colloidal nanoparticles were prepared by the liquid laser ablation of a gold metal plate in water and also by the citrate reduction of $\text{HAuCl}_4 \cdot 4\text{H}_2\text{O}$. The gold colloidal nanoparticles with the plasmonic band strongly absorb light, which is converted to the photothermal energy. This photothermal energy gives a cytotoxic effect on epithelial carcinoma cells. Interestingly, we found that the size and shape of the nanoparticles are changed by light during the photothermal process *in vitro*. The cervical carcinoma cell line (HeLa cell) was incubated with the colloidal gold nanoparticles and then exposed to continuous visible light at 400–600 nm with UV- and heat-cutoff filters. The distinct cell-killing effect was observed by this procedure. In the absence of the gold colloidal nanoparticles, only a small amount of cells were photothermally destroyed.

Chapter 4 shows the new synthesis of copper nanoparticles in water/acetonitrile mixed solvent and their characterization. Copper nanoparticles were successfully synthesized by the borohydride reduction of copper nitrate salt in water/CH₃CN mixed solvent under inert argon-purged conditions. Cu nanoparticles were synthesized in large-scale production for the first time by introducing CH₃CN into water and preventing oxidation during the preparation of nanoparticles. Nanoparticles were characterized by using UV-visible absorption spectroscopy, transmission electron microscopy (TEM), X-ray photoelectron spectroscopy (XPS) and X-ray diffraction (XRD) techniques. High resolution TEM pictures showed the formation of homogeneous cubic-structured copper nanoparticles with sizes less than 100 nm. This new kind of synthesis method shows the excellent stability compared with that of citrate-protected copper nanoparticles, which may provide an efficient way to improve the fine tuning of the structure and size of copper nanoparticles.

Chapter 5 shows the enhanced photocatalytic cytotoxic activity of Au@TiO₂ nanopellets against human epithelial carcinoma (HeLa) cells. The photocatalytic cancer cell-killing activity of the metallic Au-capped TiO₂ (Au@TiO₂) composite colloidal nanopellet has been investigated on HeLa cells under the UV-visible light irradiation. The Au@TiO₂ composite nanopellet photocatalyst with the uniform Au capped TiO₂ structure was successfully synthesized by simply reducing HAuCl₄ on the surface of TiO₂ nanoparticles. The morphological structure and surface properties of Au@TiO₂ were characterized by using UV-visible absorption spectroscopy, TEM, SEM, XPS, EDX and XRD analysis. The photocatalytic cell-killing activity of the Au@TiO₂ nanopellet was found to vary with the molar ratio of Au to TiO₂. The direct involvement of the metal particles in mediating the electron transfer from the photoexcited TiO₂ under the band gap excitation is considered to carry out the efficient photocatalytic reaction on the cells. The charge separation and the interfacial charge-transfer promote the photocatalytic cancer-cell killing more than the TiO₂

semiconductor alone. It was found that the TiO₂ nanoparticles capped with low concentration of gold (TiO₂: Au molar ratio is > 1:1) killed more malignant (HeLa) cells by 50% than TiO₂ nanoparticles alone at the same concentration.

Chapter 6 shows the cytotoxic evaluation of Ag@TiO₂ core-shell composite nanocluster against cancer (HeLa) cells. The Ag metal core-TiO₂ shell (Ag@TiO₂) composite nanocluster photocatalyst with uniform size, shape and core-shell structures were successfully synthesized by a simple citrate reduction method. The core-shell structure of Ag@TiO₂ nanocluster was characterized by using TEM, SEM, XPS, EDX and XRD analyses. It was found that the Ag core is in metallic form which is covered by TiO₂ shell with 3-5 nm thickness and that the core-shell particles size is about 30 nm. The photocatalytic cell killing performance of the Ag@TiO₂ core-shell photocatalyst has been investigating under the UV-visible light (350-600 nm) irradiation. The photocatalytic cell killing efficiency of the Ag@TiO₂ core-shell composite nanoclusters depends on the molar concentration of TiO₂. Ag: TiO₂ with molar concentration from 1:1 to 1:9 was studied and 1:7 mM was found to be optimum. The direct involvement of the Ag metal particles in mediating electron transfer between photoexcited TiO₂ under the band gap excitation is necessary to explain the photocatalytic reaction on cells. The charge separation and interfacial charge-transfer is well tailored and the photocatalytic cancer cell killing efficiency of Ag@TiO₂ is better than the TiO₂ semiconductor. It was found that the Ag@TiO₂ with low concentration killed more malignant (HeLa) cells by 80% compared to TiO₂ semiconductor nanoparticles.

Chapters 7 illustrate new simple synthesis of Cu-TiO₂ nanocomposite and successful application on cancer cell for photocatalytic cancer cell killing. The metallic Cu nanoparticles on heterogeneous TiO₂ surface have been successfully deposited by the new

simple borohydride reduction of copper nitrate salt in water / CH₃CN aqueous mixture under Ar atmosphere. The synthesized Cu-TiO₂ nanocomposite shows light absorption in the wide visible region and XPS studies show that the Cu exists in metallic form. The catalytic activity of the Cu-TiO₂ nanocomposite was evaluated by application to the photocatalytic cancer cell-killing (HeLa) under the UV-visible light irradiation. The Cu-TiO₂ nanocomposite showed higher photocatalytic activity than commercial TiO₂ (P25) under the similar experimental conditions. Based on the observed results, a plausible mechanism was proposed. The morphological structure and the surface species of Cu-TiO₂ nanocomposites were determined by using UV-vis absorption spectroscopy, TEM, XPS, XRD, and EDX techniques.

Chapter 8 shows mineralized-assisted shape-controlled synthesis, characterization and photocatalytic evaluation of CdS microcrystals. High quality, well crystallized, single crystal, wurtzite CdS hexagonal microtowers (with and without tubular structure) and CdS with octahedral geometry were successfully synthesized by tuning the solvent ratio of water and ethanol for the first time on a large scale without using any catalysts or templates. The products were characterized by X-ray diffraction (XRD), energy-dispersive X-ray spectrometry (EDX), transmission electron microscopy (TEM) and field emission scanning electron microscopy (FE-SEM). CdS with microtowers, octahedral geometry and hexagonal plates was formed by thermal decomposition of cadmium thiocyanate at 400 °C under open atmospheric conditions. The influences of solvent, initial precursor concentration, decomposition temperature and time on the morphology of CdS were investigated and the results were discussed. The XRD results showed that the cadmium thiocyanate complex is completely decomposed into CdS at 300 °C for 2 h and the wurtzite phase was formed under all experimental conditions, which open a door for well crystallized, single phase CdS synthesis on a large scale. The diffuse reflectance spectra showed that CdS microtowers

have strong visible light absorption compared with the octahedral geometry, revealing the existence of a profound shape-property relationship of CdS. The CdS microtowers with a Pt co-catalyst showed a high rate of photocatalytic hydrogen production from water containing 0.1 M Na₂S and 0.1M Na₂SO₃ as sacrificial reagents under visible light irradiation ($\lambda \geq 400$ nm). The possible growing mechanism of various types of the CdS morphology was also discussed.

Chapters 9 show the effect of thermal treatment of Fe₂O₃ films on performance of wet-typed Fe₂O₃ solar cells. A wet type solar cell based on Fe₂O₃ films prepared by the laser ablation method was investigated. The performance was increased drastically by the thermal treatment of the Fe₂O₃/FTO films. This enhancement effect is caused by the improvement of the binding interface between FTO and Fe₂O₃.

Chapters 10 gives the comparative study of plasmon-induced charge separation of TiO₂ Fe₂O₃, ZnO films loaded with gold nanoparticles. The gold colloidal nanoparticle was prepared by citrate reduction from chloroauric acid (HAuCl₄). An ITO glass was coated by laser ablation and squeegee methods with nanoporous TiO₂, Fe₂O₃ or ZnO film and the film was further loaded with Au-nanoparticles. The film was characterized by UV-visible absorption transmittance spectroscopy, SEM, XPS, EDX and XRD techniques. The gold nanoparticles which absorb visible light by plasmonic and photoexcited electrons flow to the TiO₂, Fe₂O₃ or ZnO conduction band. The cells were evaluated by short circuit current and open circuit voltage. In this study we compared the difference in semiconductors with Au-nanoparticles and found that the Au-TiO₂, Au-Fe₂O₃ or Au-ZnO film is one of the challenging photo-current producers with good efficiency and durability than the dye sensitized solar cell (DSSC).

PUBLICATIONS

1. **Md. Abdulla-Al-Mamun**, Yoshihumi Kusumoto, Aki Mihata, Md. Shariful Islam, Bashir Ahmmad, **Plasmon-induced Photothermal Cell-killing Effect of Gold Colloidal Nanoparticles on Epithelial Carcinoma Cells**, *Photochemical and Photobiological Sciences*, 8 (2009) 1125-1129.
2. **Md. Abdulla-Al-Mamun**, Yoshihumi Kusumoto, Manickavachagam Muruganandham, **Simple New Synthesis of Copper Nanoparticles in Water/acetonitrile Mixed Solvent and their Characterization**, *Materials Letters*, 63(23) (2009) 2007-2009.
3. **Md. Abdulla-Al-Mamun**, Yoshihumi Kusumoto, **New Simple Synthesize of Cu-TiO₂ Nanocomposite: Highly Enhancing of Photo Catalytic Cell-killing Observation on Epithelia Carcinoma (HeLa) cell**, *Chemistry Letters*, 38(8) (2009) 826-827.
4. **Md. Abdulla-Al-Mamun**, Yoshihumi Kusumoto, Md. Shariful Islam, Hailong Yang, **Enhanced Photocatalytic Cytotoxic Activity of Au@TiO₂ Nanopellets against Human Epithelial Carcinoma (HeLa) Cells**, *Chemistry Letters*, 38(10) (2009) 950-952.
5. **Md. Abdulla-Al-Mamun**, Yoshihumi Kusumoto, Md. Shariful Islam, **Cytotoxic Evaluation of Ag@TiO₂ Core-shell Composite Nanocluster against Cancer Cells**, *Chemistry Letters*, 38(10) (2009) 980-981.
6. **Md. Abdulla-Al-Mamun**, Yoshihumi Kusumoto, Hailong Yang, Md. Shariful Islam, **Photocatalytic Cancer (HeLa) Cell-killing Enhanced with Cu-TiO₂ Nanocomposite**, *Topics in Catalysis*, accepted articles.
7. **Md. Abdulla-Al-Mamun**, Hailong Yang, Bashir Ahmmad, Yoshihumi Kusumoto, **Enhancement of Photocatalytic Cancer Cell-Killing Activity by Using Ag@TiO₂ Core-Shell Composite Nanoclusters**, *NSTI-Nanotech*, Vol. 2, 11-14, May, 2009.
8. Manickavachagam Muruganandham, Yoshihumi Kusumoto, Okamoto Chiyo, **Md. Abdulla-Al-Mamun**, Bashir Ahmmad, **Mineralizer-Assisted Shape-Controlled Synthesis, Characterization and Photocatalytic Evaluation of CdS Microcrystals**, *The Journal of Physical Chemistry C*, 113(45) (2009) 19506-19517.
9. Shouichi Somekawa, Yoshihumi Kusumoto, **Md. Abdulla-Al-Mamun**, Manickavachagam Muruganandham, Yuji Horie, **Wet-type Fe₂O₃ solar cells based on Fe₂O₃ films prepared by laser ablation: drastic temperature effect**, *Electrochemistry Communications*, 11(11) (2009) 2150-2152.
10. Bashir Ahmmad, Yoshihumi Kusumoto, **Md. Abdulla-Al-Mamun**, Aki Mihata, Hailong Yang, **Effect of Single Walled Carbon Nanotube as Counter Electrode on Laser-deposited Fe₂O₃ and TiO₂ Films Solar Cells**, *Journal of Scientific Research*, 1(3) (2009), 430-437.

11. Bashir Ahmmad, Yasuhiro Kitamura, Yoshihumi Kusumoto, Hailong Yang, **Md. Abdulla-Al-Mamun**, **A new type of solid state solar cell based on Fe₂O₃, SiC and crystal growth inhibitors**, *Journal of Scientific Research*, 2(1) (2010), 1-8.
12. Shouichi Somekawa, Yoshihumi Kusumoto, Hailong Yang, **Md. Abdulla-Al-Mamun**, Bashir Ahmmad, **Fabrication, N-doping mechanism and evaluation of N-doped TiO₂ thin films based on laser ablation method**, *Journal of Scientific Research*, 2(1) (2010), 17-23.
13. Miyuki Ikeda, Yoshihumi Kusumoto, Hailong Yang, Shouichi Somekawa, Hayato Uenjyo, **Md. Abdulla-Al-Mamun**, Yuji Horie, **Photocatalytic hydrogen production enhanced by laser ablation in water–methanol mixture containing titanium (IV) oxide and graphite silica**, *Catalysis Communications*, 9(6) (2008) 1329–1333.
14. Shouichi Somekawa, Yoshihumi Kusumoto, **Md. Abdulla-Al-Mamun**, Makoto Nakashima, Yuji Horie, **Effect of Thermal treatment of Fe₂O₃/FTO Films on Performance of Wet-type Fe₂O₃ Solar Cells**, *Proceedings of the 6th International Symposium on Transparent Oxide Thin Films for Electronics and Optics (TOEO-6)*, June (2009) 15p-P034-1~3.
15. Bashir Ahmmad, Yoshihumi Kusumoto, **Md. Abdulla-Al-Mamun**, **One Step Synthesis of C and/or N-doped TiO₂ Submicrostructures**, *Proceedings of the 6th International Symposium on Transparent Oxide Thin Films for Electronics and Optics (TOEO-6)*, June (2009) 15p-P042-1~4.
16. Shouichi Somekawa, Yoshihumi Kusumoto, **Md. Abdulla-Al-Mamun**, Yuji Horie, **N-doping Process and Evaluation of N-doped TiO₂ thin films prepared by laser ablation method**, *Proceedings of the 6th International Symposium on Transparent Oxide Thin Films for Electronics and Optics (TOEO-6)*, June (2009) pp. 16p-P094-1~3.
17. Bashir Ahmmad, Yasuhiro Kitamura, Yoshihumi Kusumoto, **Md. Abdulla-Al-Mamun**, **Fe₂O₃ and SiC-Based o Solid State Solar Cells: Effect of Crystal Growth Inhibitor**, *Proceedings of the 6th International Symposium on Transparent Oxide Thin Films for Electronics and Optics (TOEO-6)*, June (2009) pp. 16p-P125-1~4.
18. Hailong Yang, Yoshihumi Kusumoto, Miyuki Ikeda, Hayato Uenjyo, **Md. Abdulla-Al-Mamun**, Shouichi Somekawa, Bashir Ahmmad, **Enhancement effect of laser ablation in liquid on hydrogen production using titanium(IV) oxide and graphite silica**, *Proceedings of the ISES Solar World Congress 2007*, Beijing, China, Tsinghua Univeristy Press, Volume V (2007) 2790-2794.
19. Hailong Yang, **Md. Abdulla-Al-Mamun**, Miyuki Ikeda, Yuji Horie, Yoshihumi Kusumoto, Preparation and Application of Nanoparticles by Laser Ablation in Liquid Environment, *Report on Topical Meeting of The Laser Society of Japan*, (365) (2007) 31-36.
20. Bashir Ahmmad, Hailong Yang, **Md. Abdulla Al-Mamun**, Yoshihumi Kusumoto, Tandem Cell for Photocatalytic Hydrogen Production: Material Design, *Proceeding of the 2008 Korea-Japan Symposium on Frontier Photoscience*, Jeju, Korea, September (2008)116-117.

- 21. Md. Abdulla-Al-Mamun, Yoshihumi Kusumoto, Photocatalytic Cell Killing Activity of Ag@TiO₂ Core-Shell Composite Nanocluster on Human Epithelial Carcinoma (HeLa) Cell, *The Journal of Physical Chemistry C* (to be submitted).**
- 22. Md. Abdulla-Al-Mamun, Yoshihumi Kusumoto, Enhancement of Photocatalytic Cell Killing Activity on Human Epithelial Carcinoma (HeLa) Cell by Gold Capped TiO₂ Nanopellet, *Applied Catalysis A: General* (to be submitted).**
- 23. Md. Abdulla-Al-Mamun, Atsushi Ohno, Junji Hamada, Ahmmad Bashir, Yusuke Sensai, Yoshihumi Kusumoto, Cancer Cell Killing Effect of Silver Colloidal Nanoparticles and Ag@TiO₂ Colloidal Nanoclusters on HeLa Cells, *Abstract of the 2008 Annual Meeting of Japan Society of Molecular Science*, Fukuoka, Japan, September 24-27, (2008) p.PR0822-1~2.**
- 24. Md. Abdulla-Al-Mamun, Yasuhiro Kitamura, Satoru Shiraki, Yoshihumi. Kusumoto, Cytotoxic Effect of Au Colloidal Nanoparticles and Au-capped TiO₂ Nanoparticles on HeLa Cells, *Abstract of the 61th Divisional Meeting on Colloid and Interface Chemistry, The Chemical society of Japan*, Kyushu University, Fukuoka, Japan, September 7-9, (2008) p.41, 1A05.**
- 25. Md. Abdulla-Al-Mamun, and Yoshihumi Kusumoto, Plasmon-induced Cytotoxic Effect of Au Colloidal Nanoparticles on HeLa Cells, *Abstract of the 26th Solid Surface and Photochemistry Conference*, Japan, November 26-27, (2007) pp.60-61, 208.**
- 26. Md. Abdulla-Al-Mamun, and Yoshuhumi Kusumoto, Plasmon-induced solar cells based on Au-nanoparticles, *Abstract of the 25th Kyushu Colloid Colloquium, The Kyushu Branch of The Chemical Society of Japan*, Kagoshima, Japan, August 25, (2007) p. 40, P22.**
- 27. Md. Abdulla-Al-Mamun, Yoshihumi Kusumoto, Hayato Uenjo, Cytotoxic effect of colloidal metal-nanoparticles on the HeLa-cell line, *Abstract of the 24th Kyushu Colloid Colloquium,, The Kyushu Branch of The Chemical Society of Japan*, Fukuoka, Japan, August 19 (2006) p.32, P6.**

CONFERENCE PRESENTATIONS

1. **14th -16th October, 2009, Akita, Japan**, The 12th Japan-Korea Symposium on Catalysis (JKSC 12 2009), **Oral Contribution**
2. **28th June-3rd July, 2009, Suntec City, Singapore**, The International Conference on Materials for Advance Technologies (ICMAT 2009), **Oral Contribution**
3. **3rd -7th May, 2009, Houston, Texas, USA**, Nano Science and Technology Institute, Nanotechnology Conference and Trade Show (Nanotech 2009), **Poster Contribution**
4. **25th -28th September, 2008, Jeju, Korea**, The 2008 Korea-Japan Symposium on Frontier Photoscience, **Mutual Poster Contribution**
5. **24th -27th September, 2008, Fukuoka, Japan**, Annual Meeting of Japan Society of Molecular Science, **Oral Contribution**
6. **7th -9th September, 2008, Fukuoka, Japan**, The 61th Divisional Meeting on Colloid and Interface Chemistry, **Oral Contribution**
7. **26th-27th November, 2007,Osaka, Japan**, 26th Solid Surface and Photochemistry Conference, **Oral Contribution**

8. 14th September, 2007, Ibusuki, Japan, The 365th Topical Meeting of The Laser Society of Japan, **Oral Mutual Contribution**

9. 24th-25th, August, 2007 Kagoshima, Japan, 25th Kyushu Colloid Colloquium, **Poster Contribution**

10. 19th-20th, August, 2006, Fukuoka, Japan, 24th Kyushu Colloid Colloquium, **Poster Contribution**

.....The end.....